Modular soft pneumatic actuator system design for compliance matching

Thèse N° 7594

Présentée le 2 mai 2019

à la Faculté des sciences et techniques de l'ingénieur
Laboratoire de robotique reconfigurable
Programme doctoral en robotique, contrôle et systèmes intelligents

pour l'obtention du grade de Docteur ès Sciences

par

Matthew Aaron ROBERTSON

Acceptée sur proposition du jury

Prof. A. Ijspeert, président du jury
Prof. J. Paik, directrice de thèse
Prof. K. Petersen, rapporteuse
Prof. O. Brock, rapporteur
Prof. R. Gassert, rapporteur

2019

ÉCOLE POLYTECHNIQUE
FÉDÉRALE DE LAUSANNE

Abstract

The future of robotics is personal. Never before has technology been as pervasive as it is today, with advanced mobile electronics hardware and multi-level network connectivity pushing "smart" devices deeper into our daily lives through home automation systems, virtual assistants, and wearable activity monitoring. As the suite of personal technology around us continues to grow in this way, augmenting and offloading the burden of routine activities of daily living, the notion that this trend will extend to robotics seems inevitable. Transitioning robots from their current principal domain of industrial factory settings to domestic, workplace, or public environments is not simply a matter of relocation or reprogramming, however. The key differences between "traditional" types of robots and those which would best serve personal, proximal, human interactive applications demand a new approach to their design. Chief among these are requirements for safety, adaptability, reliability, reconfigurability, and to a more practical extent, usability. These properties frame the context and objectives of my thesis work, which seeks to provide solutions and answers to not only how these features might be achieved in personal robotic systems, but as well what benefits they can afford. I approach the investigation of these questions from a perspective of compliance matching of hardware systems to their applications, by providing methods to achieve mechanical attributes complimentary to their environment and end-use. These features are fundamental to the burgeoning field of Soft Robotics, wherein flexible, compliant materials are used as the basis for the structure, actuation, sensing, and control of complete robotic systems. Combined with pressurized air as a power source, soft pneumatic actuator (SPA) based systems offers new and novel methods of exploiting the intrinsic compliance of soft material components in robotic systems. While this strategy seems to answer many of the needs for human-safe robotic applications, it also brings new questions and challenges: What are the needs and applications personal robots may best serve? Are soft pneumatic actuators capable of these tasks, or "useful" work output and performance? How can SPA based systems be applied to provide complex functionality needed for operation in diverse, real-world environments? What are the theoretical and practical challenges in implementing scalable, multiple degrees of freedom systems, and how can they be overcome? I present solutions to these problems in my thesis work, elucidated through scientific design, testing and evaluation of robotic prototypes which leverage and demonstrate three key features:

- Intrinsic compliance: provided by passive elastic and flexible component material properties

- Extrinsic compliance: rendered through high number of independent, controllable degrees of freedom
- Complementary design: exhibited by modular, plug and play architectures which combine both attributes to achieve compliant systems

Through these core projects and others listed below I have been engaged in soft robotic technology, its application, and solutions to the challenges which are critical to providing a path forward within the soft robotics field, as well as for the future of personal robotics as a whole toward creating a better society.

Résumé

L’avenir de la robotique est personnel. Jamais auparavant la technologie n’avait été aussi omniprésente, avec son matériel électronique mobile évolué et sa connectivité réseau multiniveau qui propulse les appareils «intelligents» au cœur de notre quotidien grâce aux systèmes domotiques, aux assistants virtuels et à la surveillance des activités portables. Alors que la suite de technologies personnelles qui nous entoure continue de croître de cette manière, en alourdissant et en allégeant le fardeau des activités de routine de la vie quotidienne, la notion selon laquelle cette tendance s’étendra à la robotique semble inévitable. La transition des robots de leur principal domaine actuel de configuration d’usines industrielles vers des environnements domestiques, professionnels ou publics n’est cependant pas simplement une question de déménagement ou de reprogrammation. Les principales différences entre les types de robots «traditionnels» et ceux qui serviraient le mieux les applications interactives humaines, proximales et personnelles nécessitent une nouvelle approche de leur conception. Les principales sont les exigences en matière de sécurité, d’adaptabilité, de fiabilité, de reconfigurabilité et, dans une mesure plus pratique, de facilité d’utilisation. Ces propriétés définissent le contexte et les objectifs de mon travail de thèse, qui vise à fournir des solutions et des réponses non seulement à la manière dont ces fonctionnalités pourraient être obtenues dans des systèmes robotiques personnels, mais également aux avantages qu’elles peuvent offrir. J’aborde l’examen de ces questions du point de vue de l’adéquation de la conformité des systèmes matériels à leurs applications, en fournissant des méthodes permettant d’obtenir des attributs mécaniques complémentaires à leur environnement et à leur utilisation finale. Ces caractéristiques sont fondamentales dans le domaine en plein essor de la robotique douce, où des matériaux souples et compatibles sont utilisés comme base pour la structure, l’actionnement, la détection et le contrôle de systèmes robotiques complets. Associé à l’air comprimé comme source d’alimentation, le système basé sur un actionneur pneumatique doux (SPA) offre de nouvelles méthodes novatrices d’exploitation de la conformité intrinsèque des composants de matériaux souples dans les systèmes robotiques. Bien que cette stratégie semble répondre à de nombreux besoins d’applications robotiques sûres pour l’homme, elle apporte également de nouvelles questions et de nouveaux défis : Quels sont les besoins et les applications que les robots personnels peuvent mieux servir ? Les actionneurs pneumatiques souples sont-ils capables de ces tâches ou de résultats de travail et de performances «utiles» ? Comment les systèmes basés sur SPA peuvent-ils être appliqués pour fournir des fonctionnalités complexes nécessaires au fonctionnement dans des environnements divers et réels ? Quels sont les défis théoriques et pratiques liés à la mise en œuvre de systèmes évolutifs à plusieurs degrés de liberté et comment peuvent-ils être surmontés ? Je présente des solutions à ces problèmes dans mon travail de thèse, élucidé au moyen de la conception scientifique, des tests et de l'évaluation de prototypes robotiques qui exploitent et démontrent trois caractéristiques clés :

- Conformité intrinsèque : fournie par les propriétés passives des matériaux des composants élastiques et flexibles
- Conformité extrinsèque : rendu par un nombre élevé de degrés de liberté contrôlables indépendants
- Conception complémentaire : présentée par des architectures modulaires, plug and play, qui combinent les deux attributs pour obtenir des systèmes conformes

Grâce à ces projets de base et aux autres projets énumérés ci-dessous, je me suis engagé dans la technologie de la robotique douce, son application et des solutions aux défis qui sont essentiels pour assurer la voie à suivre dans le domaine de la robotique douce, ainsi que pour l'avenir

Keywords: Soft robotics, soft pneumatic actuators, modular robots, wearable robots, assistive devices, rehabilitation robotics, physical human-robot interaction, origami robots, heuristic control, reconfigurable robots

Contents

List of Figures

List of Tables

Introduction

Robotics is advancing closer to becoming a part of our everyday lives. The recent trend toward personal, and especially wearable technology, is recognizable throughout the robotics community both in research and commercial sectors [1, 2]. Typically generalized as exoskeleton-type devices, these machines feature close physical coupling to human body joints, for assistance, rehabilitation, or augmentation of upper limb [3, 4, 5] or lower body [6, 7, 8] movements. Other devices have been developed for indirect forms of assistance, targeting daily living activities for robots that act as portable collaborators or assistants, literally lending a helping hand to compensate for basic motor function disabilities or help with shared labor [9, 10, 11, 12]. Interest in these areas has driven several wearable robotic devices to a new market that has expanded to the level of an international robot-assisted sport competition for physically disabled athletes, the Cybathlon [13, 14, 15].

Breaking from their traditional roles, serving primarily industrial tasks in isolation from human operators, robots are following a paradigm shift which trends more toward direct or proximal human interaction [16, 17]. Even among typical applications where robots are employed to function independently from people in remote or hazardous settings, robustness has been recognized as a critical feature to be considered with equal priority to other technical engineering challenges [18]. These present and forward looking objectives have provided impetus across the robotics field to embrace new approaches not only to the performance and design of the next generation of robots, but equally to their material composition, manufacturing, and control.

Soft robotics has emerged recently to address many of the challenges that have been encountered in the development of user and environmentally safe, interactive applications. This field is characterized by the use and integration of new materials and designs which leverage their implicit attributes of compliance and adaptability to afford safety and robustness. These qualities are embedded in soft robotic systems from the "ground up" so to speak, beginning with the actuators themselves which govern the nature of mechanical interactions between the system and external bodies. Although various new technologies have been explored for use in soft robotics including shape memory alloys (SMA) [19, 20], shape memory polymers (SMP) [21, 22], dielectric elastomer actuators (DEA) [23, 24], hydraulically amplified self-healing electrostatic actuators (HASEL) [25], among others [26], the principle component of a broad class of soft robots are powered by soft pneumatic actuators (SPAs)

[27, 28, 29, 30, 31, 32, 33, 34, 35, 36].

SPAs are primarily composed of naturally compliant rubbers and activated by pressurized air. Although SPAs can be fabricated and classified in a variety of ways, these common features enable robotic systems which are more safe, adaptable, lightweight, low-cost, and customizable in comparison to traditional rigid metal based robotic devices. In their most basic form, SPAs are comprised of a sealed, hollow main body structure, typically formed by casting a liquid silicone elastomer into 3D-printed or machined multi-part molds. The sealed structure nominally expands to generate motion in response to a pressure input, however with the addition of various constraints which selectively change the stiffness properties of the actuator body, more directed and specific motion paths can be achieved from the inflation of the rubber structures. The addition of an inextensible layer attached to only one side of a slender SPA forces the actuator to bend upon inflation, in the direction of the stiff layer. Another type of common constraint applied to SPAs is fiber reinforcement, a class which includes the well-known McKibben muscle [37]. These actuators utilize a flexible yet inextensible fiber wrapped around the body of a slender SPA which can be wrapped at different angles relative the axial direction of the actuator to realize different motion modes, including elongation, contraction, or torsion [38, 39].

Despite the method of constraint or final form, SPAs are nevertheless holistically soft, compliant structures which inherit the properties of the materials from which they are fabricated. Likewise, these properties are conveyed to the behavior of the robotic system they are ultimately employed to power. Rather than being added as secondary features, the compliance, flexibility, adaptability, and robustness of soft robotic systems become implicit, irrevocable attributes of the system as a whole.

Due to these advantages, SPAs have found use in a wide variety of diverse applications. Bio-inspired platforms have investigated leveraging soft morphology for robustness under extreme conditions [40] and adaptability for legged, serpentine, and even rolling locomotion [41, 42, 43, 44]. Most existing designs have not been deployed for end-use but are foreseen to provide benefit in search and rescue or remote exploration operations. Toward industrial applications, SPAs promise new capabilities in tasks including manipulation [45, 46, 47, 48], gripping [49, 50, 51], and human collaboration [52, 53] to extend the already successful existing use of soft material end-effectors and pneumatic power in product manufacturing, assembly, and distribution operations [54].

Following recent interest and progress in the development of wearable robotics, soft actuators and systems have attracted attention for their potential to greatly extend and expand applications which feature robots in direct contact with the human body, including rehabilitation [55, 8, 56, 57], daily assistance [9, 58, 59], prosthetics and orthotics [60, 61, 62], or performance augmentation [63]. While the field of soft robotics is not responsible alone for driving the development of new solutions which leverage passive compliance in mechanical design to address the high impact challenges of robust and safe robot interactions, SPAs provide unparalleled opportunity toward achieving the necessary performance, efficacy, and simplicity for this class of next-generation robotic systems. Indeed, the potential if not the inevitability of this technology is reflected even in fictional movie depictions of the future like *Big Hero 6* [64], which features an inflatable soft robot for health and personal assistance. While the technology presented in the movie as fantasy remains relatively distant from reality, the movie conveys realistic expectations for the prospect of soft technology as an integral part of interactive and practical robotic systems compatible with our daily lives or real-world settings.

In practice, many demonstrations of SPAs presented in research or implemented for simple tasks utilize single or low-DoFs. Those which do incorporate multiple DoFs lack a coherent or extensible approach to the design and integration necessary for their deployment in real-world scenarios or devices. Nevertheless, effective real-world robotic applications typically require a level of complexity which is comparable to the given tasks they are designed to perform. This prospect predicates the need for new design methodologies for SPA based systems which incorporate both the benefits of *intrinsic compliance* derived from strategically selected soft material actuator properties, as well as the requisite functionality of *extrinsic compliance* through fully controllable, high-DoF system-level designs.

Problem statement

Wearable robots offer unprecedented potential to transform our lives across a range of applications from specialized care environments to daily activities. Several limitations impede the progress of system development which allow active robotic systems to interface with human users in complementary fashion. In short, this is because **we lack core hardware solutions for wearable and interactive robotic systems.** These limitations define the needs in this field; high mobility, sufficient force, speed, bandwidth, range of motion, and full range of impedance is required to match the complex movements and capabilities of human users, system adaptability is required to accommodate varying body types and unobtrusive alignment with joints, and space efficiency or compactness is crucial for portability and reducing the potential burden of carried or worn hardware. These factors motivate scientific and technical advancements in multiple domains, which seek to explore new hardware designs, better understand strategies for interactive control, identify suitable materials and manufacturing methods for construction, and define efficient approaches to system integration, to achieve robotic solutions which are appropriately matched to real-world environments and close human interaction. Toward these goals, I therefore focused in this thesis on the challenges to:

1. Define and implement a generalized design architecture for **multi-DoF** SPA-based systems which allows **efficient design** and **reconfigurability** of portable, wearable, or compact platforms.
2. Identify new materials and fabrication methods for producing **capable SPAs** compatible with high-DoF and high-performance systems.

3. Design **sensible control strategies** for scalable soft robotic systems which preserve and complement actuator and environmental compliance.

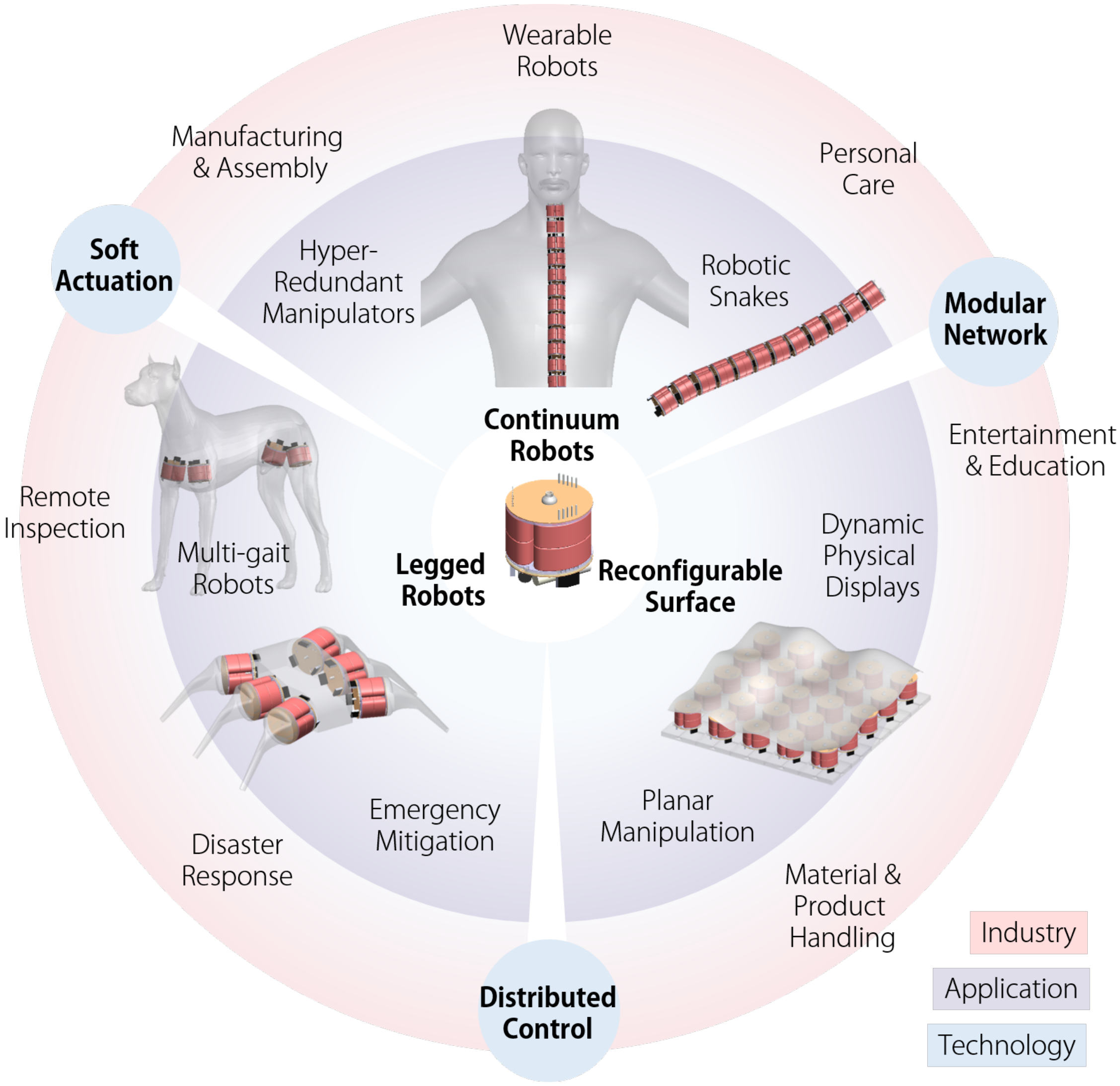

Figure 1 – Applications and broad impact of my thesis work. Highly functional soft robotic systems are made possible by bringing together the three enabling cornerstones of modularity, soft actuation, and distributed control.

Thesis Summary

My PhD research aims to extend recent progress in soft robotics research toward practical applications which demand complex functionality and multi-faceted objectives for safe and compatible use as required in dynamic environments, wearable robotics or human centered applications (Figure 1). In many cases, complexity can be measured in terms of the number of DoFs in the robotic system, and therefore is a dominant factor my research motivation.

Soft, material based robotic systems and devices have been shown to execute complex tasks by leveraging the infinite DoF nature of their actuators and constitutive components. Soft materials themselves facilitate such advantages as passive adaptability, safety, and robustness, as well as simplified control under specific conditions and scales through morphological computation [65, 66]. These advantages cannot always be exploited without interference with other system objectives. This is particularly important at larger scales, where soft robotic systems with many DoF require greater controllability. While matching compliance to system objectives through actuator design and material selection is sufficient for low-order systems, control of higher order soft robotic systems has proven to be a major challenge in the field. Fundamentally, this difficulty arises from underactuation and non-linear behavior of the soft materials. Various methods have been proposed and studied in response to the need for controlling soft robots with many DoF, however most of these approaches are built to accommodate existing hardware and system design methods.

In my research I explore the use of modularity in combination with soft material based pneumatic actuation to achieve improved design, integration, and controllability of complex, multi-DoF soft robotic systems. Exploiting the arrangement of actuators constructed as decentralized standalone modules allows moderate decoupling between the high-DoF compliance given by the soft material construction of the SPAs and the prescribed, controllable DoF of multiple actuator modules. This affords both inherent, built-in compliance from material-based passive DoFs as well as system-architecture-based compliance. The inherent compliance derived from soft material properties which exist primarily at the *component level* are what I deem **intrinsic** compliance. Alternately, compliance which arises from *system level* factors, including high-DoFs and user compatible control strategies, are what I refer to as **extrinsic** compliance. The combined design leverage over these important factors enables SPA based robotic systems applicable to practical, real-world applications, by allowing better fidelity in matching all forms of robotic system compliance (both intrinsic and extrinsic) to specified tasks.

Thesis outline

CHAPTER 1. **Modular SPA design for efficient, high-DoF soft robotic systems**

This chapter introduces the concept and exemplary implementation of a fully ‘plug-and-play’ SPA module architecture which allows high-DoF soft pneumatic systems to be readily designed and assembled to conform to complex task objectives. I present a new type of lightweight, easily manufacturable vacuum-powered SPA (V-SPA) which is used as the basis for modules in constructing a reconfigurable prototype robot to demonstrate a variety of capabilities including locomotion, manipulation, and mechanical stiffness tuning. The modular SPA structure takes advantage of decentralized control and communication hardware to simplify the pragmatic challenges in pneumatic systems power distribution in high-DoF systems, enabling many independent actuators across any number of modules in series to be powered by a single common power supply and communication signal. The design framework described in this chapter are leveraged and extended in subsequent chapters. The main contributions of Chapter 1 are:

- Modular, 3-DoF V-SPA units for plug-and-play networks which enable simplified, rapid development and reconfigurability of complex soft robotic systems with many DoF.
- A novel V-SPA fabricated from off-the-shelf foam material and powered by vacuum for lightweight and simple actuation which also facilitates fully vacuum-powered soft robots with a diverse range of capabilities.
- An architecture for simple serial networking of embedded solenoid control valves based on repurposing RGB LED drivers.
- A prototype and experimental validation of a continuum style robot constructed from V-SPA Modules, demonstrating multi-modal locomotion and hyper-redundant 15-DoF mobility with a single pneumatic supply and communication control line.

CHAPTER 2. **Control strategies for modular SPA systems**

The following three chapters discuss both open and closed loop strategies for controlling modular SPAs.

Part 1: Practical control methods for compliant actuators

In the first part, I present a simple approach to controlling SPA modules along approximated trajectories without sensory feedback to achieve positioning matched to the adaptability of the soft actuators themselves. This strategy is proposed to complement the capabilities of soft systems which are inherently more tolerant to minor deviations in alignment and therefore do not strictly require high fidelity positioning. The main contributions of this part are:

- Practical methods for implementing continuous proportional control of V-SPAs configured in decentralized modules.
- A heuristic mapping strategy for simplified control of V-SPA modules through spherical workspace.

Part 2: Physical shape and load modulation control modes for tangible interactions with soft reconfigurable surface

In the second part of this chapter, I study the performance of physical shape and load modulation control modes for tangible interactions and haptic interfacing using a modular, high-DoF, reconfigurable surface powered by pneumatic vacuum through a single port. The main contributions of this part are:

- A narrow form factor, linear V-SPA module for close-packed arrangement in a high-density matrix array
- A compact, a soft reconfigurable surface (SRS), interactive platform based on a modular actuator network to test applications in safe object manipulation, haptic interaction and variable-stiffness surfaces.
- Closed loop stiffness and force control of high-DoF V-SPA interactive SRS prototype
- Open loop shape and pattern control for object manipulation, haptic or visual display

Part 3: Embedded soft strain sensors for feedback and feedforward (bi-modal) SPA control

In the third part of the chapter, I present the development and characterization of V-SPA modules with low-profile, soft embedded strain sensors. The sensors are integrated with the SPAs to allow both feedback-based position control as well as feedforward user input control to direct the motion of a prototype soft robotic structure. The dual use of the directly integrated soft sensors enables efficient design and intuitive robot interaction for collaborative applications. The main contributions of this part are:

- The first integration and validation of soft liquid metal Ga sensors with V-SPAs, for measuring and controlling large actuator strain.
- Demonstration of SPAs with embedded sensors for both control and user interaction.

CHAPTER 3. **SPA performance and design benchmarks/standards**

Part 1: High-force SPA Packs

In this chapter I present a new type of SPA designed for high force, high-bandwidth real-world scale actuation. A novel arrangement of parallel-grouped SPAs which form a larger holistic actuator structure is shown to improve the performance in comparison to comparable monolithic actuator designs, and the redundancy of the modular *SPA-Pack* is also shown to possess additional benefits toward robustness and reliability. The main contributions of Chapter 3 are:

- Novel SPA-Pack structure suited for fiber-reinforced SPAs which demonstrates improved robustness and reliability over individual soft pneumatic actuators.
- Fiber-reinforced SPA design for high force applications above 100 N.
- Prototype and experimental validation of an active, multi-DoF platform powered by high-force SPA-packs under closed loop control.

Part 2: Low-inertia Coil V-SPAs

In this part I present a new type of vacuum-powered SPA, the Coil V-SPA which is built on actuator designs presented in preceding chapters, and extends the behavior of bending actuators to extreme range of motion (RoM). A range of Coil V-SPAs are produced with varying geometry and characterized to establish an empirically based model of V-SPA design parameters and actuator performance. The main contributions of this part are:

- Prototype and experimental characterization of a new high-bandwidth high-RoM Coil V-SPA.
- Introduced a generalized design metric for V-SPAs, the Geometric Compression Ratio (GCR), which correlates physical geometrical design parameters to actuator performance.

CHAPTER 4. **Wearable SPA systems for direct and indirect human assistance**

This chapter establishes benchmarks for wearable, SPA-based applications by presenting two prototypes leveraging modularity at different system-level scales.

Part 1: SPA Pack belt for postural support

A wearable postural support belt device driven by high-force SPA Packs, capable of affecting the large mass of the human upper body. The active pneumatically powered support belt is designed to allow custom reconfiguration of SPA Packs along its length, around the circumference of a human user. The device is shown to produce measureable effect on the medial-lateral trunk angle of subjects in a pilot study, in response to an input sinusoidal control signal used to activate the belt. The main contributions of this part are:

- A wearable postural support belt device driven by high-force SPA Packs, capable of affecting the large mass of the human upper body.
- Validation of trunk angular position guidance through experimental subject measurements.

Part 2: Modular robotic assembly for human lumbar unit and spine support

A wearable device is proposed for providing support to the human spine and lumbar unit, based on a robotic assembly of soft V-SPA modules. A computational model based on finite element methods (FEM) is developed to predict the performance and capability of the V-SPA modules which are fabricated from silicone rubber and polyurethane foam material.

The main contributions of this part are:

- A proposed wearable spine support system for matching the mobility and loading conditions of the human lumbar unit.
- A computational FEM model of V-SPA modules for predicting actuator stress, load, and displacement profiles, to enable system and actuator design.
- Experimental characterization of hyperelastic foam-based V-SPA modules and validation of FEM models for various loading conditions.

Part 3: Variable stiffness device for wearable joint support

A compliant, wearable joint support device utilizing granular media jamming to achieve variable stiffness is produced and experimentally characterized. The primarily silicone rubber prototype is fully autonomous and portable with integrated sensing and miniature vacuum pump, and can be worn over a variety of body joints to assist in rehabilitation or joint support. The unique pressure dependent stiffness functionality allows the level of joint support or constraint to be adjusted to match the level of user needs, capability or progress through recovery.

The main contributions of this part are:

- A soft, portable, and autonomous joint orthotic device prototype for rehabilitation or support.
- Demonstration of vacuum-induced granular media jamming to produce variable stiffness for wearable applications.
- Characterization and experimental testing of multiple variable stiffness component geometries and deformation modes.

Part 4: ’Pneumagami’ modules toward wearable ’Third Arm’ for task assistance

This part presents the design and characterization of a compact form-factor, 3-DoF kinematic module composed of an origami-inspired structure and low-profile pouch SPAs. The *pneumagami* module establishes the basis for a reconfigurable, multi-DoF redundant manipulator arm to be employed as a wearable, collaborative device for task assistance. The intrinsic compliance of the hardware prototype is measured and its kinematics are compared to an ideal model to evaluate the potential for load support and controllability. The main contributions of this part are:

- First example of the design and fabrication of an integrated robotic module that combines both origami-inspired structures and pneumatic actuation (pneumagami).
- Implementation and characterization of the multi-DoF pneumagami module and a novel differential pressure blow-off relay (DBR) valve for underactuated control.

- Established a framework for future research in developing compact, customizable wearable devices for task assistance.

* Supplemental videos are available to view or download online at
www.thethoughtfulroboticist.com/thesis

1 Modular SPA design for efficient, high-DoF soft robotic systems

1.1 Introduction

We introduce a vacuum-powered soft pneumatic actuator (V-SPA) which leverages a single, shared vacuum power supply and enables complex soft robotic systems with multiple-DoF and diverse functions. In addition to actuation, other utilities enabled by vacuum pressure include gripping and stiffening through granular media jamming, as well as direct suction adhesion to smooth surfaces, for manipulation or vertical fixation. We investigate the performance of the new actuator through direct characterization of a 3-DoF, plug-and-play V-SPA Module built from multiple V-SPAs, and demonstrate the integration of different vacuum-enabled capabilities with a continuum-style robot platform outfitted with modular peripheral mechanisms. We show these different vacuum-powered modules can be combined to achieve a variety of tasks, including multi-modal locomotion, object manipulation, and stiffness tuning to illustrate the utility and viability of vacuum as a singular alternative power source for soft pneumatic robots, and not just a peripheral feature in itself. Our results highlight the effectiveness of V-SPAs in providing core soft robot capabilities and facilitating the consolidation of previously disparate subsystems for actuation and various specialized tasks, conducive to improving the compact design efficiency of larger, more complex multi-functional soft robotic systems.

1.2 Background

Robots that operate in highly variable environments or in close cooperation with humans require both robustness and adaptability to ensure reliability and safety. These features can be accommodated most easily by adding compliance to a robotic system, which can be achieved either actively through impedance control methods [68, 69] or passively through

---

The material presented in this chapter is adopted from the following self-authored publications:

[67] **M. A. Robertson** and J. Paik, "New soft robots really suck: Vacuum-powered systems empower diverse capabilities," Science robotics, Vol. 2, Issue 9, eaan6357, 30 Aug 2017, DOI: 10.1126/scirobotics.aan6357

compliant mechanical components and materials. In part, the advantage of a materials-based approach to creating compliant systems is to offload some of the burden of complexity in control to morphological and material computation, in a sense, to achieve robust and adaptable behavior [70, 71]. This latter strategy has been the recent focal point of the field of soft robotics, where inherently compliant and flexible materials such as silicone rubber are used to fabricate primary structural and active robot components [72]. Various forms of soft pneumatic actuators (SPAs) powered by pneumatic pressure have been developed in this domain to compliment the nature of these soft materials, which stretch and bend through inflation or deformation of elastic chambers to produce useful mechanical work [27, 28, 29, 30, 31, 32, 39, 33, 34, 35, 36].

This relatively new approach to robotics has yielded mobile platforms, manipulators, and other soft structures which are applicable in increasingly complex applications. Rough terrain locomotion, delicate handling, and human interaction tasks all benefit from the natural quality of SPA driven systems to conform or yield safely to rigid environmental constraints without sacrificing the functional purpose of the device [73, 74, 75]. While now traditional soft pneumatic systems afford these benefits already utilizing positive pressure, recent interest in negative pressure systems aims to improve these qualities further. Exploiting the effect of mechanical buckling to generate controlled force, vacuum driven soft, muscle-like actuators have been successfully demonstrated utilizing standard soft robotic materials and fabrication techniques [76, 77]. This type of actuator offers implicitly fail-safe operation, being limited by environmental pressure from actuating beyond a maximum force and displacement, and directly enables contractile motion, more similar to biological muscle than the expansion-based motions of many positive pressure driven soft actuators.

Following previous effort [76, 77], we introduce a new vacuum-powered Soft Pneumatic Actuator, the V-SPA, to expand the diversity and utility of this versatile power source for new soft robots. In comparison to the few existing examples of vacuum driven actuators, this new type of actuator is exceptionally rapid to fabricate, for proficient iteration through multiple designs. This is a result of requiring no molds or sacrificial compounds and being constructed primarily of readily available, manufactured foam sheets. The use of porous foam structures in soft robotics has recently been investigated to a limited extent for various novel benefits. Employing self-manufactured poroelastic foam, a bioinspired fluid pump was developed to showcase the utility and simplicity of foam-based compliant actuation [78]. Following a similar method to fabricate poroelastic foam from a moldable compound infused with a fugitive salt porogen, highly customized inflatable structures can be sculpted in free form for laboratory, art, or classroom educational purposes [79]. Other work has explored the use of bicontinuous metal-elastomeric foam to achieve variable stiffness and self-healing properties [80]. While most of these methods have been applied toward the fabrication of SPA devices powered by positive pressurized air, the application of vacuum to foam structures is an approach that combines the advantages of vacuum power, with some of those inherited from the properties of foam material itself, including impact resistance, robustness, and storage-friendly “crushability” [81]. We introduce here a new type of soft actuator to exploit

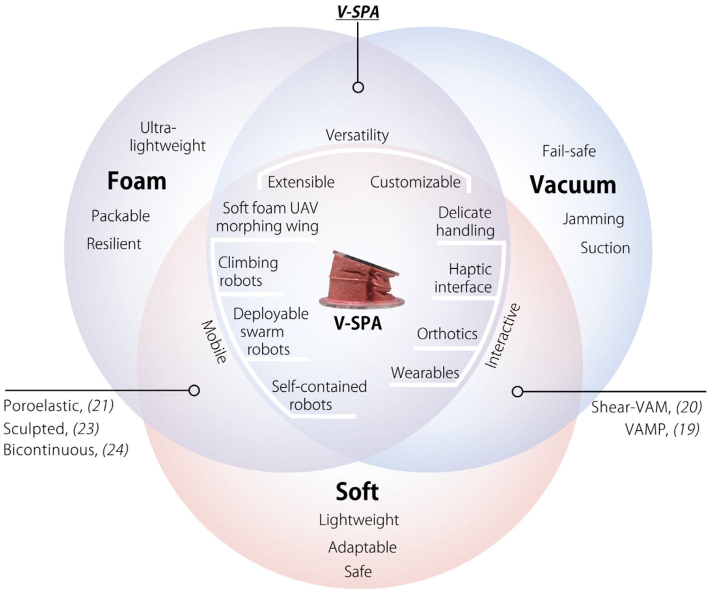

Figure 1.1 – V-SPAs blend multiple material and operational domains for diverse potential applications. Existing work independently explored the use of vacuum and foam materials respectively for the development of soft robotic systems, to leverage the unique attributes of robustness, safety, and manufacturability offered by different fabrication and actuation methods. This work explores a new approach which leverages foam and vacuum power simultaneously with an actuator called the V-SPA, to take advantage of a new construction technique which enables rapid production of soft robotic systems using minimal resources, as well as open possibility for fully vacuum powered systems which enable soft robots with expanded capabilities.

this combination, enabling a wide range of new soft robotic applications, including safe, lightweight, wearable devices, collaborative machines, or packable mobile robots that are space and energy efficient, suitable for remote deployment or even possibly flight (see Figure 1.1).

Capitalizing on the vacuum supply available for actuation, vacuum-based soft robotic systems can also leverage this source to incorporate other functions and features powered by negative pressure, without the need for an additional power supply or additional subsystem infrastructure. Vacuum powered mechanisms have been shown to enable operations useful to soft robots, including gripping [82], suction [83], and stiffness tuning [84, 85, 86, 87]. By adding to this variety of available vacuum driven mechanisms a new lightweight alternative for actuation, V-SPAs open the opportunity to expand the capability of soft robots while actually minimizing the size and complexity of their design and implementation. The seamless integration of these mechanisms through a common vacuum supply not only yields more efficient soft robot design but subsequently facilitates high-order soft pneumatic systems with many DoFs, which are still relatively scarce in the field of soft robotics. To demonstrate this facility, we employ the use of V-SPAs in a typically complex and difficult multi-DoF robot morphology, generally referred to as a continuum robot. Also known as Hyper-Redundant Robot Manipulators (HRRMs), trunks, tentacles, or snakes, these narrow structures often consist of a linear chain of repeating modular units, each with single or multiple active DoF. This concept enables a high degree of kinematic maneuverability and flexibility for either manipulation [88, 89, 90, 91, 92], positioning [93, 94, 95] tasks, to account for variable environments or system objectives. While the low-mass of the V-SPAs themselves make such an architecture with many DoF more feasible, dealing with the practical difficulty imposed by cumbersome, overlapping pneumatic supply lines routed from a central control source to many independent actuator units often limits its realistic execution. To overcome this barrier as well as allow the consolidation of multiple vacuum-based mechanisms into the same platform through a common vacuum supply line, we employed a decentralized, modular design approach.

This work validates the integration of our new actuator in multifunctional vacuum-driven soft robotic systems by experimental demonstration of interaction task versatility and mechanical performance tuning of physical properties through the use of plug-and-play control and design methods. By introducing new actuation technology and demonstrating the combination of different functions made possible through a negative pressure pneumatic power supply, we help to establish vacuum-power as a substantial alternative class of soft robotics that offers unique and important potential for realizing complex and advanced systems.

The main contributions of this chapter are:

- Modular, 3-DoF V-SPA units for plug-and-play networks which enable simplified, rapid development and reconfigurability of complex soft robotic systems with many DoF.

- A novel V-SPA fabricated from off-the-shelf foam material and powered by vacuum for lightweight and simple actuation which also facilitates fully vacuum-powered soft robots with a diverse range of capabilities.

- An architecture for simple serial networking of embedded solenoid control valves based on repurposing RGB LED drivers.

- A prototype and experimental validation of a continuum style robot constructed from V-SPA Modules, demonstrating multi-modal locomotion and hyper-redundant 15-DoF mobility with a single pneumatic supply and communication control line.

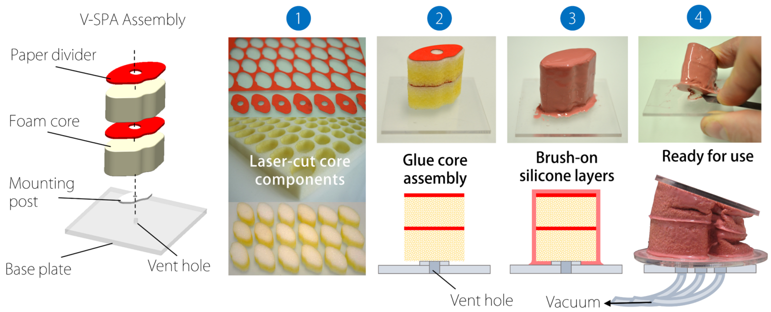

Figure 1.2 – Fabrication of V-SPAs. A four step process is shown for V-SPA fabrication. 1) Cut foam core shapes and paper divider plates using CNC CO2 laser. 2) Assemble actuator cores and dividers on mounting post of preform structure of using cyanoacrylate gel. 3) Apply two coats of silicone rubber to outer surface of foam core assembly including the space between the bottom foam and baseplate. A vent hole is included through the mounting post and base plate to reduce the formation of bubbles caused by expanding internal air in the foam core when a heating oven is used to speed curing. Allow layer cure between coats. 4) Remove actuator from preform using a razor to separate the attached foam, or directly attach vacuum line to base plate through the vent hole.

1.3 Actuator design and fabrication

The fabrication process of a V-SPA shown in Figure 1.2 begins with a basic preform structure, to act as a mount during application of the outer rubber layer and as a mask over the foam where connection of a vacuum supply to the internal actuator cavity is eventually made. For the actuators produced here the preform also served to create a smooth flat surface on the same side as the supply access mask when peeled off, so the actuator will form a good seal when glued to an equally smooth flat supply distribution plate.

The actuator itself is composed of 2D foam core shapes manufactured from a sheet of open-celled polyurethane foam (12.7 mm thickness polyurethane foam, McMaster-Carr, 8643K511) and rigid paper dividers. The porous foam cores serve as the main actuator body, while the paper dividers help reduce the buckling on the upper surface of the actuator, and at intervals along the height to enforce deformation primarily in the vertical direction. A CO2 laser was used to cut many foam core and paper divider components from a single sheet at once, allowing batch production of the actuators. The foam cores and paper dividers are assembled in a stack with cyanoacrylate gel glue, and then glued to the preform. After preparation by mixing and degassing, two coats of ELASTOSIL® M 4601 silicone rubber are spread with brush-like strokes onto all exposed surfaces of the foam core using a flexible spreader (thin cardboard), while being cured at 50° C between coats. Once cured, the actuators can be removed from the preform and attached to a vacuum supply, or used directly on the preform by applying vacuum to the vent hole through the base.

While the basic construction of V-SPAs is described above, many variable parameters affect actuator performance. One of the leading design variables is geometry, as it pertains to dimensions which are easy to change, like actuator shape, and to others which are more difficult to manipulate, like the porosity of the foam used. As a starting point, we investigated only minor changes in actuator morphology toward a very specific goal, to create a circular module with 3 actuators and room at the center to pass wiring and a central pneumatic supply. This bounded the overall shape of the actuator to be used, but small improvements were added in an effort to achieve specific behaviors and subjectively improved performance criteria, in this case maximal linear deflection. To increase the directionality of the actuators, a particular geometry was selected for the foam core which would allow inward compression and buckling of sidewalls without interference limiting the downward actuator stroke. This helped to direct actuator contraction to the axial direction, perpendicular to the top plane of the original foam sheet. Secondly, multiple foam chambers were created simply by stacking individual foam cores to increase the actuator range-of-motion. To create independent porous volumes within a single actuator, thin 0.2 mm heavy-gauge paper dividers were assembled between two foam cores glued together in a stack to form an internal membrane. The dividers contain a 6 mm hole at the center to allow air flow between chambers while still enforcing separation. Without this membrane the overall structure of the two-core actuators would yield an effectively taller actuator which for the same given cross sectional area, would yield a more horizontal than vertical mode of collapse upon vacuum activation. While a parametric study was not conducted to properly determine an ideal V-SPA compression ratio, it is plausible an optimal relationship exists to best select actuator height based on cross-sectional geometry (aspect ratio) for linear actuation. For planar fabrication methods this ratio is the most accessible parameter to optimize, however an ideal actuator shape would incorporate geometric contours along the “walls” of the foam core to increase stress concentrations for uniform buckling, much in the same way a corrugated bellows collapses. This is partly achieved by creating multi-chamber actuators, whose stiff dividers act similarly to limit the stress along designated rings around the actuator perimeter. A separate study could investigate the optimal size and number of separate foam core chambers needed to maximize deflection or force using this design method.

Other factors including foam type and composition, porosity, and elastomer coating material are expected to greatly affect the performance of V-SPAs, but the methods for testing these variations involve greater effort. To begin, different foam materials and elastomers behave differently, and not all combinations allow for full curing of multi-part elastomers which chemically interact. Open-cell foam materials of different composition and porosity are also limited as off-the-shelf components, but can be produced from scratch for testing if desired. These factors limit the possibility for ready empirical parameterization testing. Perhaps a more controlled and available approach would seem to be simulating the effect and performance of actuator deformation using finite element modeling techniques, but this proves to be as difficult as it is circular, since accurate models of this type require empirically determined values for material properties. Nevertheless, as data and models improve over time, this technique will prove to be invaluable as actuators such as the V-SPA are adopted for further use.

The use of primarily off-the-shelf materials allows this new type of actuator to be easily produced with low-resources, partly to extend the accessibility and scope of soft robot construction and research, especially toward the realm of lower education STEM (Science, Technology, Engineering, and Mathematics) outreach programs. The concept of foam vacuum actuation however is not exclusively tied to these materials and methods of manufacture. We do capitalize greatly from laser-cutting machines for fabricating 2D foam core shapes, but this tool is not required and virtually any method for cutting foam sheets will suffice. Early prototypes of V-SPAs were in fact built from scissor-cut foam cores attached to the end of wooden dowels (to serve as a mount and mask), and could be directly super-glued to a supply tube with the outer rubber skin used to seal the foam and fix the tube to the actuator in a single step. Alternative to brushing on the outer rubber layer, dipping might also be employed to coat an entire foam core for even faster manufacture time.

1.4 V-SPA Module control and characterization

Control of each V-SPA Modules connected in series is achieved over a single wire interface, enabled by a low cost and readily available integrated circuit (IC) originally designed for controlling individual LED pixels in networked displays (Worldsemi, WS2811). The IC is repurposed to supply an activation signal to onboard amplifiers for direct control over three embedded solenoid valves (Lee, LHDA0531115H) shadowing the operation of each color channel of an RGB (Red, Green, Blue) LED. A significant benefit of this IC is that it tolerates real time reconfiguration of hardware, enabling plug-and-play functionality of the V-SPA Modules. Robots can therefore be reduced or extended fundamentally to any number of modules on a single bus over relatively large spans, with only practical limitations imposed by RAM and electrical power required. Using standard microcontrollers, such as Arduino, hundreds of IC-enabled modular units can be controlled in a serial network through a single wire with little additional local electronics hardware, compared to alternative networking schemes (I2C, CAN, direct serial) which require more local computational power. Figure 1.5b depicts the topology of this network architecture, while a schematic of the internal electronic connections to the LED driver IC can be seen in the supplemental Figure S3.

To determine the performance characteristics of a V-SPA Module, a step response was empirically measured for multiple values across different conditions. Each response was averaged from three different actuators, cycled 10 times each. This process was repeated for 10 conditions of varying load, and 10 conditions of varying input vacuum. Load was applied by calibrated weights through a cable hung over a pulley and attached to a short level arm fixed to the module. Vacuum pressure was varied by changing the positive supply pressure to a vacuum ejector module (SMC ZH05B). The cycles for all three actuators in each condition were averaged to obtain a single representative step response curve from which performance metrics were extracted. The maximum angular motion is directly measured, while the rise time is found from the time between response crossings at 10% and 90% of the maximum angular deflection. The initial angular velocity is also found in this region, from a linear fit to the first half of the actuator motion (up to 50%), where the response curve is dominantly linear.

Blocked moment measurements of the V-SPA Module were obtained using a six-axis force and torque sensor (Nano17 SI-25-0.25, ATI Industrial Automation) mounted to the upper plate of the module constrained at the base in a rigid test fixture. The reported value was averaged from individual activation of three different actuators, cycled 10 times each. Using an alternate setup, the average mechanical power output of a V-SPA Module was also estimated through measurements of displacement, Δh, and time, Δt, for a known mass, m fixed to a cable hung over a pulley (assumed to be a constant force, $F = mg$), and driven by a short arm attached to the module, following $P = F \cdot \Delta h / \Delta t$. The metrics of torque and power were normalized by the mass of the module as well as the actuator alone to compute specific torque (τ_s), specific power (P_s), and specific energy (E_s). While the latter of these is relatively low compared to other vacuum powered actuators [76], with P_s=5 W kg-1 and E_s=1.2 J kg-1, the value of specific torque is found to be relatively high, with τ_s=45.3 N·m kg-1 (45.3 N·mm g-1), more than five times that of the modular DC motor powered actuators designed for a conventional rigid continuum robot, the Unified Snake [96].

1.5 Vacuum-powered Soft Pneumatic Actuator (V-SPA)

We designed and developed a critical robotic component, the V-SPA, which is characterized by its implicit reliability and safety through the utilization of vacuum power and the robust properties of a foam core. This new actuator is simple in design, and easy to fabricate without the need for either an internal or external mold. It is composed of a laser-cut, off-the-shelf foam core and thin, brushed-on layers of silicone rubber, and can be manufactured from scratch, ready to use in less than two hours. The foam core acts as an internal scaffold over which uncured silicone rubber can be applied to form a thin, sealing layer around the open-celled foam as it can be seen in Figure S1. This creates an enclosed, airtight structure which is only sparsely filled with soft, porous material. While conventional SPAs or other vacuum actuator designs feature completely hollow inner cavities, the use of foam allows the wall thickness of V-SPAs to be much thinner as it provides much of the structural support typically given by a thicker wall needed to maintain a nominal actuator shape. This difference in material wall thickness helps to offset the added mass of the core, yielding an ultimately lighter weight actuator overall. Upon activation, vacuum is applied to the internal volume through a supply channel and the entire V-SPA structure collapses inward to produce tensile force that can be used for actuation. The low-density core is easily deformed and crushed when vacuum is applied, but immediately provides elastic return in conjunction with the elasticity of the outer silicone membrane following actuation to return the actuator to its original shape. The activation of a circular V-SPA array can be seen in Movie S1.

In soft robotics, foam-based vacuum-powered actuators offer a solution to improve the efficiency of soft systems, by reducing mass in actuators, allowing for the integration of additional mass components onboard to enable fully self-contained systems, including battery or pressure (or direct vacuum) generating pumps. This reduction in the total system mass budget also makes room for larger systems with more DoF, enabling further complex behavior. While vacuum power is not suited for every application, in part due to limited force production at atmospheric pressure, for use at small scales where this force limit is perhaps beyond maximum requirements, and where this limit offers a unique safety feature as it prevents actuating beyond the force imposed by external pressure, V-SPAs hold a unique advantage at significantly low cost in weight, materials, and production effort.

1.6 Scalable, reconfigurable soft robot

We developed a robotic platform using V-SPAs to power hybrid [97] modular units, known as V-SPA Modules, which contain both soft actuators and rigid components necessary for their power and control. This architecture was chosen to practically implement V-SPAs in an example soft robotic system with enhanced and diverse capabilities. The modular design of the units enables rapid, simplified restructuring and control of various robot configurations for easy testing and validation of vacuum system extensibility. Specifically, these modules allow the addition or subtraction of mechanical DoF with little or no physical design effort through standardized pneumatic and electrical network connection ports. Other peripheral device modules with different functionalities can also be easily combined with the actuators in the same way. To eliminate the effort of developing customized control for each unique combination of modules in a scalable or multifunctional system, we employ a standard control scheme that does not change with the number or type of modules connected. While high level control planning and programming is still required to achieve specific tasks, the low-level management of multi-module integration is automatically taken care of through this flexible plug-and-play network architecture utilizing embedded control circuitry and hardware. Following this design approach, the resulting reconfigurable soft robotic system we produced embodies a typically challenging morphology, a hyper-redundant continuum type robot not easily reproduced by other existing soft robot design methods.

1.6.1 V-SPA Module configuration

We produced V-SPA Modules using three actuators each, evenly spaced in a cylindrical configuration, and connected at the top and bottom to rigid plates which house or mount electronics, valves, pneumatic fittings, electrical connectors, and distribution channels connecting to a centralized vacuum supply line. Other work has leveraged this approach for more efficient configuration of mobile snake-like robots [98, 99], and use in a surgical continuum robot comprised of a serial chain of 3-DoF soft actuator modules with miniature control valves embedded locally [100]. Our V-SPA Modules similarly exploit the advantages of decentralized hardware architecture in order to reduce complexity, space, and weight of vacuum powered systems with integrated peripheral functions.

The three V-SPAs comprising each module are used to tilt the orientation of a rigid upper plate (conventional printed circuit board, PCB) relative to one at the bottom. The actuators are attached to these end plates and contract when activated, leading to angular deflection between them in a direction and degree defined by the combination of actuators activated simultaneously and the magnitude of their activation (by duty-cycle, proportional to length). Using a purely binary scheme to control the actuators fully on or off, the module actuators can be triggered independently or in pairs to produce six unique directions of motion at a fixed angle of deflection. The co-activation of all three actuators does not produce significant linear deflection as implemented here with a stiff supply conduit through the center, but this motion can easily be achieved without it. The motion of a V-SPA Module following this simple control method can be seen in Movie S2. More complex activation of the actuators was not shown here, but can be accomplished using PWM control for each actuator to achieve variable contraction, expanding the workspace to continuous, 360° directed bending with variable angle. While the angular deflection of the module can be represented as combined rotations along two axes in space, we express this in terms of active DoF rather than spatial, to define each V-SPA Module as a 3-DoF actuated joint. Characterization testing of the V-SPA Modules presented in Figure 1.3 was performed by measuring the angular step response of a module under varied conditions. From the different response profiles, metrics were obtained relating actuator and module performance to different loading and supply pressure conditions. The measured characteristics are summarized in Table 1.1.

Each V-SPA Module connects in series to another through connections on the top and bottom to a central pneumatic supply line, power and ground lines, and communication bus, shown in Figure 1.4A. The overall structure of the resulting network of modules can be seen in Figure 1.4B with the note that this architecture is not limited to efficiently integrating actuators alone but is designed to facilitate rapid and simple extension of many different module types for vacuum (or other) pneumatic robotic systems. Commands to individual actuators in each networked module are relayed over a communication signal line using a robust serial protocol designed initially for low-cost RGB LED serial displays. Since each channel of every module in the network is identified sequentially and not through a unique address, this allows modules to be added or subtracted in a generic way that does not affect the low-level control programming. While such modules could be used in various combinations, in a multitude of different robot topologies, the nominal configuration studied here in direct linear arrangement allowed for the demonstration of many interesting features enabled by V-SPAs and vacuum power alike.

1.6.2 Hyper-redundant soft robot performance

We first tested the operation of a five module robot to quantify its performance in the simplest form, as a soft manipulator arm. The workspace and repeatability of the robot's three principle

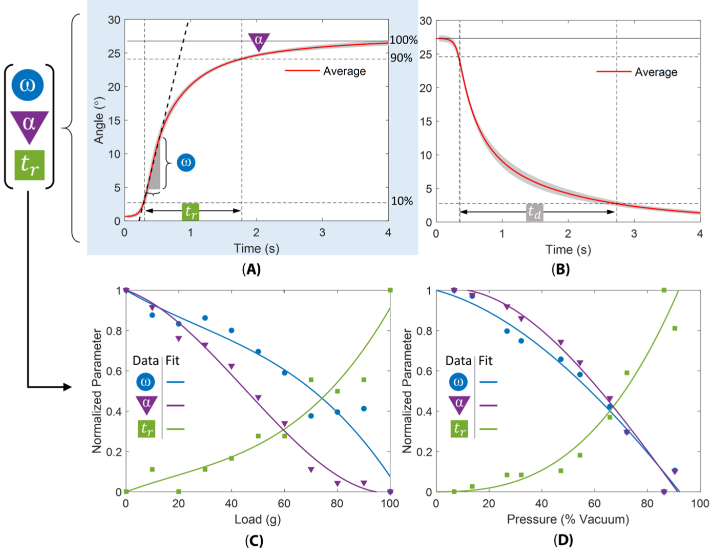

Figure 1.3 – V-SPA Module step response characterization. The step response rise time is denoted as t_r, maximum angular stroke is α, and the maximum angular no-load velocity is ω. Three V-SPAs were characterized with a step input while measuring the angular response with an IMU. The average (red curve) step response at maximum vacuum with no load are shown in (A), and the step down profile is shown in (B). A single standard deviation is also shown in light grey shading, for 30 cycles (10 cycles for each of 3 actuators) comprising the average response. The metrics found from the average step response for variable loads are shown in (C) and variable pressure in (D), and the trends plotted with a third order polynomial fit.

Properties	Value	Unit
Size (D x H)	45 x 45	(mm)
Total module weight	45.0	(g)
V-SPAs (x3)	11.1	(g)
Solenoid valves (x3)	12.0	(g)
PCBs	8.5	(g)
Acrylic and epoxy layers	8.5	(g)
Central conduit (tubes, connectors, wires)	4.9	(g)
Blocked torque	166.9	(N·mm)
Specific torque (rel. to Actuator mass)	45.3	(N·mm/g)
Angular velocity, ω (no load)	3.5	($\circ$/s)
Step rise time, t_r	1.5	(s)
Step decay time, t_d	2.4	(s)
Bandwidth	0.2	(Hz)
Max. angular stroke, α (no load)	27.3	($\circ$)
Specific power (rel. to Actuator mass)	5.0	(W/kg)
Specific energy (rel. to Actuator mass)	1.2	(J/kg)

Table 1.1 – Physical properties and performance of V-SPA Module. Performance metrics were estimated from an angular displacement step response test recorded relative to gravity using an IMU fixed to the upper stage of the module and with 86.2% vacuum supply.

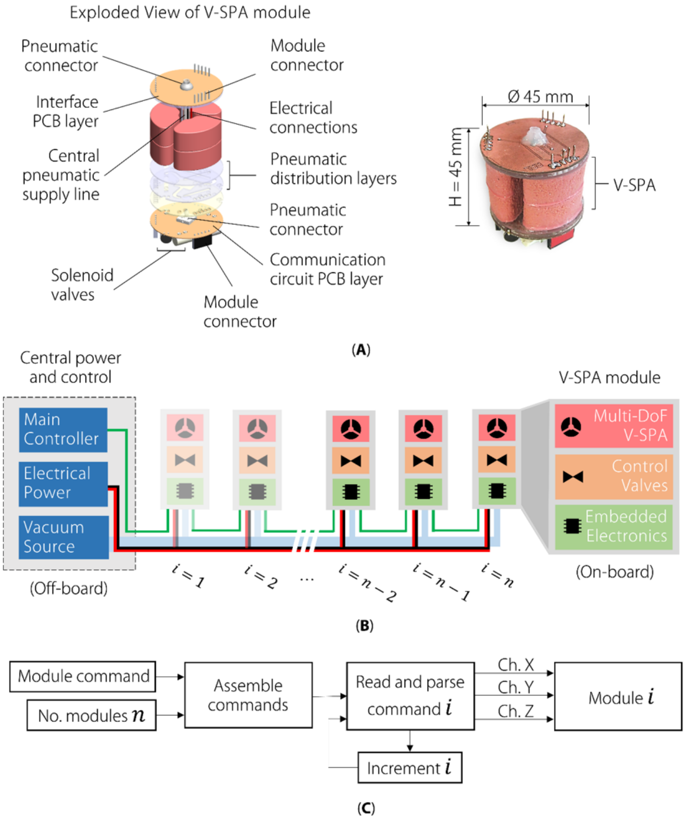

Figure 1.4 – Architecture of V-SPA Module and integrated soft modular device network. (A) Each module contains three main components: actuators (V-SPA), control valves, and electronics. (B) Each actuator in the module is paired to a valve, and dedicated channel of a communication IC. A common pneumatic supply line provides fluid power to every module simultaneously, while a common electrical bus similarly provides electrical power. (C) Control commands are assembled into data packets by a main controller, and relayed by the IC through each module connected in series. Each module has three independent channels (X, Y, and Z) which can be addressed to control up to three embedded valves in open-loop.

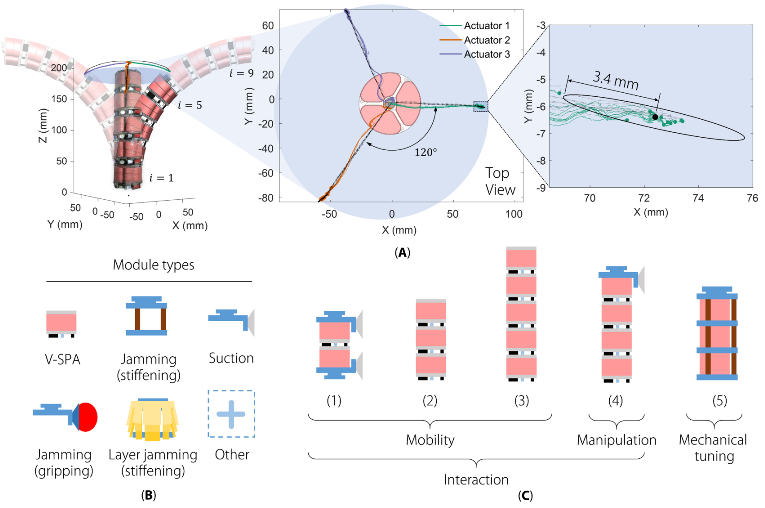

Figure 1.5 – Versatility of vacuum-powered soft hyper-redundant robot. The workspace and repeatability of 5-module soft hyper-redundant robot is depicted in (A) along with a depiction of the maximum reach for up to 9 modules. To measure the range of motion along three primary directions determined by the actuators in each module, three markers were placed on the top of the distal module, and a centroid was calculated to track the center of the module as the robot endpoint. A top view of the distal module centroid 3D trajectory is shown through a ten cycle repeatability test. A variety of module types shown in (B) can be readily integrated with the hyper-redundant robot. The configurations in (C) combining various modules are all validated experimentally in subsequent sections.

directions of motion from an initially vertical standing orientation were measured using an external OptiTrack motion capture system in order to demonstrate the practical utility of a V-SPA based system. The proximal end of the robot was fixed to a stationary base, while three markers were attached to the distal end to track the 3D trajectory of their centroid, treated as the robot endpoint. For this preliminary evaluation, every module in the robot was synchronized to move the endpoint virtual marker through three distinct locations (roughly 0°, 120°, and 240°) representing the robots principle directions of motion as shown in Figure 1.5A. Binary activation signals (on/off) were used to achieve the maximum bend in each of these directions, although independent control of each of the 15 total V-SPAs in the robot (three per module) is possible, and continuous motion of each actuator or combination of actuators in a single module could also be achieved using PWM signals to produce motion in any arbitrary angular direction.

The robot endpoint position was measured for ten cycles through each location and a 2D error ellipse (95% confidence interval) was calculated for each set of ten points in each of the three locations (see supplemental Movie S3 for video of a 10-cycle trial test). The length of the ellipse major axes, corresponding to the largest variability in endpoint positioning, was averaged for all three locations. For a five-module robot, the average error recorded across the three principle locations tested was found to be ± 3.4 mm. This corresponds to an average repeatability measure of ± 0.68 mm accuracy per module. Individually, the range of accuracy across each of the three respective directions differed slightly as a result of variable construction and individual actuator performance, with the lowest variability in a particular direction (actuator 3) measured to be ±1.9 mm for the robot as a whole, or ± 0.38 mm per module along that axis. While the path and final position of the robot endpoint in each direction are seen to be repeatable, deviations from a purely linear path (from the top view) between the neutral start point and end points can also be seen. In part this is because the actuators are driven by the inherently unstable mode of buckling of the V-SPA outer rubber skin, made variable between actuators by non-uniformity in their construction and materials. Despite this variability from manual fabrication, however, these measurements validate the use of V-SPAs for highly repeatable tasks, critical for practical robotic systems.

1.7 Validation of reconfigurable soft robot capabilities

To complement the mechanical flexibility of the hyper-redundant robot, a variety of module types can be easily integrated with it to achieve design and task flexibility. Possibilities for vacuum driven systems include those shown in Figure 1.5B. Three of the modules depicted are demonstrated in this work, while future modules yet to be implemented are proposed to further illustrate the capacity and utility of vacuum based soft robot design. We validate the diverse functionalities facilitated by these modules through demonstration of various interaction tasks between the robot and its environment, and an example of controllable mechanical tuning of dynamic system properties implemented through a plug-and-play modular design paradigm. Through the use of peripheral modules, these abilities extend the diversity of applications for soft robots, including enhanced mobility and controllability enabled by the configurations depicted in Figure 1.5C (1-4), highlighting the efficacy and versatility of V-SPAs and vacuum-based soft robotic systems as a whole.

1.7.1 Interaction task: Suction manipulation

As a first test of the versatility of the vacuum power supply, a suction manipulator component was added to the end of the positioning arm, maintaining a modular design approach. A snap-fit 3D printed part was attached to the distal robot module to provide the structural basis of the suction module, including a modified off-the-shelf soft suction cup. The new peripheral module was connected to the shared vacuum power supply, and a custom networked control valve plugged in series to the output electrical interface of the distal actuator module to be controlled along the common control signal bus. A silicone tube connected the valve output to the internal volume of a soft suction cup through a hole at the top, enabling it to be actively depressurized or vented to the atmosphere for controllable attachment or detachment to objects. The soft continuum manipulator arm was then tested in a simple reaching and manipulation task of smooth acrylic containers to demonstrate the performance of combined actuation and suction manipulation. The multifunctional system was able to successfully “grasp” and relocate objects from a starting location to target bins, as shown in Movie S4.

1.7.2 Interaction task: Vertical window climbing

Integrating lightweight actuation with other vacuum-based mechanisms enables capabilities beyond positioning and manipulation tasks. We demonstrate further advantages to combining these mechanisms by reconfiguring V-SPA Modules and suction cup modules into a soft robot capable of vertical climbing on smooth surfaces. Two vital requirements for this type of robot are readily accommodated by the actuator and architecture presented previously; to provide active motion for climbing and selective attachment and release of robot footholds while maintaining low enough weight to not hinder the effect of those capabilities. The low-mass foam-core V-SPAs are naturally well-suited to this application, and the modular, shared vacuum supply architecture of the complete soft robotic system enables the efficient integration of the active functions necessary for vertical climbing in a nearly self-contained soft robotic system that can scale surfaces such as glass windows. Using only an open-loop, fixed gait pattern controller and without optimizing timing parameters to find maximum speed, demonstrated gait was measured to be 2 mm/s, or 0.01 Body Lengths per second (BL/s). While the climbing robot we present here lacks an onboard electrical power supply and pneumatic vacuum generation source, we verified it is capable of carrying additional payload up to 70 g, which may be useful for accommodating the remaining components to enable a more autonomous robot in future. Figure 1.6A shows the progression of the climbing robot, and Movie S5 shows testing with increasing external payload, with an evident corresponding reduction in climbing speed. Although this change in climbing performance can be attributed in part to variable actuator functionality in response to load, this can also be a factor of the robot design which included a passive degree of freedom at the lower foot needed for climbing and an offset of the payload mass resulting in a moment which pulled the robot away from the wall and reduced step size.

1.7.3 Interaction task: Multi-modal locomotion

Alternate modes of locomotion were also found to be possible using the modular vacuum driven soft continuum robot system suitable for potential use in diverse and variable environments. Up to five V-SPA Modules were assembled in series and programmed to achieve two distinct gaits following strategies investigated previously for continuum style snake robots [101, 102, 103]: a wave gait and a rolling gait. The first of these is shown with a sequence of video frames in Figure 1.6B depicting the progression of the forward wave gait over a flat, level surface with a measured 5 mm/s average speed (0.05 BL/s). As a secondary but inherited feature of the modular robot structure, the reconfigurability and robustness of the continuum robot are also exhibited in Figure 1.6C where locomotion is preserved (and even improved in terms of average speed, measuring 11 mm/s (0.08 BL/s)) after two modules were removed from the robot, without requiring any changes to the gait controller. The increase in speed results only from an inherent change in vacuum supply air flow, which is restricted more for

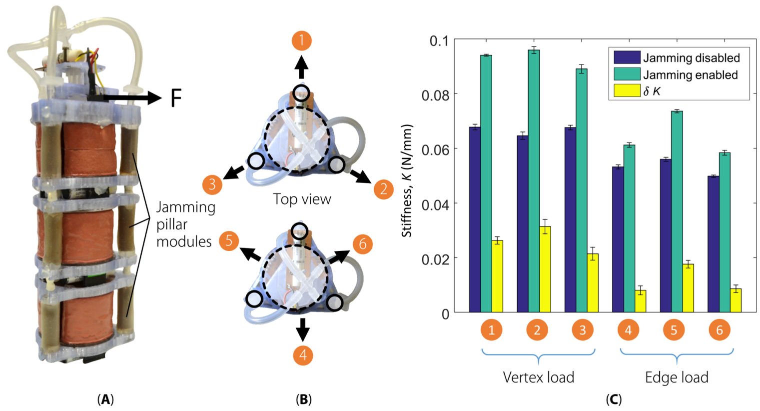

Figure 1.6 – Diverse locomotion modes of modular continuum robot. A series of frames captured from video is shown for each of four different gait modes: vertical climbing with suction cup modules (A), wave gait with 5 V-SPA Modules (B), wave gait with 3 V-SPA Modules (C), and rolling gait (D).

every module attached. Better designs could compensate for this by simply providing a central supply line with larger diameter.

Lateral motion was also accomplished utilizing a rolling gait, expanding the utility of the mobile robot to suit different locomotion objectives. This gait, shown in Figure 1.6D, is capable of much higher locomotion speeds (60 mm/s average speed or 1.33 BL/s), than the wave gait of any robot length; however, this is possible only at the cost of a larger operational workspace (wider body span relative to the direction of travel). In practice the multi-modal functionality of this type of robot may be exploited to achieve fast motion over generally wide, open terrain using the rolling gait, while slower, cautious navigation through narrow passages, gaps, or obstructions could be approached using the wave gait, which operates within a more slender body width. A demonstration of the continuum robot gaits described can be found in the supplemental Movie S6.

1.7.4 Mechanical tuning: Jamming-based stiffening

While our initial workspace testing indicated the compliance of the arm does not significantly affect repeatability, manipulation testing of the soft arm, as well as experience from literature [104], reveals the controllability of such a soft structure to precise locations remains a challenge. This was apparent from qualitative observations of object manipulation/relocation tasks, where the object mass in addition to the inertia of the arm itself led to oscillatory behavior. While closing the active control loop to better maintain positioning and path following is likely needed for the best results, these tasks would benefit from other methods of “passive control”, including the ability to tune mechanical system parameters of soft robotic devices themselves. In particular, this motivated the design and integration of a peripheral variable stiffness module, to provide the ability to change the overall rigidity or passivity of the soft arm.

Distributed across the length of the continuum robot arm, this module is comprised of multiple stiffening pillars in parallel with each actuator module, and utilizes jamming of enclosed granular media (ground coffee) driven by actively controlled vacuum to vary the stiffness of the overall structure. Figure 1.7 shows the resulting stiffness characteristics of the soft continuum robot fitted with the stiffening module, when force is applied through a high-strength nylon thread (fishing line) at the distal module perpendicular to the axis of the vertically mounted robot. Jamming pillars were spaced in three columns around each V-SPA Module, and powered together with 88.5 % vacuum when activated. The tested directions are grouped as either a pull in the direction of a jamming column, toward the vertex of the triangle formed from a top view of the three columns, or toward an edge, between two jamming columns. Five cycles were performed in each direction, with the result for each condition provided as an average of these trials. The measurements indicate an increase of stiffness in every direction when jamming is enabled, with the greatest increase always in the direction of a vertex, and hence the most direct compression of a single jamming column, with increases of 38.8 %, 48.5 %, and 31.7 % when vacuum is applied versus not. In the direction of an edge, the stiffness in was only moderately increased from their activation, by 15.1 %, 31.5 %, and 17.3 % for the three edge direction loading conditions. A diagram of the test setup is shown in Figure S2, along with a depiction of the fabrication process used to produce the granular jamming units.

The jamming modules in this demonstration are coupled and joined to the same controlled vacuum input but could equally be included as part of more advanced actuator modules with internally integrated, independently controlled jamming pillars for more selective mechanical tuning capability of a soft structure. Additionally, only granular jamming was explored for this investigation of mechanical tuning, but stiffening with vacuum can also be achieved using flexible sheet materials sandwiched between air-sealed plastic film to achieve similar or possibly improved results [86, 105].

1.8 Discussion

The actuators presented here and the combined example applications illustrate the versatility of vacuum-based SPAs constructed from simple materials and methods. The fabrication procedure for V-SPAs reduces the time, tools, and cost required for creating actuators for soft robots by employing only 2D manufacturing methods and eliminating conventional molds, which allows rapid, batch production from minimal effort in comparison to other SPA types. Although conventional molding techniques inherently produce more uniform actuator structure and reduced variability between different actuators, the accuracy and repeatability of individual V-SPAs are not significantly affected as shown here, despite the non-homogenous wall thickness produced from manual application of silicone rubber layers. This improvement in actuator fabrication serves to decrease the design and development cycle time, leaving

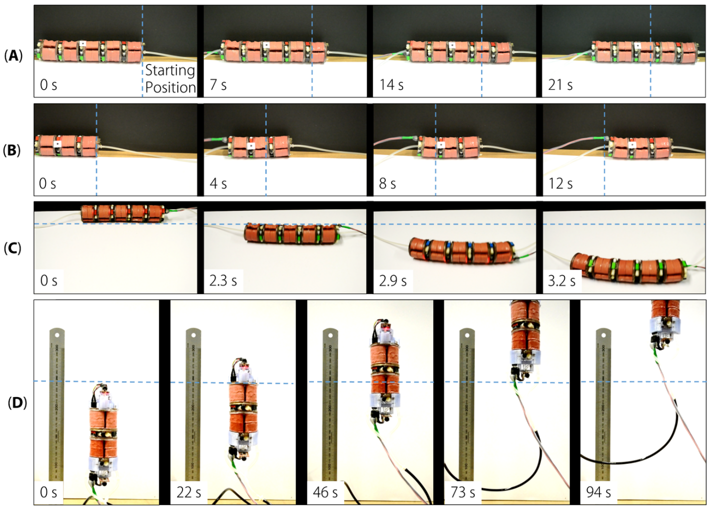

Figure 1.7 – Granular cellular matrix jamming enables active stiffness tuning of vacuum-driven soft structures. The addition of a jamming module enables stiffening of a continuum robot comprised of three V-SPA Modules (A). The stiffness was measured using a vertical material testing machine, configured with a grounded pulley to redirect vertical motion of a cable to the horizontal direction. Tensile force and displacement measured in the vertical direction were thereby mapped to the direction perpendicular to the initially vertical axis of the actuator structure. The cable was attached at the top of the distal module, and the assembly was rotated in increments of 60° to six total positions for measurements in multiple radial directions, with five loading cycles performed in each position (B). The measured stiffness shown in (C) increased in every direction when the jamming module was activated, in comparison to its inactive state. Error bars represent one standard deviation.

more room for focus on the system-level development of complete and useful soft robots. Toward the same goal, the employment of vacuum as a primary pneumatic supply source used to power V-SPAs enables more efficient integration of other vacuum-based mechanisms in a single soft robotic system allowing for more complex and diverse soft robot capability. This potential was effectively demonstrated through the use of modular units which allow many vacuum-driven mechanisms, as well as many redundant actuators to be seamlessly combined and tested in different soft robot configurations. Furthermore, unlike most other SPAs (6–16), utilizing a single source of pneumatic power significantly reduces the overhead cost of redundant subsystem infrastructure needed in comparison to the alternative case, where components, such as regulators, distribution manifolds, and central supply lines cannot be shared. This simplification saves weight and design effort.

V-SPAs likewise support the implementation of systems with many active DoF, through the use of lightweight foam material as a central component, helping to significantly reduce the weight-cost of additional actuation. In combination with plug-and-play architecture, this enables systems such as those demonstrated here with up to 15 actuators, or with fewer DoF and available payload capacity to support future integration of onboard batteries and power generation. Both of these aspects represent current goals and challenges of research in the soft robotics field, toward real-world application of the newly forming technologies coming from within it.

The simplicity of this V-SPA concept encourages the development of even more creative techniques and applications for soft actuation. Other methods of elastic foam production could be employed in the future to create complex 3D structures, possibly deviating from the strict use of off-the-shelf materials. Variable stiffness skin components of either different thicknesses or material could be used to generate more complex actuation patterns, for increasingly advanced V-SPA designs using multi-material 3D printers or other standard soft robot fabrication tools. Regardless of the implementation method or application, future soft robots will benefit from exploring and exploiting the benefits of both foam based materials and vacuum power as new viable means to achieving versatile capabilities for environmental interaction as well as controlled modulation of mechanical system performance.

1.9 Supplementary content

1.9.1 Supplementary figures

1.9.2 Movie captions

Movie S1. Binary control of 3-DoF V-SPA array without modular interface. A circular array of V-SPAs are assembled on a distribution manifold with each actuator connected to a vacuum supply through a manually triggered solenoid valve. The actuators are first activated alone to illustrate the nominal mode of vacuum-induced buckling. The addition of a plate to the top surface of all actuators with Loctite 406 adhesive prevents buckling of the actuator top

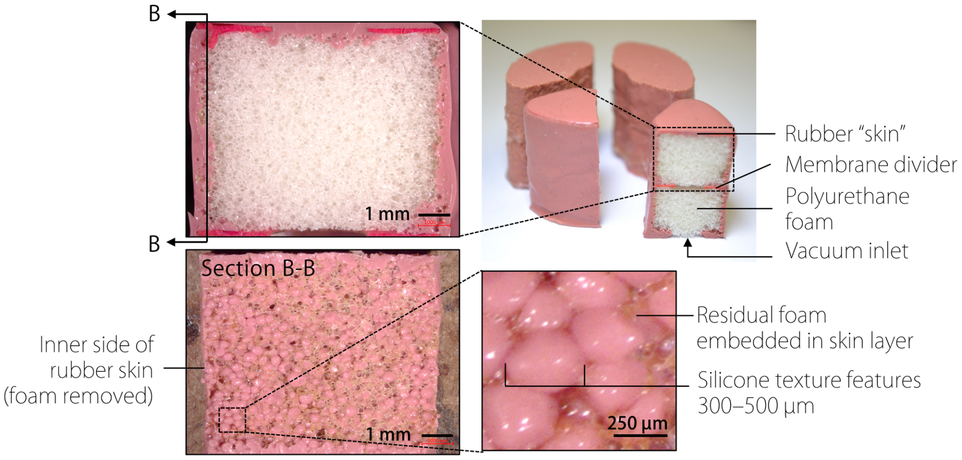

Figure 1.8 – Anatomy of a V-SPA. When uncured silicone is applied to the surface of the foam core it penetrates to a depth limited by its viscosity and liquid surface tension, and then remains primarily on the surface of the foam. The bubble-like texture features visible in the cross section are formed across the open pores of the foam core, while some foam remains embedded in the skin layer of the actuator. It can be seen that the wall thickness for V-SPAs is very non-uniform, however this does not significantly impede repeatability or robustness as the actuators perform well, with minimal variability, in testing over many cycles.

surface and the added constraint of stiffness from the other unactuated V-SPAs y an angular deflection of the upper plate. In addition to singular, binary activation of the V-SPAs, they are also activated in pairs to yield a total of 6 possible discrete angular positions of the upper plate, spaced at 60° around the center of the array. Movie_S1.mp4

Movie S2. Binary workspace of V-SPA Module. A 3-DoF V-SPA Module demonstrates rapid angular deflection as shown in randomized directions. Discrete, binary control is utilized to operate each V-SPA individually to produce motion in three primary directions at 120° spacing around the central axis of the actuator. While not shown here, finer, more continuous control of the direction of deflection or magnitude of the angle is possible with this module utilizing PWM vacuum pressure control. Movie_S2.mp4

Movie S3. Continuum robot repeatability test. A ten-cycle trial test was performed under an OptiTrack motion capture system, which accurately recorded the trajectory of the continuum robot mounted vertically. The repeatability of the robot was evaluated by analyzing the path of the robot endpoint, which in the video is shown to be a single, offset reflective marker. While the data set for the test shown in this video was not recorded properly, another test was conducted to produce the data shown in Figure 4, for which three markers were used to track the calculated center point of the distal module. Black tape was used to obscure other reflective components on the robot which interfere with the motion tracking system. The activation pattern that can be seen was selected deliberately as a progression from the most distal module to that most proximal to the base with a delay between each activation to limit the magnitude

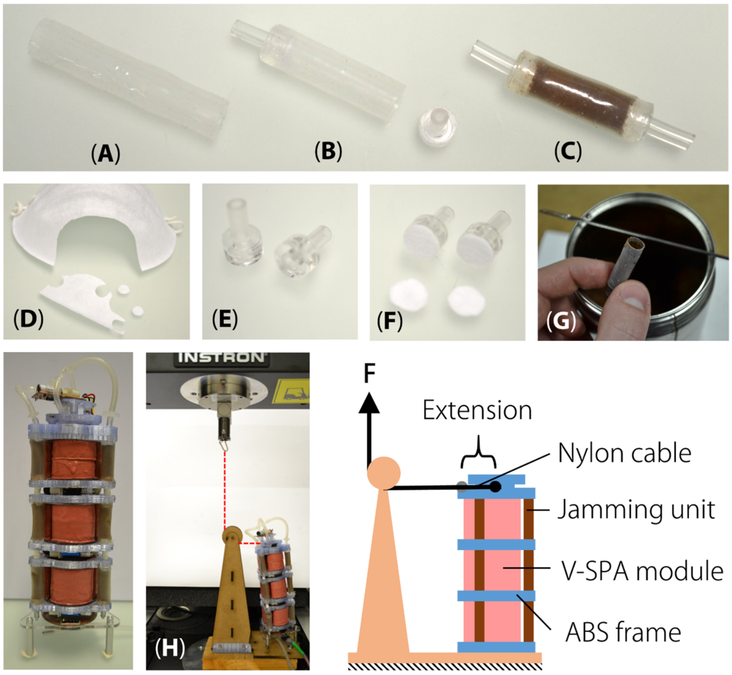

Figure 1.9 – Fabrication and testing of jamming module. Jamming units are fabricated by first creating thin walled silicone tubes using Dragon Skin-50 brushed onto a cylindrical form. The resulting cured silicone tube is peeled off the form and a segment is cut to make one jamming unit (A). End caps are attached to each end of the tube (B), after being filled with fine ground coffee particles (C). To ensure the coffee is not drawn out of the module from the vacuum supply, disc shaped filters are cut from a paper dust mask (D). Before inserting into the silicone tube, the end caps are fitted with segments of vinyl tubing to attach to the vacuum supply (E) and the paper filters are glued on the inside surface (F). Filling with coffee is accomplished by first gluing one end cap in place to the silicone tube segment, scooping and packing in a measured amount of coffee to the open end, and then finally gluing the other end cap in place (G). Photo (H) depicts the actual test set up used to measure the stiffness of the stacked modules and jamming units with a dashed red line superimposed over the translucent nylon cable. The adjacent illustration shows the setup with an explanation of important components, as well as the parameters measured during the stiffness evaluation.

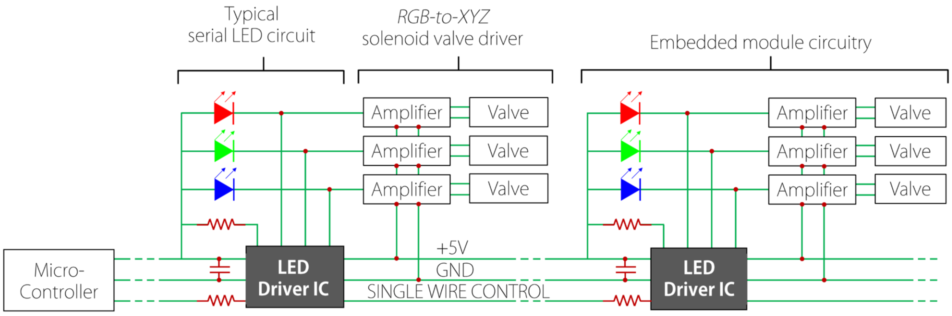

Figure 1.10 – Single wire module networking with serial LED driver IC. Circuitry embedded within each actuator module contains a three-channel IC designed and widely used for controlling multi-color Red-Green-Blue (RGB) LEDs. In parallel with the color channels, these chips can be leveraged to provide three-channel control of solenoid valves through an amplifier. Each channel is addressed over a single wire interface, using a time-based data packet structure which is passed to subsequent drivers connected in series. Communication libraries for Arduino based microcontrollers are available from Adafruit Industries on GitHub.

of oscillation caused by the actuator deflection, and not a direct consequence of the inflation or manifold dynamics. All actuators on a side can in fact be activated simultaneously, but the resulting torque from the sudden strong movement would result in longer waiting between subsequent cycles to allow dissipation of large oscillations. Movie_S3.mp4

Movie S4. Vacuum suction manipulation with continuum robot. A single active suction cup module is added to the distal end of a Vacuum-powered Continuum Robot comprised of three V-SPA Modules to serve as an end effector. A valve connected to the internal volume of the suction cup connects it to the central vacuum supply to enable selective adhesion or release of smooth, flat objects. The robot demonstrates a simple pick-and-place operation by moving empty acrylic containers from a gravity-fed supply rack to target bins on either side of the robot base. The motion of the robot is programmed open-loop and the adhesion of the particular suction cup used depends is sensitive to alignment, but could easily be replaced with a more compliant, auto-aligning variety designed more specifically for such operations. The suction cup used was adapted from a fixture system designed for long-term adhesion to smooth bathroom tiles. Movie_S4.mp4

Movie S5. Vacuum suction climbing with payload. The payload capacity of a climbing robot was estimated using increments of 10 g mass weights suspended from a nylon cable. The largest mass tolerated that did not inhibit vertical progress in climbing was found to be 70 g. The next tested increment of 80 g was found to disrupt the climbing pattern of the robot, however this may result from the given controller used for the vertical gait and as a consequence of additional passive degrees of freedom at the lower "foot" which allows the robot to briefly fall away from the wall. Beyond this threshold, better timing (faster release of footholds and body actuation) may be used to prevent falling, although previous tests also found that this would likely yield slower climbing speeds. Movie_S5.mp4

Movie S6. Vacuum robot locomotion. Three gaits are demonstrated, in four configurations; a vertical climbing gait, with two actuator modules, and two additional suction cup modules achieves locomotion at 2 mm/s, or 0.01 Body Lengths per second (BL/s). A rolling gait and wave gait pattern are demonstrated with a 5 module, 15 DoF continuum robot, while the wave gait is repeated with a 3 module, 9 DoF robot. The shorter 3 module continuum robot achieves faster forward locomotion of 11 mm/s, than the 5 module version of 5 mm/s, while the rolling gait achieves the fastest average speed at 60 mm/s. None of the gaits tested were optimized for speed, but the variety is shown to illustrate the characteristic diversity of the different locomotion modes. The robots shown are powered from dual pneumatic ports at each end of the body to compensate for pressure and flow drop in undersized module ports, although both supplies are connected to a single, internal central supply line connected to every V-SPA in the robot through localized solenoid valves. Movie_S6.mp4

* Supplemental videos are available to view or download online at
www.thethoughtfulroboticist.com/thesis

2 Control strategies for modular SPA systems

2.1 Introduction

In this chapter we present and demonstrate both open and closed loop control strategies for modular compliant systems designed for human interaction. While each subchapter, or part, within contains different physical hardware to which various control techniques are applied, a similar approach is taken for all in accounting for and leveraging the intrinsic system compliance inherited from constituent SPAs and the higher-level compliance afforded by large DoF. These factors generally promote the use of simple, distributed or decentralized control techniques, which also complement and extend the feature of system modularity. Although the strategies presented in the following three parts of this chapter favor simplicity, it will be shown that complex and diverse functionality can still be achieved which preserves the benefits of the underlying soft system components, as well as physical human-in-the-loop interactions.

The material presented in this chapter is adopted from the following self-authored publications:

[106] **M. A. Robertson** and J. Paik, “Practical control methods for vacuum driven soft actuator modules,” *2017 IEEE/RSJ International Conference on Intelligent Robots and Systems (IROS)*, Vancouver, BC, 2017, pp. 1224-1229. doi: 10.1109/IROS.2017.8202296

[107] **M. A. Robertson**, M. Murakami, W. Felt and J. Paik, “A Compact Modular Soft Surface With Reconfigurable Shape and Stiffness,” in IEEE/ASME Transactions on Mechatronics, vol. 24, no. 1, pp. 16-24, Feb. 2019. doi: 10.1109/TMECH.2018.2878621
The first author wrote the manuscript, designed the hardware architecture, conducted experiments, and supervised the second author in the fabrication of the main prototype. The third author contributed to the text and experiments on actuator characterization. The fourth author supplied the initial concept and direction of experiments and scientific objectives.

[108] **M. A. Robertson**, L. Dejace, Stéphanie Lacour, and J. Paik, “Bi-modal control of vacuum-powered soft pneumatic actuators with embedded liquid metal-based strain sensitive skin,” *2019 IEEE International Conference on Soft Robotics (RoboSoft)*, Seoul, April 2019.
The first author wrote the manuscript, fabricated actuators and the system prototype, and conducted experiments. The second author fabricated and integrated the liquid metal-based sensors with the actuators, contributed text on the sensor function and fabrication, and carefully edited the final manuscript. The second, third, and fourth author all supervised the research objectives of the work.

2.2 Part 1: Practical control methods for compliant actuators

Vacuum-powered Soft Pneumatic Actuator (V-SPA) Modules have been described to afford advantages for rapid development of reconfigurable, multi-DoF soft pneumatic robots powered by vacuum by reducing their logistical complexity, however they also present new challenges in the control of resulting systems. This framework features modules joined together over a simple embedded pneumatic and serial communication network and requires a unique approach to both low-level control implementation and high-level control strategy. We describe the structure and activation characteristics of a V-SPA Module and present practical methods for its control. These methods utilize software generated PWM activation through a unique serial protocol designed for LED networks and a heuristic mapping strategy for simplifying the spherical control of 3-DoF actuator modules.

2.3 Background

As the field of soft robotics continues to grow, new challenges presented to the community continue to expand and diversify as well. While the initial task of soft robotics research was to develop new methods of performing work and force output using both smart materials and pneumatic pressure, subsequent effort has begun to focus on the control of systems powered by these new soft technologies. Both efforts are still very present and ongoing, with a large variety of Soft Pneumatic Actuators (SPAs) to be found representing the diversity and scope of interest in the domain [34, 38, 29, 28, 109, 36]. While the cornerstone of research in soft robotics will always focus to some extent on developing new core technologies, as new fabrication process are developed [110, 78, 79], new materials are engineered [78, 79], and different applications become the target of compliant robotics [111, 112, 113], a wider, system-level view of design is becoming increasingly necessary in order to facilitate the control and integration more complex multi-DoF soft robots. Examples of such systems have been pursued and successfully implemented, including soft manipulator arms [114, 85, 115], and mobile robots [116, 117], however, they are still developed through independent effort without approaching the task of soft pneumatic system design in a truly systematic way.

Our approach to enabling more efficient design of SPA based systems is through the integration of common subsystem components into modular, interchangeable electro-pneumatic base units. Previous work presented the development of V-SPA (Vacuum-powered Soft Pneumatic Actuator) Modules which leverage this approach to realize multi-DoF soft robots with extended peripheral capabilities powered by vacuum as a single power source [67]. The use of vacuum powered actuation is not an important or necessary aspect of this method for modular soft robot design, as it is possible to develop similar modules powered by more conventional SPAs, however their function and control can be generalized for application in either case.

V-SPA modules allow for the rapid development of large-scale soft robotic systems without the need for deep consideration of low-level design. Other work has investigated the use of modularity to leverage soft-system “bottom-up assembly” [118], however this work neglects the remaining challenge of logistical integration and control. The key concept of leveraging decentralized control to accomplish plug-and-play functionality has been explored to a certain extent through robots with control valves locally integrated near the actuators [99, 100], and others which use the supply line itself to address individual actuators in series [119]. These ideas touch on the importance of decentralized control as a means to accomplish particular design objectives, but do not formalize the concept in a way that can be extended as a design rule to enable other complex, or multi-DoF soft systems to be rapidly, and easily implemented. Furthermore these do not offer solutions or methods for simplifying the control strategy for the large-scale soft systems which are produced.

It is our aim to develop and validate a topological and control framework for reducing the complexity and design effort required to realize new and more capable, multi-functional, multi-DoF soft robotic systems, through the investigation of V-SPA Modules. Here we will demonstrate:

- A plug-and-play reconfigurable, 3-DoF soft robot actuator module, the V-SPA Module
- PWM control characterization of a V-SPA Module
- A heuristic strategy for simplified control of decentralized soft actuator modules

2.4 V-SPA Module Description

V-SPA Modules enable rapid and robust design and reconfiguration of soft robots, by consolidating hardware in a more efficient and plug-and-play package. A module is comprised of two main sections: actuator units, and embedded control network hardware. The first of these is comprised of multiple V-SPAs. The second section contains integrated electrical and pneumatic control hardware key to enabling modular and reconfigurable functionality. See Figure 2.1 for the main components of a V-SPA module.

2.4.1 Vacuum-powered Soft Pneumatic Actuators (V-SPAs)

V-SPAs posess unique attributes useful in many soft robotic systems, especially with many-DoF. Being comprised primarily of foam and only a thin layer of silicone rubber, these actuators are exceptionally lightweight, for given torque output. Utilizing vacuum for actuation, they also offer failsafe operation which prevents over pressurization or explosive failure, and sets a natural saturation limit on force generation beyond the threshold dictated by ambient pressure. These actuators are arranged at 120° intervals to form a cylindrical V-SPA Module with 3-DoF, corresponding to each of the three actuators utilized (see the inset of Figure 2.2.). The top and bottom surfaces of the actuators are attached with an adhesive to rigid plates, which are only otherwise supported by a flexible central silicone tubing conduit to which the

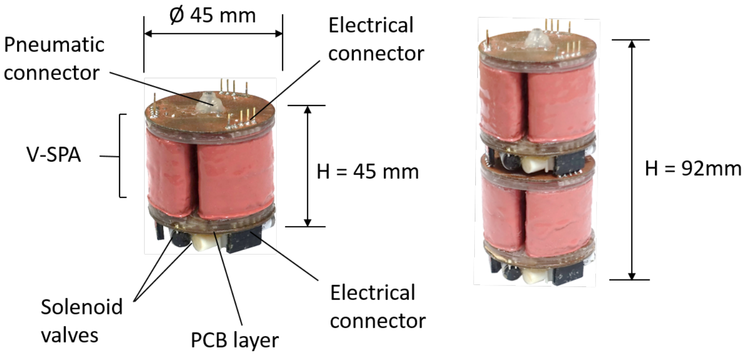

Figure 2.1 – V-SPA module structure. The upper half of a V-SPA Module contains three vacuum powered soft actuators, and an interface plate for serial stacking of other modules. The lower half contains a PCB and control valves, used to address each actuator independently.

vacuum supply is attached. This flexible central conduit acts secondarily as a constraint only to limit vertical motions of the top and bottom plates of the module, but otherwise allows angular displacement of the plates, forming the basis of a soft joint. With three actuators, this joint is capable of angular displacement in any radial direction depending on the combination and degree of activation of the individual actuator units [67].

2.4.2 Decentralized Control Hardware

The critical components required to facilitate features of modularity in V-SPA Modules include solenoid valves (Lee, LHDA0531115H), RGB LED driver ICs (WS2811), and mating interface connectors. The integration of valves directly in place with the actuator units eliminates the need for independent supply lines to peripheral control manifolds. Additionally, a single pressure supply line is utilized and distributed to each actuator through an internal onboard manifold from an off-board pressure source, while pneumatic connectors at the top and bottom of the V-SPA Module allow each to be serially connected to additional modules by simply joining the shared supply. To compliment the reduction in the number of pneumatic supply lines to many actuators across many modules, a similar reduction in electrical control lines was achieved by adopting the use of LED driver ICs to enable communication to all modules over a single electrical signal line. Typically used for independent control of 3-channel LEDs used in large matrix displays, the outputs of each IC are connected to amplifier circuits capable of then driving the solenoid valves onboard the V-SPA Modules, using the same digital protocol developed for controlling light displays. Electrical connectors serve a similar purpose to the pneumatic connectors, allowing a single signal connection in addition to electrical power from an off-board central microcontroller and power supply, respectively, to be passed between adjacent modules and shared.

A large benefit to this design is the current extensive ubiquity of the hardware and software, which makes the parts available at very low cost and at very small scales (many LEDs contain the same circuitry built into the diode housing). While some drawbacks may be found in comparison to other alternatives using dedicated, embedded microcontrollers in every module, the simplicity of the settled solution offers even more benefit in their place. Among already mentioned advantages, the RGB driver solution is demonstrably robust, allowing real-time connection and disconnection of modular devices without interruption to communication with other modules, allowing for truly plug-and-play actuator modules.

2.5 Control Methods

V-SPA Modules enable a unique capability to directly and independently control each of many active DoFs in complex soft robotic structures over a single, shared communication line in either of two possible modes, depending on the intended application. For rough positioning tasks, a fast and highly repeatable method of binary actuation may be employed. To achieve more high resolution positioning, V-SPA Modules can also be controlled via Pulse Width Modulation (PWM) of the onboard solenoid valves. Either of these methods can be adopted by other soft robots of similar or various morphologies, and are not unique to the modules developed here.

2.5.1 Binary Actuation

The most straightforward and simple method to control V-SPA Modules is through the discrete, binary activation of each embedded actuator control valve. In this mode, each valve is either completely ON or OFF, and the resulting motion of the module is limited to fixed positions, as shown by the three corners of the grey motion trajectory of a module traced in Figure 2.2a. The trajectory shown depicts the angular deflection of the V-SPA Module along the two axes defining the motion, and not the absolute position of a marker through space. In this way, although the motion of the module is spherical in nature, the angular trajectory shown encompasses this information in a 2D format. The difference in maximum deflection in each primary direction reveals stark variability between different actuators, which results primarily from the non-homogeneous manual fabrication methods employed in their construction. Despite this however, the motion of the actuators is seen to be repeatable as the shape of the trajectory remains similar for many cycles.

Many other systems have been studied both for the design of novel binary actuators, and to derive efficient methods and algorithms for computing inverse kinematics, and path planning [120, 121, 122, 123]. A particular benefit to this technique is the avoidance of transient nonlinear behavior which is often the crux of soft systems control. Only the endpoint of the actuator needs to be considered, and furthermore, the selection of configurations of a binary robot, even with many DoF is finite, greatly simplifying the effort needed to control this type of robot. With three actuators contained in each V-SPA Module, this yields three angular set-points along primary lines of action, corresponding to the activation of only a single actuator at a time. Additionally, the actuators in a V-SPA Module can be activated in adjacent pairs, yielding

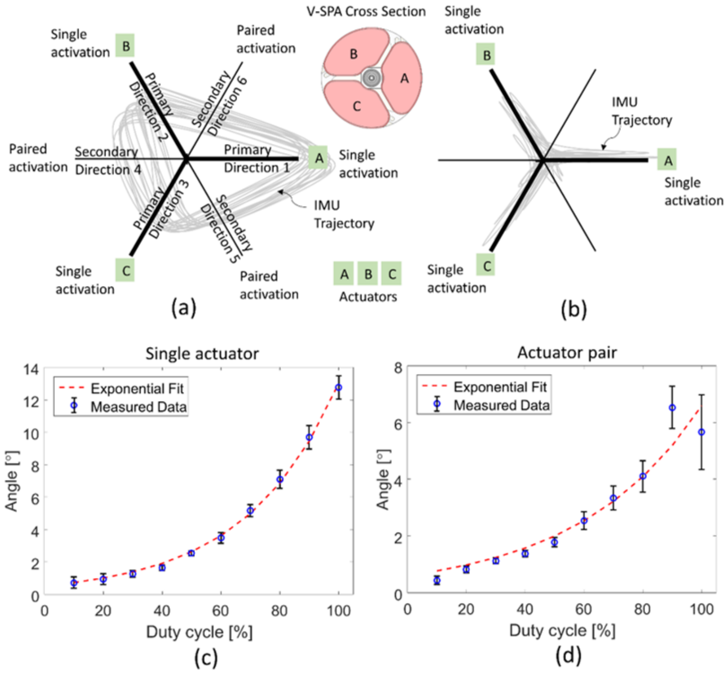

Figure 2.2 – Angular control characterization. (a) A cyclic test was performed using only binary actuation to command a V-SPA Module to each of its three primary deflection directions sequentially, and an Inertial Measurement Unit (IMU) recorded the angular trajectory shown in grey. (b) A 10-cycle test was performed on an V-SPA Module with a PWM controlled sweep of each actuator from 0-100% duty cycle. The trajectory of an IMU mounted to the module is shown in grey. While the path is not as repeatable as the binary control method, it does not deviate significantly from the primary plane of actuation. Part (c) depicts the relationship of control commands to angular output for a single actuator and shows minimal error. Part (d) shows a similar measurement taken with two adjacent actuators activated together to produce motion along the secondary directions of the V-SPA Module, yielding lower angular output and higher variability. In both (c) and (d) a model was obtained by fitting an exponential to measurements taken at multiple positions from 0-100% duty cycle.

three set-points along secondary directions, directly opposite the primary ones.

Figures 2.2a and 2.2b illustrate these six directions of motion resulting from only binary activation which can be utilized most effectively by incorporating multiple V-SPA Modules in a given system, particularly in serial configuration. In this arrangement, the combinatory multiplication of fixed positions yields even greater possibilities for workspace coverage. In applications where great accuracy is not required this may be sufficient alone, however the same modules can be used for intermediate, or continuous positioning if desired using an alternate mode of activation, through PWM.

2.5.2 Continuous Actuation using PWM

Continuous, non-discrete, operation of V-SPA Modules may be found useful in applications requiring accuracy greater than that made possible by discrete actuation alone. Soft actuators can achieve intermediate positions, between entirely at rest and fully inflated, by varying their supply pressure. One way to regulate the pressure supplied to an actuator is indirectly through the modulation of flow, using PWM control of high-bandwidth solenoid valves. By changing the duty cycle of electrical activation for a valve connected to an SPA the actuator can be commanded to variable positions determined by an often nonlinear relationship. This mapping varies with the specific actuator, valve, and pneumatic components used to connect the system together, but can be characterized and fit with a model to provide a useful reference for open and closed loop control. Figure 2.2b shows the trajectory of a V-SPA Module through multiple cycles of single actuator under PWM control, sweeping through a full range of duty cycle input values. An exponential trend was revealed across varying duty cycle values relating to the output angle of deflection, for single and paired V-SPA activation, shown in Figure 2.2c and Figure 2.2d, respectively.

While the method of PWM control of flow and pressure is not novel in the field of soft robotics [124], the implementation of this method in the framework of the V-SPA Module architecture requires an indirect and unique approach to achieve the same goal. As the valves are built into the modules and networked through a dedicated communication IC over a shared signal line, they cannot be directly powered from a PWM signal generator, as is typically done. Instead, every channel of the onboard communication IC is addressed using a timed, 24-byte protocol regulated by a centralized microcontroller and software functions. For this reason, a custom “soft PWM” signal generator was necessarily created to send encoded command updates at high frequency from a 32-bit, 48MHz Teensy-LC microcontroller to the valves inside the V-SPA Modules. This method thus allows for PWM control of the solenoid valves embedded in a network of modules to be independently controlled with varying duty factors, in much the same way as they would from independent, non-shared power lines. The drawback to this method, however, is a greatly increased load on the controller itself. To generate the required signal, an interrupt based timer was implemented which reduced the amount of time available to execute control commands, resulting in interrupted communication to the actuators, and a

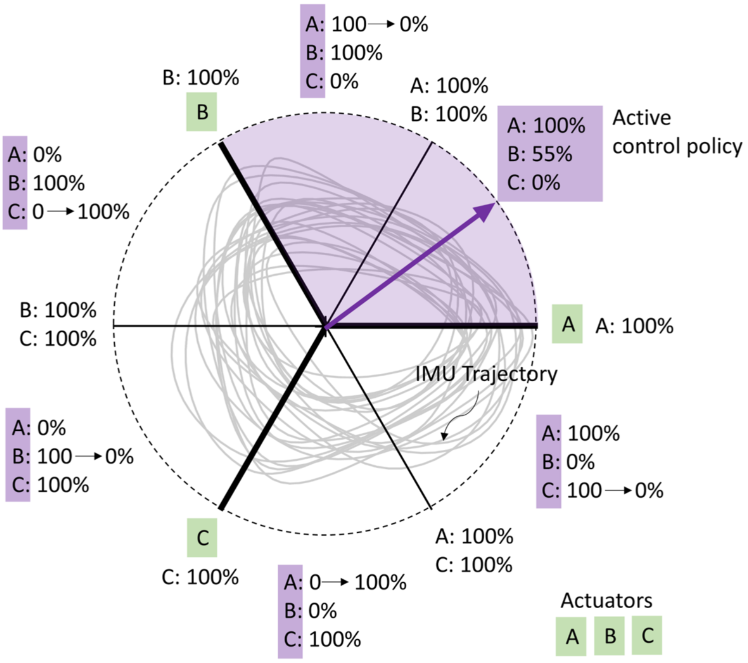

Figure 2.3 – V-SPA module heuristic control map. This heuristic control map translates a two-dimensional virtual control vector (large purple arrow) into actuator commands for a V-SPA Module. Each of the three major regions bounded by the actuator lines of action are subdivided further in half to yield 6 distinct regions wherein the control policy to each actuator unit is unique as a function of the control vector. The allocation of control effort in terms of duty cycle is proportionally determined as a function of angular proximity to adjacent actuators. This model was used to translate two-axis joystick commands to approximate spherical motion control, as well as for following a repeating cyclical trajectory, measured by an IMU and traced out in light grey.

moderately unstable output. Figure 2.2d shows the resulting trend of duty cycle versus angle with higher variability for a pair of actuators activated simultaneously to produce angular deflection along a secondary line of action. Only one actuator unit in a V-SPA Module was found to perform reliably at a time under PWM control, with minimal noise. Consequently, this was found to be a leading cause of difficulty in implementing fully three-dimensional control. Nevertheless, utilizing more efficient programming methods and a simplified control scheme, it was possible to demonstrate more complex motion profiles.

2.5.3 Open loop spherical control

A simple open loop control algorithm was developed to approximate spherical motion with a V-SPA Module, leveraging the 3D workspace afforded by its multiple actuators without the need for a complex kinematic model. This method maps a two-dimensional unit control vector to the three actuators in a module based on its virtual superposition over six regions bounded by the module's primary and secondary directions of deflection. (Figure 2.3.) The magnitude of the control vector is taken to be the maximum "control effort" available for allocation as a duty cycle command prescribed to the two actuators bounding the active region represented by the vector, while the direction of the vector determines the proportional distribution of that effort between the actuators. While the actuator in closest proximity or direct alignment with the control vector is activated to full effort, the proportion of activation for the second actuator is determined by the angular distance of the virtual vector to its location. The activation is scaled linearly with this angular distance in such a way to achieve 100% of available "control effort" when the vector is directly between two actuators, thus yielding a deflection along one of the secondary lines of action, and decreasing to 0% as the vector approaches the other actuator set to full activation, yielding net motion along the primary line of action of that actuator.

This heuristic technique provides only a coarse emulation of spherical motion, but nevertheless demonstrates that V-SPA Modules can be utilized for wider workspace and range of applications than allowed by nominal binary control alone, and provides a useful representation as the basis for more refined control in a closed loop system. Moreover, this improvement in utility can be achieved without complex kinematic modeling of a generally nonlinear system.

2.6 Discussion

The trajectories plotted for different conventional pneumatic actuator control methods in Figure 2.2 reveal a tradeoff between repeatability and workspace for the V-SPA Modules presented here. The simplest method utilizing only binary control does appear to track a wide path covering area apparently equal or greater to that covered by the most elaborate control schemes shown here, for approximated spherical control. The figure does not show however that much of the trajectory plotted is in transience between the vertices of each rounded triangular curve, corresponding to the fixed points reached at the end of every actuator units' stroke. Thus in reality, this is the sparsest workspace illustrated. On the other hand, the tracked path of the IMU does in fact to be repeatable in size, shape, and position. These trends are the opposite with the plot of the module angular trajectory under full 3-DoF control. This mode combined the use of PWM control of actuator pressure to achieve intermediate actuator positions, with a heuristic control map to quickly set the output angle of the V-SPA Module without explicit kinematic derivations or nonlinear modelling. While expectedly less accurate than a rigorous control scheme, the method demonstrates a simple means of control that may sufficiently serve needs underrepresented in the field of controls – that generally being the practice of mechanically informed control policy estimation.

It was also shown that the mapping of a PWM duty cycle control input to the resulting individual actuator angular deflection can be characterized relatively well using a single exponential fit, however a different fit was obtained for the same measurement of adjacent actuators in pairs. The implication of this fits the expectation that when used in different combinations, of different actuators and duty cycles, the relationship between the control input and angular motion output is very nonlinear. Moreover, the trend obtained for the actuator pair characterization showed an increase in variability which presents a challenge to designing any kind of closed loop controller.

While the V-SPA Modules studied here are powered by vacuum, a nearly identical design could be implemented with any type of pneumatic supply or actuator. Similarly the practical control methods and simplified approach to expanding the utility of a multi-DoF soft actuator without the need for more complex control techniques to satisfy certain performance metrics can easily be adapted to any soft pneumatic system.

2.7 Conclusion

Following a methodical approach to system-level soft robot design, V-SPA Modules employ a network based architecture pertinent not only to modular robots, or vacuum based actuation, but to the entire field of soft robotics as it moves towards more complex, robust hardware and corresponding control. With this new approach to soft robot design enabling plug-and-play reconfigurability and facilitation of higher-DoF systems, a corresponding adaptation of control strategies may be applied to accommodate both increased DoF and new hardware topology. For V-SPA Modules, it has been shown here that variable actuation modes and heuristic strategies can be used to mitigate some of the complexity derived from scalable, modular soft robotic systems. These methods can be generalized for use by modules based on similar hardware architecture toward improving the cycle time and efficiency of soft robot design and development.

2.8 Part 2: Physical shape and load modulation control modes for tangible interactions with soft reconfigurable surface

A variety of reconfigurable surface devices, utilizing large numbers of actuated physical "pixels" to produce discretized 3D contours, have been developed for different purposes in research and industry. The difficulty of integrating many actuators in close configuration has limited the DoF and resolution and performance of existing devices. Utilizing vacuum power and soft material actuators, we have developed a soft reconfigurable surface (SRS) with multi-modal control and performance capabilities which resolves these obstacles to achieve a compact form factor. The SRS is comprised of a square grid array of linear vacuum-powered soft pneumatic actuators (linear V-SPAs), built into plug-and-play modules which enable the arrangement, consolidation, and control of many DoF. In addition to the practical benefits of system integration, this architecture facilitates the construction of customized assemblies with an overall compact form factor. A series of experiments is performed to illustrate and validate the versatility of the SRS for achieving diverse tasks including force controlled modulation of interface pressure through integrated sensors, lateral manipulation of a variety of objects, static and dynamic shape and pattern generation for haptic interaction, and variable surface stiffness tuning. This SRS concept is scalable, space efficient and features diverse functional potential. This will extend the utility and accessibility of tangible robotic interfaces for future applications from industrial to home and personal use.

2.8.1 Background

A reconfigurable surface is a nominally 2D structure which can be transformed to render 3D shapes and contours. This is often achieved by discretizing the surface into an array of height-variable physical pixels, pins or rods which are used to construct digitized or physically interpolated (via a flexible covering) geometric features [125, 126]. This concept has attracted interest for diverse applications in a variety of interactive and physical user interfaces.

In the field of Human-Computer Interaction, reconfigurable surfaces are considered as a subclass of "shape-changing interfaces" [127]. In this field, reconfigurable surfaces may be used, for example, to create physically 3D visual displays [128, 129, 130, 131]. The ideas behind these displays have found their way into (and likely out of) science fiction movies such as X-Men (2000) [132].

The changes in surface elevation can also be used to create tactile displays for the visually impaired. Such is the goal of "refreshable braille displays" [133]. These devices display different braille characters by toggling pins between raised and lowered positions. Though traditionally these devices have relied on relatively large piezoelectric actuators, proposed actuation concepts include microfluidics [134, 135, 136], electro-active polymers [137, 138, 139] and shape-memory alloys [140, 141, 142].

Other displays have been designed to render tactile or haptic information to unimpaired users. For example, inflating pneumatic cells have been combined with a jamming-particle surface to create a haptic surface that can render different shapes and mechanical stiffness [143, 144]. Another display, FEELEX, includes force sensors on each pixel, allowing it to react to the interaction forces from the user [131]. These tactile displays can also be placed on the body to provide tactile cues without visual distraction [145, 146, 147, 148].

The principles behind these shape/pressure adjusting technologies are also found in more personal applications. For instance, medical mattresses can be overlaid with “dynamic support surfaces” that actively alternate or adjust pressure distributions to prevent bedsores [149]. Air bladders or mechanical devices allow the seats of luxury automobiles to adapt to different users and preferences [150]. And the ubiquitous “massage chair” uses its surface to create dynamic pressures on the back, legs or feet of its users.

A changing topology can do more than just change its shape or pressure profile, it can also transport objects on its surface. This may be accomplished, for instance, by creating wave-like profiles that cause the object to roll or slide in the desired direction [151, 128, 152]. FESTO’s “WaveHandling” system relies on a network of bellows under a flexible surface [151]. A braille-display-controlled manifold of soft blisters has been used to control the rolling of a ball [152]. Other surfaces can move flat objects without rolling. Taking inspiration from the locomotion of caterpillars, these “soft tables” can manipulate objects in three degrees of freedom by controlling the elevation and translation of an array of soft legs [153].

In the manufacturing industry, controllable topology has been leveraged to develop reconfigurable die and mold tooling concepts for reducing production costs. This method allows forming of sheet materials with different curvature patterns or shapes using a single mold. This technique has been proposed for sheet metal forming [154, 155] and composite molding [156]. A commercially available “adaptive mould”, produced by Adapa, can aid the production of custom double-curved panels out of composites, thermoplastics, concrete, and glass [157].

Every reconfigurable surface device with many DoF involves a significant challenge in the integration and control of a large number of actuators necessary for its function. Different designs are constrained by different practical limitations. Purely mechanical systems require either very small actuators embedded below each physical pixel, or transmission elements such as flexible cables to relay force from actuators separated from the active surface elements by distance and scale. Typically the latter results in systems which are much larger than the functional area of the reconfigurable surface itself, which limits the applications of such devices to effectively stationary and unconstrained environments. Other surfaces which are driven by small embedded actuators usually rely on such mechanisms as smart materials including SMAs, electroactive polymers, piezoelectic actuators, or miniaturized voice-coil linear motors [133, 158]. While principally ideal for applications matching their physical scale, these technologies are generally characterized by low force, and stroke limitations. Other solutions which utilize fluid as a transmission medium often combine both the advantages and disadvantages of both types of systems; incorporating compact actuators while relying on inefficient architecture for managing fluid power distribution and control. Some progress has been made in existing work to address these challenges, specifically through the development of modular soft actuators which were leveraged to produce robot morphologies powered by pneumatic vacuum that could not have otherwise been implemented practically [67]. *The objective of this work is to study the performance of physical shape and load modulation control modes for tangible interactions and haptic interfacing using a modular, high-DoF, reconfigurable surface powered by pneumatic vacuum through a single port.* This contribution will extend the existing utility of reconfigurable surface systems and present new alternative uses or practical potential to leverage further benefits.

We developed a new, compact interactive platform, a soft reconfigurable surface (SRS), based on a modular actuator network to test applications in safe object manipulation, haptic interaction and variable-stiffness surfaces. The SRS concept we present is modular, allowing the "plug and play" modules to be rearranged into arbitrary footprints with little design effort. This modular, embedded hardware approach also facilitates the use of versatile and powerful actuators while maintaining an overall space and weight efficient embodiment. Our system's unique combination of performance potential, physical design efficiency, and customizability could lead to use in new, unexplored domains, including personal and portable use outside of industrial and scientific research settings.

The main contributions of this section are:

- A narrow form factor, linear V-SPA module for close-packed arrangement in a high-density matrix array
- A compact, a soft reconfigurable surface (SRS), interactive platform based on a modular actuator network to test applications in safe object manipulation, haptic interaction and variable-stiffness surfaces.
- Closed loop stiffness and force control of high-DoF V-SPA interactive SRS prototype
- Open loop shape and pattern control for object manipulation, haptic or visual display

2.8.2 Physical System Architecture

Base platform

The SRS prototype shown in Fig. 2.4 is comprised of 16 modular actuator units arranged in a 4x4 grid layout. This configuration is chosen to enable a diverse variety of system capabilities and behaviors, however due to their modular construction, any arrangement of actuators is possible. A functional base platform dictates the overall size, shape, and resolution of the final system and may be easily customized. The platform provides mechanical interface features which allows actuator modules to be plugged into it and physically joined to form a single system. The base also serves as a pneumatic supply manifold and electrical control

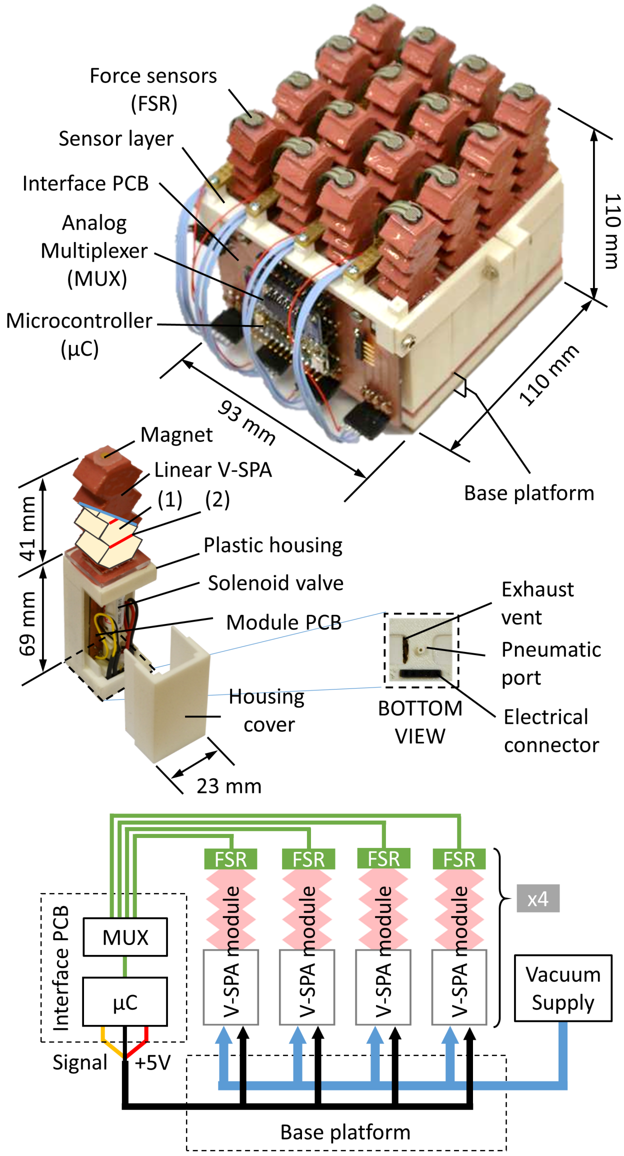

Figure 2.4 – The 16-DoF SRS prototype. The SRS is comprised of 16 independently controllable single DoF modular actuators powered by vacuum pneumatic pressure, a force sensor layer, and control and interface electronics. Each actuator module is interconnected through a multi-port interface from below to a base platform which provides pneumatic and electrical power supply in addition to a computer control signal. A module consists of a single control valve, communication electronics, and a Linear V-SPA, shown with an illustrated cross section depicting the foam chambers (1), and dividing membranes (2).

network interconnection. For fluid power, every module is connected through a port to a shared negative pressure supply distributed through parallel branched channels embedded in the base manifold. Only a single pneumatic supply line is required to power the base platform, irrespective of the its shape, or the number of modules attached to it. For electrical power, the modules are also connected in parallel, while for control each module is electrically connected through the base platform in series on an extensible single wire communication bus.

Module

The module body contains embedded hardware and electronics which enable attached actuators to be powered and controlled locally. The integrated components include one solenoid valve (Lee, LHDA0531115H) mounted internally on a Printed Circuit Board (PCB) and a communication IC (Worldsemi, WS2811) that allows commands to be sent to every module independently over a single signal line. These decentralized components are key to the practicality of the final system as they reduce the complexity of connecting many pneumatic actuators required to achieve high-DoF in the reconfigurable surface. The modular architecture also yields a complete system which is relatively compact compared to other reconfigurable surface systems.

Linear V-SPA

A linear vacuum-powered soft pneumatic actuator (V-SPA) is attached to the top of the module body. When combined with other modules in close arrangement, the distal endpoints of the actuators constitute an interactive, variable geometry surface. To render adaptable shapes or stiffness profiles, the vertical height of each actuator is controlled by modulation of a vacuum pressure pneumatic supply. In this way every actuator module only has a single DoF while the system as a whole consequently consists of 16 independent DoF.

Linear V-SPAs are composed of an open-cell polyurethane foam core assembled in separate pieces sequentially between stiff paper dividers, separating the whole actuator into a stack of multiple chambers following methods and materials similar to previous work [67]. To accommodate the attachment of sensors to the end of the actuator, a rigid 1 mm thick acrylic plate is glued to the top of the core. The linear core assembly is then manually coated with two thin layers of Elastosil M4606 silicone rubber to seal it from the environment, leaving an uncoated portion at the proximal end to attach to a mounting plate with a hole for the pneumatic supply. Under the negative pressure of the vacuum supply, the actuator is driven to collapse. The relatively stiff paper dividers and the hexagonal shape of each foam core segment directs the structure to create large compressions in the actuator length. With the actuators oriented vertically at the top of the modular units, this retraction produces a height displacement which changes the shape and contour approximated by the endpoints of all the actuator modules combined in the SRS. By controlling the vacuum pressure in the modules we can modulate the actuator position, end-force, or effective stiffness.

Sensors

To enable optional feedback control of the SRS, an additional modular force-sensing layer can be attached to the assembled grid of actuator modules. The sensor layer is comprised of a 3D printed ABS plastic structure which surrounds and clamps onto the assembly, and houses thin PCB rails which fit between the rows of linear V-SPAs comprising the upper portion of the SRS. Adjacent to every V-SPA along the rails, the thin, flat cable of a 4mm diameter flexible Force Sensitive Resistor (FSR 400, Interlink Electronics) is attached. The actuator modules as well as the sensor layer are connected through an interface PCB which houses a microcontroller unit (Teensy LC) and an analog multiplexer which facilitates reading all 16 surface sensors from a single analog and four digital microcontroller inputs. The PCB also contains a three-wire control connection header to attach the actuator to the module base platform, and a final header to receive high-current 5V power from an external supply (every valve draws 150 mA current, for a total of 2.4 A possible when all modules are active).

To physically interface with the actuators, a small, high-force neodymium magnet is glued to the back side of the functional, distal end of the sensor, which is oriented to compliment a magnet of opposing polarity embedded in the end of the surface actuator. This allows removable temporary attachment or detachment of the sensor assembly to the main SRS body. When the actuator modules and sensor layer are combined, each actuator is paired through software to the sensor attached to its end, enabling individual force control of every actuator in the complete surface.

2.8.3 System control

Experimental Module Quasi-static Characterization

A single actuator module was tested in compression with vacuum gauge pressure levels between 0 kPa and -30 kPa. These tests were conducted under quasi-static conditions in an Instron 5965 with a 500 N load cell. A tack was glued to the top of the module to keep it oriented to the load-cell during compression. The long-slender actuator buckled and rebounded under the compressive loads. A polynomial surface was fit to the data. This surface related the compression (5th-order regression) and pressure levels (2nd-order regression) to the measured load. The results of this regression are shown in Fig. 2.5a. The R^2 value of the regression was 0.933 and the RMS of the residual error was 0.427 N. The smooth polynomial function used for the regression allowed was used in the analysis of the module behavior.

Position Control

The polynomial surface regressed to the module characterization data can be used to identify an approximate relationship between actuator free contraction and pressure (Fig. 2.5b). The true behavior of the actuator for a given pressure will vary from the curve shown in Fig. 2.5b because of hysteresis. The maximum free contraction, with -30 kPa, was approximately 1 cm

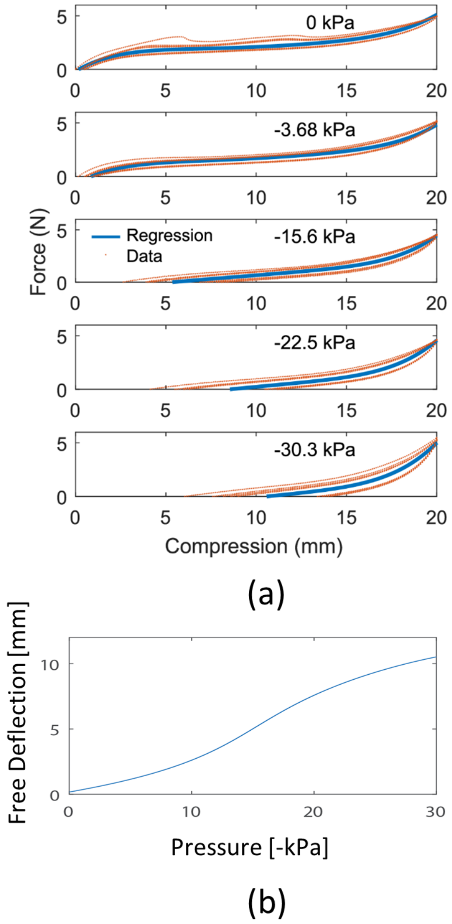

Figure 2.5 – Linear V-SPA position control characterization. (a) An individual actuator module was tested in compression. Increasing the magnitude of the vacuum pressure increases the free deflection of the actuator. To compress the actuator beyond this point, external forces are required. This load-behavior of the actuator was captured well by a two-variable (compression and pressure) polynomial surface. (b) The relationship shown here between the point of zero external force and pressure was identified from the polynomial surface regressed to the characterization data.

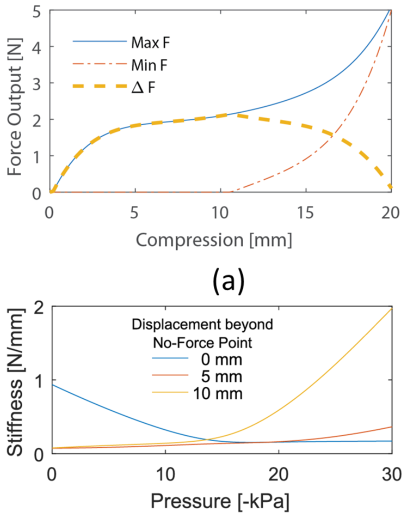

(a)

(b)

Figure 2.6 – Linear V-SPA force control and stiffness characterization. (a) The achievable force output of the actuator is constrained by its compression level. At low-levels of compression, only small forces can be achieved. The largest range of achievable forces occurs at approximately 1 cm of compression. As the compression approaches 2 cm, higher forces can be achieved but the vacuum pressure loses its ability to reduce the force from the foam. (b) The instantaneous stiffness of the actuator (evaluated at the free deflection point) decreases with increasing magnitudes of vacuum pressure. An approximately five-fold decrease in stiffness (over small deflections) can be achieved. With vacuum pressure magnitudes above about -15 kPa and for compressions on the order of 1 cm beyond the no-force point, the effective stiffness of the modules increases with increasing magnitudes of vacuum pressure.

(for a nominal relaxed module height of 4 cm).

Force Control

The force at the actuator tip comes from the compression of the foam within the actuator (Fig. 2.6a). For small levels of compression, only small forces can be achieved. For moderate levels of compression, the force remains roughly constant. For example, between 5 mm and 12 mm of contraction, the maximum tip force as characterized by the polynomial regression increases from 1.8 N to only 2.3 N. This force can be modulated lower through the application of vacuum pressure. For compressions smaller than 1 cm, the output force can be decreased to zero (with a maximum vacuum gauge pressure of -30 kPa. Beyond this point, the force can still be decreased but the change in force, ΔF, achievable through vacuum decreases gradually until 2 cm of compression is reached.

Stiffness Control

The vacuum pressure can be used to modulate the passive stiffness of the modules. For a module at a given free displacement, the stiffness quantifies how quickly the force increases for a given displacement beyond its un-forced level. The partial derivative (with respect to displacement) of the polynomial surface for module force can provide a measure of stiffness. Evaluating this partial derivative at the free-displacement point (Fig. 2.6b) shows that increasing the magnitude of the vacuum pressure decreases the stiffness of the system for small deflections. This small-deflection stiffness decreases from 0.94 N/mm with no pressure to 0.17 N/mm at -30 kPa, an 82 % reduction. At larger displacements (e.g. 1 cm), the instantaneous stiffness increases for pressure values with magnitudes above about -15 kPa. At this deflection beyond the no-force point, the instantaneous stiffness can be as high as 1.9 N/mm.

We validate the practical capability of the SRS for use in different applications by demonstrating a variety of distinct, programmable control modes. Utilizing integrated force sensors coupled to every linear V-SPA module, we present the operation of the SRS in force control mode for interface pressure redistribution and input device functionality. An alternate mode, controlling actuator position in open-loop and neglecting the stiffness change coupled to displacement, is shown to generate different shapes and patterns for haptic display or direct physical manipulation of external objects. Finally, leveraging the variable stiffness characteristic of the actuators as a function of pressure, we achieve a stiffness control mode which yields a soft surface with tunable passive compliance.

2.8.4 Force Mode: Interface Pressure Modulation

Closed-loop force control was implemented for each linear V-SPA module to permit active modulation of the interface pressure (IP) between the top of the SRS and an external load. Individual sensors were attached to the endpoint of each linear V-SPA and a binary (bang-bang) control scheme was employed to achieve two different force modulation capabilities: IP redistribution and IP reduction.

The same simple control strategy resulted in the behavior for both types of loading. Using the control with a fixed load results in an IP redistribution behavior. Fixed displacements result in an overall IP reduction. These scenarios are analogous to different potential applications for a compact SRS, including an active pressure-point reductive bed or seating surface (fixed load) or dynamically adjustable body interface for wearable robotic devices (fixed displacement). Fig. 2.7 illustrates these behaviors.

The performance of the force control mode was evaluated through a set of tests designed to simulate these potential use conditions and illustrate the efficacy of the different control behaviors. Fig. 2.8 shows the results from the validation experiments performed using the SRS and various physical test objects used to produce variable load distribution. For both test conditions, two force targets were tested, corresponding to 29% and 68% of the maximum

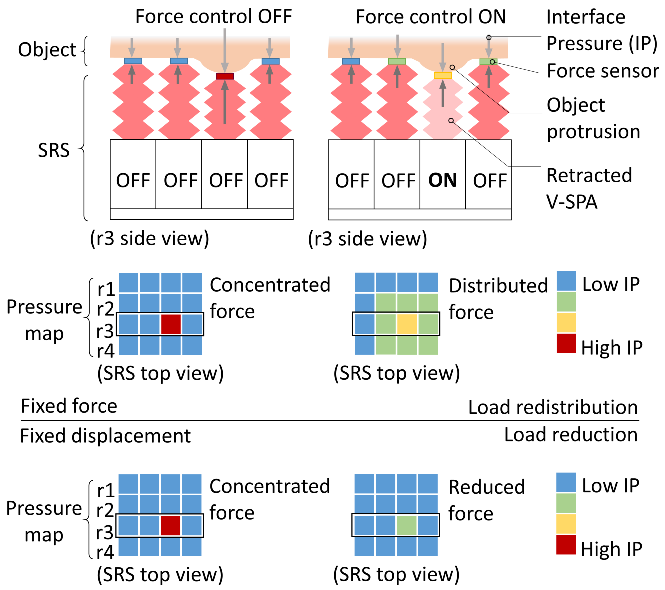

Figure 2.7 – Active interface pressure modulation. Through retraction of the actuators we compensate for uneven interface pressure distributions based on contact force detection. For a fixed force load, representing an object resting on the surface, interface pressure concentrated at a single point is distributed among other actuators when the load is reduced at the concentration point. For fixed displacement loads, the reduction of interface pressure (IP) at the concentration does not affect adjacent areas of the surface.

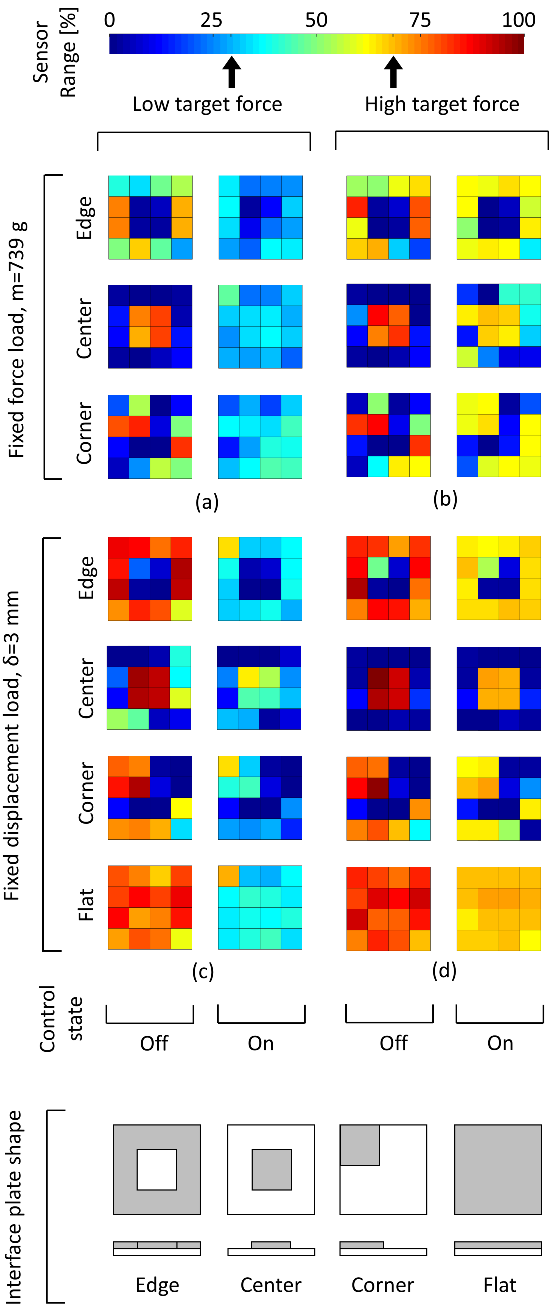

Figure 2.8 – Experimental closed-loop control of surface interface pressure. Different patterns of non-uniform IP were imposed by interface plates in contact with the surface, with a variety of physical profiles. The physical profiles on the interface plates included protrusions at the edge, center, or corner of the surface. The pressure maps between controller off and on states show the effect of the active force control. With fixed loads, the IP was redistributed and with fixed displacements, it was reduced.

measurable force for a single sensor (roughly 1/3 and 2/3 of the sensor range respectively, to demonstrate two distinct targets within the nominal regime of the sensor separated from both extremes at the minimum and maximum of the range).

For the fixed load tests, a square, rigid medium-density fiberboard (MDF) plate was placed resting on top of the surface, to support an object of 739 g mass. In addition to the plate with a flat contour on both sides, three other interface plates were tested with protrusions around the edge, in the center, and in the corner. These plate variations produced different interface pressure patterns used to highlight the effect of the active force control. A measurement was initially taken of all 16 sensors with the force control deactivated, and then again after it was turned on.

For the fixed displacement tests, a heavy duty scientific ring stand was used hold the MDF plate against the surface at a pre-set deflection of 3 mm below the nominal, unpowered resting height of the actuators. Again, measurements were made before and after activation of the force control.

2.8.5 Position Mode: Shape and Pattern Generation

Tactile display

The SRS can be utilized as an output device to physically display meaningful information through static shape reconfiguration or dynamic pattern propagation. As the active surface of the device consists of an inherently soft structure, it can be safely operated in direct or close contact with sensitive body areas where the structural data representations may be perceived. Using shapes, patterns, and motion profiles, a variety of information could be transmitted to a user. This method of haptic representation could be used to render geometric or non-geometrical data. This includes topological graphics, simulated structures, feedback from other devices, or incoming communication.

We implemented some examples to illustrate the possible application toward a tactile display device. Fig. 2.9 shows both static and dynamically rendered shapes and patterns. These were generated with the prototype to form at least ten unique tactile primitives which could be used to encode information. Using these primitives in combinations to form tactile words, an even wider range of complex tactile communication is possible.

Object Manipulation

Surface shape patterns can also convey and manipulate physical objects. By producing variable height profiles, the SRS is capable of directing the motion of objects placed on it from high to low spots, leveraging gravity. As the topology of the surface changes dynamically, the position and orientation of any objects resting on it follows the low-energy wells formed around prominent features, allowing the objects to be moved either by rolling or sliding in the

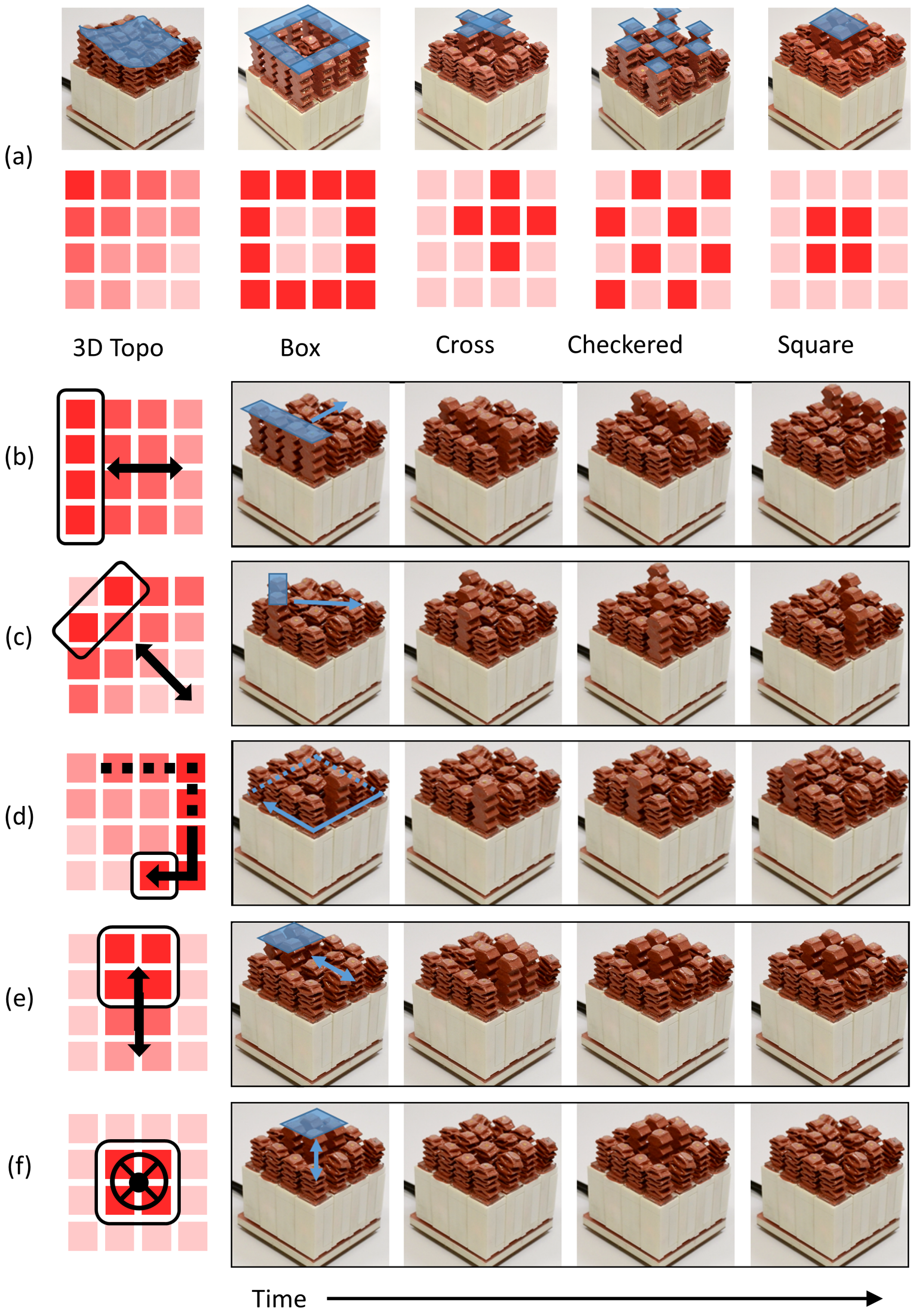

Figure 2.9 – Shape and pattern rendering for haptic or visual display. The SRS can render a variety of shapes and patterns which can be discerned by visual display or through safe tactile interaction to convey information or feedback to a user. A selection of static shapes are depicted in (a), and examples of dynamic patterns are shown including, (b) orthogonal wave, (c) diagonal wave, (d) path trace, (e) moving shape, and (f) blinking shape, although many more alternatives are possible with the high-DoF reconfigurable surface.

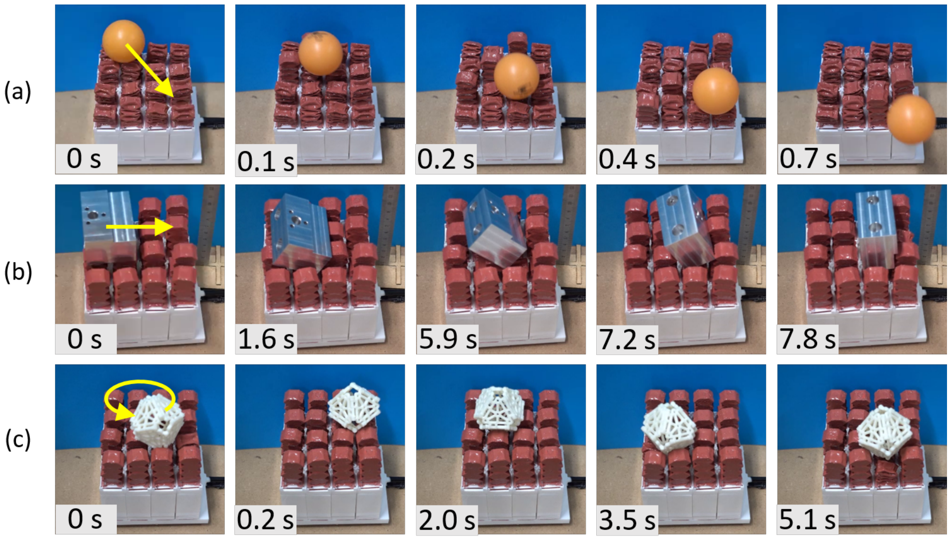

Figure 2.10 – Object transport with dynamic surface shaping. Three objects were transported across the SRS with different dynamic shape patterns: a lightweight ball transported via positive (convex) diagonal wave (a), a heavy block via positive orthogonal wave (b), and a delicate object transported in a circular path with negative (concave) wave along a traced path (c).

direction of traveling waves. In addition, static features may be produced to provide passive object constraints that can be used to guide objects in motion or arrest them.

We demonstrate these capabilities experimentally using the SRS prototype to manipulate three different types of objects categorized as lightweight, heavy, and delicate, respectively, as shown in Fig. 2.10. Both negative and positive waves were tested to transport the objects; the former produced by the progression of a concave feature across otherwise nominally extended actuators, with the latter formed by a convex feature traveling across a surface of otherwise fully retracted actuators. Both methods were effective in transporting objects across the surface, although a trade-off was found between speed and controllability for certain objects which would prescribe the advantage of one over the other depending on application requirements. This difference is mainly due to the presence or lack of fully defined object support by the surface during object transport. With negative waves, objects maintain quasi-static equilibrium throughout the process of translation, being borne by multiple extended actuators surrounding a concave surface feature, allowing better control. For positive traveling waves, a prominent convex feature is used instead to push an object across the surface, leading to behavior closer to continuous falling for less controllable but more dynamic and high speed transport. This was particularly apparent through observations of the movement of a lightweight spherical object which is prone to rolling freely away from a prominent, positive wave at high speed, while a negative wave maintained control of the object at all times. The average linear velocity of the ball-shaped object in translation was estimated to be 27.5 cm/s, while the large, heavy, rectangular object was observed to be 0.7 cm/s.

2.8.6 Stiffness Mode: tunable passive compliance

The variable stiffness behavior of the actuators as measured in Section II-B can also be leveraged in combination with shape and pattern rendering to augment the position control capabilities mode described above. The nominal stiffness of the surface can be tuned for either application by adjusting the nominal range of operation for the actuators. At different overall displacement levels or actuator heights, the surface can render the same features used for tactile display or object manipulation within controllable regimes of compliance. This feature extends the utility of both by adding additional haptic information or mechanical control. While integrated sensing can also be used to achieve active force control for the same purpose, the method of tuning the passive stiffness of an SRS allows a more robust guarantee of safety for objects in contact, independent of control system dynamics and speed which affect other active stiffness control methods.

In this paper we present a new reconfigurable surface concept based on a new type of modular, linear vacuum-powered soft pneumatic actuator (linear V-SPA), which is capable of operating in position, force and stiffness control modes. A 16-DoF prototype was experimentally tested for validation of the control modes in the context of realistic potential applications. The design is fundamentally modular and extensible to different footprints with high numbers of modules.

Using force sensors on the surface of each actuator, closed-loop force control was utilized to actively modulate the interface pressure between the SRS and non-uniform objects in contact. This mode was was able to reduce and redistribute the forces on the surface. This could enable applications such as mechanical human interface devices to alleviate discomfort or tissue damage from extended duration pressure concentration from wearable robots or from body weight support.

In open-loop position control mode, the SRS also demonstrated the ability to render physical shapes and patterns to function as a non-visual tactile display. Static and dynamic primitives were generated which could serve as elements for a tactile language. These could convey complex information for use in machine feedback or communication applications. While not demonstrated here, the force control mode could also be combined with this application to provide another level of feedback, or the sensors could be used for touch driven device input. The position control also enabled the transport of physical objects. By creating traveling waves along the surface, the SRS is able to manipulate objects through rolling. This could enable industrial conveyor applications for delicate objects. We also demonstrated the functionality of the SRS as a variable stiffness device. This control mode could be combined with position control to create haptic displays with controllable passive stiffness. It could also be used to passively mitigate impacts or dampen motion without the need or limitations of active stiffness control.

As a result of a modular architecture and the use of soft material actuators powered by vacuum to provide safe and compliant reconfigurability, the SRS presented here demonstrates a unique combination of performance and design efficiency. With a diverse range of potential functions along with a compact and scalable design, the multi-functional SRS device enables new and extended applications limited in previous similar devices by practical size or actuator performance constraints. The unique features of the SRS afford benefits to high-DoF manipulation, interaction, or communication tasks with potential in both industrial and personal use by providing safe and compliant reconfigurability.

2.9 Part 3: Embedded soft strain sensors for feedback and feedforward (bi-modal) V-SPA module control

Soft robotic systems are composed of active and passively deformable structures which are intrinsically compliant, flexible, and elastic. Although these features offer benefits of adaptability, robustness, and safety, controlling these types of robots is a significant challenge, in part from the difficulty of obtaining feedback from sensors which provide state information without hindering the advantageous material properties which grant these systems their unique mechanical behavior. We demonstrate here the first integration of a flexible, stretchable, liquid metal-based strain sensor with vacuum-powered soft pneumatic actuators (V-SPAs) for simultaneous controlled feedback of the soft actuators as well as user input and soft robotic device interaction. The soft sensors which are encapsulated within a Polydimethylsiloxane (PDMS) membrane are directly embedded in the outer body skin of the soft actuators, and can be used to correlate the deformation of the body under vacuum actuation to overall actuator strain or to detect external disturbances. This information is used to compute and control the angle of a rotational 3-DoF actuator module, as well as detect implicit user input control signals by direct interaction without the need for an external control interface. The dual use of embedded sensing shown in this work provides a fundamental strategy for soft collaborative robot applications.

2.10 Background

Soft robots are designed to leverage benefits that many biological organisms are known to exploit for achieving compliance, robustness, and adaptability to their environment [159]. These features have been described as the basis for what has been termed morphological computation [160, 66], allowing the mechanical properties of the constitutive soft body tissues of the living systems to passively conform to objects around them without invoking complex control to do so. This effectively reduces the problem in tasks such as manipulation or locomotion [161, 65] but does not completely eliminate the need for higher level control [162].

In soft robotics the issue of control is at the front of current challenges in the field. Although the best approach to this problem has not been settled, primarily between model-based and model free control methods [31, 163, 164], a widely accepted starting point is the acknowledged need for implicit sensing strategies. The baseline requisite for sensors which are compatible

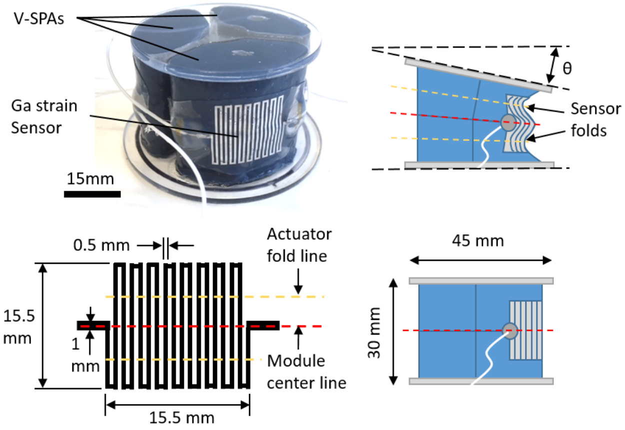

Figure 2.11 – Sensorized V-SPA module. A soft, liquid metal strain sensor integrated with a 3-DoF vacuum-powered soft pneumatic actuator module enables sensing of its angular deformation upon activation. A single sensor is bonded to each actuator in the module and comprised of a meandering path which is positioned at the centerline of the actuator. This pattern extends above and below the two longitudinal locations where folds occur due to buckling when activated.

with soft structures makes even this starting point a challenge.

In order to preserve the benefits of soft material robot body and actuator compliance, any sensing system used in a fully integrated soft robotic system should be likewise compliant. While most commonly available robotic sensors are rigid, various types of soft, flexible, and stretchable sensors have been investigated in research toward developing soft robots which are innervated with sensing abilities to interact with the environment [165, 166] as well as provide feedback for control. The sensing principles utilized in previous work varies between resistive, capacitive, and optic types [167, 168].

Among the diverse soft sensor types that have been explored, liquid metal based sensors achieve some of the highest performance in terms of stretchability, accuracy, and highly thin form factor [169, 170]. This type of sensor also stands out from the perspective of fabrication, as some can be readily printed by direct writing methods while others can be produced using a variety of versatile deposition techniques, allowing application to wearable devices or soft robotic structures and actuators [171, 172, 173, 174, 175]. The low-profile form factor and exceptional softness of these sensors have even made them suitable for use in medical and implantable applications [176, 177]. In comparable efforts, roboticists have also integrated these sensors directly into soft actuators and robotic bodies to provide proprioceptive feedback to control grasping force and detect objects for gripping [178, 179].

Although liquid metal type sensors show diverse advantages and applications, these have primarily been utilized for modes of deformation which induce strain of the sensor. This mode has made integration of these sensors with positive pressure soft pneumatic actuators (SPAs) readily feasible, however, recently studied SPAs powered by vacuum (V-SPAs) do not operate in the same way [180, 181, 76]. Rather than stretching from inflation of soft elastomeric chambers, V-SPAs generate force and motion primarily from buckling and folding of flexible but not necessarily elastic encasement. Although the dominant mode of this type of actuator does not directly match the main functional mode for many soft sensors, the versatility of liquid metal-based sensors enables output when used in either stretching or compression mode, making them a preferred candidate for use with vacuum powered actuators. The benefits afforded by V-SPAs include enhanced failsafe behavior since they do not rely on elastic deformation and thus do not store energy while active, as well as their being power limited since their force output relies on environmental pressure conditions which are generally held constant. These features thus offer new opportunities to explore for unique integrated actuator and sensing systems for the benefit of extending versatility and safety in soft robotics as a whole.

The main contributions of this section are:

- The first integration and validation of soft liquid metal Ga sensors with V-SPAs, for measuring and controlling large actuator strain.
- Demonstration of SPAs with embedded sensors for both control and user interaction.

2.11 Soft robotic system hardware

2.11.1 V-SPA modules

Actuators are fabricated individually on preform structures, with two open-cell polyurethane foam body ‘chambers’, and a single central dividing plane, as described in previous work [180]. When activated by vacuum depressurization, this rigid membrane component (heavy gauge paper) helps to enforce buckling primarily in the vertical direction. The soft foam actuator cores are coated with two manually brushed layers of Elastosil M4601 mixed with a blue color additive for improved visual contrast, to become sealed actuator structures. Circular acrylic plates are laser cut for the top and bottom module structures, between which three V-SPAs are glued using Loctite 406 adhesive, formulated specifically for silicone rubbers. Before the actuators are separated from their preforms and acrylic plates are attached to form a 3-DoF rotational module, a strain sensor is first bonded to the outer surface of each as described in the subsequent fabrication steps.

2.11.2 Liquid metal sensor skin

The actuator skin sensor is first fabricated independently from the actuator on a PDMS membrane substrate using microfabrication processes to produce an exceptionally thin sensor structure. Similar types of sensors have been achieved by other fabrication techniques, including liquid metal injection, however the resulting metallization in these sensors are an order of

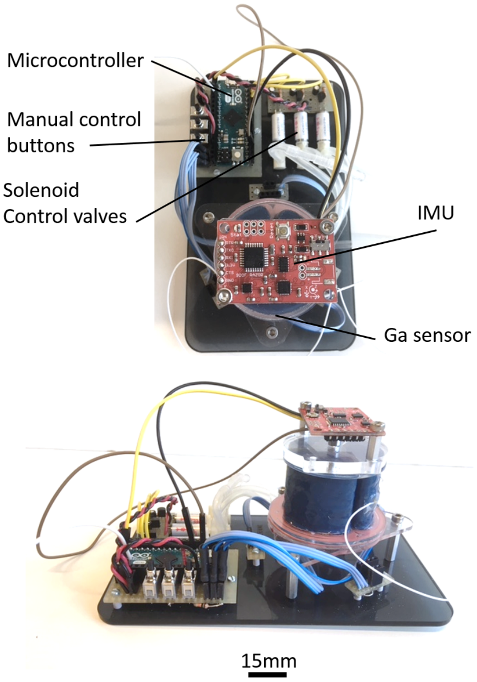

Figure 2.12 – Pneumatic control platform. A control board was constructed and utilized for performing characterization and control testing.

magnitude thicker in other cases than the process used here. The substrate is prepared with an array of micro-scale pillars fabricated by soft lithography, and precoated with a thin film of sputtered gold (Au) to enhance chemical affinity of Ga to the substrate layer. These features act to uniformly collect and distribute vapor deposited Ga with controlled thickness (1.5 μm) into continuous thin film liquid metal patterns. Once the electrically conductive patterns have been rendered, a top layer of PDMS is applied to enclose the liquid metal traces within a thin membrane sensor structure, 150 μm in thickness [182]. Although the resulting liquid metal features are highly stretchable with low electrical resistance, the electromechanical coupling (gauge factor) of Ga is low (roughly 1), such that meanders are needed to increase the cumulative resistance change produced by sensor strain which in turn increases the sensor's read-out signal strength. The winding pattern chosen for integration with the V-SPAs can be seen in Figure 2.11 The conductive traces are positioned to span across the direction of actuator folding and buckling induced by vacuum activation. This ensures the most traces of the sensor are subjected to compressive deformation at the inside of a fold, consequently resulting in high electrical sensitivity to actuator strain. As the connected traces are deformed in compression, the total resistance of the liquid metal pathway is reduced. This change in resistance is measured using a voltage divider connected to a 10-bit analog input pin of a microcontroller, with a 2.5 V reference.

2.11.3 Actuator-Sensor integration

The V-SPAs and liquid metal skin sensors are combined using a plasma bonding technique. The outer surface of the actuators and back side of the thin sensors are chemically activated by 30 seconds of exposure to oxygen plasma in a sealed vacuum chamber, and then the two active surfaces subsequently bonded upon contact with each other. The parameters used for plasma generation were 10 W with an O_2 pressure of 0.5 mbar. The free ends of the sensor traces are positioned at the middle of the winding pathway to coincide with the position of the rigid dividing membrane of the actuator, since this location undergoes the least deformation during activation, and is therefore ideal for the placement of wires attached to the sensor. Thin sensor output wires are attached to the liquid metal traces with silicone sealant for mechanical strain relief.

2.11.4 Multi-module robotic arm platform

Two sensorized, 3-DoF V-SPA modules were produced and stacked in series to form a soft robotic arm with embedded sensing capabilities. With three actuators, each module can produce rotational tilting motion through activation of different combinations of the individual actuators. The two complete modules are arranged inline, such that each actuator of a module is situated above one from the module below. The pneumatic vacuum source is then shared and controlled together along one axial side of the robot arm, for the sake of simplicity, although future implementations and studies could just as easily operate each actuator independently to allow more total degrees of freedom. The arm is built onto a pneumatic control board (shown in Figure 2.12) which contains a microcontroller and three solenoid valves each connected to one linear side of the soft robot arm. The valves can be controlled either in feedback control mode dictated by the embedded sensors and microcontroller programs, or through direct operation from three manual button switches also built into the board. While the manual switches only allow binary control of the V-SPAs in each module, a PWM signal from the microcontroller can be used to activate the valves at high frequency to simulate regulated pressure. The PWM control method is used to control the module angle, where varying the duty cycle produces variable angle output.

2.12 Experiments

2.12.1 Embedded sensor characterization

A single sensorized actuator module was characterized to correlate the embedded sensor measurements to the final output angle of a 3-DoF module. An inertial measurement unit (IMU) was attached to the top plate of a V-SPA module, and both the measurements from the IMU and the voltage output of one embedded strain sensor were connected to the microcrontoller. While logging both sensor readings, a series of ten binary step inputs were commanded to the actuator with the combined strain sensor at 85.1% vacuum. These ten steps were divided and

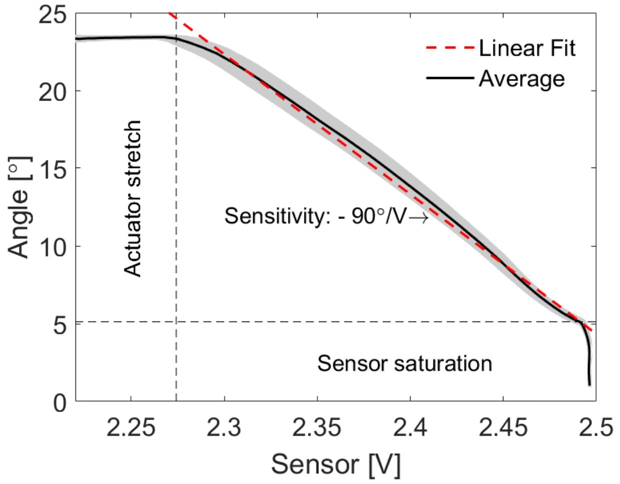

Figure 2.13 – Strain sensor characterization. The sensitivity of the Ga sensor integrated with the actuator of a V-SPA module is shown with a dominantly linear relationship between sensor output, and actuator module angle.

averaged together for both sensor readings, and the resulting measurements plotted against each other to obtain the plot shown in Figure 2.13. This figure shows the relationship between the voltage output of the embedded strain sensor and output angle of a V-SPA module is generally linear, which allows the calculation of a sensitivity factor from a first order fit, of approximately -90°/V, where

$$Module\ angle = -90 * sensor\ voltage. \tag{2.1}$$

The plot also shows two discontinuous effects near the ends of the actuator displacement caused mostly likely by actuator and sensor stretching near the maximum module displacement, and sensor saturation at low displacement (higher sensor voltage output). The total measured range of the soft Ga sensor is seen to be within roughly 0.5 V, which was measured with over 100 bit resolution using the analog signal microcontroller inputs.

2.12.2 Closed loop control

Using the sensitivity factor derived from the characterization experiment, we implemented a proportional closed-loop angular position controller for a sensorized V-SPA module. A series of step input targets were prescribed and the integrated soft sensor was used to provide feedback to track the set points, spaced at 10, 15, and 20 degrees. In order to achieve variable displacement, the pressure and flow to the tested actuator was required to be variable. Since the solenoid valves used are not proportional, a pulse width modulated (PWM) duty cycle was used to drive the valves, and achieve and approximately proportional pressure regulation. The frequency of the duty cycle was set to 30 Hz. Although the measured angular deflection of the module followed the set points closely, fluctuations were observed around these targets as a

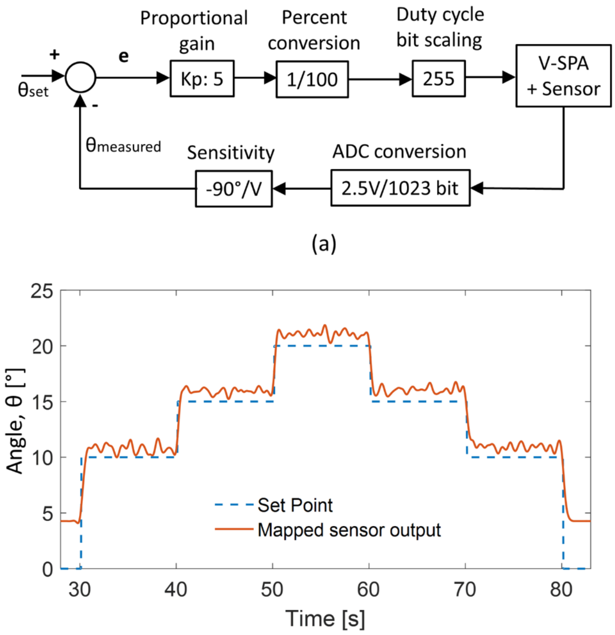

(a)

(b)

Figure 2.14 – Closed loop sensorized V-SPA angle step tracking. (a) Block diagram of the control scheme (b) The angular trajectory of V-SPA module is shown relative to a prescribed set point target. An offset in the sensor reading is observed before and after the initial and final steps, but this is below the threshold of sensitivity as shown from initial characterization study.

result of driving the valves in an intermittent manner. This effect was partially attenuated by the inclusion of a flow restricting membrane with a small hole between the vacuum supply from the valve and the actuator itself. This passive element introduced a small delay between valve activation and actuator motion, negligible for relatively lower frequency actuator motions but effective for the higher frequency supply line fluid oscillations. The block diagram for this control scheme and the resulting performance of the position tracker is shown in Figure 2.14.

2.13 Collaborative robot control

The multi-module robotic arm was tested to demonstrate an alternative utilization of the embedded actuator skin sensors, as human user input detection. In this tested scenario, no peripheral user controls are needed to direct the motion of the robotic arm. Rather, a more intuitive form of commands are issued by direct contact with the soft robotic structure, similar to the instruction which may be given between humans in supervised motion learning tasks. In the robotic case, similar hands-on motion teaching is feasible as illustrated by the simple demonstration shown in Figure 2.15. This capability leverages the embedded sensory skin combined with the V-SPA modules, which can then in turn also be used to carry out the directed motions under closed loop control, either in response to continued human user interaction, or to follow primitive programmed motions or behaviors.

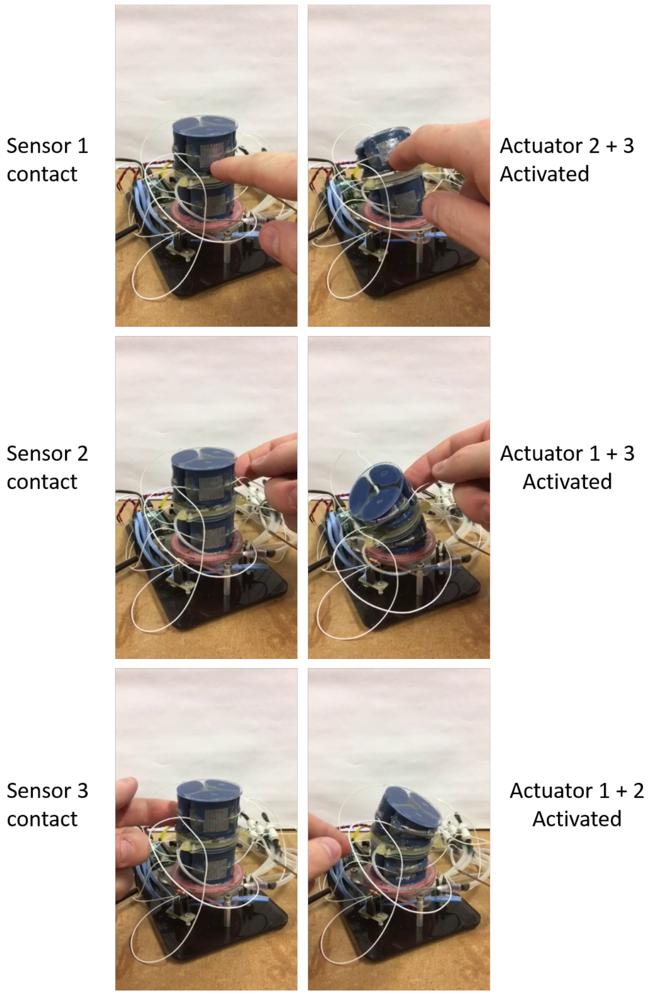

Figure 2.15 – Implicit user control. Embedded soft sensors enable intuitive, direct manual control of a two module soft robotic arm.

2.14 Discussion

In this work we demonstrated the first integration and validation of soft liquid metal Ga sensors with V-SPAs, for measuring and controlling large actuator strain. The mode of deformation unique to V-SPAs includes primarily buckling and folding, which is complimented by the compliance and ability of liquid metal-based sensors to deform without impeding the natural motion of the soft actuator. This compatibility gives rise to measurable resistance changes due to the compression of the actuator and embedded sensor structure. We validated the capability of localized deformations induced by V-SPA activation to be sufficient for generating useful sensor output signals for both control and user interaction, which are critical features of soft robotic systems that are particularly well suited operation in close proximity to humans in the framework of collaborative applications.

3 SPA performance and design benchmarks

3.1 Introduction

As the concept of modularity is leveraged through system architecture to extend the performance and feasibility of creating complex soft robotic systems, new benchmarks are presented in this chapter to further extend the range of their possible applications. While SPA based devices have been investigated in prior work for direct human body interaction at small scales, high-force applications have been inhibited by the limited force production capabilities of SPAs, as well as the lack of practical design methodologies. The task of specifying actuator parameters to meet desired performance output typically requires complex analytic or computational modeling, however it will be shown that after this process has been done once for a unit SPA, larger actuators can be assembled and scaled with proportional force output, enabling a more simplified approach to SPA system customization. In this chapter, we present a novel, modular approach to fabricating high-performance SPA Packs, consisting of smaller SPAs arranged in parallel, fascicle-like groups, which demonstrate redundancy and failsafe operation matched well to human body-scale wearable interaction. A demonstrative study of such device will be visited in the following chapter. In the second part of this chapter we will present a design methodology for fabricating V-SPAs, which operate using different materials and principles than most SPAs. A simplified, bending-type V-SPA is conceived and studied through empirical testing to reveal a generalized design metric for optimizing speed and force output.

The material presented in this chapter is adopted from the following self-authored publications:

[67] **M. A. Robertson**, H. Sadeghi, J.M. Florez, and J. Paik, "Soft pneumatic actuator fascicles for high-force and reliability," Soft Robotics, 4:1, pp. 23-32, 2017.
The first and second authors contributed equally to this work. The first author wrote the final manuscript, fabricated prototypes, and conducted experiments. The second author initiated this work, drafted the manuscript, and refined the design of the actuator concept with the assistance of the second and third authors, who all helped to edit the manuscript.
[108] **M. A. Robertson** and J. Paik, "Low-inertia vacuum-powered soft pneumatic actuator coil characterization and design methodology," *2018 IEEE International Conference on Soft Robotics (RoboSoft)*, Livorno, 2018, pp. 431-436. doi: 10.1109/ROBOSOFT.2018.8405364

3.2 Part 1: High-force SPA Packs

Soft pneumatic actuators (SPAs) are found in mobile robots, assistive wearable devices, and rehabilitative technologies. While soft actuators have been one of the most crucial elements of technology leading the development of the soft robotics field, they fall short of force output and bandwidth requirements for many tasks. Additionally, other general problems remain open including robustness, controllability, and repeatability. The SPA-pack architecture presented here aims to satisfy these standards of reliability crucial to the field of soft robotics, while also improving the basic performance capabilities of SPAs by borrowing advantages leveraged ubiquitously in biology; namely the structured parallel arrangement of lower power actuators to form the basis of a larger, more powerful actuator module. An SPA-pack module consisting of a number of smaller SPAs will be studied using an analytical model and physical prototype. Experimental measurements show an SPA-pack to generate over 112 N linear force, while the model indicates the benefit of parallel actuator grouping over a geometrically equivalent single SPA scales as an increasing function of the number of individual actuators in the group. For a module of four actuators, a 23% increase in force production over a volumetrically equivalent single SPA is predicted and validated, while further gains appear possible up to 50%. These findings affirm the advantage of utilizing a fascicle structure for high-performance soft robotic applications over existing monolithic SPA designs. An example high-performance soft robotic platform will be presented to demonstrate the capability of SPA-pack modules in a complete and functional system.

3.2.1 Background

Soft Pneumatic Actuators (SPAs), which are intrinsically compliant and readily manufacturable, are paving the way for a future of new robotic systems that benefit from inherent safety, adaptability, and customizability [183, 184, 159, 185]. While the force output of a robotic actuator is an important performance metric for many applications, it does not always accurately reflect the requirements of a full robotic system in others. Among other common performance standards, robustness and controllability stand out as key features that should not be underestimated in the development of a reliable robotic device. A common method for improving the robustness of some engineered systems is the introduction of a fail-safe, or a secondary mechanism that can be activated in the case of unexpected primary mechanism failure [186]. In some systems this fail-safe operation may be an emergency shut-off or similar irreversible action, while in others it may be accomplished by the addition of redundancy or parallel multiplicity. In the biological world this is demonstrated in many different domains. Certain insects are capable of maintaining mobility despite the loss of nearly any number of their legs [187], and larger order animals' muscular tissue, essential for maintaining nearly all activities of daily living, is arranged with parallel cellular structures that serve the dual purpose of redundancy as well as the summation of parallel action to increase strength [188]. This latter example is as applicable to engineered systems, such as robots, as it is to biology.

The concept of grouping smaller actuators to form larger ones is not uncommon in nature, as muscular tissue makes use of this to a great effect. The strategy is likewise not uncommon in the world of robotics, and even within the realm of soft actuation. Attempts have been made to utilize conventional Pneumatic Artificial Muscles (PAMs) such as the well-known McKibben type of SPA in a bunched parallel configuration, but they have not been without difficulty imposed by interference between the individual actuators [189]. PAMs feature an inflatable elastomer core surrounded by a braided fiber outer sheath [189, 190] which expands radially when activated. This expansion is orthogonally coupled to the actuation stroke, and consequently does not allow the necessary freedom of movement between individual fascicles of these actuators in a close group when inflated. Parallel grouping of Mckibben actuators was explored in [191] for the primary purpose of achieving multi-DoF activation of continuum robot segments rather than force enhancement alone, but avoided the issue of internal actuator interference by providing adequate spacing between artificial muscle units. In the biological analog, muscles evade the issue in part because they are inherently a form of “wet-ware”, being self-contained in a self-lubricating, fluidic environment that allows muscle fibers to move freely among each other while still combining their output effort. A related concept demonstrated the use of a specific “functional arrangement” of multiple PAM units embedded in a compliant matrix to enforce actuator separation and constraint [192]. In this latter case, multidimensional actuator grouping was used to achieve a soft actuated material with programmable multi-DOF motion.

Soft actuator literature is predominantly concentrated on single actuators instead of arrays of multiple units. Soft actuation technology such as shape memory material (shape memory polymers [SMP], shape memory alloys [SMA]), Electro Active Polymers (EAPs) and Fluidic Elastomer Actuators (FEAs) have drawn attention for soft systems [193, 194, 195, 196], but SPAs are still the most common actuation choice for applications where intrinsic safety and adaptability is needed. A variety of soft actuated wearable hand exoskeleton and glove devices have been developed to leverage the adaptability, natural bending motion, and relative strength of SPAs for assistive and rehabilitation applications [197, 198, 111, 109, 199]. A large body of work also targets augmentation of lower extremity muscle and joint work to improve healthy normal functionality for walking or restore and assist deficiencies in gait dynamics [200, 201, 202, 203, 204]. Compared to previous exoskeletons engineered for these tasks, these soft-actuated devices are remarkably lower in weight, inertia, and mechanical impedance, and consequently very well suited to wearability in both structured therapeutic environments as well as in daily living.

Although the precise construction of SPAs can vary, they are commonly found in the form of a slender, thin-walled, hollow, cylindrical structure externally constrained by inextensible fibers, and driven by a readily available pressurized air supply. The actuators are activated by applying positive relative pressure to the hollow internal cavity, and can be designed to produce linear [197], bending [27, 34], and torsion forces [205], or even any combination thereof [38], by including restraining features [29], or by selecting an appropriate angle of constraining fibers relative to the direction of applied motion or force. As a result of their fundamentally simple construction, SPAs have already been employed in a broad range of applications including rescue robots [42], rehabilitation [200, 201], bio-inspired robotics [206], and wearable technologies [207, 208, 198, 109, 199]. This is due in part because they are highly customizable, easy to fabricate, lightweight and low cost [209].

While the straightforward design of individual SPAs is not amenable to generating the typically high forces required of traditional robotic applications or human body-scale wearable devices, SPAs are a notably attractive candidate for use in the development of an alternative type of high force soft actuator composed of a parallel grouped assembly of smaller SPAs. The simple and self-contained design of single SPA units facilitates *a novel method of integration to enable functional grouping of soft pneumatic actuators.* Short of mimicking biological architecture directly, the SPA-pack developed here draws inspiration from the idea of “constrained isolation” necessary for utilizing actuators in parallel – keeping each actuator effectively free to move independently while sufficiently and not overly bounded.

3.2.2 Objectives

In this work, a unit fiber-reinforced, linear-extending SPA will first be produced as the basis for a larger parallel pack configuration. A 4-unit pack (4Pack) will then be fabricated and characterized to demonstrate and motivate the principles of the design architecture. To show the effectiveness of the new SPA concept in application, a high-force, multi-degree-of-freedom platform actuated by SPA-packs will be introduced, and briefly studied. Finally, a discussion will include a summary of the primary benefits of the SPA-pack configuration and comparison to current alternatives, extensibility of the actuator modules to further applications, and some logistics of a more independent architecture for control and power distribution.

The main contributions of this section are:

- Novel SPA-pack structure suited for fiber-reinforced SPAs which demonstrates improved robustness and reliability over individual soft pneumatic actuators.
- Fiber-reinforced SPA design for high force applications above 100 N.
- Prototype and experimental validation of an active, multi-DoF platform powered by high-force SPA-packs under closed loop control

3.2.3 New SPA concept: SPA-Packs

By grouping SPAs in parallel, actuator packs can be formed which outperform individual SPAs of comparable size. Not only can higher force output be achieved with this configuration, but the benefit mutually increases with the number of constitutive actuator units utilized in the pack. This is to say that the more unit actuators are combined in parallel, the greater the gain in force output can be attained. This improvement in spatial-force efficiency allows for either stronger actuation in a given physical space, or more compact actuation for a given required force. These features hold considerable value as they extend the design space within the soft robotics domain.

Beyond the improvement of existing performance metrics over volumetrically equivalent single actuators, the SPA-packs also introduce new measures of performance not realizable without the grouped configuration. Robustness and reliability are improved as a result of the inherently modular pack structure. In the event of an SPA unit failure within the pack, the parallel actuator is still capable of functioning at an only slightly reduced capacity. In certain use cases, there may even be no decrease in functionality at all, as a unit actuator loss may be compensated by shifting work (increasing pressure) to the remaining units in the pack. This extends the utility of soft actuators in robotics even further to applications where safety not only benefits from the use of compliant materials, but from the improved controllability of devices powered by soft actuator packs.

The simple nature of this concept also reflects no dependency on pack structure beyond the parallel arrangement of the grouped actuators, enabling multiple possible form factors to be considered for a given required force output. This design freedom allows for highly customizable actuator units. The variability in structure can be used to accommodate applications with different size or geometric requirements. Furthermore, the concept of design modularity can be extended not only to the actuators themselves, but equally to the applications where high-performance packs are particularly well-suited, such as the realm of wearable robotics. Taking advantage of this modularity, parallel groups of SPA-packs may be configured to produce further cumulative output, as well as the potential for utilizing individual packs to generate directional, multi-DoF actuation at the system level. Figure 3.1 illustrates the evolution of the SPA as a modular base unit, giving rise to high-performance soft robotic systems.

3.2.4 SPA-Pack fabrication

A single unit SPA is first fabricated for use as the basis of the SPA-pack. The individual actuator is designed to produce linear extension force and displacement, with a high-angle fiber wrapped around a single chamber hollow elastic body. The inextensible fiber acts to restrict the radial inflation and expansion of the actuator, while allowing it to extend in length as pressure is applied to the internal cavity. PAM actuators make use of a relatively low fiber angle (less than 54.7°) [190], to produce high tensile force. However, it has also been demonstrated that at higher angle fiber arrangements, extension and torsion forces can be achieved [193]. To allow operation at high pressure, a smooth geometry is used along the surface of the inner chamber with no sharp internal corners to minimize the stress concentration as the actuator swells. The fiber angle set at roughly 75° relative to the longitudinal axis of the actuator is chosen deliberately to be above the zero force threshold (54.7°) derived from a simplified analytical actuator force model, shown in (3.1), introduced in [190], to produce a linear extension motion and low enough to allow easily repeatable and consistent wraps of

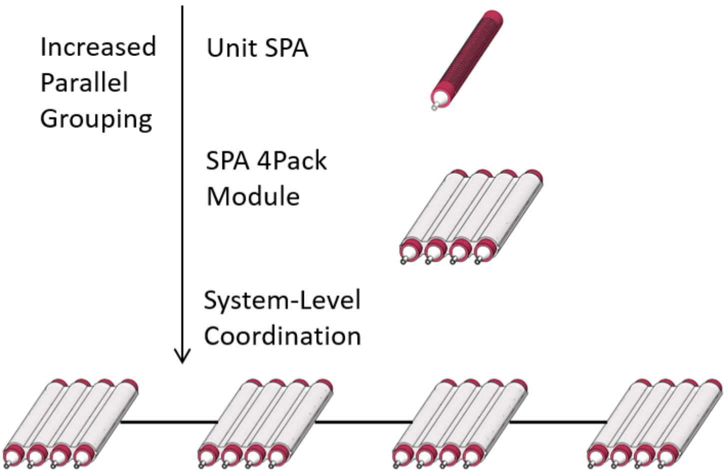

Figure 3.1 – Extension of SPA modularity. Parallel grouping of SPA packs enables system-level high performance that can be utilized for wearable applications or high-force multi- DoF soft actuation.

the fiber, which is wound onto the actuator manually. The hollow elastic body of the actuator constructed here is manufactured following a series of conventional and lost wax casting methods. A solid wax core is constrained by a 4 mm diameter metal rod at the center of a rigid, hollow, ABS plastic mold fabricated rapidly by 3D FDM printing, into which uncured silicone rubber (Elastosil®M4601) is poured between the core and mold. The chosen material is appropriately designated to allow flexibility (up to 700% elongation at break) as well as strength (6.5 N/mm^2) for use with high pressure [210]. On the outer surface of the overall cylindrical structure of the actuator body, a row of raised bumps are also formed from the body mold which are used to accurately align and guide consistent wraps of a Nylon fiber wound four times along the length in alternating directions. After the silicone rubber is allowed to cure at room temperature for 12 hours, the actuator is removed from the mold and wrapped with the outer fiber before removing the rigid wax core. Once the outer fiber has been wrapped and secured with a silicone based adhesive (SilPoxy®), the internal wax core is heated in an oven above its melting point and poured out with the supporting rod removed. Additional SilPoxy® is used to attach silicone pneumatic supply tubes at one end of the actuator, and to seal the opposite end. The resulting structure is a completed single unit linear SPA. The dimensions of the final SPA unit are 145 mm in length, and 17 mm diameter.

Each unit SPA in a pack is held together by a soft connecting interstitial membrane, and behaves the same as an individual SPA despite being bonded together. The highly elastic membrane easily stretches in response to the output force of each actuator and relative motion between actuators from uneven pressure distribution or inconsistencies from fabrication is accommodated. While providing the necessary and subtle bond to hold the SPA-pack together as one module, the interstitial membrane also provides another important function, enforcing

Parameter	Value
P'	200 kPa
P_{atm}	101,325 kPa
L	145 mm
D	17 mm
t_k	3 mm
θ	75.2 °
N	16 wraps

Table 3.1 – The parameters given below are used for the fabricated actuators and the analytical model to estimate their force output.

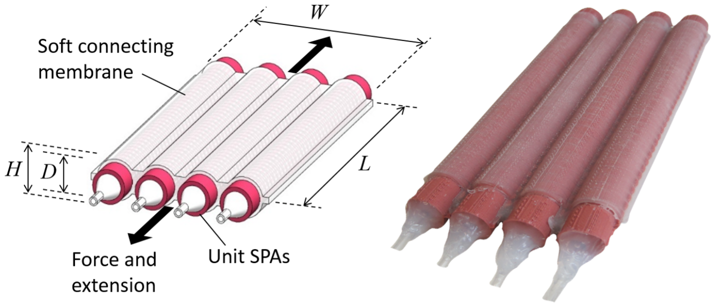

Figure 3.2 – Diagram and photograph of 4Pack actuator. The dimensional parameters given in Table 3.1 are illustrated with the basic components and operating mode of a four unit SPA pack.

adequate spacing between unit SPAs to eliminate sliding friction and interference effects. This flexible constraint enables each actuator unit in the pack to function individually uninhibited while still acting together as a functional group.

The fabrication of an SPA-pack shown in Figure 3.2 follows a basic casting procedure to integrate four partially completed unit SPAs. Before the wax cores are melted out, individual actuators are inlayed between a 3D printed ABS two-piece mold which allows for empty space surrounding the central segment of the actuators. Uncured low-elastic modulus silicone rubber (Ecoflex®00-30), is then poured into the mold to fill the space and subsequently bond the unit SPAs together within a shared flexible membrane housing. After curing at room temperature for four hours, the SPA-pack is removed from the mold. The pack is placed in an oven to allow the wax cores to melt for removal. SilPoxy® is then used to attach a silicone tube to each SPA unit in the pack, and seal the opposite end, as in the case of the individual actuators.

The simplicity of this actuator design enables the application of a likewise simple analytical model to predict output force performance. While this model is developed in literature for another type of tensile soft actuator, it is equally applicable to the extension type studied here.

3.2.5 Actuator analytical model

A simple analytical model can be used to estimate the force output of a single unit SPA, shown in (3.1) [190]. For this kinematic model, the actuator is represented as a perfect hollow cylinder with wall-thickness, t_k, and the assumptions that the system is lossless and without energy storage. Furthermore, this model is not effective for describing quasi-static or dynamic characteristics of fiber reinforced pneumatic actuators. Although non-comprehensive, this model nonetheless provides a sufficient result for use in comparison between different SPAs. While the result will not be used to describe the best theoretical fit to the experimental performance of an SPA with given parameters, it is still expected to provide a reasonably close approximation of blocked force capacity where actuator elongation is restricted. The simplified static model of force output F for a fiber-reinforced SPA is given as

$$F = -\frac{P'b^2(3cos^2\theta - 1)}{4\pi N^2} + \pi P'[\frac{b}{N\pi}t_k(2sin\theta - \frac{1}{sin\theta}) - {t_k}^2] \tag{3.1}$$

where,

$$b = \sqrt{L^2 + (D\pi N)^2} \tag{3.2}$$

and L is the actuator length, D is the cylindrical diameter, θ is the angle of a single wrapped reinforcing fiber relative to the axial direction, N is the number of wraps of the fiber around the actuator body, and b is the length of the fiber shown shown in 3.1 as a function of actuator dimensions and the number of fiber wraps. The pressure $P' = P - P_{atm}$ is the pressure applied to the internal chamber relative to atmospheric pressure, P_{atm}, with P as the absolute internal pressure. For the parameters given in Table 3.1 and depicted in Figure 3.2, the corresponding theoretical output force of a single unit SPA is expected to be 30.5 N. In addition to predicting the output for unit SPAs, this basic model can also be used to extrapolate and anticipate the effect of parallel actuator grouping, as well as for comparison of such actuator packs to equivalent monolithic SPA designs.

3.2.6 SPA-Packs vs. single SPAs

Estimating the output of an SPA-pack in a parallel fascicle arrangement following the simple unit SPA model is trivial under the assumption that the soft interstitial membrane connecting the units does not store energy or add significant impedance to the pack system. The output is therefore the total theoretical output of individual SPA units modeled by (3.1) multiplied by the number of units in the pack. In the example SPA- pack fabricated here, the number of units is four, so the total force output is expected to be $4F$. Again using the parameters given

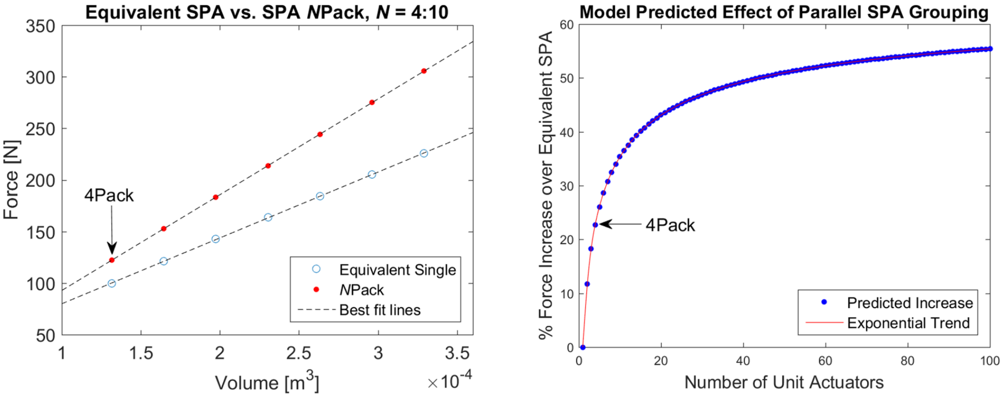

(a)

(b)

Figure 3.3 – Comparison of SPA pack to Equivalent SPA. (a) For comparable volume and the same construction parameters, an SPA pack produces a larger force output than an equivalent single SPA. As the number of individual units in an SPA pack increases, the difference calculated as a percentage also increases following the trend shown in (b).

in Table 3.1 this simple model yields an estimate of 122 N per SPA-pack.

Using the force model for a single SPA it is also possible to estimate the performance of actuators volumetrically equivalent to an SPA nPack, where n is the number of unit actuators contained in the pack. For a cross sectional area, A, of an individual unit actuator, the "equivalent SPA" is defined to have equal volume to a pack of n unit actuators, by defining its cross sectional area as $Aeq = nA$. For a pack of $n = 4$ actuators, the area of an equivalent SPA is then held to be $Aeq = 4A$. This simple relationship for the equivalent area defines the necessary diameter for an equivalent single SPA. All other actuator parameters, as shown in Table 3.1, are held equal.

Within the range plotted in Figure 3.3 (a), the model follows a primarily linear trend with a consistently greater force output by the SPA-pack in comparison to an equivalent SPA. The divergent slopes between the SPA-pack and equivalent SPA force output suggests an increase in the gain of grouped actuator output over the corresponding equivalent SPA as the number of actuator units in the pack increases. Looking further, it is apparent from Figure 3.3 (b) that the trend is in fact bounded, but up to and above the range of unit actuators shown indicates a diminishing return that may be inefficient as well as impractical in real use. The optimal number of units for a specified volume to maximize spatial-force efficiency of an SPA- pack in this model framework will not be investigated here, but it may be observed that that using 20 or fewer unit SPAs in an actuator pack, which is subjectively manageable under the paradigm of current popular SPA manufacturing methods, can still yield a theoretical gain up to 40%.

From this analytical model investigation it is found that the gain in the predicted performance of actuators in a grouped parallel configuration offers an additional advantage to the improved robustness and modularity afforded by the architecture, which can be seen as a significant

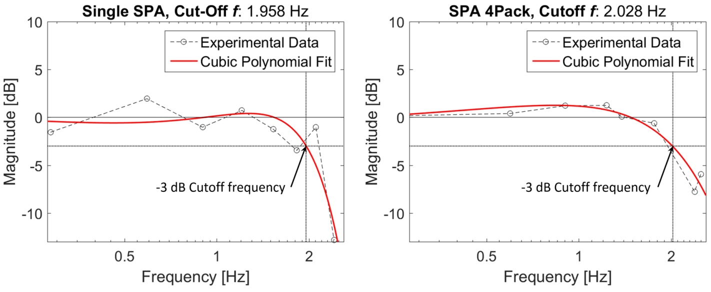

(a) (b)

Figure 3.4 – Frequency response of individual SPA and 4Pack. The corresponding force output of an individual SPA, and a pack of four unit actuators to a sinusoidal pressure input is tested at multiple frequencies to obtain the bode diagrams above. These diagrams indicate a cutoff frequency of nearly 2Hz for both the individual actuator (a) and the 4Pack (b), and no loss of bandwidth performance from parallel actuator grouping. The figures do qualitatively indicate an increase in the damping ratio of an actuator pack compared to a single SPA, by the apparent "flattening" of the frequency response; however, this was not calculated.

benefit of SPA-packs over single SPAs of equivalent volume. The result of the spatial efficiency dictated by this force-volume relationship can be leveraged to design higher force actuators within a given space, or smaller actuators for a prescribed force. Regardless of the utilization however, the unique, parallel fascicle arrangement of SPAs presented here enables a new alternative to high force soft actuation.

3.2.7 SPA-Pack characterization and application

The SPA-pack described here previously is evaluated experimentally for characterization as well as comparison with the simplified force output models presented above. Given a maximum force output of 122 N estimated by the model, the linear SPA-pack is tested using a single axis load cell which can measure forces up to 200 N (BCM 166H). Additionally the test setup consists of two rigid outer supports, a pressure regulator, a data acquisition system, and a pneumatic solenoid control valve. The experimental test results yield a maximum output force of 112 N per module, roughly 8.2% lower than the expected value.

To determine the bandwidth of the SPA actuators, a sinusoidal input pressure with amplitude of 1 bar is applied to the unit and module at varying frequencies. In Figure 3.4 the frequency response to the sinusoidal input reveals the -3dB bandwidth of both the individual SPA and the pack module to be around 2 Hz. The consistency in the measured bandwidth between the single and parallel grouped actuators indicates that the flexible constraint used to assemble the SPA-pack does not interfere with the performance contributed by each of the individual internal actuators.

To demonstrate the integration of the high force actuator packs developed here in a complete robotic system, an active, multi-DoF platform was constructed and tested. The platform and test fixture was fabricated using rigid aluminum plates and an extruded aluminum frame. The fixed base section of the platform is comprised of a 3D-printed ABS plastic shell, around which a modular, reconfigurable circular array of SPA-packs are constrained laterally by 3D-printed locating features, and held in place radially by a flexible fabric belt to restrict the motion of the actuators to their respective linear output axis. The actuator configuration is depicted in the top view shown in Figure 3.5 (b). The upper moving section of the test setup consists of a plate suspended from above and below by springs mounted to the frame which enables preloaded degrees of freedom in all directions.

The performance of the SPA prototype was evaluated using the test setup shown in Figure 3.5 (a) designed to simulate basic concentric geometric and multi-axial loading conditions. The SPA-packs in the prototype are connected to a benchtop electro-pneumatic system and controlled directly from a virtual instrument (VI) in Labview, through a National Instruments cRIO-9082 integrated real time controller with a 1.33 GHz dual core processor and a LX150 FPGA. An ITV1031-21F1N-Q pressure regulator (SMC) enables digital control of the pressure supplied to each SPA up to 5 bar, and one solenoid valve per pack module is used to enable or disable the SPA-packs independently.

The test setup was reconfigured for three different system measurements. To measure the maximum vertical force that can be applied by the platform, a 600 N-range, single axis load cell mounted to the frame was positioned at the center of the moving upper plate. A ball joint was utilized at the interface of the load cell with the plate to eliminate moment transmission and effectively measure a pure point force. The configuration is illustrated in Figure 3.5 (c). All four SPA-packs in the surrounding the platform were activated simultaneously at maximum operating pressure (2 bars) to steady state at the full extension. The resulting blocked force on the load cell was recorded to be greater than 432 N. In addition, the preloaded upper plate of the actuator platform was measured alone to apply 36 N of force at the position of actuator module maximum extension, such that the cumulative force capacity of the actuator modules independent of the platform is the sum of these forces, for a total force of 468 N. This value is 4.1% lower than the expected force capacity of 488 N predicted by the model and based on the simple additive effect of actuators packs working in parallel.

A similar configuration was used to measure the maximum moment applied by the SPA platform, as shown in Figure 3.5 (d). The load cell used to measure blocked force was relocated to a position between the axis of rotation at the center of the plate and the location of the vertical actuator force, to a radial distance of 60 mm from the center of the plate. Two actuator packs applied force at 94 mm from the center of the plate to produce the maximum moment from the given configuration and number of packs in the system. Again the load cell was mounted to the frame rigidly and force from the plate was applied through a ball joint to record only force at a point. To simplify measurement and isolate the rotational behavior from linear actuation, the center of the moving upper plate was constrained relative to the frame using a ball joint. The principle axis of the moment applied by the SPA-packs was then assumed to be orthogonal to the radius of action where the linear force was applied. The

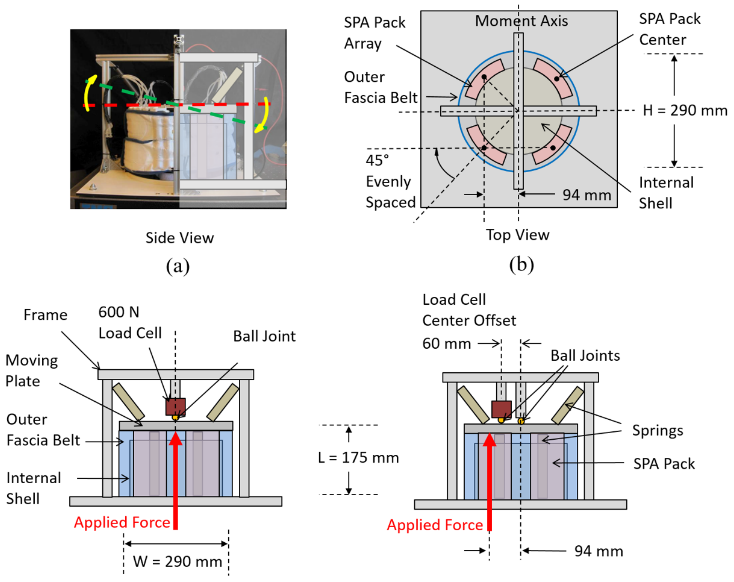

(a) (b)

(c) (d)

Figure 3.5 – High-force soft actuated platform. Photograph (a) depicts the actual multi-DoF platform surrounded by a rigid aluminum frame, along with a depiction of the angular DoF used in moment measurement. Diagram (b) illustrates the configuration of the platform from a top view, showing the concentric array of SPA packs. The blocked force measurement configuration (c) is used to measure total vertical force capacity of the actuated platform. The blocked moment measurement configuration shown in (d) is used to measure the maximum moment applicable on the pitch axis by two synchronized modules, as well as to measure the moment frequency response of the system. The curved arrows indicate the direction of angular displacement upon activation from rest at horizontal.

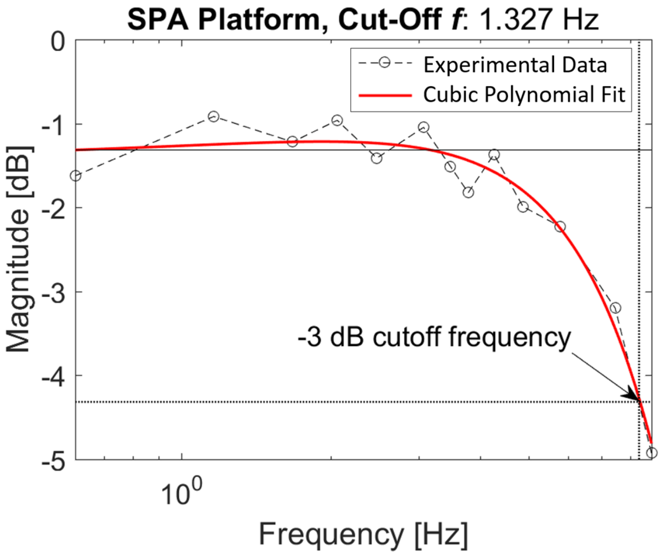

Figure 3.6 – Frequency response of the high-force SPA platform. The plot shows the magnitude of moment response to a sinusoidal pressure input for a spectrumof frequencies from which the system cutoff frequency at -3 dB is found to be 1.33 Hz.

	Single	4Pack	Multi-DoF Platform
Dimensions (W × H × L) or (D × L), mm	17 × 175	84 × 19 × 175	290 × 290 × 175
Weight, g	28	185	945
Maximum load force capacity, N	26	112	468
Bandwidth, Hz	1.958	2.028	1.327
Maximum moment capacity, N-m	-	-	18
Angular range of motion, °	-	-	± 5

Table 3.2 – Summary of modular SPA characteristics.

maximum moment applied was thus calculated from the blocked force measurement from the load cell and the known location of the applied constraint force, yielding a blocked moment of nearly 18 N-m along the radial pitch axis of the platform.

The measure of system bandwidth was conducted using the blocked moment measurement configuration. A sinusoidal pressure input was used to actuate the platform while the resulting moment output was recorded by the load cell. The amplitude of the resulting sinusoidal moment output of the plate was compared to the amplitude of the input sinusoid for various frequencies to create a frequency response diagram shown in Figure 3.6, from which the bandwidth of the SPA pack array and test platform system was calculated to be 1.33 Hz.

The characteristics of the SPA-based, high-force, multi-DoF actuated platform developed and measured here are summarized in Table 3.2 below. Additionally, characteristics of the constitutive actuators are also included in the table for comparison and summary.

While the highest force measured for an SPA module under individual testing only reached 112 N, the inconsistency between that and the average force per module calculated from the platform testing of 117 N can be attributed to the difference in actuator constraints used during each measurement. This also likely contributed to the slight difference between bandwidth measurements for the single and 4Pack modules, which were calculated from their respective force outputs. In single module testing, deflection caused by buckling of the flat actuator plane was restricted using rigid, immovable parallel plates on both sides of the module to enable a purely linear reaction against a single axis load cell. A similar effort was made in the multi-DoF platform to apply the necessary constraint to the modules while also allowing linear extension of the actuator with minimal impedance, but in this case a flexible outer fascia belt was used instead of a fixed rigid constraint on the outer side of the modules. The outer belt provided radial constraint, but was not fixed to the grounded structure, and free to move linearly in the directions of force application with the actuators. This additional freedom reduced the impedance to the actuators yielding an average force per module when tested as part of the multi-DoF platform of roughly 4% above the individually measured 4Pack, and nearly 4% below the output predicted by the analytical model used in Section 3. Similarly, higher force measurements were attained for the SPA-pack module in comparison to a single actuator during blocked force testing as a result of buckling in two dimensions which was even more difficult to constrain.

3.2.8 Reliability testing

The multi-DoF robotic system was also tested with a proprtional-integral-derivative (PID) controller following a sinusoidal trajectory of the platform angle, measured using an Inertial Measurement Unit (IMU) mounted on the upper plate. The controller follows the desired trajectory, as seen in Figure 3.7, but suffers from hardware limitations imposed by the unidirectional actuators, and a consequently discretized control strategy. With antagonistic pairing of actuator pack modules, only one of each opposing actuator in the circular SPA pack array is operated at a time, dictated by the direction of motion required. Switching between these modes, namely between positive and negative angular motion, adds an inherent delay determined by the control system hardware that includes an IMU, solenoid valves, data acquisition (DAQ), and a laptop computer communicating over multiple USB peripherals, in addition to the dynamics of the actuator units themselves. This results in sharp overshoot upon mode switching, visible in the Figure 3.7 as short twitches in the measured angle. Regardless, closed loop control of the actuated platform is achieved and the raw response shown in the figure below.

As a demonstration of fascicle structure robustness to individual actuator unit malfunction or degradation, the SPA platform is tested with simulated failures by cutting off the air supply to different numbers of units in a given module. The mock failure is induced reversibly by tightly pinching the silicone pneumatic supply tube to individual units in the pack, using a plastic locking zip-tie. Reversal of the action is accomplished by cutting the plastic tie

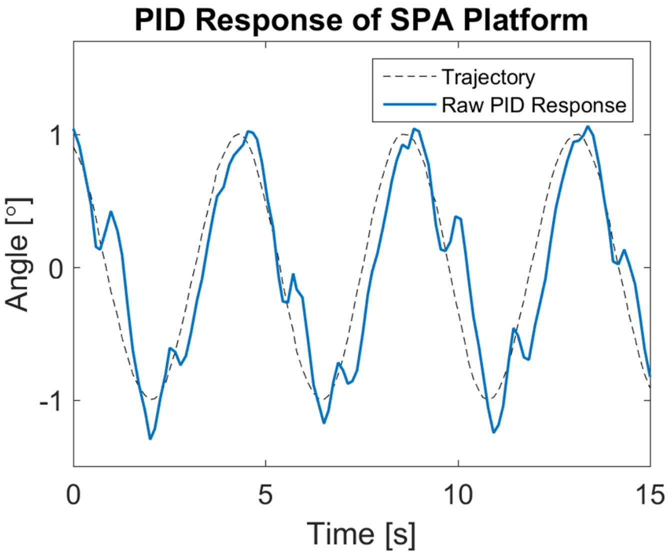

Figure 3.7 – Closed loop control of quadruple SPA-pack platform. The actuated platform follows a sinusoidal trajectory under proportional-integral-derivative (PID) control, with transient disturbances evident from discretized control logic imposed by antagonistic pairing of unidirectional actuator modules.

without damaging the flexible supply tube to restore the particular unit to full functionality to allow iterative testing. Figure 3.8 shows that as individual actuators in a pack are cut-off from the controlled air supply, the platform is able to maintain reduced capacity tracking on the affected side, and nearly unchanged tracking on the unaffected side. Overall, the platform also maintains general controllability despite the loss of any number of units in the pack (with the clear exception of losing every unit in the pack, not shown). Sinusoidal fits were made to the controlled response data to more clearly represent the subsequent change in the platform behavior to actuator reduction.

Given the repeated structure of independent constitutive elements composing SPA-packs, the actuator modules of parallel grouped SPAs exhibit a capacity for reliability and robustness against failure modes common to any engineered system. As safety is regarded a leading promise of soft robotics, these qualities elect the SPA-pack architecture studied here to be among the most essential elements of technology for use in future applications.

3.2.9 Discussion

SPA-packs can be used to create soft robotic systems with high performance capabilities. In much the same way that conventional SPAs are integrated into active, multi-DoF applications, these actuator modules utilize standard electro-pneumatic control systems to deliver high force, and reliability for a newly accessible range of tasks. The soft actuated multi-DoF platform generated 18 N-m of moment, and demonstrated cumulative vertical force production of

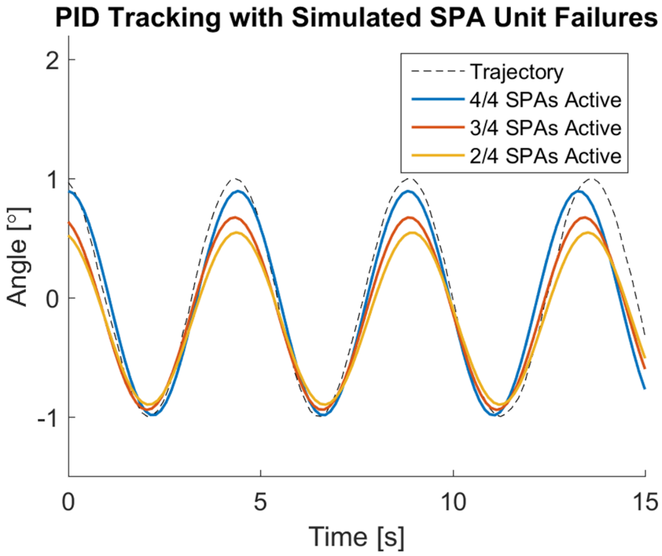

Figure 3.8 – Demonstration of quadruple SPA-pack robustness. The closed loop response of the SPA-pack actuated robotic platform following a sinusoidal trajectory shows reliable stability and controllability with different numbers of active units, despite an asymmetric drop in performance.

468 N, corresponding to an average output of 117 N per actuator pack. An open loop system bandwidth over 1.3 Hz was recorded for the multi-DoF platform, while the bandwidth of a separately tested SPA 4Pack and individual unit SPA was found to be 2 Hz. While the frequency response independently measured for the actuators showed no significant effect from the soft interstitial coupling used to fabricate the pack, the additional dynamics from integration in the multi-DoF platform contributed to the reduction in overall system bandwidth. Due to the repeated, parallel structure of smaller SPA units, the SPA-packs also demonstrated a unique robustness to potential failures, by permitting the loss of one or several units without an overall loss in functionality of the actuator group or system at large under closed loop control.

It is shown that a *fascicle arrangement of SPAs is capable of generating more linear force than an equivalent single SPA of comparable volume*. Moreover, the gain in force production continues to increase within practical bounds as the number of units in a parallel configured SPA-pack is increased. This model-based finding indicates that high-performance SPA design favors multiplicity and can be exploited as a new actuator design strategy which takes into consideration the effect of multiple unit actuators in parallel coordination as well as the individual unit actuator design parameters to achieve desired performance. Although extensive effort was not made to ensure the absolute accuracy of the kinematic analytical model used for this analysis as introduced, validation was achieved by comparison of actual actuator pack force measurement to the model-predicted value. The measured result of an SPA 4Pack performance was found to be 4% lower than expected. Better results in future work might be obtained either by use of a dynamic model [211], or through finite element analysis tools for soft pneumatic actuators [212].

As it is shown and discussed in [212], varying the fiber angle of fiber reinforced SPAs can yield either extension or contractile behavior. As seen in [191] the nonlinear relationship between fiber angle and force output is different above and below this functional fiber angle threshold of 54.7°, dictated by the model shown in [190]. Prior to this study, it has not been shown that higher fiber angle, extension type SPAs can be used to perform in the range of force output over-100 N. Between the two generalized regimes of SPA fiber arrangement, from 0° to 54.7°, and from 54.7° to 90°, only those in the lower angle category, have demonstrated performance up to this force magnitude. As this work has successfully shown, high-fiber angle SPAs offer an intrinsically safe, soft actuation alternative for high-performance applications when used in modular, parallel groups. Furthermore, the architecture affords reliability and customizability not readily available from other soft actuation technologies.

As SPAs advance toward use in increasingly complex multi-DoF soft robotic systems, the complexity of the soft pneumatic sub-systems required to operate them is also expected to follow. While the problems inherent in the logistics and control design of conventional complex pneumatic systems have been addressed to the point that there exist commercially available solutions, these have not been well defined in the world of soft robotics, where weight, size, and power are an objective concern. Off-the-shelf pressure regulators, valve manifolds, integrated sensors, and electronic controllers are built for industrial scales, and consequently not readily appropriate for many applications where SPAs best serve. In this regard, it is therefore worth noting that at this point, the future development of soft robotics may not be entirely restricted to the development of better actuators alone, but in the integration of actuator modules purpose built for robotic applications. Although the SPA-pack design presented here incorporates only morphological changes to accomplish readily beneficial progress toward robot-centered soft pneumatic systems, future work may also include the evolution of SPA modules with embedded sensing, control, or even low level processing capabilities to further enforce the concept of their modular utility.

3.2.10 Conclusion

We proposed a design method to address one of the major challenges of current soft robotics: shortcomings of soft actuators. By strategic actuator grouping, we have demonstrated with a prototype that we can augment mechanical performance and reliability in soft actuators. Diverting from single SPAs and adopting the use of SPA-pack modules affords several useful benefits. The first, maybe most obligatory, benefit is that of increased force production. Biological muscles are named and denoted singularly following a simple notion that an arrangement of multiple single actuators in a group outperforms multiple scaled single actuators: they in fact are comprised of infinitesimal smaller actuators at the cellular level. In this view it is then no less acceptable to produce a higher performance SPA module by parallel configuration of smaller SPAs. Efforts have been initiated to demonstrate this effect with PAM actuators but with limited success owed to interference between closely grouped actuators caused by the coupled relationship of actuator bulging upon inflation to force production. Here we demonstrated that the concept extends more elegantly to SPA type actuators. These actuators by comparison do not expand significantly upon inflation and work well in a closely bundled configuration when packaged appropriately within a soft, pliable interstitial constraint to produce a high cumulative force output. In this fascicular arrangement, SPA-packs also show improved robustness to failures induced by material rupture, blockage, or fatigue effects, as permitted by the advantage of multiplicity. With multiple independent active units comprising a single grouped SPA-pack, the module as a whole is able to continue in operation with the consequence of unit failure limited to an inherent decrease in performance overall, and not a total loss of control. These features are critical for realizing safe and reliable high-performance soft robotic systems.

3.3 Part 2: Low-inertia Coil V-SPAs

Recently developed soft pneumatic actuators (SPAs) powered by negative pressure have demonstrated great potential in the future of soft robotics for their high strength, intrinsic safety, low weight, and often simple design. The majority of these limited examples have only provided linear force and motion profiles, however, despite the general prevalence of bending actuators common to positive pressure powered SPAs. The benefits of such bending type SPAs follow from the direct production of moment and angular motion that are highly desirable for diverse robotic applications and activities, which allows more simple design of soft robots with complex motion behavior. Following this motivation, a new vacuum powered bending actuator is developed here as an extension of a previously presented vacuum powered actuator, the V-SPA, which features simple, lightweight material construction and rapid fabrication. Leveraging these attributes, an empirical study of a new Coil V-SPA performance is conducted across a spectrum of eight actuator prototypes. The force, speed, and stiffness of the actuators are characterized, and a generalized design metric, the Geometric Compression Ratio (GCR), is defined to quantify the relationship between physical geometric parameters of Coil V-SPAs. Finally, the results of testing reveal the new low-inertia actuator is capable of high-speed, and high-bandwidth motion, up to 0.97 m/s and 1.59 Hz, respectively.

3.4 Background

Bending type soft pneumatic actuators (SPAs) have been a cornerstone of soft robotics since its first and relatively recent inception. These actuators generate mechanical moment from pneumatic pressure input and can be used as a form of artificial muscle to do work in soft robotic systems. The ability to generate torsional moment from single actuators allows more direct use in soft robot applications, such as in actuation of moving joints or grippers, without the need for constraint mechanisms, linkages, or transmission elements (e.g. tendons). Typically, bending SPAs are fabricated from silicone rubber elastomers cast into hollow structures which convert nominal inflation to directed bending motion from asymmetric stiffness properties along their length. To achieve this behavior, various designs have been previously developed and studied utilizing external fiber or shell reinforcement [38, 213, 27, 214], multi-chamber networks with strain limiting layers [34, 215, 36, 205], and asymmetric air chamber wall thickness [216]. The wide variety of bending SPAs have also been employed in a broad range of applications, including wearable devices [109, 111, 28], continuum robot manipulators [114], mobile robots [74, 217], compliant grippers [73, 75].

While most bending SPAs are powered by pressurized air, a new class of soft actuators deriving power from vacuum has begun to emerge as a viable alternative for safe robotic systems. Being driven by the differential between low internal and higher external pressure, these actuators are inherently force limited by the environment in which they operate. This failsafe quality ensures that they can never exceed their rated design output limits through their control input; absolute pressure supplied to the internal actuator cavity can never be reduced further than zero. Through deformation primarily induced by buckling rather than elastic strain, these actuators also do not store significant energy during activation, and subsequently are not capable of sudden or explosive failure. These characteristics make this type of actuator valuable choice for applications. Due to this advantage, a limited field of work has explored the concept of vacuum actuation through the development of linear buckling actuators [218, 77], rotary actuators [219], origami inspired artificial muscles [220], and complete soft robotic systems [67]. The latter of these examples utilized vacuum actuators known as V-SPAs, manufactured with open-cell polyurethane foam coated with a thin layer of silicone rubber, to achieve lightweight, torque-dense, multi-DoF modules.

Although V-SPAs were integrated with rigid control hardware in previous work to facilitate their modular functionality, the added components did not provide structural support in any other way – rather, this was provided by the actuators themselves. This key feature distinguishes foam-based V-SPAs from other types of vacuum actuators, in that the materials and fabrication techniques used notably allow the creation of lightweight, soft structures which can be intrinsically actuated, while also providing self-support enabled by the mechanical integrity and relative stiffness of the internal foam cores. Moreover, the elastic foam core provides an essential restoration force following activation which returns the actuator to its nominal shape and configuration. Such freestanding soft actuators (which do not explicitly require an external support structure, or body) allow the creation of monolithic type soft robots comprised of active regions within an overall integrated multifunctional morphology, providing both action and support.

For complete robotic systems composed of active structural elements such as V-SPAs, diversity in motion capabilities at the actuator level is important to preserving constitutive simplicity and design efficiency. Although linear motion V-SPAs have been achieved and leveraged in multi-DoF actuator modules to create rotational motion using the constraint of other actuators to provide an effective pivot support, true independent bending motion from single foam V-

SPAs have never been shown. In this work, therefore, we seek to develop and characterize a new bending type foam based V-SPA which can be directly employed to produce lightweight and simplified robot designs. Specifically, we will present a new actuator design and experimentally measure the performance of prototypes across a spectrum of geometric variation.

We will characterize and discuss the unique attributes of the Coil V-SPA which extends the behavior of bending actuators to extreme range of motion (RoM). These actuators follow a trajectory evocative of a Fibonacci spiral during free actuation, and feature an adaptable radius of curvature analogous to biological tentacles used for coil grasping.

Finally, we will investigate the role of important design parameters through empirical testing and evaluation of Coil V-SPAs to establish a generalized methodology for V-SPA design.

The main contributions of this section are:

- Prototype and experimental characterization of a new high-bandwidth high-RoM Coil V-SPA.
- Introduced a generalized design metric for V-SPAs, the Geometric Compression Ratio (GCR), which correlates physical geometrical design parameters to actuator performance.

3.5 Coil V-SPA Fabrication

Coil V-SPAs are manufactured following the general method described in previous work for non-bending V-SPA fabrication [67]. The main components of a Coil V-SPA, illustrated in Figure 3.9, are similar to the design in prior work; however, some of the materials used were replaced with those better suited to the mechanics of actuator bending. While open-cell polyurethane foam was used for the primary structure of the actuator chamber cores as previously described, the paper membranes used were substituted for 0.5 mm thick rigid acrylic plates which resist bending or folding when subjected to the highly asymmetric forces seen in Coil V-SPAs. Rectangular foam chamber cores were cut from a sheet with a CNC laser, and then glued in alternating series with the acrylic membrane plates to create a linear stack that forms an actuator core. The core is terminated at both ends with another plate. Each of the acrylic membrane plates also contains a 5mm hole to allow passage of air between adjacent chambers. To generate bending motion, a layer of 0.2 mm thin plastic is attached on only one side of the rectangular shaped core, flexible enough to bend over the length of the actuator, yet rigid enough to resist folding and buckling locally between each chamber. This layer is glued to each of the acrylic plates to fix it in place, and then manually coated and sealed with a mixed two-part silicone elastomer, Elastosil M4601. The asymmetry enforced by the reinforcing layer ensures that when the final actuator is activated, only the un-reinforced side of the actuator will contract, while the stiff layer-reinforced side will only bend without changing length. This interaction yields bending which can be used directly to perform work

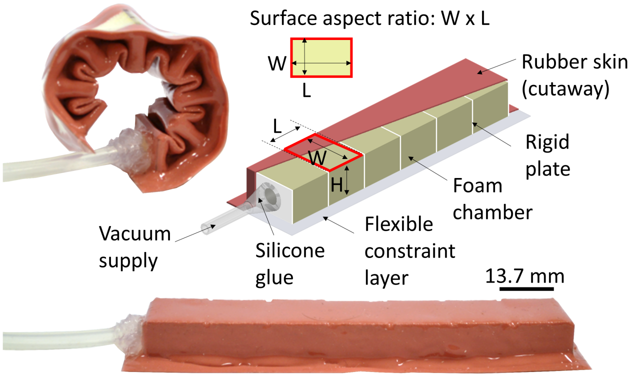

Figure 3.9 – Coil V-SPA structure. Coil V-SPAs are fabricated from lightweight foam blocks, glued in a series stack with rigid plates and coated with a thin layer of elastomer skin. The plates are fixed on the bottom to a flexible constraint layer which resists compression once the foam core of the actuator is depressurize with vacuum. The asymmetric stiffness between the top and bottom surfaces enforces a bending or curling motion, and the very low overall mass of the actuator body allows this motion to occur very rapidly.

in soft robotic applications.

3.5.1 Geometric Parameter Variation

A sets of eight Coil V-SPAs were fabricated following the described method. The set was produced to allow empirical testing of their performance, particularly to measure the effects of geometric parameters on both their force and speed profiles. All of the eight actuators were fabricated with a fixed total length, width, and height of 100 mm, 20 mm, and 12.7 mm, respectively. These dimensions were chosen to be comparable to other bending SPAs studied in literature, but are not important for analyzing the effect of relative actuator parameter variation. To study the role of chamber size and proportion, each actuator was produced with a different number of chambers, varying from two to nine chambers. With all other parameters held constant, the length of each chamber varied in consequence to changing their number. This difference relates to the real parameter of interest expected to govern the function of V-SPAs – the GCR, which will be defined and explained in the following section.

3.6 Coil V-SPA Characterization

The set of actuators fabricated with different geometry were tested to empirically evaluate their performance, and the effect of design parameter variation.

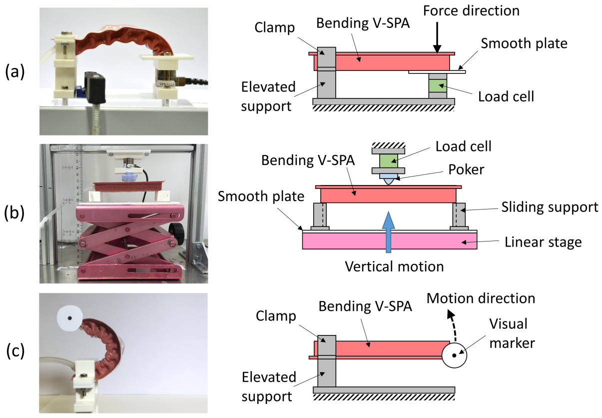

Figure 3.10 – Experimental setups. The experimental setup for blocked force testing is shown in (a), while (b) depicts a different setup utilized for performing a 3-point bending test to measure actuator stiffness in the powered state. The final test fixture shown in (c) was used for measuring actuator tip speed in free displacement.

3.6.1 Tip Force Characteristics

A blocked force test setup was used to measure the tangential force at the tip of each actuator as it was activated to bend downward against a single load cell force plate. The test fixture, shown in Figure 3.10a, consisted of a 3D printed ABS plastic elevated support and bracket for mounting the fixed end of an actuator, and a load cell (Nano17) fitted with a smooth flat acrylic plate to support the actuator free end at the same height as the elevated support. When inactive, the actuator being tested is thereby initially horizontal. Although the free actuator tip is restricted from downward motion by the force plate, it is not otherwise constrained to it. A small piece of paper is included between the tip and plate to reduce friction and allow free sliding. In addition, the body of the actuator is not constrained, consequently deflecting away from the plate due to its inherent compliance. Only the vertical component of the force generated by the actuator, orthogonal to the force plate, was used for comparison of actuator performance and parameter evaluation as this force best represented the actuator moment produced. A series of ten on-off step input cycles was performed for each actuator, with a pneumatic input of 80% vacuum. The maximum force for each of the ten cycles was averaged and a single maximum force value determined for every actuator in the test set.

The performance of each actuator tested depends on the geometry of its constitutive chambers to convert negative pressure to force and motion. Qualitatively, it was found that certain relative dimensions for square shaped chamber geometry produced larger motion in the desired direction, while others did not generate significant effects. The more "successful" actuator chambers collapsed in a manner which contributed to bending and coiling of the Coil-VSPA, while others which were less effective simply collapsed inward without producing useful directed motion. In order to quantify the effectiveness of the chamber toward producing a given output, a new metric is proposed for evaluating the effect of different geometric parameters on the performance output of the Coil V-SPAs, referred to as the Geometric Compression Ratio (GCR). This metric can be calculated for each actuator as a function of the outer surface aspect ratio of the actuator chambers relative to the chamber height;

$$\mathrm{GCR} = \frac{\text{Height}}{\text{Surface Aspect Ratio}} = \frac{H}{W/L} \tag{3.3}$$

This new parameter was used to then compare the force output of each tested actuator in generalized terms. By graphically plotting the force as a function of GCR as shown in Figure 3.11a, a peak was identified which suggests an optimal design relationship for achieving the maximum force output and corresponding actuator bending moment. The criteria for this optimal force design relationship is established by the GCR incident with this force peak, GCR_F=8.7 mm. This value is associated in this case with a 7-chamber actuator with a specific set of dimensions, however the same value may be achieved through other combinations of geometric parameters for similar shaped Coil V-SPAs to ensure they are designed close to their maximum force output.

3.6.2 Actuator Stiffness

In blocked force testing with only partially constrained actuators, the compliance of the actuator body allowed the Coil V-SPA prototypes to deflect up and away from the force plate. To quantify this compliance, an alternate setup was constructed to enable a three-point beam bending measurement for each actuator. The setup, depicted in Figure 3.10b, consisted of a load cell (Nano17) fixed to a rigid frame, positioned under a vertically mobile platform on which the actuator was placed across independent elevated free sliding ABS plastic supports at both ends. A smooth, flat acrylic plate was installed on the platform to reduce surface friction. A prominent, rigid 'poker' component was added to the end of the load cell to maintain contact with the center of the actuators during deflection without interference. For testing, the actuators were initialized in an unloaded horizontal position across the end supports, with the constraint layer side of the actuator facing up and just in contact with the end of the load cell poker. The stiffness of each actuator was measured in the 'on' and 'off' state, with and without applied pneumatic pressure of 80% vacuum, respectively. In both conditions, measurements were performed by manually raising the non-backdrivable, screw-driven vertical platform via a knob in 2 mm increments up to 10 mm total deflection. At each 2 mm interval, a high impulse tap was imparted to the frame supporting the load cell to mark the position level in the recorded force data. The collected force data was finally correlated to each displacement level to produce the stiffness relationships depicted in Figure 3.12.

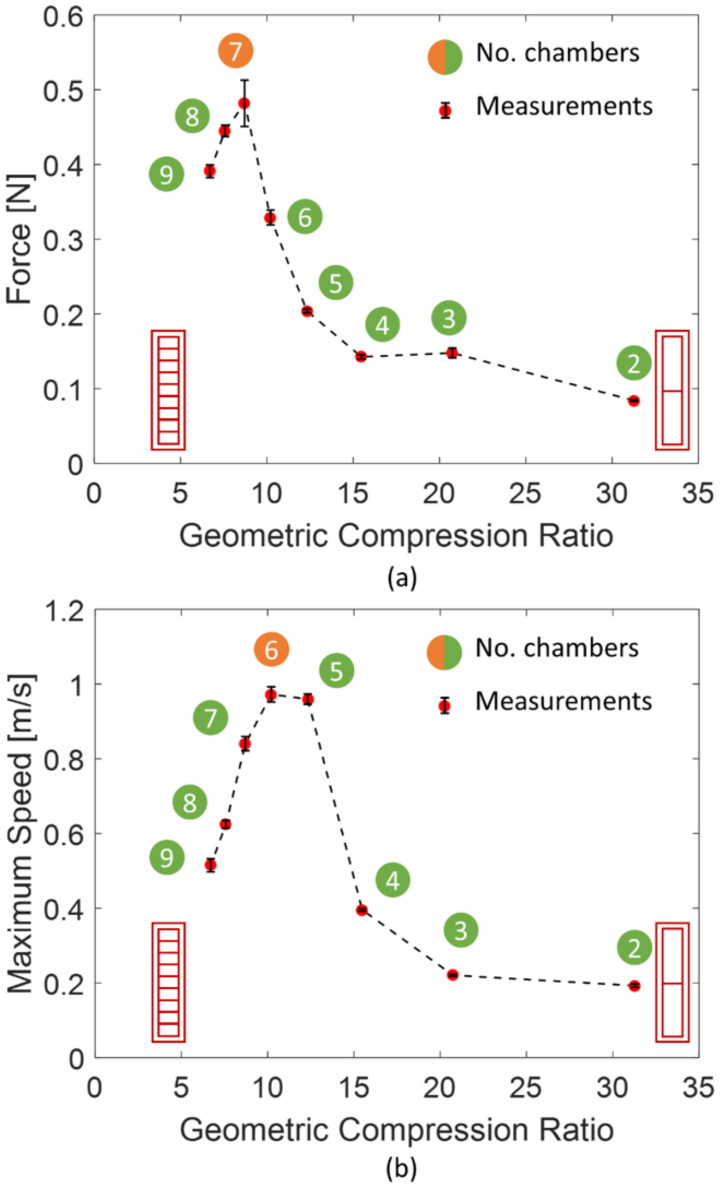

(a)

(b)

Figure 3.11 – Actuator performance in terms of GCR. The maximum force output recorded among the set of Coil V-SPA prototypes is shown in (a) and the maximum speed measured in testing is shown in (b). In both figures, data points are labeled corresponding to the number of chambers in the actuator which produced it, while peak actuators are shown with orange numbers. Error bars represent a single standard deviation for multiple measurements.

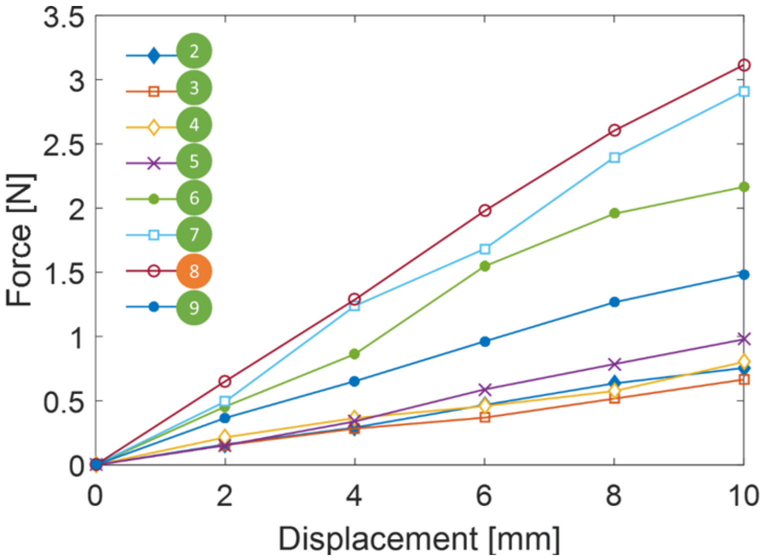

Figure 3.12 – Measured Actuator stiffness. A dominantly linear stiffness was measured for each Coil V-SPA while powered, which generally increased with the number of chambers. The reduction in stiffness for the 9-chamber actuator suggests a limit as the chamber number becomes too large (shorter chambers, smaller GCR), the actuator body is compressed, and the effect of the internal pressure is diminished.

3.6.3 Speed Characteristics

The set of geometrically diverse Coil V-SPAs was also characterized in free displacement to measure their maximum bending speed and bandwidth. This was accomplished by first fixing one end of the actuator by a plastic bracket to an elevated support fixture, while the other was left free to bend upward (Figure 3.10c). A visual marker was attached to the free end of the actuator and a 240 fps high-speed video camera recorded the motion of each actuator trial consisting of five on-off cycles. Motion analysis software (Kinovea) was used to post-process the recorded video from which marker travel distance and velocity measurements were obtained. Additionally, the software was used to generate a visual trajectory overlay of all 5 cycles for each actuator test, shown in Figure 3.13a. From the recorded measurements, the peak velocity for each test cycle was averaged for every actuator, and the resultant trend of maximum velocity with respect to GCR was plotted to obtain a similar relationship to that found in the previous force experiment (Figure 3.11b). A peak was again identified in the performance among the different actuators indicating the estimated location of optimal design criteria to maximize Coil V-SPA velocity. This peak, however, was found to occur under a different condition than that for peak force. The maximum velocity measured corresponds to the 6-chamber actuator, which yields, GCR_V=10.2 mm. In more absolute terms, the maximum speed recorded for this actuator was 0.97 m/s at peak and the average step input rise time was calculated to be 0.22 seconds. The corresponding bandwidth (BW) was calculated from the measured rise time t_r as BW=0.35/t_r to be 1.59 Hz (only gravity loaded). This can be seen in Figure 3.13b.

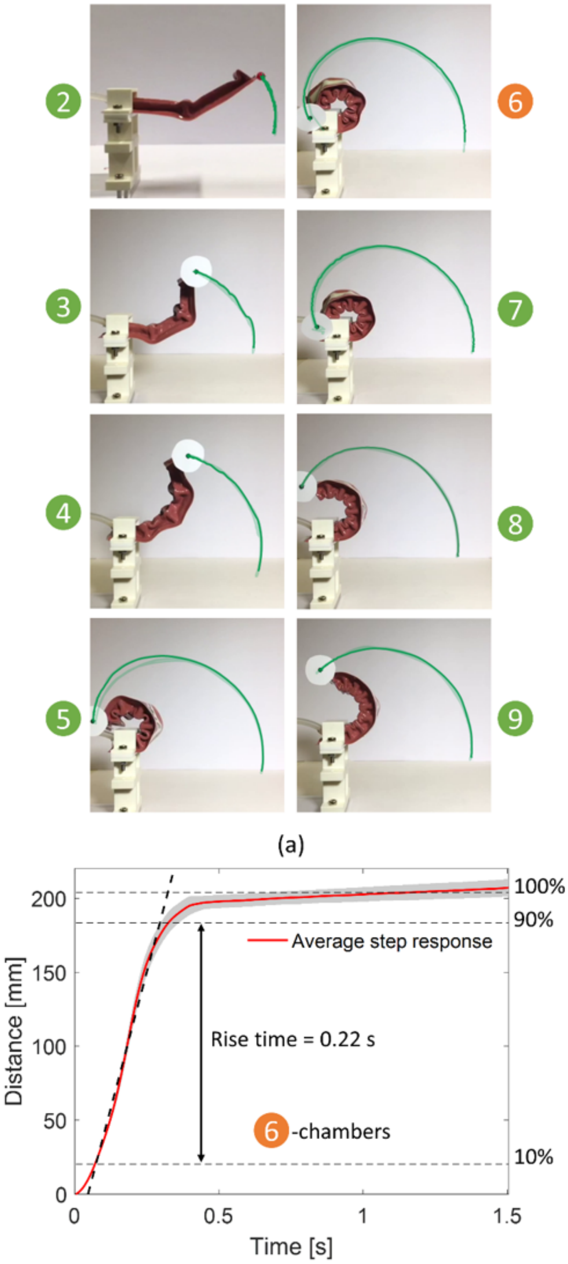

(a)

(b)

Figure 3.13 – Visual tracking is used to measure and record the trajectory of a marker attached to the free end of a cantilevered Coil V-SPA for velocity testing. The trajectory for each of the multi-chamber actuators tested is shown in (a), while the step response for the fastest measured actuator can be seen in (b), with the rise time measured from the 10%-90% maximum displacement along the arc length of the endpoint trajectory.

Bending V-SPA Measured Performance and Geometric Parameters						
	Parameters		**Performance**			
	No. Chambers	***GCR [mm]***	***Max. force [N]***	***Max. speed [m/s]***	***RoM [mm]***	***Band-width [Hz]***
	2	31.3	0.08	0.19	41.8	0.56
	3	20.7	0.15	0.22	70.3	0.76
	4	15.5	0.14	0.40	101.4	0.82
	5	12.3	0.20	0.96	193.6	1.26
	6	10.2	0.33	0.97	203.9	1.58
	7	8.7	0.48	0.84	190.5	1.55
	8	7.6	0.44	0.62	180.7	0.80
	9	6.7	0.39	0.52	170.8	0.72

Table 3.3 – Bending V-SPA measured performance and geometric parameters

3.6.4 Summary of Actuator Performance

The results from testing a spectrum of Coil V-SPAs with variable chamber multiplicity and geometry are shown in Table 3.3.

3.7 Discussion

The Coil V-SPAs presented here extend previous work into foam based V-SPAs, to enable new motion capabilities for these types of actuators, and demonstrate advantages including high-speed actuation resulting from their lightweight, low-inertia, structure. Additionally, these actuators are shown to possess a linear stiffness profile in the activated state, allowing more predictable modeling and control in the future, or perhaps opening the possibility for their use as a variable stiffness mechanism. The simple composition of these actuators lends itself not only to their high performance in certain aspects, but as with other, linear type V-SPAs, to enable easy, rapid fabrication which make this type of vacuum powered actuator attractive for efficient iterative soft robot design and prototyping. This quality was found to be particularly beneficial to this study, wherein all eight unique actuators in the set characterized experimentally were constructed from start to finish in less than a day. Although the purpose of this study was not explicitly to demonstrate this feature, it is an important example of the value of rapid and cost effective manufacturing to the design process of soft robots. The empirical testing of multiple actuator varieties allowed a relatively straightforward method for identifying important physical design parameters relevant to optimizing Coil V-SPAs for speed and force output, distinguished by a single parameter, GCR, without the use of a rigorous analytical or computational model. This methodology for quantifying and characterizing

V-SPAs by geometric parameterization was validated through the experimental measurement of Coil V-SPAs, but may be extended to the design and development of other types as well, serving to further motivate the continued progress and broad adoption of vacuum power in the field of soft robotics.

4 Wearable SPA systems for direct and indirect human assistance

4.1 Introduction

In this final chapter I will present two examples of SPA-based robotic platforms for wearable applications. The first example of a wearable postural support belt device utilizes SPA-Packs and body-mounted sensors to respond to changes in upper body position with moments applied by the actuators surrounding the waist for *direct assistance*. This function is tested in a pilot study with real healthy users and shown to be effective in supporting human-scale loads. The second example presents a concept and hardware framework for a compact wearable *task assistive* device, which can be best referred to as a “third arm”. This system is intended for daily use and is thus designed with criteria towards meeting this objective; low-weight, compact, reconfigurable to accommodate different tasks, and intuitive to control. The modular platform utilizes a novel hardware composition, blending lightweight robotic origami materials and fabrication techniques in combination with low-profile SPAs to attain a hybrid soft robotic

---

The material presented in this chapter is adopted from the following self-authored publications:

[221] **M. A. Robertson** and J. Paik. “Trunk postural tracking of assistive soft pneumatic actuator belt,” *Presented at Dynamic Walking Conference*, Holly, MI, 2016.
[222] G. Agarwal, **M. A. Robertson**, H. Sonar and J. Paik, “Design and Computational Modeling of a Modular, Compliant Robotic Assembly for Human Lumbar Unit and Spinal Cord Assistance”, Scientific Reports, Vol. 7, Article number: 14391, 2017.
The first author wrote the manuscript, analyzed data, and performed simulations. The second author designed and fabricated actuator prototypes, conducted experiments, and contributed text on actuator design. The third author conducted material characterization tests and helped analyze results.
[223] S. Hauser, **M. Robertson**, A. Ijspeert and J. Paik, "JammJoint: A Variable Stiffness Device Based on Granular Jamming for Wearable Joint Support," in IEEE Robotics and Automation Letters, vol. 2, no. 2, pp. 849-855, April 2017. doi: 10.1109/LRA.2017.2655109
The first author wrote the manuscript, designed and fabricated the hardware, conducted experiments, and analyzed results. The second author helped conceive the initial device concepts, conduct experiments, and contributed background text. The third and fourth authors helped in revising the manuscript.
[224] **M. A. Robertson**, O. Kara, and J. Paik, “Soft pneumatic actuator driven origami inspired modular robotic “pneumagami”’, International Journal of Robotics Research, 2019, In review.
The first author wrote the manuscript, designed and fabricated the prototype, and conducted experiments. The second author fabricated critical hardware components and contributed to the manuscript.

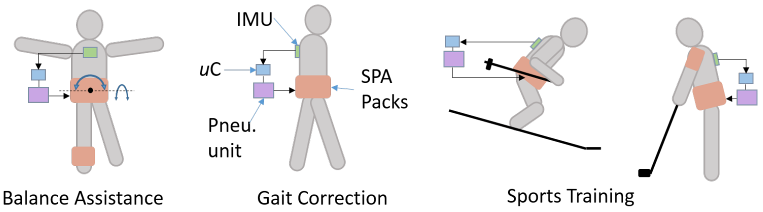

Figure 4.1 – High-force SPA belt applications. A wearable SPA powered belt could be used for balance assistance (a), gait correction (b), or sports training exercises (c).

structure that is mechanically optimized toward safe, wearable, everyday use.

4.2 Part 1: SPA Pack belt for postural support

SPA Packs provide high actuation force in the 100 N range, suitable for human body-scale interactive applications. While there has been limited progress in the development of overall small-scale wearable SPA powered devices, there has been less advancement in developing solutions for more demanding body interaction tasks, due largely to the lack of appropriate high-force SPAs. While an ambitious goal is to affect motion or assist in complete full body actions, such as providing direct assistance in walking, there is a considerable benefit to pursuing assistance of upper-body stability which is indirectly linked to many full-body motions. By applying a moment at the midpoint of the lower trunk region of the body, a powered, wearable belt device could be used to assist in various activities including balance, gait correction, or sports therapy for rehabilitation, or training (Figure 4.1). As a preliminary investigation towards these opportunities, an active wearable belt will be presented to demonstrate the capability of SPA pack modules to affect human trunk posture while standing, while further work may enable active modulation of trunk angle during walking to provide corrective assistance or gait modifying perturbations.

4.2.1 Introduction

The natural characteristics of SPAs are especially well-suited to human-robotic interface applications, where an active device is designed to directly affect the human body. A variety of soft actuated wearable hand exoskeleton and glove devices have been developed to leverage the adaptability, natural bending motion, and relative strength of SPAs for assistive and rehabilitation applications [198, 111, 109]. A large body of work also targets augmentation of lower extremity muscle and joint work to improve healthy normal functionality for walking or to restore and assist deficiencies in gait dynamics [201, 202, 203, 204]. This latter group of applications which require high forces have primarily utilized a particular type of SPA, the Pneumatic Artificial Muscle (PAM) also known as the McKibben actuator. At present, these actuators have provided the only successful demonstration of SPAs in this high performance regime. This work seeks to develop and employ a new type of SPA architecture to service this realm while also permitting additional unique, advantages critical to reliable robotic systems.

The main contributions of this section are:

- A wearable postural support belt device driven by high-force SPA Packs, capable of affecting the large mass of the human upper body.
- Validation of trunk angular position guidance through experimental subject measurements.

4.2.2 Methods

Individual SPAs are fabricated from silicone rubber (Elastosil®M4601) and SPA packs of four unit actuators are assembled using a low-elastic modulus silicone rubber (Ecoflex®00-30) to join them. Using a single-axis load cell and a linear constraining test fixture, the force output of a module inflated to 200 kPa was measured. To convert the linear action of a pack to bending motion, an inextensible sheet of fabric is attached to only one “face” of the flat actuator pack using SilPoxy® flexible adhesive.

A wearable belt is fabricated from 1.5” inextensible nylon webbing and 1” elastic straps, sewn together. From the same materials, an enclosure is also fabricated for each of four SPA packs produced, to provide a structural interface with the belt. A band of hook-and-loop fasteners is included along the belt and on each bending-type SPA pack enclosure to enable attachment and reconfigurable positioning of the modules. Finally, an outer, inextensible belt is used to constrain the actuator packs and ensure transmission of force and bending moments to the user.

To initially characterize the belt, a test platform was constructed with human proportions and used to measure the maximum vertical traction force and maximum moment applicable by four modules distributed evenly around the circumference of the “waist”. The frequency response of blocked force to a range of sinusoidal pressure inputs was measured to obtain a system bandwidth, and the angular position of the “torso” segment of the test platform was measured using an accelerometer to demonstrate closed-loop PID position tracking of the test system. A final test of robustness was conducted by closing off individual SPA units in a given pack to simulate failure and the resulting trajectory under PID control was recorded.

The actuator belt was then tested on human subjects with four bending modules positioned in pairs on the medial-lateral plane at the hips and below the rib cage. Subjects were instructed to stand with arms crossed, feet together, and eyes closed while listening to white noise (rainfall) to disguise visual and audio effects of the pressure regulator and valves used to control the belt. A low frequency (0.1 Hz) sinusoidal control input was used to drive the belt in alternate directions and subjects were asked to “follow” the belt as if it were the guiding hands of a physical therapist or trainer. The angular position of subjects was recorded using

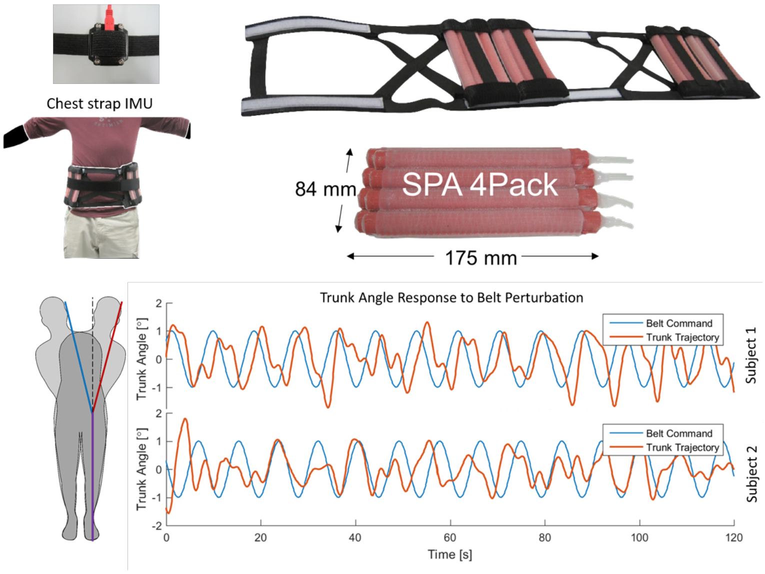

Figure 4.2 – SPA belt induced posture modulation. The trunk lateral flexion of two human subjects wearing the SPA belt are depicted over an input sinusoidal signal used to activate the belt in the medial-lateral body direction. Postural sway was measured using an IMU mounted to the chest of the subject.

an accelerometer attached by a tight elastic strap around the chest. Raw output data was low-pass filtered at 6 Hz.

4.2.3 Results

Individual SPA pack characterization revealed a linear force output capacity of 112 N per module, although measurement of the belt consisting of four modules shows 468 N total vertical force, which corresponds to a slightly higher average force capacity of 117 N per pack. The maximum moment measured using the test platform was shown to be 18 Nm. The test of robustness indicated an asymmetric decline in capability under PID control, but the maintenance of overall tracking behavior.

From human subject testing, the wearable SPA belt successfully demonstrated the ability to influence trunk posture in standing, as shown in Figure 4.2. Using FFT analysis, the dominant mode of both subjects' response trajectories were found to match the frequency of the input sinusoids at 0.1 Hz.

4.2.4 Discussion

The SPA packs shown here offer an alternative source of actuation for high-force wearable devices, or any application that may benefit from safety, reliability, and customizability. Drawing inspiration from biological analogs, parallel grouped SPAs afford advantages of robustness to failures, and modularly scalable force output not available from other soft actuator designs. The potential is illustrated by the short evaluation study presented of an example wearable SPA belt, but is not demonstrable of the actuators full capability. The active belt imposes a controllable influence on a human subject wearer, but from this study it is unclear how much this is directly mechanical and what amount may be informational feedback. Development of more adequate constraint and body interface features may yield stronger results from a wearable system or enable a study involving participants with partial or more severe postural impairments to benefit from a fully active soft wearable device for postural support.

4.3 Part 2: Modular robotic assembly for human lumbar unit and spine support

Wearable soft robotic systems are enabling safer human-robot interaction and are proving to be instrumental for biomedical rehabilitation. In this chapter, we propose a novel, modular, wearable robotic device for human (lumbar) spine assistance that is developed using vacuum driven, soft pneumatic actuators (V-SPA). The actuators can handle large, repetitive loads efficiently under compression. Computational models to capture the complex non-linear mechanical behavior of individual actuator modules and the integrated assistive device are developed using the finite element method (FEM). The models presented can predict system behavior at large values of mechanical deformations and allow for rapid design iterations. It is shown that a single actuator module can be used to obtain a variety of different motion and force profiles and yield multiple degrees of freedom (DOF) depending on the module loading conditions, resulting in high system versatility and adaptability, and efficient replication of the targeted motion range for the human spinal cord. The efficacy of the finite element model is first validated for a single module using experimental results that include free displacement and blocked-forces. These results are then extended to encompass an extensive investigation of bio-mechanical performance requirements from the module assembly for the human spine-assistive device proposed.

4.3.1 Background

Spinal cord injury (SCI) resulting from a traumatic movement leads to a deformation of the neural and vascular structure of the spinal cord [225]. In addition to accidental SCI cases, clinical observations have indicated that the physiological changes in comprising soft tissues throughout human lifetime lead to an overall reduction in the available space for the neural structures (spinal cord, medullar cone and roots) and that this effect is amplified by vertebrae slip due to the weakness of vertebral facets, ligamentous ossification, vertebral joint fusion and other factors such as osteoporosis. The biomechanics of different components of the spinal column, including the spinal cord and the vertebrae, is fairly well described and quantified in literature including computational studies using FEA [226, 227]. However, solutions to help restore the lost mechanical strength and functionalities of the lumbar unit and the spinal cord even in part, following the injury situations described above, and enabling the overall mobility and high flexibility for the patient are still lacking. In the cases of lack of spinal mobility, along with several other scenarios, such as one where a patient may be suffering from a stroke in which cases repetitive motions have been reported to be highly beneficial [228] in order to restore normal motor control, an artificial wearable device for spine assistance can be very desirable.

The functional building blocks and key system structural requirements required to achieve such an assistive system are presented in this work (Fig. 4.3), after analyzing mechanically related pathologies of the lumbar unit and the spinal structure by observing spinal cord deformations under different loading scenarios [226]. By studying the localization and the magnitude of maximum equivalent stress and shear stresses on the lumbar unit and the spinal cord, design requirements are elaborated for the assistive wearable device proposed. Physical properties of the vertebrae, ligaments, intervertebral discs, and the spinal cord are taken into account under loading such as compression, and combined loading, flexion and lateral bending to evaluate the pressure undergone by different components of the lumbar unit. Since the primary mode of mechanical failure is in compressive loading, high compression withstanding capabilities are desired from the proposed system, in order to replicate and efficiently assist with the diminished functionalities of the injured spinal column.

Soft materials and systems are light weight, highly flexible and adaptable, and inherently safer, making them better suited for building such systems as compared to their rigid counterparts. Due to these advantages, soft robotics [229, 41, 40, 230, 231, 47, 55, 232] has recently emerged as a dynamically evolving field, to create novel systems with pre-programmed and predictable capabilities out of elastomeric materials, capable of withstanding large deformations. Apart from applications in diverse fields, ranging from bioinspired and biomimetic systems [41, 40, 230], adaptable locomotion on unstructured terrains [231] and operating surgical tools [47], soft robotic systems and structures are particularly well-suited for applications in biomedical rehabilitation and assistance [55, 232, 192, 203]. Soft actuator based robots and devices have been studied in the recent past for biomedical rehabilitation and assistance applications including an assistive hand glove [55], an artificial heart [192, 233] and artificial muscle packs [234] that can potentially be implemented on various parts of the human body that may require assistance, such as the trunk carapace for gait assistance. Soft pneumatic actuators (SPA) [55, 232, 234, 235, 34, 236], fabricated using elastomeric silicones and typically composed of air corridors and chambers where input air pressure is applied, are particularly attractive for implementation in such robotic systems due to their ease and safety of operation, high power-to-weight ratio and low cost. Classical soft pneumatic actuators such as the McKibben actuators or pneumatic artificial muscles [237, 238] comprise of inflatable bladders wrapped inside braided mesh structures, where the motion of the actuator can be tuned by changing mesh patterns. Other soft actuator designs such as the PneuNets [34] have multiple air chambers with narrow connecting passages and require multiple molding steps for fabrication. More recent actuator designs involve the actuators being fabricated in a single molding step,

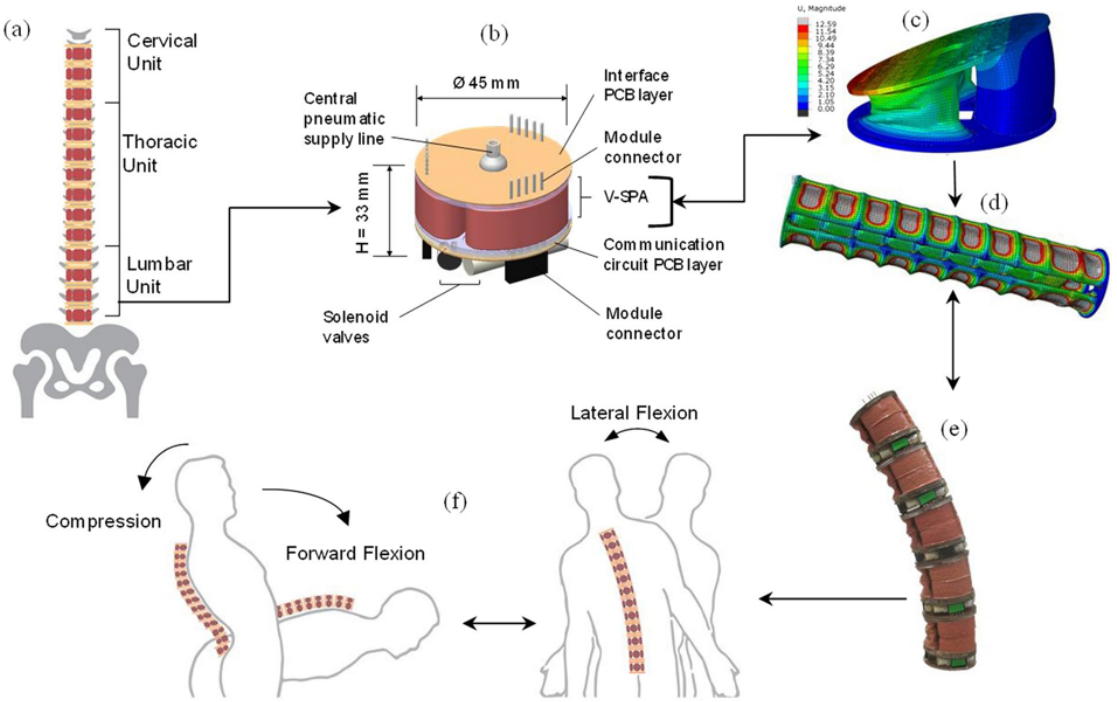

Figure 4.3 – Assistive spinal support device concept. (a) Human spinal column representation comprising of the lumbar unit consisting of the vertebrae, intervertebral discs, spinal cord and other components. (b) Representation of the spinal column unit with a vacuum driven soft pneumatic actuator (V-SPA) module. (c) Numerical simulation results for a single V-SPA module. (d) Simulation results for a pressurized V-SPA module assembly with fixed ends. (e) V-SPA assembly undergoing free bending displacement. (f) Schematic representation of replication and assistance of spinal column motion with the help of the robotic assembly.

and reinforcement with fibers windings or stiffer shell structures to constrain any excessive inflation of the actuator body [232, 236]. While a large majority of the currently existing actuator designs utilize positive air pressure input as the driving agent, recent developments have also demonstrated the successful implementation of soft actuators by reducing the pressure level inside elastomeric chambers to below that of atmospheric pressure (that is, to negative pressure, or partial vacuum) and achievement of compressive or buckling actuation motion profiles [239, 240].

The vacuum-driven soft pneumatic actuators (V-SPA) used to assemble the spinal column assistive device proposed and modeled in this work have an interconnected open-pore network and do not require additional molded air channels. The leading motivation for their development was to achieve simple actuation through the use of lightweight, readily available materials and minimal fabrication steps, to reduce mass and production effort. Their resulting simple composition and construction, consisting of foam encased with brushed-on silicone rubber skin, facilitates rapid development of customizable actuators for unique applications, or design iteration.

While soft materials such as foams and rubbers offer high agility and versatility, predicting the mechanical performance of the systems under consideration can be challenging due to the highly non-linear behavior of the materials used and the complex interaction between multiple materials employed. To capture more detailed information on stress-strain distributions within the actuators and model the non-linear effects observed more accurately, finite element analysis (FEA) of SPA has also been carried out in the past for several silicone-rubber based assistive soft systems for applications in hand rehabilitation [55] and a prototype for a human heart [192]. Non-linear soft material behavior in silicone rubber based SPAs for a variety of different applications has been captured across a large range of realistic strains in [29] using appropriate hyperelastic models. While silicone rubber based soft robotic systems have recently been well characterized, there is a lack of any study using FEA for SPA-based systems developed from alternate high-performance materials such as foams, targeted towards biomedical rehabilitation and biomechanical assistance. There is only a handful of examples in literature where soft robotic devices have been developed using foams [233, 241] and these studies have focused solely on experimental characterization, thereby lacking predictive capabilities for optimal system design.

In the present study, we present major findings from the development of a novel actuator design for an assistive device and its experimental results compared to predictions from the FEA. The presented actuator design, which forms the integral functional unit of the spinal column assistive device proposed, allows low-cost, manufacturable prototyping of functional modular units with highly versatile motion capabilities (e.g. both bending and linear motions achievable with the same module) and produces results in the desired performance range. The presented numerical models using FEA accurately predict the complex mechanical response and the performance obtained with the designed actuators, while allowing design iterations to optimize the critical functional parameters for the assistive system.

The main contributions of this section are:

- A proposed wearable spine support system for matching the mobility and loading conditions of the human lumbar unit.
- A computational FEM model of V-SPA modules for predicting actuator stress, load, and displacement profiles, to enable system and actuator design.
- Experimental characterization of hyperelastic foam-based V-SPA modules and validation of FEM models for various loading conditions.

4.3.2 Spine Assistance Module Design, Fabrication and Testing

Current methods of soft pneumatic actuator fabrication [231] commonly involve the casting of silicone rubbers into machined or 3D-printed molds which use either a sacrificial wax core or a two-part body construction to create hollow, inflatable structures. The necessary molds are time consuming to produce and cannot be reused following a change in actuator design. Without the need for such molds, V-SPA do not consume excess material or time greater than what is necessary for their own production. The technique used to fabricate the V-SPA presented in this work also ensures robustness and repeatability in manufacturing. The core component of the robotic module is a highly compressible actuation chamber, which forms the actuator body. To achieve large amounts of motion in compression, a light-weight, highly compressible polyurethane foam is used to form the base material for the chamber body. This foam core provides what is effectively an internal “mold” that can remain inside the actuator during use, while also providing the restoration force for actuator recovery following use. To strengthen the foam walls and achieve greater repeatability in overall mechanical performance of the V-SPA, the foam units are reinforced by painting the external surface of the foam walls (Fig. 4.4(a)) with a 0.5 mm thin coating of an elastomer which is an order of magnitude stiffer than the foam in the cured state. A schematic view of the actuator is shown in Fig. 4.3(b). The fabrication steps for the module are described in greater detail below.

A core in the shape of the final actuator is laser cut from an open-cell, polyurethane foam sheet (Fig. 4.4(b)). The cut-out shape is then mounted with glue to a small form, and coated with a layer of elastomeric polymer, to effectively form an air-sealed outer “skin”. Two coats are manually applied with a solid, flat, flexible brush onto the outer surface of the foam core to ensure complete coverage and sealing. To work properly, the chosen polymer must be compatible for curing in contact with the polyurethane foam, with adequate viscosity and surface tension properties to span the open cells in the outer surface of the foam core without entirely soaking into it.Silicone-based ELASTOSIL® M 4601 was found to be ideal for this purpose. Two other products tested, Ecoflex® 30 and Dragon Skin® 10, were not compatible with the foam tested. After a roughly 1 hour oven assisted curing time, the actuators can be used immediately. The glue form is removed with little relative force, enough to tear away a small portion of the foam surface to which it was attached, leaving an unsealed opening to

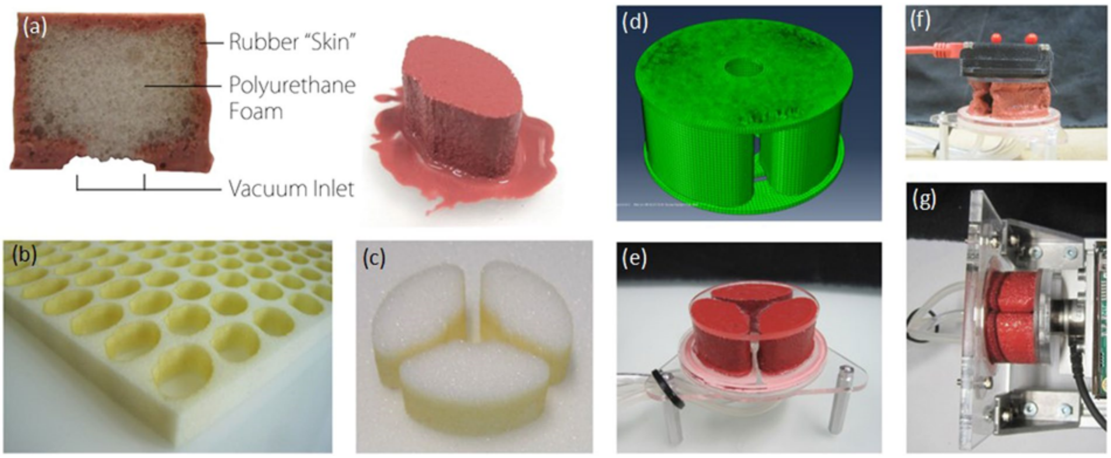

Figure 4.4 – Design and testing of V-SPA module. (a–c) Fabrication of the V-SPA module using a cutout polyurethane foam chamber which is painted with molten Elastosil rubber that acts as a restoring "skin" for the foam. Three such chambers are aligned as shown in (c) to form the 3-DOF module. (d) FE model for a single module containing the three chambers covered with top and bottom end-plates. (e) Fully assembled V-SPA module with top and bottom fiberglass end-plates. (f) A module undergoing free displacement testing, using an inertial measurement unit mounted on the top plate to measure displacements. (g) A module undergoing blocked force testing, using a load cell attached to the plate on the right side.

which a vacuum supply line can be attached as an input to the actuator. When the resulting V-SPA is supplied with vacuum pressure, the flexible rubber outer skin is able to bend and collapse while the internal foam is easily crushed. The restoring force of both the outer skin and the internal foam act as a spring to return the actuator body to its original, unactuated form. The reinforcement skin coating on the compression chambers limits the level of buckling of the contained compressible material, so as to avoid excessive buckling and irreversible permanent deformation of the actuator body.

The use of foam as the fundamental physical element of V-SPA construction facilitates not only lightweight structure, but also their characteristic operational feature of utilizing vacuum as a primary power source. While conventional positive-pressure driven SPAs operate by converting inflation to a bending or linear profile through stretching of an elastic body, V-SPA operate as a result of the buckling and folding of a flexible structure induced by negative pressure. This difference affords two advantages for V-SPA in terms of efficiency as well as safety. The mode of deformation seen in V-SPA does not entail significant energy storage, which directly corresponds to a wastage of energy needed for activation, as well as a potential hazard in the case of sudden release upon actuator failure. Since the inflation of positive-pressure SPAs requires substantial elastic strain of its rubber structure, energy which is stored during activation can potentially discharge subsequent to a rupture, creating an abrupt and possibly dangerous impulsive shock to the system. In contrast, if a V-SPA is punctured during operation, it will simply cease to function, providing only the restoration force and passive stiffness of the remaining foam core which does not depend on maintaining internal vacuum.

In addition, the possibility of failure caused by over-pressurization of typical SPAs is completely removed using vacuum as a power source because it is inherently limited by the environment from over-depressurization. Since the activation of a V-SPA depends on the reduction of its internal pressure, the greatest force and displacement which can be achieved will never exceed a bound imposed by the “maximum” input of zero pressure. This feature provides and additional layer of safety to vacuum-driven soft systems which serves to counter and protect against accidental or erroneous actuator commands, or the mechanical failure of subsystem components including valves and pressure regulators which could cause unintentional system behavior.

Various chamber structure patterns were compared and tested to evaluate the dependence of the mechanical performance of the actuator structure and the assistive device on the shape of the chamber. The chamber shape resulting in an optimal mechanical performance of the actuator structure for the assistive device is shown in Fig. 4.4(c). Rectangular, square or triangular cross-sectional shapes lead to larger stress concentrations due to sharp corners. Hence, those were not selected for further study. Circular cross-sectional shapes were also tested for the chambers and were found to yield larger mechanical instabilities in deformation response under compressive loading schemes. In addition to providing optimal mechanical strength, the chamber shape selected is also similar to the shape of the vertebrae comprising the human lumbar unit, leading to high conformance with the human body. The optimal height of the foam chambers was chosen in accordance with the transversal width, to provide adequate level of deformation during buckling, which is closely dependent on the slenderness ratio of the structure. The robotic module comprises of three such identical foam-skin V-SPA chambers, which are arranged at equal spacing as shown in Fig. 4.4(d,e). Selective pressurization and actuation of the chambers governs the pattern of displacement obtained with the actuator in the present study. Although it is possible to achieve other motion profiles by varying the arrangement and actuation pattern of the compression chambers, bending and linear motion were selected for further study in this work since these are sufficient to replicate and assist with the functionalities of the human lumbar unit.

Several experimental tests were done to characterize the performance of the actuators. These include performance in terms of free displacement, blocked force and blocked torque. The actuators were tested in free displacement to study the range of motion achieved as a function of the level of vacuum pressure applied. A venture principle vacuum ejector was used to generate the vacuum at different levels. To vary the level of vacuum used for actuation, the positive pressure input to the ejector was connected to a regulated pneumatic wall supply, varied manually using a flow control valve. By changing the input flow, the output vacuum flow and pressure was consequently varied. As this method did not allow repeatable setting of a desired vacuum pressure, instead the input supply was changed approximately and the actual resulting vacuum pressure on the output was measured directly with a pressure sensor (Honeywell, 24PCCFA6G). For these experiments, it was not important to achieve a particular pressure setting, it was only important to know what each pressure was for the sake of comparison. All measurements were then taken for a given pressure setting before changing to the next. For these experiments, the bottom end-plate with the vacuum inlet was clamped in a rigid fixture. The top end-plate of the actuator was permitted to move freely while applying vacuum pressure, thereby generating a curved or straight trajectory, depending on how many chambers of the actuator were pressurized. To track the position of the actuator with a high speed camera, an inertial measurement unit (IMU) is mounted on the top end-plate, as shown in Fig. 4.4(f). To generate a curved trajectory, either one or two chambers of the actuator were pressurized. To generate a linear trajectory, all three chambers of the actuator were pressurized simultaneously at an equal level of vacuum pressure. After extracting the path for the actuator as a function of time, bending angles and linear displacement were characterized as a function of input vacuum pressure. The experiments were performed multiple times with each combination of chambers to analyze the positioning repeatability as well as the pressure-to-angle repeatability.

To test the maximum blocked force delivered by the linear actuators, each end-plate of the actuator was rigidly clamped, with the actuator in an un-pressurized state. On the distal clamped end of the actuator (i.e., the end opposite to the end with the air inlet), a six-axis force/torque sensor (as shown in Fig. 4.4(g)) was used to measure the force as well as the torque produced by the end-plate face of the actuator as the vacuum pressure was ramped up from zero. To characterize a single module, end-plates made from a relatively rigid material (Fiberglass, in this case) are glued to the top and bottom surfaces of the V-SPA assembly to facilitate attachment of fixtures for gripping the actuators during testing and ensure maximum force/torque delivery. To connect multiple modules for assembling and testing the assistive device proposed, interface PCB (Printed Circuit Board) layers, composed of FR4 fiberglass substrate coated in thin copper layers, were used. These boards serve the dual purpose of providing structural support for the mechanical interface and containing electrical circuits and components necessary for communication between modules and a central off-board controller. Additionally, the PCB layers contain outward-facing complementary male and female pin headers at the top and bottom, respectively, which are used for both joining actuator modules and sharing electrical signals and power.

4.3.3 Mechanical Testing and Constitutive Material Model Fit

Computational modeling was done by using Finite Element Analysis (FEA) in ABAQUS/Standard (Simulia, Dassault Systems) to simulate the performance of the V-SPAs. 3-D models were created for the individual modules as well as for the entire assistive device. Models were developed to simulate both the linear and the bending modes of motion obtainable with each module. The details of the models are described below.

To model the highly non-linear mechanical behavior of the foam actuator body, an appropriate constitutive model needs to be used. Two general constitutive laws which may be expected to produce reasonable results were evaluated, the Hyperfoam model and the Low Density Foam model. Hyperfoam materials are typically highly compressible. After testing compatibility with the material data, the model ultimately selected for the foam used to build the modules was the Hyperfoam model. The Abaqus Hyperfoam model is a nonlinear, isotropic material model that is valid for cellular solids with porosity that permits large volumetric changes, and is suitable for hyperelastic foams. Material properties were determined through multiple tests on small material samples, performed across a large range of relevant strains. The types of experimental data that are used for modeling foam materials include uniaxial, biaxial, planar, simple shear and volumetric. Since the actuator module under current study is primarily designed for loading in compression and bending, multiple cycles of uniaxial compression tests and simple shear tests were performed (shown in Fig. 4.5). The Hyperfoam model is defined by a strain energy potential function (U) in the form:

$$U(\hat{\lambda}_1, \hat{\lambda}_2, \hat{\lambda}_3) = \sum_{i=1}^{N} \frac{2\mu_i}{\alpha_i^2} \left[\hat{\lambda}_1^{\alpha_i} + \hat{\lambda}_2^{\alpha_i} + \hat{\lambda}_3^{\alpha_i} - 3 + \frac{1}{\beta_i}((J^{el})^{-\alpha_i \beta_i}) - 1 \right] \tag{4.1}$$

The model can be used with any number of terms N, where μ, α and β are the primary fitting parameters. The independent variables λ_1, λ_2 and λ_3 are the three principal stretches, and are related to the strain in a continuum. The term J^{el} is the elastic volume ratio, and is a function of the principal stretches. The β_i parameters may be estimated directly from a given Poisson ratio, v. The formulas for stress given strain can be determined for the different tests through differentiations of1 with the appropriate strain conditions. A material density of 0.0378 g/cm^3, calculated experimentally using mass and volume measurements is assumed for the foam in the model.

In addition, time-dependent behavior of the foam within the duration of the loading is taken into account by incorporating viscoelastic effects into the model. To accomplish this, stress relaxation data is gathered to study the decay of the shear modulus as a function of time. To perform stress relaxation testing, a high tensile compressive strain is rapidly applied to a test specimen and held constant for a period of time, during which the stress is measured. The testing is carried out on a 20 mm cube sample of the foam. Cross-sectional area of sample is 400 mm^2. Testing is carried out by compressing the sample upto 80% of its original volume, waiting for 10 seconds and observing the decay of stress at constant strain input (shown in Fig. 4.5(e,f)). Then the sample is taken back to its original position. This procedure is repeated multiple times. The decay of the stress is recorded as the material relaxes internally and then fit to the Prony series mathematical model in Abaqus. According to this model, the decay of the shear modulus (G) and the bulk modulus (K) as a function of time is expressed as:

$$G(t) = G_0 - \sum_{i=1}^{N} G_i \left[1 - e^{-t/\tau_i^G} \right] \tag{4.2}$$

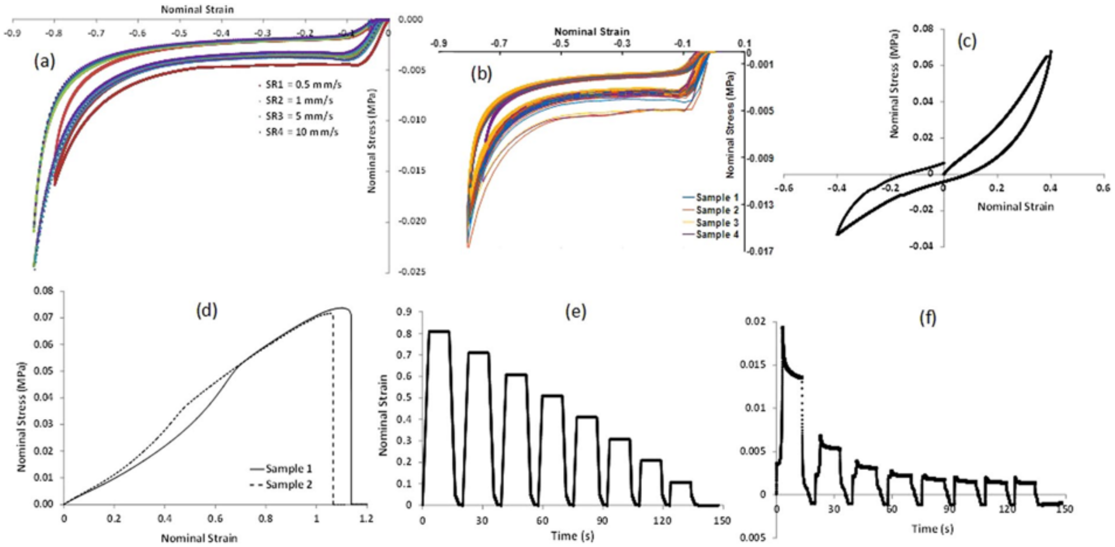

Figure 4.5 – Elastic foam material characterization. Stress-strain data for polyurethane foam samples undergoing mechanical testing under different modes of deformation. (a) Stress-strain data from uniaxial compression tests at different strain rates. The sample undergoes compression up to 80% of its original volume. (b) Cyclic test results in uniaxial compression. (c) Test results from simple shear testing. (d) Uniaxial tension test results. (e,f) Stress relaxation test results showing the decay of strain and stress vs. time, respectively.

$$K(t) = K_0 - \sum_{i=1}^{N} K_i \left[1 - e^{-t/\tau_i^K}\right] \tag{4.3}$$

where G_0 and K_0 are the instantaneous values of the moduli immediately after loading, G_i, K_i, τ_i^G and τ_i^K are the fitting parameters and N is the number of summation terms for the fit. In this case, 13 terms were chosen in the Prony series so as to provide a good fit.

Since the foam-based actuator chambers are designed to undergo rapid deformations over multiple loading sequences, the foam material samples were also subjected to cyclic loading tests to understand and incorporate the stress-strain behavior of the samples over repetitive loading conditions. Permanent deformations were observed in the foam after loading for a few cycles. Thus, the samples were conditioned for 20 cycles before the stress-strain curve saturated to a repeatable level. The saturated stress-strain curves were then used as an input to the FE model to capture the module behavior post multiple cycles of loading and predict the long-term operation performance obtainable. Using the above described sets of experimental data as an input, the coefficients of the material model were calculated using the in-built functionality in Abaqus™. These fitted coefficients for the material model were then directly used in the simulations without any further changes. The coefficients thus obtained are reported in Table 4.1 for the Hyperfoam model fit and in Table 4.2 for the Prony series fit.

I	MU_I	ALPHA_I	NU_I
1	0.284002	13.2805	0.00000
2	-0.283367	13.9800	0.00000
3	4.680466E-07	-4.77281	0.00000

Table 4.1 – Hyperfoam Model Coefficients.

I	G_I	K_I	TAU_I
1	0.30030	0.30030	1.00140E-02
2	0.19970	0.19970	0.10016

Table 4.2 – Prony Series Fit Coefficients.

To model the non-linear behavior of the reinforcement skin material (Elastosil), an incompressible, hyperelastic model was used. The Yeoh material model [242], described by a strain energy function of the form $U = \sum_{i=1}^{N} C_i(I-3)^i$ was used to describe the mechanical behavior of the skin. The material coefficients used for this model were C_1 = 0.11 MPa, C_2 = 0.02 MPa [236]. A material density of 1.07 g/cm3 is assumed for Elastosil in the model. Since the fabrication procedure for the modules involves painting the skin material onto the foam body, as described earlier in Section 4.3.2, it stays in contact with the foam at all instants of time. In the simulations, a tie constraint is imposed between the inner surface of the skin and the outer surface of the foam body along the entire circumference of the module to replicate this adhesive contact between the two interacting surfaces.

The Fiberglass material used to form the end-plates to grip the actuator modules in place during performance characterization was modeled using an elastic, brittle cracking model. A density of 1.9 g/cm^3 was used in the model for this material. A Young's modulus of 1770 MPa and Poisson's ratio of 0.38 were used to describe the linear elastic range. Direct stresses after cracking and direct cracking strains were included in the model, with a cracking stress of 120 MPa at a cracking strain of 0.5. The end plates were attached to the top and bottom surfaces of the skin-foam assembly using tie constraints. The boundary conditions implemented on the plates depend on the type of test being carried out and are discussed in the next section. Finally, an external pressure was applied to all of the outer surfaces of the elastomeric skin, to model loading of the actuator module under vacuum. This external pressure level was varied to simulate varying levels of vacuum pressure that the actuator is subjected to during testing. Figure 4.4(d) shows the FE simulation model with three chambers.

The actuator chambers are designed to undergo large mechanical deformations with buckling during pressurization. To model the buckling effects accurately, different solving schemes were tested to study the loading of the actuators. The implicit solving technique was first tested using an eigenmode superposition analysis with the Riks static method. This analysis was helpful in determining the critical buckling loading factor (load proportionality factor) as well as typical mode shapes expected (shown in Fig. 4.6(a–d)). Due to much larger solution times required to capture the dynamic behavior of the system using the Implicit method (as a result of the mandatory convergence checks enforced at each step and large, non-linear deformations involved in short time durations), ultimately an explicit solving scheme was utilized as the primary, robust solution method for all of the results presented in the subsequent section. The dynamic, explicit solver with a time period of 0.1 seconds and global minimum stable time increment estimator was used for the explicit solving scheme. The results obtained are presented and discussed in the next section.

4.3.4 Single Module Characterization and Validation of Experimental Results

Experimental data is gathered for the single module actuators undergoing free displacement, in both linear and bending motion profiles, and blocked force testing, and compared to the simulation results. To characterize the actuators, the input vacuum pressure generated in the foam is decreased in steps from a maximum value of 78% to 0%, in steps of approximately 8–10%. Computationally, these tests are modeled using external pressure application, with the chamber face containing the vacuum supply inlet fixed in all directions. Figure 4.6(e–j) compare results from experiments and simulations for free displacement obtained as a function of input vacuum pressure. The pattern of deformation observed from the deformation contour plot for a single chamber obtained from simulations and shown in Fig. 4.6(e) is comparable to that observed in a single chamber in the experimental image shown in Fig. 4.6(g), for linear actuator motion. Similarly, for the bending mode, the deformation pattern obtained for a module from simulations and shown in the displacement contour plot in Fig. 4.6(f) is similar to the bending deformation shown in the corresponding experimental image in Fig. 4.6(h).

Tests are first performed for the modules undergoing free displacement in bending profile free displacement conditions and compared to the simulation results. The bending performance obtained is compared for the cases when only a single chamber is vacuum-pressurized versus when two chambers are pressurized. As expected, pressurizing two chambers leads to larger bending angles, although this difference is more pronounced at intermediate pressure values with more comparable bending angle values obtained at the highest pressures. The capability to tune the bending motion within the range shown in Fig. 4.6(i) demonstrates the large working space available with a single module and provides a great platform for building assistive devices that require high adaptability and flexibility. To simulate bending performance, the pressure load is applied only on the chambers that are subjected to vacuum, with all other surfaces being free to deform.

The contour plots for displacement obtained from simulations for bending performance, along with the matching images of the actuators at the corresponding values of input pressure are shown in Fig. 4.6. Figure 4.6(i) compares results from both experiments and simulations for bending free displacement obtained as a function of input pressure. At lower pressures, the simulations predict lower displacements, potentially due to the effects of residual permanent deformation in the modules over multiple cycles of testing and some preferred buckling modes. With further increase in pressure, simulation results catch up and rise slightly above

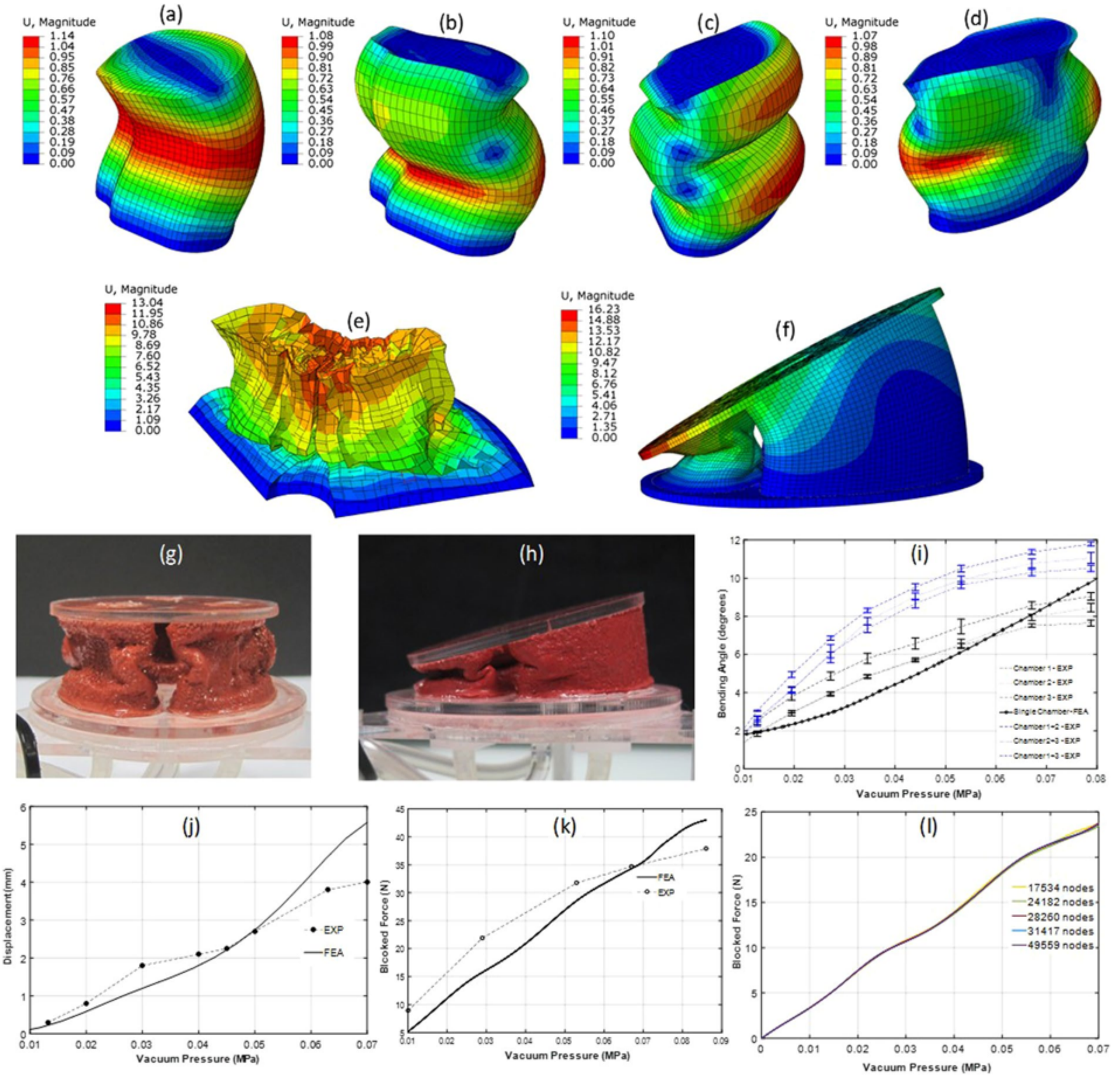

Figure 4.6 – Simulation results of actuator deformation. (a–d) Different eigenmodes of buckling for a single foam chamber subjected to compression loading. (e) Post-buckling collapse of a foam chamber using explicit analysis. (f) Free displacement simulation of the entire V-SPA module under bending conditions, with two foam chambers pressurized. (g) Image of the module exhibiting linear displacement profile with all chambers subjected to vacuum pressure. (h) Image of module exhibiting bending motion profile with two chambers subjected to vacuum pressure. (i–k) Comparison of simulation and experimental results for bending, linear displacement and blocked force tests, respectively. (l) Mesh convergence test results with varying total number of nodes in the system comprising the V-SPA module.

the experiments at vacuum pressure levels of between 60–70%. A similar comparison is carried out for the actuators undergoing free displacement testing to obtain linear motion profiles. This is done by pressurizing all three chambers in the module at the same time, as opposed to selective chamber actuation for the bending case. The corresponding pressure load is applied in the FEA as well. Figure 4.6(j) compares results from both experiments and simulations for linear free displacement obtained as a function of input pressure. A similar trend is observed from the comparison in linear displacement as in the bending.

The blocked force tests for the modules are modeled with both the top and the bottom end-plate outward faces fixed in all directions (encastre), and applying the external pressure load with ramp increment. The net reaction forces generated at the nodes on the top end-plate face are summed up to obtain the blocked force generated. In the experimental configuration, the top and bottom end-plates are rigidly fixed with a load cell mounted on the top end-plate. All three chambers of the module are simultaneously pressurized at the same level to record the maximum force delivered by the module under linear compression and the measurements on the load-cell are recorded. Figure 4.6(k) compares results from experimental measurements and simulations for the blocked force testing.

Since the skin's inner surface acts as the master surface and the foam's outer surface is the slave surface in the contact between the skin and the foam, a smaller mesh element width is used to model the foam chambers as compared to the skin surfaces in all the cases modeled. A coarser mesh is used for the plates as the plate elements undergo smaller deformations than the foam and the skin. A uniformly sized mesh (i.e. no bias) is used in all the regions since there are no particular geometric stress concentration regions in the module. Mesh convergence testing effectively removed all mesh sensitivity from the analysis. The results are plotted in Fig. 4.6(l) and show the effect of mesh element size, along with the effect of changing the total number of nodes in the mesh for the entire system, on the blocked force obtained as a function of input vacuum pressure.

4.3.5 V-SPA Module Assembly for Human Lumbar Unit and Spinal Cord Assistance

A case study of the biomechanics related to the human lumbar unit including the spinal cord is carried out in order to identify the design requirements and study the performance obtainable with the module assembly for potential application in assistive wearable systems. The primary modes of motion of the human spinal column include flexion-extension, lateral bending and twisting. Out of these different modes, the current 3-DOF actuator modules possess the capability to achieve flexion and lateral bending profiles with a large range of motion.

Flexion and lateral bending capabilities predicted from simulations and corresponding experimental measurements are described in further detail below. The results are first presented for the assembled assistive device created with the 3-chamber modules. While the 3-chambered module assembly possesses a large range of motion as a result of the resulting three DOF, a flatter and more compliant system interface surface would be required to conform to the human body to make the entire unit more wearable. Thus, simulation results are also presented for the proposed device comprised of 2-chamber modules which can be layered directly onto the vertebral portions of the back, so as to provide large forces and adequate conformity to the wearer's spinal column.

Representative of the five vertebral sections comprising the lumbar unit, five identical V-SPA modules were connected in series and tested in free displacement and blocked conditions. The corresponding simulation results are obtained are shown in Fig. 4.7. Table 4.3 contains the experimentally recorded bending angles, blocked forces and blocked moments at the tip of the actuator modules placed at each level of the device forming the assembly representative of the lumbar unit, when the modules are pressurized through a common vacuum supply. The peak Von Mises stress data values recorded at any point within each module, obtained through numerical simulations, are also tabulated in Table 4.3. When the modules are connected in series, the pressure drops along the length of the assembly. The pressure level experienced at each individual module in unit is reported in Table 4.3. In the simulations, the progressive vacuum pressure drop along the length of the assembly is represented with the help of progressively decreasing pressure loads at each module.

Location	Length (mm)	Vacuum Pressure (MPa)	Bending Angle (°)	Peak Mises Stress at any location (MPa)	Blocked Force at Tip (N)	Blocked Moment at Tip (N.mm)
First Module, L1	45	0.035	10	1.14	0.92	41.40
Second Module, L2	89	0.044	20	0.95	0.84	74.76
Third Module, L3	133	0.053	30	0.85	0.92	122.36
Fourth Module, L4	178	0.065	40	0.76	0.73	129.94
Fifth Module, L5	224	0.078	50	0.57	0.48	107.52

Table 4.3 – Design parameters for the V-SPA robotic assembly to enable spinal column assistance.

These results are then compared with FEA studies of the human spinal column. The pressurized V-SPA modules are capable of withstanding the peak Mises stresses within the range encountered by the spinal cord when subject to test compression forces in the ranges of 400-1200 N, as reported in [226], implying their suitability for handling high compressive forces. The modules are also suitable for replicating or assisting with the first three vertebrae units and intervertebral discs. Additional structural stiffness would be required to replicate the set of mechanical functionalities of the fourth and the fifth lumbar units of the vertebrae under compressive loading conditions, since for these units the stress withstanding capabilities need to be double that of the first three units. This can potentially be achieved with minor changes such as covering the foam core with a thicker coating of the molten Elastosil or another elastomer with a higher stiffness. It should also be noted that the torque reported in Table 4.3 is at the very tip of the actuator where the top plate attached to the actuator is otherwise in a completely free configuration. Larger levels of torque may be achieved in other module configurations, such as the blocked-blocked configuration, where both the top and the bottom end-plates attached to the modules are fixed. Also, the torque obtained at the tip alone can be increased easily by coating the outer layer of the foam with a stiffer material or using a stiffer foam to form the core of the actuator, while keeping the overall design concept

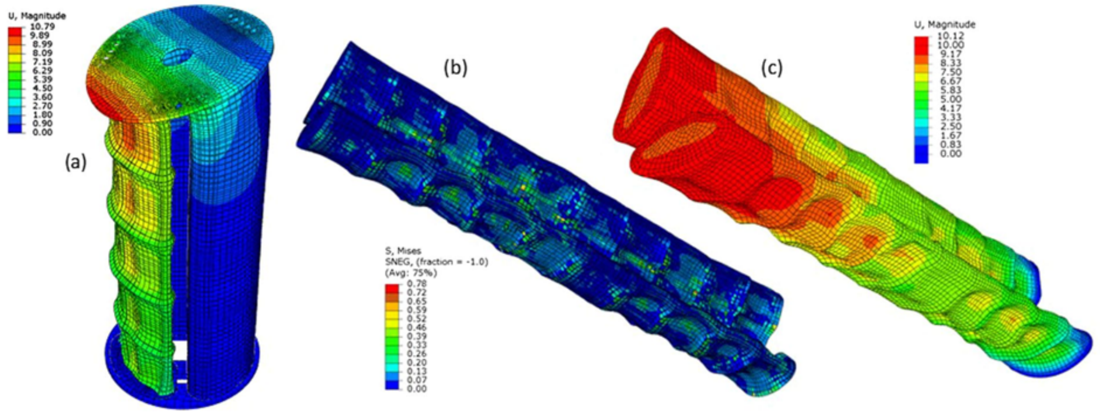

Figure 4.7 – (a) Simulation result for a three column V-SPA module assembly in free displacement condition. The bottom plate is kept fixed. (b) Simulation result for a two column wearable V-SPA assembly made of the same structural units (comprising the foam core and Elastosil skin) as the three column assembly, in blocked ends condition, and under a distributed pressure loading scheme. The stresses generated in the assembly are closely representative of the stresses generated in the spinal column under high compression loading. (c) Displacement profile for the device under the same conditions as in (b).

of the actuator the same.

In addition to adequate compression resistance, high flexion capability is desired at the same time. Due to the flexible foam core of the modules, the farthest V-SPA module can deliver a bending angle up to 50° in each DOF, as reported in Table 4.3. The lumbar spine is capable of generating a lateral bending motion of up to 35°. Thus, this range of motion is well within the capabilities of our proposed system. In forward movement, the lumbar spine can generate flexion of up to 75°. The presented five module V-SPA assembly can achieve up to 50° bending motion, but a larger range desired for forward flexion can be obtained by attaching more modules on top of the existing system. As observed from Table 4.3, the bending range of motion increases by 10° for each additional module attached. It is to be noted, however, that attaching more modules would potentially be at the expense of the compression withstanding capabilities of the system and that this would need to be carefully compensated for by increasing the stiffness of the system in strategic locations, so as to still deliver the desired range of motion.

4.3.6 Discussion

Foam-based actuator modules provide an ideal platform for spinal cord assistance due to their inherent high compression and flexion capabilities, required to replicate the majority of the functionalities of the lower human spinal column. This can be potentially achieved with the help of the novel actuator design and predictive modeling capabilities presented in this work. Since the modules are designed to operate primarily under compression with the help of vacuum so as to enable energy optimization and easier manufacturability, extension motion is not supported in the system presented here but this could be enabled in future prototypes by integrating conventional SPAs (that extend linearly under the action of pressurized air input) into the module assembly alongside the V-SPAs. It is also possible to integrate twisting motion capability into the same V-SPA based platform by winding the elastosil outer skin layer with alternate sets of fiber reinforcements, similar to the concept demonstrated with SPAs in [212].

The development of the assistive device proposed here is also motivated by the potential benefits of directly integrating actuation with other complimentary soft technologies. By utilizing a shared power supply, vacuum driven soft robots can also easily be enabled with stiffness tuning capabilities through layer or granular media “jamming”. Additionally, vacuum can be used to activate a variety of gripping or adhesive peripheral devices, including universal grippers for complex object manipulation and suction cups for inverted or inclined robot mobility. To enable these capabilities in addition to actuation on a common platform by conventional soft robotic standards would otherwise require separate power supply lines, with positive and negative pressures. Through the use of V-SPA and the corresponding fusion of independent pneumatic supply sub-systems, the complexity of multi-functional soft robots can be greatly reduced.

Although a detailed study on the interaction of the robotic module assembly proposed here with the human body and its implementation towards wearable assistance as well as portability is beyond the scope of the current work, the framework for such a device has been investigated through parallel studies. As with all wearable applications, key considerations for the development of a complete and operational device as proposed here include the careful selection of body attachment points, control strategies, and portability. For a lumbar region assistive device, it is envisioned that the active functional spinal elements would be integrated with a close-fitting vest or jacket-like base layer worn on the body, composed primarily of flexible fabrics and straps. To transfer forces and moments, specific areas of this device would be reinforced through stiff layers and braced against more prominent load carrying points on the body, particularly the hips and shoulders. For use outside of a fixed setting such as a workplace or clinic, the wearable spinal assistance apparatus may also be combined with a hip or back mounted portable computer control unit and pneumatic power supply, either capable of pressure generation or storage of a fixed charge of pressurized air. As this integration would increase the load on the body, the robotic lumbar support unit for assistance in these applications would require adequate scaling in design and performance to match and compensate for the additional load, and would be a subject of future study.

The actuator presented in this work is quite versatile due to its unique architecture and resulting motion capabilities. Furthermore, the actuators are easily manufactured and are scalable. The combined bending as well as linear motion achieved using the same actuator module platform, as shown in this work, holds promising potential for biomedical rehabilitation and wearable assistance not only for the discussed spinal column assistance but indeed for offering assistance in the form of artificial muscle pack/bundle- comprised soft exoskeletons for other body regions and limbs that may need motion assistance/restoration capabilities, such as the neck, hands or waist.

4.3.7 Conclusions

Despite the availability of an adequate description of the biomechanics of the human spinal column, there is a lack of an existing solution to help restore the lost mechanical strength and mobility of the lumbar unit and the spinal cord while still enabling the overall mobility and high flexibility for the patient in the event of spinal cord injury. Soft actuators integrated into soft robotic systems hold great potential for implementation in such biomedical rehabilitation applications since they are capable of delivering flexible and safe motion profiles at low costs. Existing designs for soft pneumatic actuators suffer from limitations in manufacturability. Furthermore, conventionally used soft actuators and incorporated materials do not enable multi-mode locomotion capabilities and yield limited DOF. This work presents a new approach to design, fabricate and assemble vacuum driven soft actuators, along with computational models for these actuators, for application towards a spine assistive wearable device. This work presents the results obtained for actuator modules which deliver bending and linear displacement profiles using the same platform, depending on the actuator loading conditions. The motion profiles achieved with the modules are shown to replicate the functionalities of the human lumbar unit in forward flexion and lateral flexion movements.

Accurate and experimentally validated computational models have been developed using FEM for the actuator modules as well as for the assembled device. The FEM models enable the simulation of the actuator and device performance under a variety of different loading scenarios and provide predictions on their capabilities prior to fabrication. The stress concentration regions indicated in the simulations provide useful information regarding the design of the system and its failure regime. The findings from the models have been tested through experimental characterizations, enabling an understanding of the key factors influencing the performance of the proposed system.

4.4 Part 3: Variable stiffness device for wearable joint support

In robotics, controlling the stiffness of the joints that contribute to the robots' degree of freedom dictates the adaptability, versatility and safety of the whole system. We can achieve variable stiffness or impedance in a robotic system purely by the control or by introducing new material or mechanisms to address cases that require innate safety through system compliancy. This chapter presents JammJoint, a compliant and flexible wearable robot which uses jamming of granular media to vary its stiffness. It consists of a silicone sleeve with hollow sections that are filled with cubic rubber granules and subjected to different levels of vacuum pressure. Unlike contemporary vacuum based actuators or systems, JammJoint is wearable, portable and autonomous: it uses a powerful miniature vacuum pump, a small battery and bluetooth enabled electronics. Experiments revolving around bending and torsional stiffness show that the system is able to achieve up to a fourfold increase in spring stiffness. Further measurements of individual variable stiffness structures indicate that for other modes of deformation, including simply supported bending or compression for alternative linear applications, higher changes in stiffness over a factor of seven are possible. These aspects make mobile jamming-based stiffness variation as wearable joint assistance promising for future applications such as rehabilitation after injuries and joint support in challenging working conditions.

4.5 Introduction

In the case where the energy efficiency is a crucial design feature of a robot or a robot is required to safely interact with humans, new compliant actuator designs are better suited than classical, stiff robot designs which typically excel in pick-and-place applications. Such compliant actuators have the ability to reduce impact forces, store and release energy through their compliance, and add safety. Thus, these actuators are the preferred choice in various applications such as rehabilitation, prostheses, manipulation, bio-inspired robotics and wearable robotics [243]. However, the compliance in the system often needs to be well-tuned to a specific task. If a robot is to perform a variety of tasks, a corresponding prescription of different compliance settings is required, giving rise to variable stiffness mechanisms.

The design of variable stiffness manipulators and joints is an active field and many prototypes have been developed in the past. Some of them use pretensioning of a spring to stiffen a joint [244]. For highly articulated robots (e.g. [245]), the stiffness usually cannot be changed unless a compliant element is integrated in the design [246]. This essentially represents a series elastic actuator (SEA) which has the ability to adjust its stiffness by changing the elastic element [247]. For continuum robots [248], tightening tendons [249] and Shape Memory Polymers (SMP) [36] are used to vary the stiffness. Magneto-rheological dampers can adjust their damping properties which in turn also has an effect on their spring stiffness (e.g. [250]). This can be also considered as a variable stiffness joint, although rather as a side effect.

Recently, the field of granular jamming is receiving more attention since on the one hand it can be used as a continuum robot and on the other hand it offers state switching, i.e. a transition from a soft to a hard state. In an open area, a granular medium (e.g. sand) behaves fluid-like (continuum) where the granules can freely slide around each other, thus being soft and adaptable. By confining the space around the granules, the inter-particle friction increases drastically, transforming the pack of granules into a solid-like state, resulting in a hard structure [251]. The material and shape of the granules has found to play a key role in the mechanical properties of a filled membrane. Likewise, the material of the membrane influences the behavior. A comparison between membrane materials and different types of granules can be found in e.g. [252] and the concept has been investigated for a number of applications such as grippers [253] [254], dampers [255] [256] and actuators [257] [258].

In [259], a proposition of a variable stiffness joint based on granular jamming can be found.

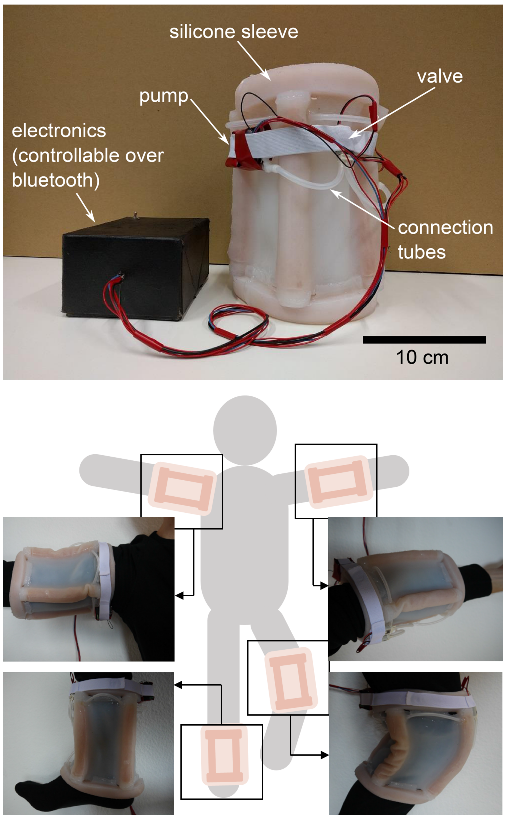

Figure 4.8 – The JammJoint device. Top: the electronic box on the left contains a microcontroller, bluetooth module and battery. A miniature pump, small-scale valves and connection tubes are mounted directly on the silicone sleeve. The sleeve with pump and valves weights 700 g, the electronic box is 250 g of which the battery weights 100 g. Bottom: application examples of the JammJoint device on different human joints.

The usual hard granules used for jamming are replaced with compliant granules. This resulted in a vacuum-dependent stiffness of the joint. In their experiments, a finger-like membrane filled with different types of compliant granules has been tested for its ability to increase the bending stiffness depending on the pressure level inside the membrane. Their idea was to fix an array of such columns around a joint and vary the stiffness by controlling the pressure in these columns. The joint can either be active (actuated by inflating the columns) or passive (the columns only vary their stiffness but do not provide actuation).

This concept was the inspiration for creating the proposed JammJoint which is designed to support and stabilize human joints during post-injury rehabilitation or for daily assistance of chronic biomechanical impairment. Similar to existing orthotic devices for this purpose, this device provides constraints to joint motion in selected directions to reduce unwanted loading and motion, while allowing free or low impedance motion in other directions for maintaining principle joint functionality. In general, most existing devices are only uni-axial, providing support and restriction in all but one direction, or they offer only fixed or manually adjustable levels of supporting stiffness. The JammJoint enables automated tuning of both the direction and magnitude of joint axis support by applying distributed, independently controlled variable stiffness elements in parallel with the biological joint. The variable stiffness is enabled by vacuum induced jamming of compliant granules, as previously investigated. The novelty of the design is that the structural part of the device doubles as the enclosing membrane to enable the jamming, which also directly facilitates its wearability around a joint. Additionally, in contrast to other applications of granular jamming where a large, powerful vacuum pump is required externally, JammJoint uses a miniature vacuum pump directly integrated in the device. This makes the system unique in the field of granular jamming as it is as a whole wearable and - adding a battery to power the electronics - portable and autonomous.

The main contributions of this part are:

- A soft, portable, and autonomous joint orthotic device prototype for rehabilitation or support.
- Demonstration of vacuum-induced granular media jamming to produce variable stiffness for wearable applications.
- Characterization and experimental testing of multiple variable stiffness component geometries and deformation modes.

4.6 Methods of joint stiffness variation

4.6.1 Variable Stiffness Designs

The design of variable stiffness manipulators and joints is an active field and many prototypes have been developed in the past. Some of them use pretensioning of a spring to stiffen a joint [ref, kamilo VSA]. For the continuum robots [ref], tightening tendons can also be used to vary the stiffness. For highly articulated robots [ref], the stiffness usually cannot be changed unless a compliant element is integrated in the design (ref Massimo). This essentially represents a series elastic actuators (SEA) which have the ability to adjust their stiffness by changing the elastic element (e.g. [ref]). Magneto-rheological dampers can adjust their damping properties which in turn also has an effect on their spring stiffness (e.g. [ref]) which can be also considered as a variable stiffness joint, although rather as a side effect.

4.6.2 The jamming of granular media

Recently, the field of granular jamming attracted more attention since on the one hand it can be used in a continuum robot and on the other hand variable stiffness is achievable. In an open area, a granular medium (e.g. sand) behaves fluid-like where the granules can freely slide around each other, thus being soft. By confining the space around the granules, the inter-particle friction increases drastically, transforming the pack of granules into a solid-like state, resulting in a hard structure. The material and shape of the granules has found to play a key role in the mechanical properties of a filled membrane. Likewise, the material of the membrane influences the behavior. A comparison between membrane materials and different types of granules can be found in e.g. [252] and the concept has been investigated for a number of applications such as grippers ([253], [254]) and dampers ([256], [260], [261], [262]). In [259], a proposition of a variable stiffness joint based on granular jamming can be found. A finger-like structure filled with different types of granules has been tested for its ability to increase the stiffness depending on the pressure level inside the structure. The idea was to fix an array of such columns around a joint and vary the stiffness by controlling the pressure in these columns. The joint can either be active (actuated by inflating the columns) or passive (the columns only vary their stiffness but do not provide actuation). This concept was the inspiration to create the proposed design of JammJoint. The novelty of the design is that the structural part of the device doubles as the enclosing membrane to enable the jamming. Additionally, in contrary to other applications of granular jamming where a large, powerful vacuum pump is required externally, JammJoint uses a miniature vacuum pump directly integrated in the device. This makes the system as a whole wearable and - adding a battery to power the electronics - portable and autonomous.

4.7 Description of the JammJoint device

The JammJoint device consists of several parts: the sleeve with its jammable columns and fixation rings, the pump together with the valves and tubes, the electronics controlling the system and the user interface on a bluetooth enabled smartphone. The complete device can be seen in Fig. 4.8 (except for the smartphone) and each separate part is described in detail below.

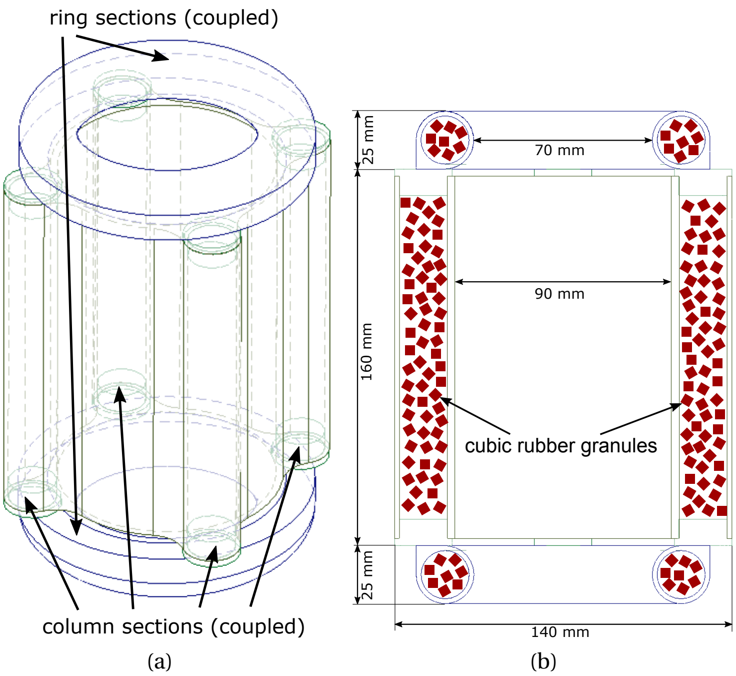

(a) (b)

Figure 4.9 – Silicone sleeve. Left: The complete sleeve. Two hollow rings (blue; coupled to share the same pressure) are attached at each end of a cylinder with four integrated, hollow columns (green; coupled to share the same pressure). Right: Cross-section of the sleeve. The hollow sections in the rings and columns are filled with cubic rubber granules.

4.7.1 Silicone sleeve

The sleeve is made out of highly stretchable silicone (Ecoflex 00-30) and consists of three parts. The main section is formed by a cylindrical shape with four evenly distributed hollow columns integrated along the cylinder and a total height of 210 mm. These columns are coupled together by tubes and share the same pressure. The diameter of the hollow cavity in the columns is 20 mm. On each side of the cylinder, hollow rings are attached, likewise with a hollow cavity of 20 mm and coupled together. Both rings and the hollow sections of the cylinder are filled with cubic rubber granules with a side length of 4 mm (Neukadur ProtoFlex HS 75). Schematics of the sleeve are depicted in Fig. 4.9. The figure displays the active controllable 2 DoF of the system: 2 rings and 4 columns are independently controlled.

4.7.2 Pump and valves

A miniature pump (Schwarzer SP 100 EC-DU, serial configuration) creates a vacuum up to -800 mbar versus atmospheric pressure inside the rings and columns (200 mbar absolute pressure). The airflow of the pump is controlled with three miniature solenoid valves (SMC S070C-SAG-32) and the level of vacuum is measured with a single pressure sensor (Honeywell 015PAAA5).

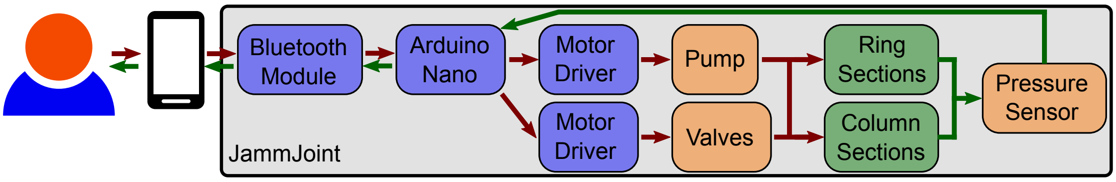

Figure 4.10 – Schematics of the full JammJoint system. A user (on the left) inputs the desired commands into a smartphone which communicates with a bluetooth module attached to the Arduino microcontroller. It controls the pump and valves over motor drivers, changing the pressure level inside the ring and column sections. The pressure is measured by a sensor and fed back to the microcontroller which also shares this information with the user over the smartphone interface.

4.7.3 Electronics and bluetooth interface

A microcontroller (Arduino Nano V3.0) controlls the pump, valves and pressure sensor. Additionally, a bluetooth module (JY-MCU) is attached to the microcontroller, allowing a bluetooth serial communication. The electronics are powered by a 12 V LiPo battery (Conrad energy BEC 11.1V 1300mAh 12C). A bluetooth enabled smartphone can establish a connection to the bluetooth module. For this work, the free app BlueTerm2 has been used. The device is controlled with a few simple commands: “r” and “c” direct the airflow either to the rings or columns, the numbers 1-8 are used to set the pressure in the respective section from 900 mbar to 200 mbar absolute pressure and the number 0 sets a section to atmospheric pressure. The complete system can be seen in Fig. 4.10 where the smartphone is the only external hardware; JammJoint is fully autonomous otherwise.

4.8 Experiments

4.8.1 Full-device characterization

The objective of the experimental measurement of the complete device is to obtain the range of its stiffness variability. Since the device is designed for the use on human joints, these joints are approximated by balljoints for the purpose of this investigation. A balljoint has 3 degrees of freedom: 2 rotations around the joint in 2 perpendicular planes (further called “bending”) and 1 rotation around the main axis of the joint (further called “torsion”). Whereas the torsion movement is symmetric in case of the device, bending is directional, depending on the orientation of the bending plane to the columns. For these experiments, only bending where the bending plane is in between two columns is analyzed (see Fig. 4.11). This is expected to more evenly distribute the bending torques as each column is engaged in a similar way, to simplify both quantitative and qualitative results. The case where the bending axis coincides with a column is not studied as one column would receive a large compressive force and one

---

available for Android in Google Play store column a large strain respectively compared to the columns located outside the bending plane. This type of loading is likely to yield unique stiffness characteristics, including enhanced effects of buckling, however this is considered to be only important for a full quantification of the device stiffness, beyond the intention of this study.

It is important to note that in a balljoint, all possible movements can be superposed. This is also achievable with the device. The two rings only serve as the way of fixing the device on the respective joint through passive adaptation and solidifying. Only the level of vacuum in the columns determines the final stiffness, therefore coupling both bending and torsional stiffness. The experimental procedure for the experiments is defined as follows: (i) fit the device around the joint, (ii) pair the JammJoint with a smartphone, (iii) solidify the rings by setting the pressure inside the rings to the lowest value (200 mbar absolute pressure), (iv) increase the level of vacuum inside the columns in steps of 100 mbar from atmospheric pressure (approx. 1000 mbar absolute pressure) to 200 mbar absolute pressure by selecting the desired pressure on the smartphone and (v) measure the torque for different angle of rotations. Fig. 4.11 shows the experimental setup. A camera takes pictures of the device and a force meter. Two colored dots allow the calculation of the rotation angle through image analysis and the force meter provides the applied torque, given the length of the lever.

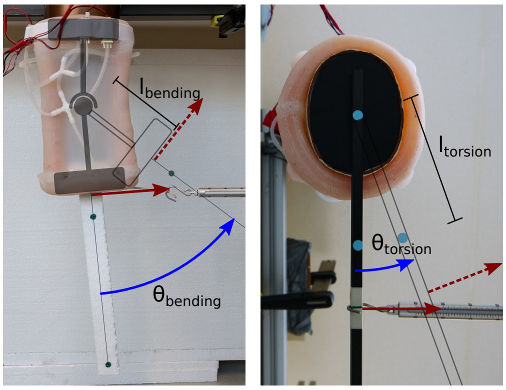

Figure 4.11 – Experimental setups. The red arrows show the direction of the force at resting position; the silhouette and the red dashed arrows show the orientation of the lever and the direction of the force at the rotation angle $\theta_{bending/torsion}$ (blue arrow). Left: Side view of the bending setup. The mechanics of the balljoint is overlaid in gray. Right: Bottom view of the torsion setup.

Bending torque

For measuring the bending torque, the device is put over a balljoint where torsion is restricted. The two rings are both fit over circular disks, each with the height of the ring (25 mm). The joint is located exactly in the middle of the device, resulting in a lever length $l_{bending}$ of 105 mm. The upper part of the joint is fixed to a table. Each configuration is tested 3 times. A force is applied perpendicular to the lower part of the joint until the rotation angle reaches approximately 45 deg. The force then is slowly released back to zero to also measure a potential hysteresis in the rotation angle, caused by the displacement of granules. This leads to a different resting angle because the displacement of granules generates plastic deformation of the device. After every test, the columns therefore are set to atmospheric pressure to allow to manually "reset" the position of the granules inside the columns. Although this is only considering the most ideal loading case and does not represent real operation conditions where a reset would not take place (and thus hysteresis effects would occur), preventing the rearrangement of granules will be further discussed in section 4.10. Effects caused by the viscoelacity of the silicone have been neglected as the response time of silicone is roughly between 50 ms and 200 ms [263] which is assumed to be one order of magnitude faster than the expected movement of a human joint. The results of this series are normalized to the initial resting angle of the respective test (meaning that initially, zero applied force is zero rotation angle).

Torsion torque

For measuring the torsion torque, the balljoint is removed, keeping only the upper circular disk. To avoid slipping, the upper part of the device is additionally secured and the lower circular disk is replaced by an ellipsoid. This change is assumed to have only a minor influence on the measurements. The ellipsoid has a lever attached (lever length $l_{torsion}$ is 150 mm) where the force is applied in a rotational manner, twisting the device. The number of trials (3) and measurement methods are kept the same as for the previous experiments.

4.8.2 Sub-component characterization

Additionally, experimental measurements are taken to individually characterize the change in stiffness of the sub-components of the wearable device, namely the rings, and the columns. A three point bending setup is used to apply a linear force at the center of a single column segment simply supported at the ends, while the applied force is recorded through a displacement range and different pressures. While the force and displacement measurements can be used to estimate the true angular bending stiffness of a column following analytic beam bending models, only the linear transverse stiffness of the column as directly tested is reported to illustrate the qualitative effect of pressure variation on column stiffness. Similarly to the column measurements, the stiffness profile of a single ring segment is measured across a range of displacements and pressures. The compressive force applied across the ring is used to calculate the overall radial stiffness of the structure. The setup for each characterization test can be seen in Fig. 4.12.

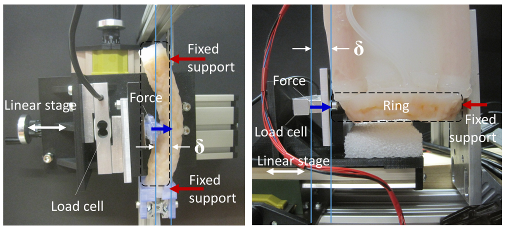

Figure 4.12 – Sub-component experimental characterization. A 3-point bending setup is used on the left to apply a force at the centerpoint of a single variable stiffness column. A single-axis load cell records the force applied to the column. On the right, the same apparatus is reconfigured to apply a force to the variable stiffness ring segment. In both experiments a linear stage is manually advanced and the deflection, δ, is recorded at 2 millimeter intervals from 0-20 mm, equal to the width or diameter of a single column.

4.9 Results and Discussion

4.9.1 JammJoint performance in bending

Fig. 4.13a shows the results of the experiments performed in the bending series. Each curve is calculated with the interpolated average of the three trials per vacuum level and for each curve, the stretching phase (solid), relaxation phase (gray) and the maximum torque (red cross) is indicated. From these curves, the increase of the torque needed for a certain rotation angle is clearly visible. However, especially in higher vacuum, a buckling of the columns under compression can be observed, leading to a decrease of torque with larger angles. The buckling also plastically deforms the columns by rearranging the position of granules which changes the loading conditions for the relaxation phase. This can be seen from the increase in resting angles after relaxation where a hysteresis of several degrees starts to form. As the resting angle gets shifted, the respective torque at certain deflection values is lower in the relaxation phase compared to the stretching phase. Resetting the granules after each trial made sure that this hysteresis would not transfer into the next trial.

4.9.2 JammJoint performance in torsion

In Fig. 4.13b, the results of the torsion experiments are shown. Similar to Fig. 4.13a, the interpolated average is shown for stretching (solid) and relaxation phase (gray) together with the maximum torque (red crosses). The increase of the required torque is not as pronounced as in case of bending but nevertheless observable. In contrast to the previous experiments, no buckling occurs and a hysteresis in resting angles is less noticeable.

4.9.3 Sub-components of JammJoint

The results from characterization of a single column at different pressures is shown in Fig. 4.13c. Each curve shown represents the average of three separate trials taken for each pressure.

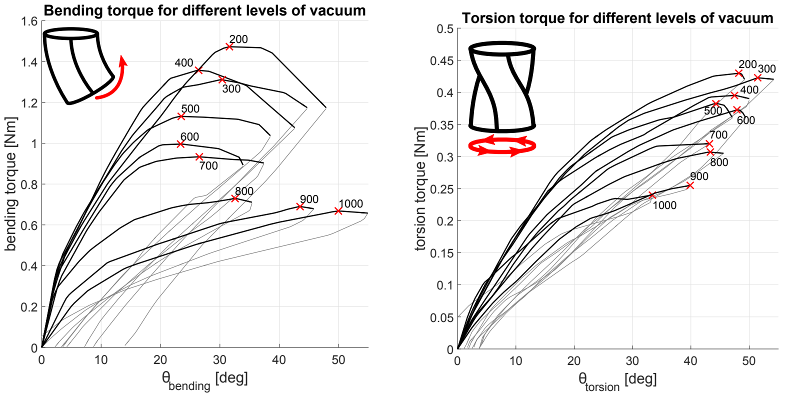

(a) Bending angle versus bending torque; buckling and hysteresis effect observable.

(b) Torsion angle versus torsion torque.

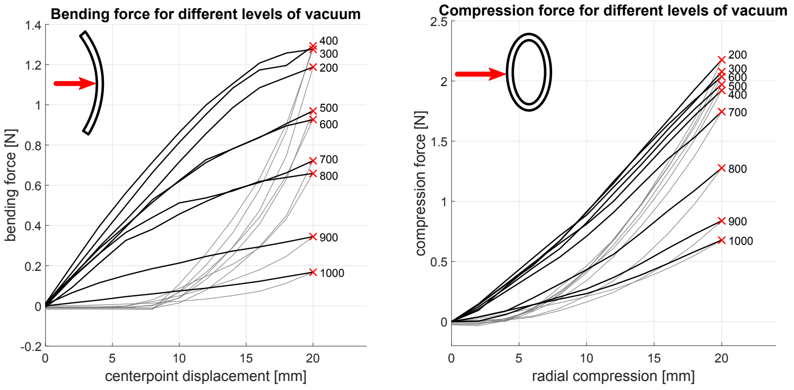

(c) Force versus column deflection; hysteresis effect observable.

(d) Force versus ring deflection

Figure 4.13 – Characterization experiments. Red cross: maximum torque per curve with the level of vacuum in mbar; Solid: measurements during stretching; Gray: measurements during relaxation. In all experiments, increasing the level of vacuum results in an increased reaction torque/force.

The curves show a nearly linear stiffness relationship during stretching with a maximum force at the maximum deflection. There is also a large hysteresis observed resulting from plastic deformation at high vacuum pressures.

The stiffness profile generated from the ring sub-component measurements can be seen in Fig. 4.13d. The radial stiffness of the ring can be seen to be very nearly linear, with minimal plastic deformation at any pressure, and hence minimal hysteresis upon unloading.

4.9.4 Change of spring stiffness

The results of Fig. 4.13a and 4.13b are summarized in Fig. 4.14 where the change of the respective spring stiffness is shown. For each curve in the previous experiments, the maxima (red crosses) are connected to the origin with a straight line. The slope of each line can be regarded as a hypothetical linear spring stiffness with $D_{\text{bending/torsion}} = \Delta\text{torque}/\Delta\text{angle}$ where Δtorque is the maximal torque in Nm, Δangle the angle in deg corresponding to the maximal torque and $D_{\text{bending/torsion}}$ the spring stiffness coefficient in Nm/deg. Fig. 4.14 shows these spring stiffnesses for bending and torsion for the different levels of vacuum with the error bars calculated from the standard deviation of the interpolated average at the maxima. For bending, the increase in the spring stiffness is significant: the experiments show an almost fourfold increase (from 0.0134 Nm/deg to 0.0514 Nm/deg) with the maximum stiffness value being reached at 400 mbar. For torsion, the difference is much smaller with an increase of torsional spring stiffness of 40% (from 0.0064 Nm/deg to 0.0089 Nm/deg). Even though these results are obtained by simple linear approximations of the nonlinear spring stiffness coefficients where the true “instantaneous” stiffness is angle-dependent, the goal of this study was not to precisely define the stiffness (possibly with the help of models) but rather to give an overview of what qualitative overall stiffness change the system can achieve.

Likewise, the results of Fig. 4.13c and Fig. 4.13d are summarized in Fig. 4.15. For each curve in the respective experiments, the maxima (red crosses) are again connected to the origin with a straight line. The slope of each line is obtained as $D_{\text{column/ring}} = \Delta\text{force}/\Delta\text{deflection}$ where Δforce is the maximal force in N, Δdeflection the distance in mm corresponding to the maximal force and $D_{\text{column/ring}}$ the spring stiffness coefficient in N/mm. Error bars are calculated from the standard deviation of three measurements taken at each pressure level. Both trends for the column and ring show a significant change in stiffness for different pressures. The ring stiffness increases more than threefold from 0.0339 to 0.1088 N/mm following a pressure change from 1000 to 200 mbar. Over the same pressure range, the column stiffness changes from 0.0084 to 0.0646 N/mm; the maximum stiffness value is again observed at an intermediate pressure of 400 mbar. The maximum range indicates that an increase of stiffness over a factor of 7 is possible.

Ideally, these changes in spring stiffness are linked to a change in intrinsic material properties. In the case of jamming, the applied level of pressure suggests that the pack of granules changes its Young’s modulus which is closely related to the overall spring behavior. However,

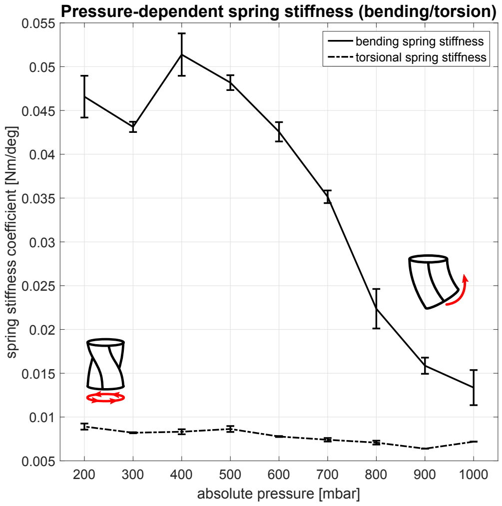

Figure 4.14 – Spring stiffness increase depending on the level of vacuum for bending and torsion. The values of the curves are calculated by approximating the spring behavior of each experiment with a linear spring stiffness coefficient from the origin to the maximal torque from Fig. 4.13a and Fig. 4.13b.

modeling the effect of jamming on the Young's modulus has not been investigated as such characterizations usually require unidirectional loading of the substrate (typically compression and tension). The performed experiments were not specifically designed for such cases. Therefore, instead of a change in intrinsic material properties, only the simple comparison of these changes to a linear spring stiffness are presented here. It is subject of ongoing research to model inter-particle reactions and define, which experiments qualify for material property characterizations in different loading scenarios.

4.9.5 Additional modes

Firstly, besides a coupled bending-torsion-mode, an additional bending-only mode is available. This can be achieved by fitting one ring around the base of a joint and only loosely fitting the second ring (by enlarging it to a slightly bigger diameter than the other joint base). This results in the device being held in place by the fit ring but leaving the torsion rotation of the joint unrestricted. The bending stiffness still can be adjusted in the same manner as in the normal mode.

Secondly, the initial orientation of the device can be freely chosen and does not need to be known beforehand. For the purpose of the performed experiments, the initial orientation was chosen to be straight. However, with the rings solidified but the columns under atmospheric pressure, the joint can easily be moved into any desired orientation where it can be fixed by solidifying the columns. This process is reversible and can be repeated whenever required.

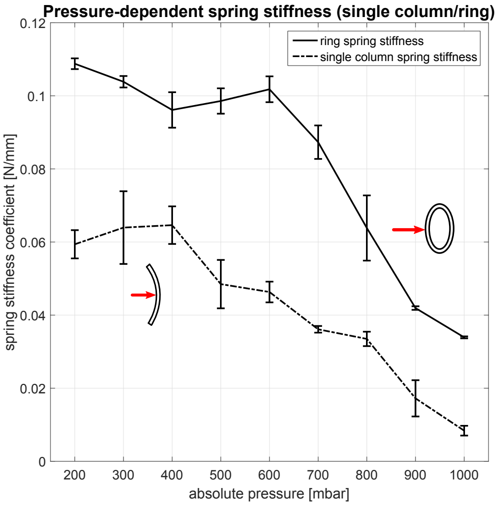

Figure 4.15 – Spring stiffness increase depending on the level of vacuum for a single column and ring sub-component. The values of the curves are calculated by approximating the spring behavior of each experiment with a linear spring stiffness coefficient from the origin to the maximal force from Fig. 4.13c and Fig. 4.13d.

4.9.6 Passive adaptability, safety and operation time

The soft silicone of the sleeve and the nature of the granules allow the JammJoint to passively adapt to the wearers anatomy. Moreover, the rings and cylinder can easily be stretched to twice their circumference, making the device applicable on different joints. This also counts for joint shapes which are not circular where the rings conform around. Once fit, after solidifying the rings to attach the device to the joint, the rings keep their conformed shape without further power. Additionally, thanks to the soft silicone, the solidified rings and columns still possess a certain softness, allowing a certain deformation of the joint e.g. through moving muscles or blood flow. The examples in Fig. 4.8 depict the application of the device on elbow, shoulder, ankle and knee joint.

Since the device - except the miniature pump and valves - is entirely made out of soft materials, the risk of injury for the user is greatly diminished. Moreover, since the functionality of the device relies on successfully maintaining a vacuum, puncturing any part of the silicone sleeve simply results in a slow inflation of the section to atmospheric pressure. The device therefore loses its functionality without harming a potential user (as opposing to e.g. a technology based on inflation where puncturing a membrane might result in explosion of the section). These properties are promising for the usage of such a device as joint support.

Concerning the operation time, most of the battery power is consumed when the pump is evacuating. Even though the evacuation time is somewhat slow (roughly 20 seconds; see video for details) as a result of the usage of a miniature vacuum pump with low airflow, it has been assumed that the application of a joint assistance does not require a fast change in stiffness. In contrary, the advantage of the pump to be powerful but portable was regarded as being more important. It is important to notice that a set pressure level in the sections is held without power by the off-position of the valves (assuming the sections are airtight; the current device inflates at around 25 mbar per minute due to sealing imperfections). Thus, the operation time depends almost only on the number of evacuation cycles the pump is able to perform with one battery charge. All testing and experiments were performed with one single charge of the used LiPo-battery, performing roughly 150 evacuation cycles without completely discharging the battery.

4.10 Conclusion

In this chapter, a joint assistance device based on the jamming of granular media is presented. Cubic rubber granules are filled into two separate hollow sections of a silicone sleeve, rings and columns. These sections can independently be evacuated to a desired level of vacuum by a powerful miniature vacuum pump directly integrated in the device. A small LiPo-battery powers the electronics and the microcontroller with an attached bluetooth module. This enables the system to communicate with e.g. a bluetooth enabled smartphone, making it portable and autonomous.

The level of vacuum inside the sections varies the stiffness property of the device, measured for two different modes: bending stiffness and torsional stiffness. Decreasing the pressure from 1000 mbar to 200 mbar absolute pressure results in an almost fourfold increase in bending stiffness and a 40% increase in torsional stiffness. Additionally, besides the normal mode of a coupled bending-torsional stiffness change, a bending-only mode is available. Individually, the subsections of the wearable device are shown to have high versatility with a large range of stiffness adjustment available (up to seven times stiffer) for alternate deformation modes, including simply supported bending and radial compression. Further, given by the method of jamming granular media, the device can be moved in any orientation when the sections are under atmospheric pressure and fixed in this orientation by solidifying (evacuating) the sections. The pressure level then can be kept without additional power. At last, the highly stretchable silicone in combination with rubber granules creates a safe to use, adaptable, versatile device which can be applied on different joint sizes and shapes.

For future work, different directions could be followed. The mechanical design of the sleeve could be changed to include more columns to make their distribution more uniform for bending. If required, the columns could be separated from each other to control the vacuum in each column independently (contrary to the current design where all the columns are connected together to share the same pressure). Although this would require more valves, the independent control of multiple columns in parallel would also increase the robustness and reliability of the total system [234]. Designing custom electronics would allow for a full integration into the sleeve, eliminating the need for additional cables. A different design to increase the torsional stiffness could be tested. Alternate mechanical configurations with different combinations of sub-component elements (columns and rings) might also be used to create entirely new forms of a variable stiffness wearable device. Further, the materials used for the sleeve and granules can be subject to future studies. While the soft silicone enables the jamming of the granules, it also adds much softness to the system even when the sections are under the highest vacuum. If necessary, a harder material or a different combination of materials could further increase the overall stiffness and the achievable change in both bending and torsional stiffness. Although it has not been tested here, the method of jamming does not interfere with actuation through inflation. Thus, with the integration of additional valves only, the same system can be used to provide active actuation. The design and choice of materials might change if inflation is also considered. One issue in the current design is that if the columns are inflated, the granules collect on the bottom of the enlarged cavity, making further jamming impossible which relies on uniformly distributed granules. A way of preventing such an undesirable rearrangement in the enlarged volume has to be developed. This could also enable automatic resetting of the granules (e.g. under atmospheric pressure) to diminish hysteresis effects, as described in section 4.8. Lastly, further experiments are needed to provide the basis to model changes in intrinsic material properties such as Young’s modulus.

4.11 Part 4: ’Pneumagami’ modules toward wearable ’Third Arm’ for task assistance

This part presents a new modular robotic platform for enabling reconfigurable, actively controlled, high-DoF systems with compact form factor. The robotic modules exploit advantages of origami-inspired construction methods and materials, and soft pneumatic actuators to achieve an actuator embedded, parallel kinematic mechanism with three independently controlled “waterbomb” base legs. The multi-material, layer-fabricated body of the modules features selectively compliant flexure hinge elements between rigid panels which define the module as a kinematic 6R spherical joint. The precision layer-fabrication technique is also used to form embedded distribution channels within the module base to connect actuators to on-board control hardware. A decentralized control architecture is applied by integrating each module with small scale solenoid valves, communication electronics, and sensors. This design approach enables a single pneumatic supply line to be shared between modules, while still allowing independent control of each leg joint, driven by soft, inflatable pouch actuators. A passive pneumatic relay is also designed and incorporated in each module to leverage the coupled, inverted inflation and exhaust states between antagonistic actuator pairs allowing both to be controlled by a single solenoid valve. A prototype module is presented as the first demonstration of integrated modular origami and SPA design, or pneumagami, which allows predefined kinematic structural mechanisms to locally and actively prescribe specific motions, not just through passive compliance, to dictate task space and motion. The design strategy facilitates the composition of lightweight, high strength robotic structures with many DoF for benefits in various fields such as wearable robotics.

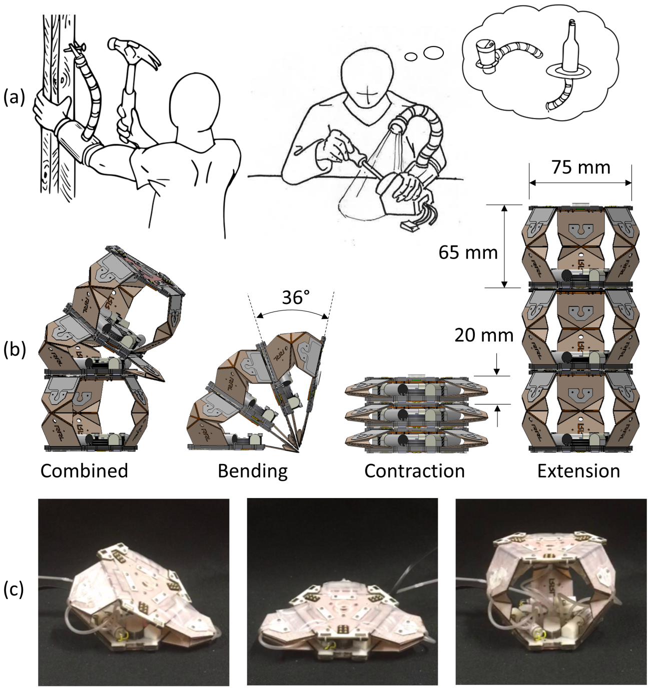

Figure 4.16 – A Pneumagmi-based modular robotic system. Lightweight, high-strength, and compact pneumagami modules hold potential to enable new forms of wearable robotic devices for general task assistance in daily activities (a). With three independently controlled DoF and high RoM in both angular bending and linear motion (b), the modules can be reconfigured to suit a variety of objectives. A physical prototype module is implemented and shown in (c).

4.12 Introduction

New methods, materials, and manufacturing techniques are recently redefining the field of robotics with regard not only to expanding the diversity of practical applications, but also toward improving the capabilities of new systems. In particular, these new developments complement the demands of a quickly growing area of interest within the robotics community, in wearable devices. Prior work has demonstrated the potential for wearable robotics, through applications targeting rehabilitation, augmentation, and assistive support [264, 265, 55, 266, 221]. Although some of these provide ready solutions to a narrow scope of problems confined to fixed settings due to their reliance on tethers for off-board power and control, the extended prospect of such technology is its application to mobile or daily use. In order to achieve more practical systems which can be applied to more general Activities of Daily Living (ADLs) in the real world, the challenges of human-robot interaction and wearability for various applications motivates the design of new systems which are concurrently portable, safe, reconfigurable, and with high-DoF to meet diverse needs.

In recent years, a new type of wearable device has been explored that can be operated as an additional (third) arm or appendage to enhance the manipulation capabilities and dexterity of a human user by providing task assistance. Supernumerary Robotic Limbs [11], composed of a backpack and two 3-DoF arms, have been developed to aid a wearer in tasks that require stabilization and positioning. Similar in terms of scale and weight, a 3-DoF wearable robotic forearm has also been proposed for the needs of construction workers [10]. Soft robotic systems offer a convenient alternative to these in terms of lower weight and smaller scale, as well as implicit safety for human-robot interactive related tasks. The common form of soft robotic solutions is a monolithic body [267, 268, 269, 270, 271, 272, 273] however Soft Poly Limbs are proposed as a system of exchangeable limbs which can be mounted on different parts of the human according to various tasks [9].

To achieve a similar type of wearable assistive device with high mobility, but significantly lower size and weight for less demanding tasks, an origami-inspired robotics design approach presents advantages over previous device design and fabrication methods. Utilizing nominally 2D components to achieve complex, active and passive 3D structures [274, 275], this design framework naturally affords compact physical form factors in robotics, yielding systems which are lightweight, scalable, easy to store and transport, and conducive to rapid, low-cost, mass manufacturing, and even self-assembly [276, 277, 278, 279]. Leveraging these benefits, origami design methods have thereby been employed to create various types of mobile robots [280, 281, 282, 283, 284], deployable structures [285], biomedical devices [286], manipulators, [287, 288, 289], and other mechanisms [290]. The range and extensibility in terms of performance and DoFs across these examples highlight the versatility enabled by the origami design approach, which represents a promising strategy for implementing new wearable and human-interactive devices.

The robotic origami concept is adaptable to producing robots from many different materials, for both structural and active elements, and from a variety of fabrication techniques [291]. Passive kinematic structures are formed by combining rigid body elements with compliant hinge joints (similar to the many folds utilized in traditional paper origami) to create reconfigurable, virtually soft, yet strong assemblies capable of supporting loads. The generally planar components can be cut from thin sheet materials such as cardboard, glass-fiber composites, or plastics, often using a CNC laser. Alternately, origami designs can be easily implemented by 3D printing [292, 293]. Flexible hinge joint elements between rigid body components can either be combined as a separate layer bonded to the planar (commonly Kapton polyimide) , unfolded form of the origami structure, or directly through 3D printing with soft materials.

Similar to the assembly of different passive layers in robotic origami, actuator elements can also be directly incorporated in the layered structures to provide joint motion and stiffening [294], and to creat fully integrated robotic origami structures [295]. This previous work has successfully demonstrated Shape Memory Alloy (SMA) and Shape Memory Polymer (SMP) layers in integrated robotic origami designs, although a variety of other actuation techniques have also been investigated, including the use of anisotropic heating [296], fluid absorption [297], dielectric elastomers [298], piezoelectric actuators [299], and magnetics [300]. While these embedded actuator solutions provide robotic origami structures with controllable shape changing abilities, the practical utility of such systems is generally restricted due to their limited force and power output. Soft pneumatic actuators (SPAs) offer both a high power-to-weight ratio as well as an implicitly safe alternative source of actuation through the use of flexible and compliant materials [301]. Moreover, due to their generally simple construction, SPAs can be customized by design and operation at various supply pressures to match the scale of assistance needed for wearable assistive devices [302]. The integration of pneumatic systems and SPAs with origami-inspired structures, however, remains a significant challenge as they are generally non-compatible with the style of layer manufacturing employed. One promising exception to this is the pouch type SPA, which is layer fabricated from plastic sheets and has been shown to be directly compatible with origami topology [303]. Nevertheless, a complex, high-DoF robotic system comprised of origami-based structures and powered by SPAs has not been shown as a consequence of other open challenges such as the need for embedded pneumatic power distribution and decentralized control.

Origami based robotic continuum structures have been developed in previous work which utilize tendon cable transmission for actuation. One such example employs waterbomb pattern origami structures to create a continuum robot morphology driven by three tendon cables [287]. The cable actuation method complicates the control of a multi-DoF arm, however, and limits the workspace as every module and DoF is mechanically coupled together. Other work has addressed these limitations by incorporating truly modular units that can be serially combined to form a robotic arm structure, with onboard DC motors which drive internal cables to allow independent control of each of the modules 3-DoFs [304]. These modules use a different, Yoshimura origami pattern structure which also allows bending and contraction or extension RoM. In both examples of prior work, however, neither utilize the origami-inspired structure for more than kinematic constraint to afford torsional rigidity in resistance to bending in unwanted directions or to provide restoration force to oppose contractile cable tension. This latter attribute means that the modules or complete robotic assembly can only be actuated in one direction (cable tension), while only an elastic restoration force is available to act against antagonistic loads. Furthermore, while these designs utilize 2D fabrication techniques to produce the origami inspired structural elements, these are incorporated and assembled with other components following inherently traditional methods.

Following a modular design approach leveraging benefits and design methods of previously described modular pneumatic [180], and modular origami [305] systems, we present a novel platform which consists of a multi-functional origami-inspired structure, low-profile soft pneumatic pouch actuators, and embedded networking hardware for enabling reconfigurable, actively controlled, high-DoF soft systems with a compact form factor.

This pneumatically powered origami, or pneumagami, module is constructed from a 3-DoF waterbomb pattern which constrains the kinematic workspace to three independent joint angles for controlling the module platform angle and linear displacement. With a pair of antagonistic pouch SPAs controlling each of these joints, the module is fully controllable. To enable manufacturing ease and scalability, the module as a whole is principally designed to allow complete fabrication and assembly using 2D and layer manufacturing techniques, with minimal added components. Consequently, the presented module employs a dual-function main body structure which contains embedded air distribution channels to serve as an active manifold, connecting all onboard pneumatic components and supply lines. Additionally a layer-fabricated pneumatic relay element is designed and implemented to simplify the control of antagonistic actuators and minimize weight. The multifunctional use of the origami body structure and integration of other functional components amenable to 2D manufacturing techniques are novel and useful strategies for realizing compact and lightweight multi-DoF, pneumatically powered modules.

The main contributions of this section are:

- First example of the design and fabrication of an integrated robotic module that combines both origami-inspired structures and pneumatic actuation (pneumagami).
- Implementation and characterization of the multi-DoF pneumagami module and a novel differential pressure blow-off relay (DBR) valve for underactuated control.
- Established a framework for future research in developing compact, customizable wearable devices for task assistance.

4.13 Design

A pneumagami module consists of an origami-inspired structure, soft pneumatic pouch actuators (pouch SPAs), and embedded power and control components. The onboard hardware allows multiple modules to be connected in series with independent control over every powered degree of freedom (three antagonistic joint pairs, with two actuators each), while allowing only single lines to be used for pneumatic power distribution, forward control signals, and IMU sensor feedback between the modules. This efficient architecture enables the assembly of large networks of modules, including a linear arrangement to form a continuum style robotic manipulator arm.

4.13.1 Functional origami-based integrated structure

A preliminary objective of the module structure is to achieve 3-DoF spherical RoM with high performance in a compact, low-mass form factor, as one potential purpose for the modules is for use in portable robotic systems. These requirements motivate the use of origami inspired design, materials, and fabrication methods for the frame. Following this approach, a classical origami pattern known as the waterbomb is used to create a spherical joint with from 2D rigid plate structures connected by 1 DoF hinge joints in place of folds. A waterbomb-based parallel kinematic design for the module is employed to enable 3DoF motion of a moving upper platform. When produced using sufficiently thin body plates and sufficiently wide flexure-based joint hinges, this structure furthermore facilitates collapsibility, allowing the

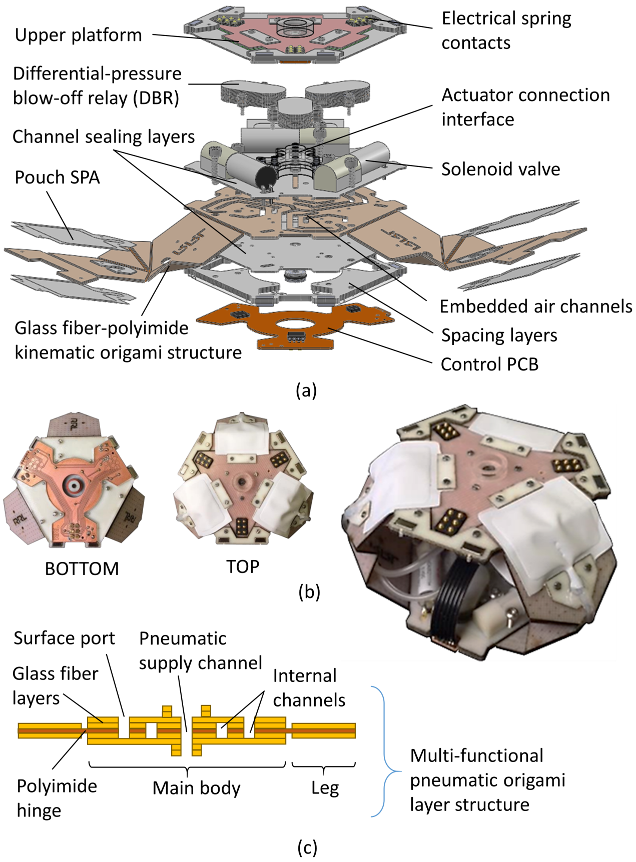

Figure 4.17 – An exploded view of the pneumagami module CAD model is shown in (a), while the actual prototype in the fully assembled and complete state can be seen in (b). The layer-fabricated structure of the module serves dual purposes, as both parallel kinematic spherical linkage and a functional supply pressure distribution manifold used to connect on-board pneumatic components (c).

module to be folded down to a predominantly flat shape roughly 11 mm in thickness from a fully extended height of 50 mm.

The structure of a module is comprised of three main components: a lower base section, an upper moving platform, and three waterbomb pattern linkages (legs). The complete module frame is formed by connecting the lower and upper platforms by the legs. This parallel kinematic arrangement allows the upper platform to move relative to the lower platform through a spherical workspace, as well in linear displacement.

The kinematic origami frame serves several important purposes. The primary role is to simply join the mobile segments of the module through linkages which allow high RoM as desired, and limited mobility otherwise. The parallel configuration of the waterbomb legs produces many coupled degrees of freedom, which provides that the angular position and location of the upper platform is geometrically defined by only three independent variables. This allows the structure to be physically reconfigured by controlling the actuation of only three joints to set the platform to a new position and orientation. In this manner, the frame consequently acts as a functional component, as part of the mechanical work transmission from actuators to final output.

The origami frame also plays an important role in increasing the overall stiffness of the multi-DoF module. Although the structure features three independent degrees of freedom, it's mobility is not infinite. One significant constraint is preserved through the use of the hinge-jointed waterbomb linkages, which acts to restrict any torsional motion on the axis normal to either platform. This results in a structure which is fully controllable in all its allowable DoF, and rigid in all others to the limit of its component material stiffness. In a robotic arm configuration, with a large serial continuum assembly of modules, this torsion constraint acts to resist passive "off-axis" deformations. In typical soft robotic systems which rely on compliant materials for their primary structure and actuation, such uncontrolled deformations reduce the stiffness of the overall system and yield to bending in cantilevered or overhanging orientations (such as reaching tasks).

The origami frame is fabricated in two main parts, with the majority and largest part formed by a single, monolithic base structure which is folded into its final shape. This base structure (seen in Fig. 4.17), contains the lower base platform connected to each of the three legs which are fabricated together from 2D glass fiber sheets and kapton polymide layers. The central base platform not only joins the legs together, but like the kinematic mechanism formed by the legs, it also serves additional multipurpose function. While the rigid components of the legs are formed by solid plates consisting of a central kapton hinge layer sandwiched between two glass fiber layers (3 layers total), the base structure is extended by an additional two glass fiber layers above and below the layers common to the leg structures. The common layers in the base structure are then manufactured with open channels which are sealed by the outer glass fiber layers to form an embedded network within the platform for pneumatic power distribution. The topside layer (on the inside of the complete module) contains port

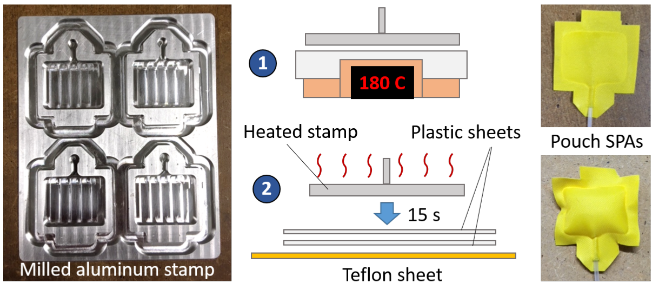

Figure 4.18 – Pouch SPA fabrication. Pouch SPAs used to drive the module legs are fabricated from plastic sheets, sealed by heat using a machined aluminum stamp. The resulting actuators are high strength, being driven at up to 60 kPa pressure, lightweight, and extremely thin and flexible.

holes for interfacing control valves, relays, supply lines, and actuators with the embedded layer-manufactured distribution manifold.

4.13.2 Pouch actuators

To actively change configuration, the modules are powered by soft, nominally flat, low-profile pneumatic pouch actuators which are form compatible (nominally 2D) with the origami structural frame. Each actuator is fabricated from polyethelene or PEVA plastic sheets material, heat and pressure bonded together with a custom made stamp. The CNC machined aluminum stamp is heated on a hot plate to 180 C, and then transferred and pressed by hand onto two plastic sheets placed on a teflon surface for 15 seconds. The extruded stamp makes contact with the sheets which fuse to form a sealed countour around an unsealed inner chamber. The inner volume of the actuator is inflated through an inlet neck where small pneumatic supply tubing can be inserted. The fabrication process and photos of the aluminum stamp and produced SPAs can be seen in Figure 4.18.

The pouch SPAs are used to actuate the three joints which connect the legs to the upper platform, although the respective joints fixed to the base structure could also be used instead. Two actuators are located at each joint around the platform, with one on the inner (lower) and one on the outer (upper) sides of the joint. Each actuator is positioned across the joint at the center, and mechanically fixed at two opposing ends with mounting screws to the two rigid bodies of the joint, the platform and leg section. When inflated, the pouch actuators exert a tensile force between the two end attachment points, as well as a compression force imparted at the joint center itself, which both act to decrease the joint angle on the side of the actuator.

The two actuators on either side of the upper leg joints act antagonistically to drive the joint in both directions, however they cannot be independently controlled. Rather, the states of the antagonistic actuator pairs are coupled such that one of the two actuators is always active. This design was chosen for several reasons. For one, this provides controllability and module stiffness at all times. Being fabricated from thin plastic, the pouch SPAs provide no stiffness or structural support when not active, and the origami kinematic structure itself provides only very light passive stiffness from the bending of very thin (50 μ) flexure hinge joints. In this way, the structure is very susceptible to deformations caused by external loads. Although a larger spring element could be included to replace the second antagonistic actuator, the force or torque provided by this spring is passive and fixed by a constant displacement relationship, limiting its ability to counteract loads. Furthermore, the active joint actuator would need to provide additional power to overcome both the spring stiffness and any driven load. This requires a stronger actuator, and yields a less efficient system. By coupling the actuator states, the module does not rely on passive stiffness to recover its joint configuration, and active control can be applied in both directions to ensure full authority.

The bidirectional joint control is inversely coupled to also reduce the number of required solenoid valves needed to activate each pouch SPA (6 in total). In order to achieve modularity, this decentralized control hardware is built into each module and thereby contributes to the overall size and mass of the module itself, which has a direct effect on its performance. When multiple modules are assembled in a serial configuration, as with a manipulator arm, every attached module imposes a load on its preceding module. In an effort to maximize the work output of such a multi-module configuration, the size and weight of every module can be significantly reduced by minimizing the number of valves onboard. This strategy of controlling coupled states in two actuators with a single control valve is common in industrial pneumatic systems where 5/2 valves - 5 ports with 2 states - are used. At small scales, this type of valve is not common however. Instead, we employ a novel solution inspired by industrial pneumatic logic control systems, which allows two actuators to be controlled by a single common 3/2 port solenoid valve in combination with a custom designed, layer fabricated passive relay valve.

4.13.3 Pneumatic relay

In the most common pneumatic system set-up, actuators are typically individually controlled by 3/2 port solenoid valves. This type of valve has two states, in which a common port is either connected to a pressurized supply port or to an exhaust port. The common port is usually then connected to the actuator to be controlled, thereby switching between providing pneumatic power to the actuator, or allowing air in the actuator to vent back through the valve and exhaust port. In an alternate configuration that is seldom used, the pressurized supply can be connected to the common port, allowing the two valve states to switch between providing supply pressure to either of the other two ports. In principle, this allows both states of a single valve to be used to supply pressure to two different outputs. In practice however, this is impractical on its own since actuators cannot vent themselves, so would never be able to release the pressure supplied in this manner after a single use. The solution to operating two actuators with a single valve is to use a different type of valve, with 5 ports which allow simultaneous venting inversely coupled to the activation of both output ports, however this style valve is currently unavailable at the scale of the pneumagami module.

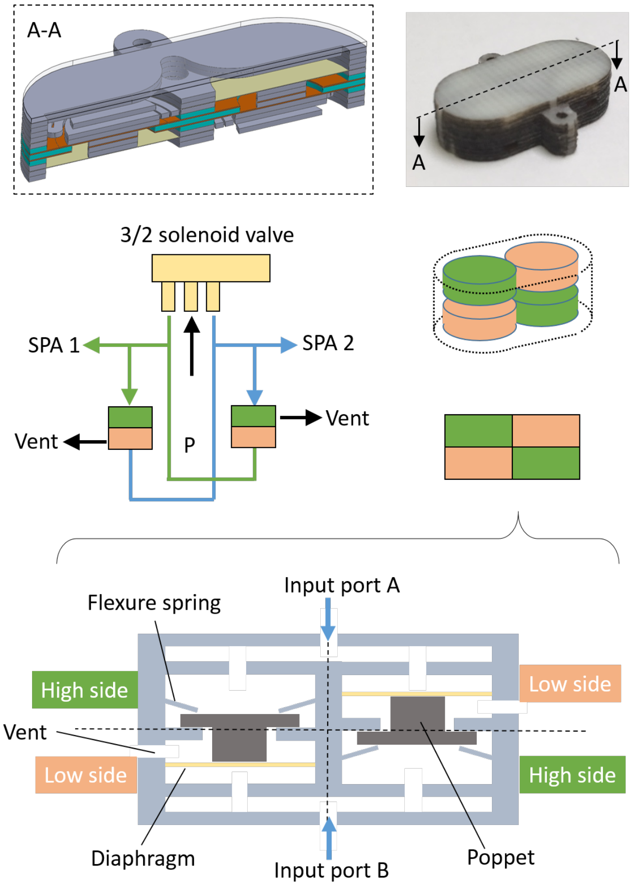

Figure 4.19 – Diagram of DBR valve.

In order to control the antagonistic pouch SPAs integrated with the pneumagami module, we leverage the two states of a single small scale 3/2 valve by incorporating a custom designed and layer fabricated differential-pressure blow-off relay (DBR). Although two DBR components are required to pair with each solenoid valve for controlling two coupled actuators, the combination occupies less volume with lower mass than two active solenoid valves. The key principle of this device is that it utilizes the pressure supplied to one actuator to trigger a mechanical vent which allows the opposite SPA to release its pneumatic pressure. This thereby facilitates control of two actuators connected through a 3/2 valve in common supply orientation. When an actuator is connected to the supply and activated in one state, it is correspondingly disconnected from the supply and vented to atmosphere in the other state, and vice versa for its antagonistic pair. This process is depicted in Figure 4.19.

Relay operating principle

The operation of the DBR follows a simple force balance relationship, induced by pressure and a bias spring. The free body force equation for the internal moving poppet is represented by 4.4,

$$PA_p + F_k + PA_d = 0 \tag{4.4}$$

where A_p is the area of the poppet upper side, F_k is the force from the bias spring, and A_d is the area of the diaphragm below the poppet.

The DBR contains two control ports, a high and low side, and one vent chamber. The high side is exposed to the upper side of the poppet, while the low side allows pressure to flow to the diaphragm. The vent is nominally isolated from the high and low side ports of the device due to a bias spring which holds a poppet closed. When opened, the poppet allows airflow from the high side of the DBR to the vent, however the low side remains isolated at all times by a non-permeable but flexible diaphragm. A single actuator is simultaneously connected to the opposite sides of two different relays, as well as one side of the control solenoid valve. When one actuator is active (A-1), the high side of one relay (DBR-1) is pressurized forcing the poppet and vent to close. At the same time, the low side of the other relay (DBR-2) is pressurized which causes a flexible diaphragm to displace upward, pushing directly on the bottom side of the internal poppet seal. Since the area of the diaphram exceeds that of the top side of the poppet, the net force from equal pressure on both sides force the poppet up. Once open, the pressure on the high side of DBR-2 is relieved through the vent. The steady conditions in this state are DBR-1: closed, and DBR-2:open. Once the solenoid valve state is switched, the process reverses. The other actuator A-2, the high side of DBR-2, and the low side of DBR-1 are connected to the supply pressure. This closes the DBR-2 poppet, and again, while pressure remains in A-1 and on the high side of DBR-1, the larger diaphragm area pressurized by the same source causes the poppet to move upward and the vent in DBR-1 to open, exhausting pressure in A-1.

4.13.4 Embedded control hardware

Each pneumagami module contains embedded hardware which allows it to be connected together directly with other modules and reconfigured in a 'plug-n-play' manner to form larger robotic systems. To enable this functionality, a printed circuit board (PCB) is integrated in each module with electronics for communication and control of the on-board solenoid valves. Activation signals to the valves are routed through an integrated circuit (IC) on the PCB over a common, single wire control bus which is shared among all connected modules. The IC (WS2811) decodes the position ID of the module as well as the independent actuator channel within the module. In addition to forward control signals, feedback from an IMU on the PCB can be accessed through a two wire I^2C interface which is also shared among all connected modules in a system assembly.

4.14 Experiments

4.14.1 Linear stiffness

The linear stiffness of the module was tested in the vertical direction using a stress-strain material testing system (Instron 5965). For each test the module was placed on the rigid base of the testing machine directly below the load cell attached to the movable linear stage. The load cell was initialized to zero force and displacement just after contact with the top of the module, and the force and displacement were then recorded for ten cycles of downward deflection, $\delta = 15mm$. The module was tested in two configurations: unpowered and powered. In the first condition, only the passive stiffness of the polyimide joints as well as tubing connecting the upper and lower stages of the module contributed to the stiffness. In the second condition, the pouch SPAs in all three legs were activated with a supply pressure of 60 kPa to force the upper module platform up vertically to its maximum position. The results of the two linear force-displacement tests are seen in Figure 4.20, where the active linear stiffness is shown at $K_\delta = 0.2$ to be a factor of 40 times greater than the passive linear stiffness at $K_\delta = 0.05$. In the active state, the increase in stiffness is a direct effect of the pouch SPAs stiffening from pneumatic inflation, and is therefore not a fixed value, but dependent on the supply pressure.

4.14.2 Passive torsional stiffness

The torsional stiffness of the origami structure was measured in a torque-angular displacement setup. An unpowered module was fixed in a horizontal position at the base to a rigid structure while the upper platform of the module was attached to a freely rotating torque arm. The torque arm is constrained by a shaft aligned with the axial center of the tested module, and extends to a length of 100 mm where it is terminated by a rounded endpoint feature. The same vertical materials testing machine was used to apply a load on the end of the torque arm, while the rounded shape of the arm endpoint helps to ensure that the load is transmitted at the same distance for small displacements through the flat contact surface protruding from

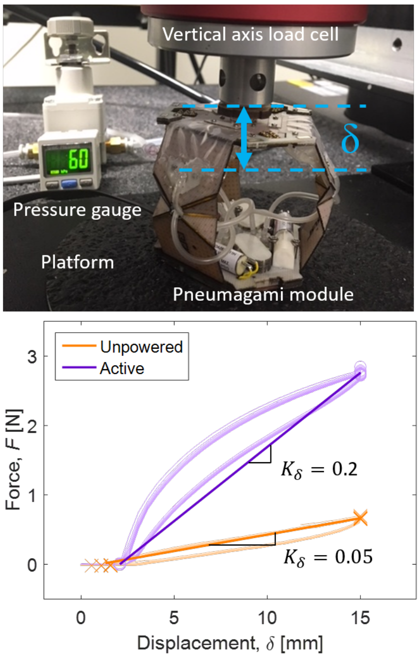

Figure 4.20 – Linear stiffness experimental setup.The experimental setup is shown for performing linear stiffness measurement tests with the module in powered (SPAs pressurized) and unpowered (SPAs deflated) states using a vertically oriented material testing system.

the load cell.

Although the module test setup was fixed in place relative to the load cell and only linear force and displacements were directly measured, a corresponding torque applied to the module and resulting angular displacement were calculated from the known geometry of the setup, neglecting the effects of load redirection at relatively small angular deflections. For each measurement trial, a linear deflection of 2 mm was prescribed corresponding to less than 1.2deg of angular rotation.

Two trials of 10 cycles each were performed to test the torsional stiffness of the modules in two different configurations; fully extended and fully collapsed. The raw and averaged results of the experimental tests are shown in Figure 4.21, which indicate a value of higher stiffness in the compact state compared to the extended state. This result follows the reasoning that in the contracted state, the flexible cross joints at the center of each leg are positioned radially further from the axial center of applied torque and resulting rotation of the upper and lower module platforms, where the force on each flexure hinge joint is therefore reduced. In the extended state, as the legs straighten and intermediate hinge joints move closer to the axis of applied moment, the resulting force acting through the legs on the joint is greater, resulting in higher off axis deflection of the flexible hinge material and a lower measured torsional stiffness.

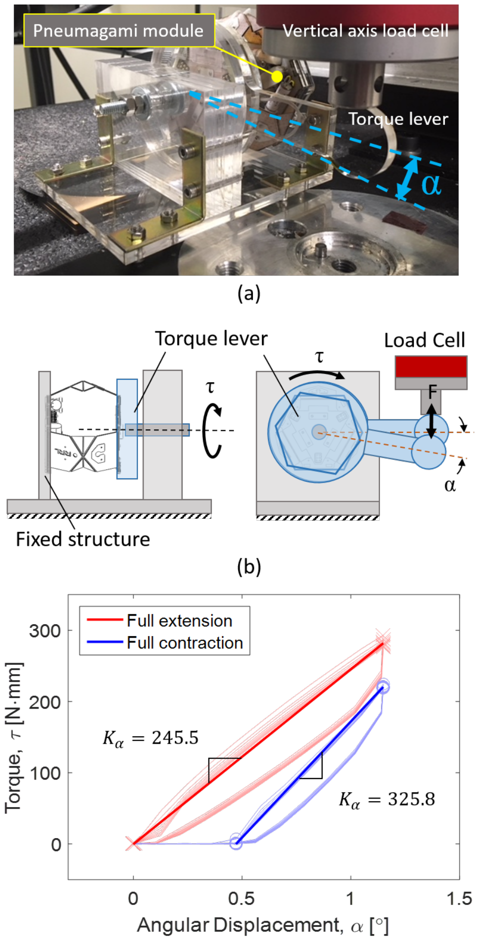

(a)

(b)

(c)

Figure 4.21 – Torsional stiffness experimental setup. The torsional stiffness of the pneumagami module was tested by applying a torque load to the upper platform of the module along its central axis while the lower base platform was fixed. A test setup was designed to transmit force from the linear material test machine into torque, while both the load and displacement were measured. The test rig includes a rotational shaft constraint to ensure that only pure moment is applied to the module without any orthogonal linear force.

4.14.3 Actuator and relay valve characterization

A single module leg was fabricated to test the step response of antagonistic pouch actuators, as well as characterize the observed delay effect of the DBR. The test leg comprises a single joint fabricated to the same specifications and material as those found in the legs of the complete module. Two pouch SPAs are mounted on either side of the leg hinge in an antagonistic configuration as seen in Figure 4.22a and supplied with pneumatic pressure from independent supply tubes. With the leg fixed to a mounting structure, the actuators were activated at least 15 cycles in each direction to maximum deflection at 60 kPa, by two different control methods. In the first method depicted in Figure 4.22b, two independent solenoid valves were used to command the activation of the two SPAs in a periodic, alternating pattern. A digital pressure sensor (Honeywell, 001BGAA5) in parallel with each actuator recorded the changes in pressure resulting from the cyclic activation through an analog port of an Arduino microcontroller. The same test was then repeated using a single solenoid control valve coupled to the two ports of a DBR and each of the antagonistic SPAs, as seen in Figure 4.22c.

The cyclic pressure profiles for each experiment were averaged for 15 cycles and can be seen in 4.23. From these measurements, the 10-90% rise times from neutral to fully pressurized state are calculated yielding 0.041 seconds for SPA 1 and 0.031 seconds for SPA 2. The longer response time for SPA 1 can be attributed to a small leakage which is visible as a short duration drop in pressure visible in the recorded data.

The actuator pressure profiles for the second configuration controlled by a solenoid and DBR pair are seen in the lower plot of Figure 4.23, which indicates rise times of 0.18 and 0.094 for SPA 1 and SPA 2 respectively. While the leakage effect is also visible in SPA 1 as previously seen, another effect is introduced by the inclusion of the DBR component, seen as a momentary delay in the pressurization of the actuator as its antagonist is depressurized and the pressure in both actuators is roughly equal, leaving only the force imbalance on the internal poppet of the relay caused by asymmetric areas to drive state switch and fully vent the opposing SPA. Although different DBR geometries were not tested in this study, future work could investigate methods for reducing this momentary delay by optimizing the ratio of functional areas, and hence forces, acting on the relay poppet.

The difference in pressure profile timing can also be used to quantify the effect of the DBR valve in terms of its maximum operating bandwidth. Taking the difference between the rise time of SPA 2 (the best performing measured actuator, with no apparent leakage) in the two configurations, the added delay from the DBR is found to be 0.063 seconds. Taken to be a characteristic of the relay response time, this correlates to roughly 5.6 Hz bandwidth for the DBR.

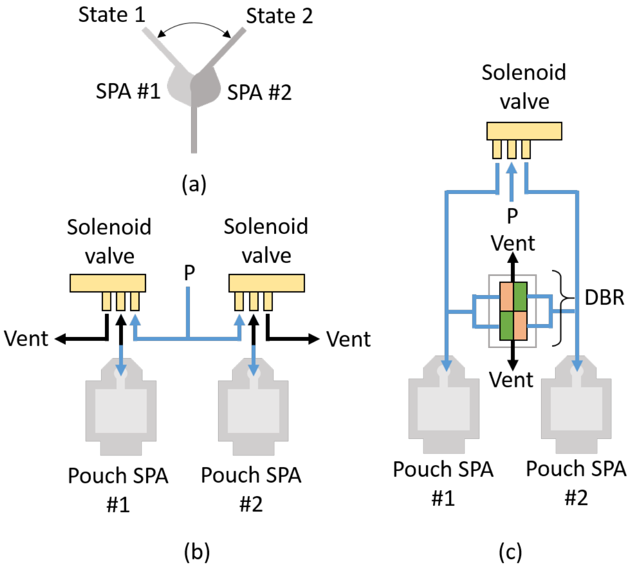

Figure 4.22 – Test configurations for the DBR valve. The two configurations used for characterizing the DBR and actuator response to cyclic pressure step inputs are shown. The two states shown in (a) are achieved by alternating activation of antagonistic SPAs through two control configurations illustrated in (b) and (c).

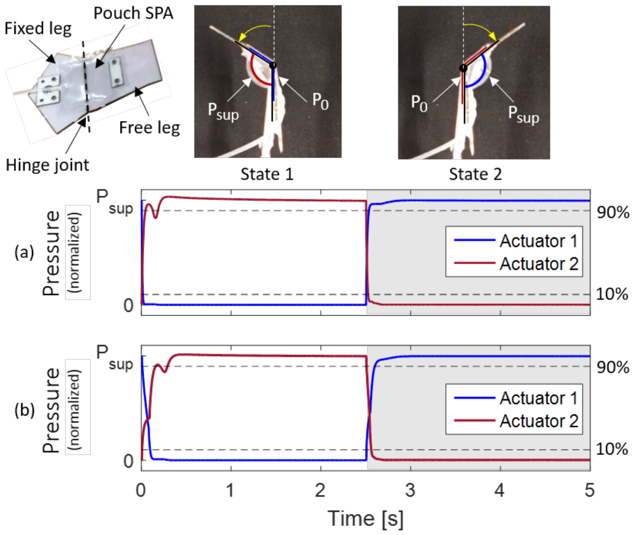

Figure 4.23 – Pressure response for antagonistic SPA cycling. Two averaged pressure profiles are shown for cyclic actuation of antagonistic SPAs fixed to an origami leg for joint characterization, corresponding to two different control methods. (a) shows the pressure profile associated with dual solenoid control, while (b) shows the profile associated with single solenoid valve control utilizing a custom, layer fabricated DBR valve for state switching.

4.14.4 Kinematic model validation

The trajectory of the module upper platform angle, α, was tracked using the video analysis software Kinovea, and the result used to validate the applicability of an existing kinematic model for the waterbomb based parallel structure to the prototype presented here. A video camera was placed above the module for testing and two markers in the plane of the platform rotation were tracked. The corresponding change in platform angle was computed based on the change in distance between the two points on the projected xy-plane (camera focal plane), δ, and following the geometrical relationship

$$\cos\beta_1 = \frac{l_{leg}\cos\beta_0 + \delta}{l_{leg}} \tag{4.5}$$

where the initial leg angle, β_0, and leg length, l_{leg}, were measured separately at the start of the experiment.

To validate the model, the platform angle trajectory was first recorded for seven cycles and averaged to produced a mean measured trajectory. The mean trajectory was then used as the input to the inverse kinematic model from [306] shown in A.1, which is used to calculate leg joint angles B_i for given legs of the structure. For simplicity, this analysis considers only one leg, $i = 1$.

$$\beta_1 = 2\tan\left(\frac{-D_1 + \sqrt{{D_1}^2 - 4C_1E_1}}{2C_1}\right) \tag{4.6}$$

For a single leg aligned with the global frame x-axis, $y_b = 0, \delta = 0, \phi = 0, \psi = \alpha/2$, simplifying the coefficients to

$$\begin{aligned}
C_1 &= r_p + 2x_b\sin\frac{\alpha}{2} - 2r_a\sin\frac{\alpha}{2}\\
D_1 &= 4r_a\cos\frac{\alpha}{2}\\
E_1 &= -r_p + 2x_b\sin\frac{\alpha}{2} + 2r_a\sin\frac{\alpha}{2}
\end{aligned}$$

With the parameters of the given module $y_b = 25, r_p = 48$, and $r_a = 24.4$, the leg joint angle β_1 was calculated from the known upper platform angle trajectory. This theoretical result is then compared to the measured angle also measured through video analysis. Figure 4.24a shows

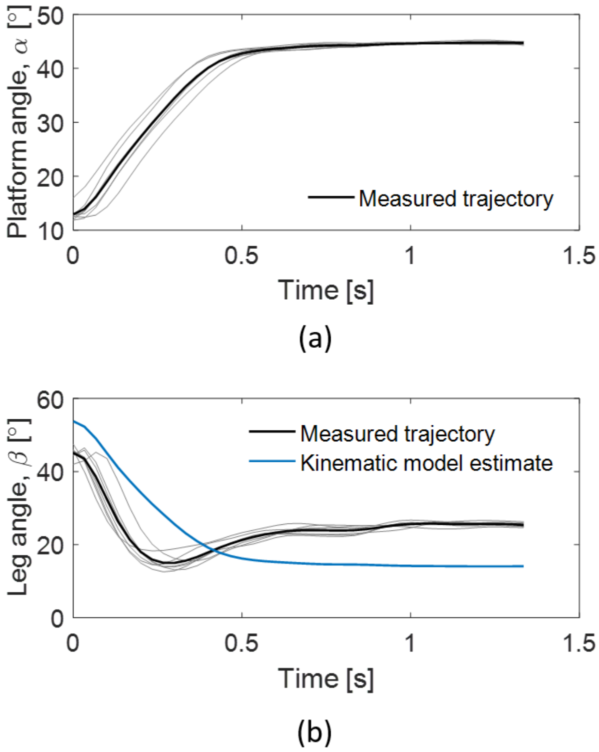

Figure 4.24 – Module platform kinematic trajectory. The angular trajectory of the module upper platform is shown in (a), averaged from seven cyclic, binary activation of a single leg joint. An inverse kinematic model is used to calculate the theoretical trajectory of the activated leg joint, while the actual recorded measurements are shown for comparison.

the measured platform trajectory used as the independent variable above in Eq. A.1. Figure 4.24b shows the predicted leg angle trajectory in comparison to the actual recorded trajectory. A general trend appears consistent between the two curves, however significant deviations are also clearly evident. The difference in the measured data to the theoretical model is likely due to at least two main factors: poor visual marker tracking which caused drifting in steady state conditions, and perspective distortion resulting from markers moving vertically, out of the recording camera's focal plane.

4.15 Discussion

The position of three independent joint angles theoretically prescribe the final position of the pneumagmi module platform, however, practical manufacturing and design differences from the physical module and the ideal model contribute to deviations in predicted performance. A prominent difference is the use of flexure based joints in place of single axis rotational joints throughout the structure. The polymer based hinges produce a dominant mode of bending which can be approximated as a single axis, however multi-axis rotations and deformation of the compliant structure allows motion in other directions. This joint "play" allows deviation from pure rotational motion and idealized kinematics which would inhibit the application of

Table 4.4 – Performance Table

PROPERTY	SPECIFICATION
Total mass	56 g
Valve mass (3)	4 g
DBR mass (3)	2.5 g
Contracted size	65 x 70 x 20 mm
Extended size	65 x 70 x 65 mm
angular RoM	42.5 °
linear RoM	45 mm
actuation speed	81.6 °/s
DBR bandwidth	5.6 Hz
extended torsional stiffness	245.5 Nm/°
contracted torsional stiffness	325.8 Nm/°
active linear stiffness	0.2 N/mm
passive linear stiffness	0.05 N/mm

model based control methods for controlling this type of module to precise desired positions. This method of control is not necessarily needed or appropriate for this type of module however, due the the intrinsic compliance of the pouch SPAs which are used to drive module joint motion. This intrinsic compliance allows the module to be physically adaptable to misalignment of the end effector relative to target positions. While this may not be the objective of every application for this type of module, the inherent compliance allows this actuator structure to be utilized in collaborative, wearable, or interactive applications to provide safe and compatible functionality.

The force output of the pneumagami module tested here is also comparable or lower than some existing actuator modules designated for use in continuum robot arm structures, however, this is not a fundamental limitation of the design. The closest functional equivalent to the pneumagami architecture utilizes origami structure modules driven by onboard DC electric motors to produce greater output force. The performance of DC driven systems is limited, or at least coupled to other factors including size and weight. In this respect, conventional motor powered systems are not independently scalable so their force output represents a relatively fixed value at a given scale. Pneumagami modules on the other hand, allow scalability of force output with no change in scale and only minimal change in design through new materials and fabrication methods. As the modules are powered by pressurized air, the force output of the modules can be increased by increasing the supply pressure. The actuators tested in this work were operated near the limit of the pouch SPAs before failure at their heat-fused edges, and from the plastic deformation of the plastic pouch material. The capacity of pouch SPAs to tolerate higher operating pressures and thus produce higher force output can be increased by utilizing stronger pouch materials and different methods for bonding the sealed structures. Additionally, various adhesives and sheet composite types may be substituted to accommodate higher pressure in the embedded distribution manifold as well as to tolerate the higher forces in the kinematic structure. These design choices are seen as design parameters rather then fundamental limitations of the pneumagmi concept, and allow the module design and performance to be scaled according to desired metrics.

The onboard, embedded control hardware allows multiple modules to be connected directly in series with each other to form a hyperredundant manipulator arm in the simplest multi-module form. The modules are not limited to use in this configuration, however, as they can be connected to alternate platforms as modular actuator units. serially through standardized connections extend and connect the electrical and pneumatic supply lines. This greatly simplifies the task of designing robotic pneumagami systems with high DoF.

4.16 Conclusion

A single 3-DoF pneumagami module is presented and characterized to establish the baseline performance and properties of a fully integrated hybrid robotic system combining pneumatic actuation and origami design methods. The inherently low weight and compact form factor traits common to both soft actuators and origami robots enable a space and weight efficient robotic platform which does not sacrifice strength, high mobility, or RoM. The robotic modules facilitate the construction of larger scale, reconfigurable robotic assemblies through the use of embedded plug-and-play connection interfaces for both a shared positive pressure pneumatic supply and on-board electronics hardware. The ability to design and construct scalable robotic systems from pneumagami modules powered by inherently soft actuators consequently allows the exploitation of both the intrinsic compliance of the components themselves, as well as the effective extrinsic softness resulting from high-DoFs. This design configuration affords high-RoM systems which maintain controllability and independently prescribed compliance, conducive to safety in wearable and human-robot interactive applications.

5 Conclusions and future directions

The overall objective of my PhD research was to extend and expand opportunities for robotics in complex, real-world applications through the development of novel actuator and system solutions. This thesis is designed to identify and address the conceptual and practical challenges which are vital to achieving these goals. Among the most promising yet difficult areas for robots to fulfill a more dominant and high-impact role are in collaborative, interactive, and personal applications. Unlike the historically conventional duties assigned to robotic automation in highly structured environments, however, these tasks are characteristically unpredictable, diverse, and variable. This necessitates a paradigm shift in robot design strategies as well as fundamental performance requirements. Specifically, this includes a greater need for application specific, customizable robot topologies, passive adaptability, inherent safety, portability, and robustness to enable effective operation and widespread deployment of robotic assistance in settings not strictly designated for robots. Although the field of soft robotics has emerged in recent years to answer to some of these challenges by promoting the many advantages of primarily material-based, implicit compliance in actuator and hardware design, not all benefits afforded by independent technological advancements can be properly leveraged at the system-level. My thesis work supports real-world applications for robotics in unstructured environments and tasks by contributing new actuator component designs, material selection, and system integration and control methods in consideration of holistic system characteristics and objectives. This facilitates closer approximation and coordination of compliance between interactive or wearable robotic systems and the users they are designed to interact with.

5.1 Conclusions

The unique modular actuator concept presented in this work fundamentally redefines the approach to high-DoF SPA based robotic system design. The arrangement of SPAs in modular actuator units allows complex soft robotic systems to be designed, configured, and controlled at the system-level, without the need to redesign low-level architecture or subsystem components. Systems composed of SPA modules can be reconfigured or extended simply via "plug-and-play" connections for electrical and pneumatic power, and control communication. This powerful yet simple approach not only facilitates more easy and rapid development of new soft robot designs, but also enables the actual feasibility of particularly constrained designs that would otherwise be impossible to implement. By incorporating decentralized control and communication hardware, modular SPAs eliminate excess space and weight normally required for routing pneumatic power tubing, while simultaneously simplifying the design process of high-DoF systems further. In a pragmatic sense it may be noted however, that modularity as a design concept also may not be the optimal configuration for certain product level, end use soft robotic systems which require minimalist and dedicated functionality to save weight, space, or cost.

Prior to my work, the task of integrating many SPAs in a single system required significant low-level design effort, which was both complex and time intensive, as well as fixed in terms of scalability and reconfigurability. My approach allows such soft actuator systems powered by pneumatic pressure to be more rapidly and easily constructed to allow future efforts in soft robotic system design to address more high-level application challenges.

As the concept of modularity in SPA system design applies equally to positive pressure actuators as to vacuum powered, or negative pressure SPAs, a new type of vacuum-powered foam based SPA, the V-SPA, is presented. This novel actuator further facilitates large scale soft robotic systems, as they are readily manufacturable, cost-effective, and lightweight compared to most other SPAs. The presented V-SPA modules utilize these new actuators to leverage additional benefits from vacuum power through efficient integration with modules of varying types. Some features enabled include gripping by suction, mechanical stiffness tuning, and adhesion for vertical climbing. By connecting to the same control and pneumatic power supply ports built-in to actuator modules, these beneficial features expand the capabilities of the soft robotic system without requiring a separate power supply from the actuation. All together, the many advantages of modularity enable SPA systems to be applied to more complex applications with high-DoF at a lower cost in design effort. The present limitations of the modular actuators presented here are a lack of integrated feedback for embedded proprioceptive sensors and the scale of available solenoid valves which determine the minimum size of each single module.

The new V-SPA design and fabrication process presented in this work remain unique in the field of Soft Robotics. Few examples of vacuum-powered soft actuators were developed previously, however none utilize a compliant foam internal structure which minimizes the mass of higher density silicone rubber, can be fabricated without molds or sacrificial porogens, or can be operated with minimal energy storage resulting in failsafe, lightweight, and readily manufacturable actuators. The V-SPA presents these advantages, and enables the rapid development and iteration of intrinsically safe, high-DoF systems. The maximum force V-SPAs are able to produce is fundamentally limited by the pressure of the environment in which they are used, which limits their application in fixed environments. In more diverse settings, however, the limits of vacuum power can be exploited to achieve high force performance and would be particularly beneficial underwater where ambient pressure increases with depth allowing much more powerful vacuum driven actuation.

To complement large-scale soft robotic systems with many-DoF, I explored new control strategies which provide methods to leverage their full range of cababilities for human-centric applications. One of the first steps toward designing and implementing control of compliant systems is to identify and select the parameters of the control scheme which match the physical system capability and performance. Recognizing the advantages promised by soft robotics for compliant materials to perform *morphological computation* to provide position and force tolerance reduces the effort necessary for precise control. In designing control strategies for soft systems, I therefore leverage this concept to specify reduced order or simplified control schemes which are not overdefined for a given task. Given a soft robotic system that may be prone to extreme deflections in passive DoF under loads or disturbance, I demonstrate minimalist yet effective approaches to control which achieve only the approximate position or force control necessary, allowing the built in compliance of soft materials to contribute the remaining physical adaptation needed to execute ultimate task objectives.

Similar to the effect of compliant materials, control strategies for wearable or interactive applications also benefit from matching to the *effective compliance* of human user activity. With a high degree of variability both in action and intent, human users introduce additional perturbation and influence which interacts directly with the hardware and its control. Strategies which act to preserve mobility are therefore derived to accommodate this uncertainty. Utilizing heuristic planning and control mapping methods, simple controllers can be obtained without the need for extended systems dynamic modeling, which for highly non-linear elastic materials, is known to be a difficult task. Alternately, controlling system mechanical properties such as stiffness (hardware design-based impedance control) can be used to influence or passively control interactive soft robotic system operation without imposing position or trajectory constraints which might otherwise interfere with user behavior or material responses. In cases where very precise actuator trajectories are required, different approaches from those discussed here may be needed, which may include greater use of sensing and state feedback, or possibly extensive modeling and online learning methods.

Although the simplicity of these control techniques reduces the complexity of developing and controlling large scale systems, it nevertheless still permits complex system-level behavior. This is demonstrated by the shape and load modulation control of a 16-DoF soft reconfigurable surface (SRS). Using only simple open-loop binary control techniques, various, dynamic, programmable shapes and patterns can be rendered in 2.5D with the SRS. These patterns can be utilized to manipulate objects for more industrial type purposes across the planar array of soft actuators, or can otherwise be employed as a haptic interface. These forms of interactions with the device, by passive objects or human users, rely on both the compliance of the device itself, as well as the large number of active DoFs to achieve versatile and diverse functions, with only minimal reliance on the control applied. Adding sensory feedback expands the possible functions of the high-DoF SRS, but does not necessarily increase the complexity of necessary control. Simple control strategies can be leveraged to achieve high-level force and stiffness control across the surface of the SRS by utilizing localized sensors without the need for coordinating multiple actuator modules. Moreover, with such decentralized feedback in a modular architecture, systems are scalable and do not require reprogramming to achieve the same function in any configuration.

Sensory information in robotic systems is commonly used for singular objectives, to act in a common configuration as a mode of state feedback, or in feedforward as a device input. For soft systems which are designed for wearable or collaborative applications, these two integrated sensor modes may be combined by utilizing the same sensor for both purposes. To serve “learning by demonstration” programming methods, for one example, sensors embedded in the body of a soft robotic system may provide essential information about user intent or directions. Subsequently, these sensors can then be used in feedback to execute “learned” program modes, leading to a *bi-modal control* scheme for soft interactive robots. This concept is illustrated on a simple soft robotic arm platform, with embedded liquid metal strain sensors. The ultra-thin, stretchable sensors were bonded to the outer body of 3-DoF V-SPAs modules and used to measure both manual directional commands from a user as well as the buckling deflection of the actuator body to estimate angular position and deflection of the robotic arm structure to control its position in closed-loop.

In addition to directly improving system-level design and performance, I applied modularity at the actuator level to improve the force capability and reliability of SPAs themselves. This novel idea borrows inspiration from biological muscle, by grouping multiple smaller actuators together to form a larger more powerful SPA structure. For the first time, SPA Pack architecture demonstrated force output above 100N, and provides new opportunities for using SPAs in high-force applications including direct interaction with the human body. Through an analytical model and experimental testing, parallel grouping of positive pressure SPAs in fascicle-like arrangements reveals higher force output proportional to the number of smaller grouped actuators, within practical bounds. Moreover, redundant parallel actuators allow continuous function as a failsafe in the case of failure or leakage in one of the individual component SPAs. To realize practical redundancy and robustness, the individual actuators within SPA packs would require separate active control or shut off valves to disable actuator units in the event of unit failure, however this was not implemented in this work and should be addressed in the future. These design improvements expand the utility of SPAs to a new regime of high force applications while also ensuring factors of reliability, robustness, and safety. By discretizing the force output of the grouped actuator structure, the modular topology of the SPA Packs also simplifies the design of actuators to meet specified performance requirements to a tractable, linearized solution.

While multi-DoF V-SPAs were produced and utilized to illustrate system-level benefits of modularity and user interactive control methods, actuators were initially designed to meet only subjective criteria for optimal performance. To obtain better understanding of V-SPAs toward improving their design to achieve desired performance metrics, an empirical parameterization study was conducted. A new bending type of actuator, the Coil V-SPA with an exceptionally high-RoM and a simple geometric structure was developed to facilitate testing of two primary performance metrics, speed and force. The internal geometry of the new actuator was varied between test samples while maintaining overall equivalent dimensions across sample to identify the relative effects of different actuator dimensions. A generalized design metric, the GCR, was found to correlate actuator performance to its internal chamber geometry, and revealed the existence of a unique design optimum for each metric.

The efficacy of soft material actuation, modular actuation design and system architecture, as well as simple control techniques toward wearable systems was evaluated by the study of a wearable device for postural support or modulation. A modular belt was fabricated to allow multiple SPA packs to be positioned along its length, around the body perimeter, to affect posture in different, customizable directions. The reconfigurable belt functions by applying a moment on the upper body above the hip and lower abdominal region, and could be used for rehabilitation assistance in postural asymmetry correction resulting from spinal cord injury, or for 'live' intervention by a remote therapist in teaching proper body form during exercise or sports training. The SPA belt is controlled by an electro-pneumatic control system integrated with body worn sensors, which ultimately yields a repeatable, quantifiable tool for prescribing body interactions. This gives clinicians the ability to accurately adjust and apply postural support through different phases of intervention, and potentially enables targeted assistance in real-time during dynamic exercise activities that might be difficult or not at all possible for a physical therapist to achieve.

Although the wearable belt successfully demonstrated the ability to interact with pilot subjects by applying human-scale forces, transmitting those forces from actuators to the human body remains a significant challenge that reduces the effectiveness of actuation with all wearable robotic devices designed to provide direct physical assistance. Better placement of actuator anchoring points across the body, especially extended to more load bearing, structural bony landmarks would allow greater effect from the actuators to modulate posture in future device improvements. More effort is also required to develop effective implicit user control strategies to inform or direct the activation and use of wearable, interactive robotic systems.

An alternate type of wearable device for task assistance was also targeted through the development of a compact modular robotic manipulator system. To achieve low-mass, a low-profile form factor, and high mobility while also maintaining structural integrity against external loads as well as its own weight, a 3-DoF SPA powered module was produced using techniques borrowed from robotic origami design. The approach utilizes both new materials and new manufacturing methods, that were integrated with modular SPA control and power distribution architecture to leverage the benefits of each. The origami fabrication process facilitates the construction of complex structures with a nominally 2D form factor, and make use of fiber composite materials which are lightweight and high-strength to allow highly functional yet compact systems well-suited to portable, wearable applications. This structural element is combined with soft, nominally 2D pouch SPAs, which allow intrinsically compliant control of the module angle, as well as total linear deflection in powered retraction or deployment. This type of *pneumagami* module, combining pneumatics and origami elements, can be combined in series with other plug-and-play actuator modules to form a robotic manipulator arm with many-DoF that is highly-adaptable, safe, and robust.

Previous research has shown some benefits of origami-based design, as well as the effectiveness of low-profile pouch type SPAs for providing its actuation, however few have implemented robotic origami specifically designated for their efficient combination at the actuator and system levels. My work extends these examples by following an approach to comprehensive robotic origami design which facilitates both efficient use and reconfigurable design of actuator and robot structures. While other work has utilized origami components in robotic system design, my work demonstrates that origami structures and layer-manufacturing techniques can be leveraged for multi-functionality, compatible with full system integration. The direct inclusion of embedded pneumatic distribution channels *within* the origami structure itself, as well as the fabrication of passive control valve hardware and the on-board PCB, serve as prime examples of the fully layer-manufacturable design. Although many of the components used in the pneumagami module presented are still off-the-shelf additions, including the valves and actuators themselves, one main achievement of this work is the establishment of a framework and methodology which can readily incorporate these functional elements from nominally 2D fabricated materials and techniques.

Being designed specifically for lightweight, mobile applications, with the ability to fold into a collapsed, storage state, and also extend to perform high-DoF positioning and manipulation, pneumagami modules provide the framework for creating a task assistive wearable device for daily use. Rather than providing assistance to a user directly by affecting the body, this type of device would provide assistance during activities of daily living that generally only require coordination, to effectively act as a “third arm”.

Some of the largest challenges and limitations in this work are those which are globally inherent to the field of soft robotics. These challenges include the reliance on a large offboard pneumatic power supply to provide pneumatic pressure, and managing the interface between different compliance materials where high stress concentrations can lead to mechanical failure in soft actuator structures. These may be mitigated by future improvements in other fields, through the development of smaller, lighter, and more efficient pneumatic pumps for onboard use, and though soft material 3D printing technology to allow better control of transitions between materials of different stiffness.

In this thesis I presented new actuator, control, and system level design solutions for creating an advanced class of scalable soft robotic systems with high-DoF towards developing interactive and wearable robotic devices. Crucial to this goal, I first focused on developing an architecture for integrating many SPAs together which would also allow customizability through plug-and-play reconfigurability. The feature of customizability itself is important for wearable systems to accommodate the highly variable needs and body types of human users.

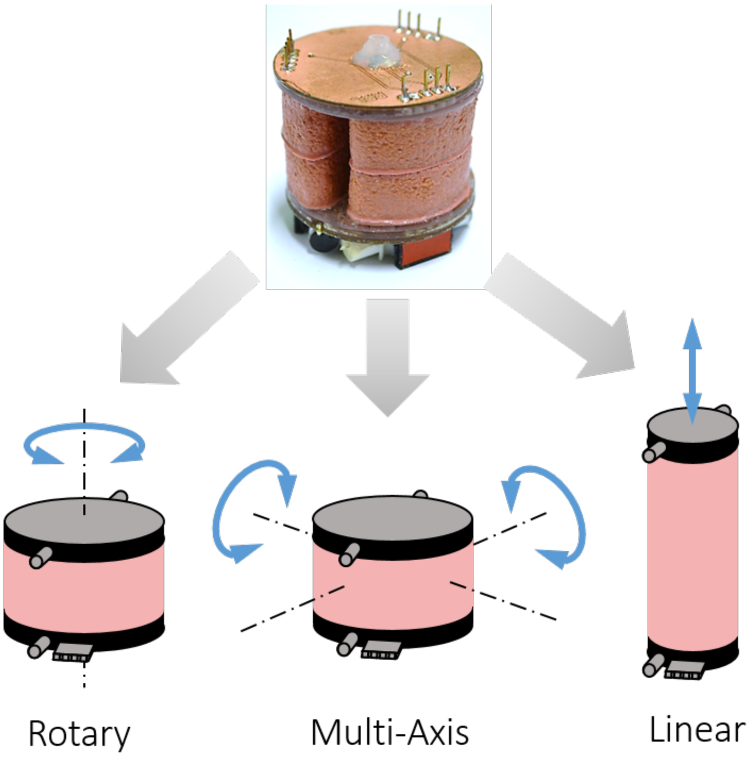

Figure 5.1 – Soft servos. Modular soft pneumatic actuators can be adapted to a variety of alternate output configurations, as the examples here show. This concept can be extended to create off-the-shelf components for developing soft robotic systems, eliminating much of the need for low-level design and allowing more seamless integration of soft technology for practical applications.

These parameters also benefit from the adaptability, and inherent safety of soft materials used to fabricate the actuators which power a soft robotic system. Across different platforms I then demonstrated different specialized approaches to control which leverage both the extrinsic compliance of high-DoF systems, and the intrinsic qualities of highly compliant systems - utilizing binary control on a soft reconfigurable surface to render dynamic patterns or passive manipulation of objects, and heuristic control mapping for passively compliant actuator modules, for example. Finally, I prepared the frameworks for future evaluation and scientific investigation of functional, real-world soft robotic system applications through the development of wearable hardware. This work collectively brings us closer to a world of truly useful personal robots capable of matching the diverse factors of compliance which allow us to embrace and engage with them in a safe and natural manner.

5.2 Future research directions

5.2.1 The future of modular soft pneumatic actuators

The development of soft robots is still currently an art form. While soft robotic actuator technology is highly approachable given the simplicity and relatively low cost of materials for their fabrication, their integration and ultimate utilization relies on system level design and integration methods which are far less developed or standardized. This severely limits the success and potential for soft robotic systems to be widely adopted and further explored for practical use. Our investigation and development of modular SPAs in this thesis provides one example solution to this unresolved challenge. In future work I would take this further in several ways.

Drawing a parallel to the current industry of hobby robotics, I envision a future with off-the-shelf soft robotic modules that can be best described as *soft servos*. Similar to the way in which fully plug-and-play DC motor based actuator systems are packaged and utilitzed, with electronic communication hardware, sensory feedback, and commercially standardized interface connections, soft servos will also be pre-assembled and capable of closed-loop, abstracted use. Rather than designing new soft robotic systems from the ground up, users will be able to construct soft systems with only baseline system-level knowledge of their functionality, allowing more focus on application development.

Secondly, I have only presented a limited example of the potential functionality of soft servos. In reality, a variety of other actuator "building blocks" could be realized, including standalone modules which can apply inline torsion or extension-contraction, and those which could incorporate various different forms of embedded feedback (see Figure 5.1). These device options would furnish discretized solutions to soft robotics engineers to draw from in order to match hardware to device requirements. Before reaching the level of commercial availability however, these new concepts should be investigated and to determine the appropriate module types and standards which would serve the broad interest and needs of soft robot developers.

5.2.2 The future of wearable SPA-based systems

Building on the established frameworks for different types of soft wearable devices presented here, there is opportunity in each to extend both system-development research as well as begin collaboration with other fields. The wearable SPA belt device demonstrated successful function but remains to be improved in several ways. The positioning of more optimal and effective anchor points for the SPA packs to impart forces to the body, and the quantified benefits of direct assistance from a soft wearable system in realistic or patient specific scenarios are largely un-resolved, and important matters which could likely sustain the subject of a full PhD study. These further investigations could involve the biomechanics and medical communities to conduct studies with large and diverse user populations. In feedback with results from such studies, the wearable belt system could be expanded and optimized leveraging the simplified

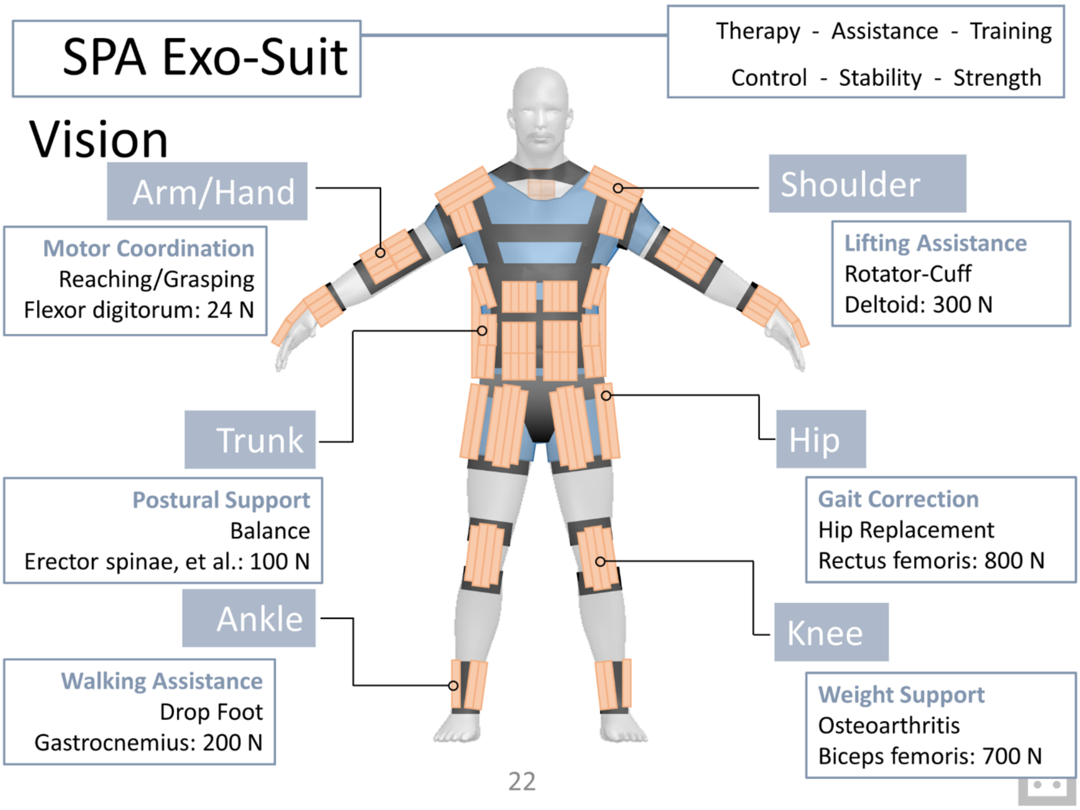

Figure 5.2 – SPA exo-suit. A future vision of soft wearable direct assistance technology foresees the realization of a complete, full-body suite of solutions to a wide variety of impairments or applications.

design method for SPA Packs to meet requirements for use across the human body. Effectively this work would build toward the possibility of implementing an *SPA suit*, to provide direct mechanical assistance to any select body region or biomechanical impairement (see Figure 5.2).

Beyond direct assistance from wearable robots which apply forces directly to the human body, the class of task assisstive wearable devices can be further developed to resolve a different set of needs in daily activities. What has been presented in this thesis as the *pneumagami* module is only the cornerstone to a grand vision of a fully implemented, wearable and deployable robotic arm system for everyday use. While the hardware framework is a significant step toward this goal, great effort in future work is required to develop the complete system to evaluate its efficacy and potential. The intended benefit of the final device is to provide aid during situations when a user is manually occupied, requiring that assistance by the device be provided through hands-free or automated control. A simple approach would be to incorporate various existing solutions to issue user control commands, including voice recognition and eye tracking. While these would serve interface requirements, device function would still need to rely on automated behavior driven most likely by a form of artificial intelligence based program to interpret commands and execute the desired assistive function. Finally, a portable pneumatic pressure system will need to be integrated with the assistive arm, possibly situated on the body in an alternate, more removed location, such as the back.

5.3 Final remarks

This research has shown that developing component level technology is critical to improving the capabilities of robots, but alone it is not enough. This must be pursued in conjunction with system-level design and development. This dual approach, in considering functional requirements and design criteria at both the hardware and integration levels, ultimately affects the resulting system behavior and facilitates improved authority over application level performance. This is especially important for controlling soft systems, where compliance often dominates over constrained kinematics. In this case, compliance can be viewed as part of the control strategy for a soft robotic system and not simply something to accommodate or compensate for. From the holistic system perspective, it is therefore reasonable to choose hardware designs, component materials, and control methods which are congruent and which benefit from each other. The solutions presented in this thesis which demonstrate this approach, and the collective body of future work which it supports serve not only to progress the field of robotics and wearable devices by permitting new, advanced capabilities, but also in turn to positively transform our society as we know it.

A RoboScallop: A Bivalve inspired swimming robot

Underwater swimming robots permit remote access to over 70% of the Earth's surface that is covered in water for a variety of scientific, environmental, tactical, or industrial purposes. Many practical applications for robots in this setting include sensing, monitoring, exploration, reconnaissance, or inspection tasks. In the interest of expanding this activity and opportunity within aquatic environments, this paper describes the development of a swimming robot characterized by simple, robust, and scalable design. The robot, named RoboScallop, is inspired by the locomotion of bivalve scallops, utilizing two articulating rigid shell components and a soft elastic membrane to produce water jet propulsion. A single-DoF, reciprocating crank mechanism enclosed within the shell housing of the robot is used to generate pulsating thrust, and the performance of this novel swimming method is evaluated by characterization of the robot jet force and swimming speed. This is the first time jet propulsion is demonstrated for a robot swimming in normal, Newtonian fluid using a bivalve morphology. We found the metrics of the robot to be comparable to its biological counterpart but free from metabolic limitations which prevent sustained free swimming in living species. Leveraging this locomotion principle may provide unique benefits over other existing underwater propulsion techniques, including robustness, scalability, resistance to entanglement, and possible implicit water treatment capabilities, to drive the further development of a new class of self-contained, hybrid-stiffness underwater robots.

The material presented in this chapter is adopted from the following self-authored publications:

[307] **M. A. Robertson**, F. Efremov and J. Paik, "RoboScallop: A Bivalve inspired swimming robot," in IEEE Robotics and Automation Letters. doi: 10.1109/LRA.2019.2897144
The first author wrote the final manuscript, analyzed data, and supervised the second author in the development of the prototype. The second author also conducted experiments and drafted the initial manuscript. The third author initiated the project and helped direct revisions of the manuscript.

A.1 Background

Underwater robots, classified as either autonomous underwater vehicles (AUVs) or remotely operated vehicles (ROVs), have been used for exploration, reconnaissance, or sensing and monitoring [308, 309, 310, 311, 312, 313, 314, 315] of remote areas which are otherwise difficult to access. In the wake of disasters, these robots have been deployed for search and rescue efforts to locate and survey wreckage sites, or to evaluate and mitigate potential future risks from water contamination or other hazards such as mines [316]. In other scenarios, robots have provided means to identify and study lost or sunken archaeological artifacts [317], and for unobtrusive scientific observation of animal behavior [318]. More frequently, underwater robots are being deployed for inspection tasks to evaluate condition of critical infrastructure. With water environments comprising over 70% of the Earth's surface, and the economic value of aquatic activity in oceans and lakes for the US alone estimated at $352 billion in gross domestic product (2% of total GDP) for 2014 [319], the clear importance of proficiency in marine logistics underscores the demand for capable robots and technology suited to this domain.

In the broadest terms, underwater robots can be categorized into two main types by the strategy they utilize for locomotion: propeller driven and bioinspired swimmers. The former category includes the widest selection of underwater robots (and other water vehicles in general) by far, for which their basic drive method – the use of motorized spinning propellers - can be seen as the standard method for underwater locomotion and navigation [320]. In contrast to this conventional approach, the latter category includes a more diverse set of robots which utilize alternative mechanisms to derive propulsion under water. These actions can be described holistically as swimming, not only to differentiate from the other primary underwater locomotion method, but in part because they more closely resemble the natural actions and propulsion methods of biological animals described in the same way.

The majority of swimming robots are inspired by fish locomotion, with a variety of different swimming methods corresponding to an equivalent variety of species [321]. Some robots utilize the method of anguilliform swimming, generating low pressure zones along the body for thrust using whole-body wave motions, similar to lamprey and eels [322, 323, 324]. Other robots employ the more familiar carangiform method of body-coupled, tail driven swimming patterns to provide thrust analogous to the style of salmon, trout, or tuna [325, 326]. Completing the spectrum of fish inspired swimming techniques, another set of robots have leveraged the ostraciiform method which only directly uses the tail fin to generate thrust, as with the boxfish [327, 328].

An alternative bioinspired swimming method gaining interest for use in underwater robots is jet propulsion. This method has been explored through the development of synthetic jets [329, 330, 331, 332, 333, 334] to power underwater systems, as well as others which leverage biologically inspired morphology, including soft bodied robots inspired by cephalopods [335, 336, 337]. This form of thrust generation has attracted attention for its relative simplicity, robustness, and low-speed control fidelity in comparison to other methods [338]. A particular benefit of these qualities make jet propulsion an ideal candidate for producing small-scale robotic systems, either for use in constrained environments or in swarm applications which draw advantages from redundancy and large area coverage in low-cost, distributed robotic networks [339, 340, 341].

A small variety of simple, small-scale, and low-cost robots have drawn inspiration from lesser known jet-propelled swimmers of the underwater animal world, belonging to the class of bivalve mollusks. Scallop-inspired microscopic swimming robots exploit the dynamics of non-Newtonian liquids to generate forward motion from an induced change in fluid viscosity surrounding the robot [342]. While taking cues from their biological counterpart for overall shape and cyclic “flapping” or “clapping” motion behavior, these robots do not directly employ the fluid dynamic principles which drive natural scallop swimming. In nature, this capability is achieved by producing jets which propel the scallop forward via momentum exchange with high velocity water through two holes near the hinge of its upper and lower shells. While opening its shells, the scallop intakes water through soft, extensible velar lobes which are separated across the top and bottom of the large front opening. To perform a swimming stroke, the scallop rapidly closes from its fully opened position. During this rapid closing, the flexible lobes make contact across the shells sealing water in, causing the pressure inside the scallop to rise and propulsive jets to form out of the smaller openings near the rear hinge [343, 344, 345, 346, 347].

No robots are known to explicitly leverage the morphology and swimming technique of scallops as found in nature, however this method would enable systems which are a unique combination of robust to hazards or sustained use, safe in delicate environments, and simple by design. Scallop-inspired robots offer useful potential as an alternative to existing underwater robots which either pose risks of entanglement, environmental damage, or disruption, or feature more complex design and functional structure. Emulating natural animal behavior and comprising minimal moving parts, this robot concept illustrated in Fig. A.1 may find use in standard underwater AUV applications, including remote sensing, monitoring, and exploration, or in a variety of specialized tasks conducting work in delicate ecosystems or use in underwater robot swarms.

Objectives

In this work, a bioinspired robot, RoboScallop, is described which leverages the swimming principle employed by bivalve organisms for underwater locomotion. A simple, single-DoF mechanism for generating cyclic opening and closing of the structural valve, or shell, components of the robot is employed, while the use of a thin, stretchable membrane enables asymmetric impulse generation from water jet thrust for net forward motion. To quantify the utility of the robot for practical underwater robotic applications, its performance is characterized by measuring the jet force produced and the resultant swimming speed. Various benefits

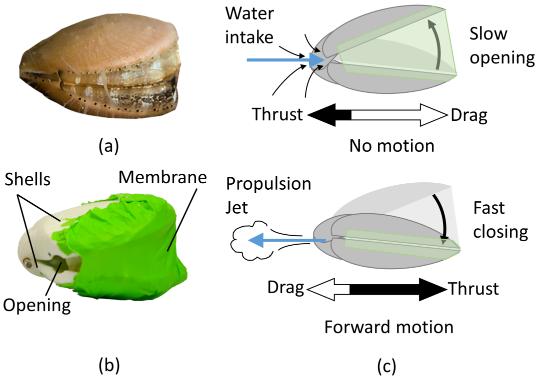

Figure A.1 – Scallop inspired robot locomotion. The morphology and function of a biological scallop depicted in (a) are reflected in the robot prototype shown in (b) which consists of two shells connected at a hinge and enclosed by a flexible elastic membrane. The robot and animal both achieve swimming by rapid, cyclic opening and closing of their shells to generate water jet thrust for propulsion. When the robot shells open, water is drawn into the body interior through rear openings near the hinge. Upon more rapid shell closing, the water is forced out backwards to produce a reaction force which facilitates net forward motion (c).

of the robot locomotion mechanism and morphology are discussed, including amenability to manufacturability and scalability through the use of a wide variety of methods and materials and various alternative drive mechanisms or low-cost robot swarms, hermetically sealed design, robustness in cluttered environments, and potential suitability for functional applications to actively filter or treat polluted water environments. In summary, we will demonstrate (1) a robust underwater swimming robot design based on the morphology and functionality of bivalve animals, including scallops, (2) forward thrust generated by a simple, single-DoF crank mechanism, and configuration dependent asymmetric drag, and (3) validation of locomotion effectiveness by experimental measurement of prototype robot in free swimming speed up to 16 cm/s (2 BL/s) with measured propulsion thrust of 1 N.

A.2 Mechanical Design

The RoboScallop robot approximates the morphology of a biological swimming scallop bivalve mollusk, consisting of two articulated shells, a soft, water-sealed connecting membrane structure spread between them, and single motor actuator as seen in Fig. A.2. Swimming is achieved via cyclic opening and closing (“flapping”) of the shells which draws water into the enclosed volume of the robot interior on the intake stroke (opening) and subsequently forces water out of openings at the rear to produce thrust. While the robot prototype is operated underwater, it receives electrical power through a tether of thin, insulated wire from a power supply located outside the water. Weight was minimized where possible in the design to enable faster swimming speeds, however the mass of all components was not distributed symmetrically across the robot. To offset the weight and balance its distribution, small pieces of closed cell insulation foam were glued to the inside of the shell strategically, until stable, neutral buoyancy was achieved.

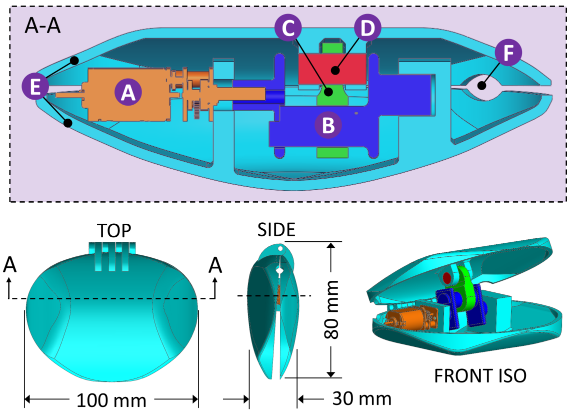

Figure A.2 – Mechanical overview of RoboScallop prototype. A 3D CAD model of the robot is shown in different views with a cross section through A-A depicting the critical components of the internal mechanism of the robot: A-motor, B-crankshaft, C-connecting arm, D-hinge pin, E-body shells, and F-intake/jet aperture. The front covering membrane is not shown.

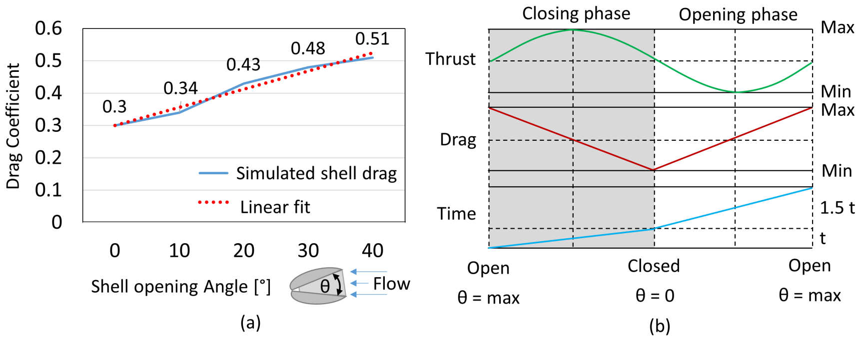

Figure A.3 – Steady state flow simulation of shell drag. Larger opening angles correspond to larger predicted drag coefficients (a). Drag is only considered from flow induced by relative motion of the robot in the forward direction (inset figure, indicated by arrows), which contributes to the net force acting on the robot during swimming; drag decreases during forward jet thrust (closing phase) and increases only during water intake while the shells are opening, as qualitatively illustrated in (b). A representative plot of the average opening and closing times for a single period of the swimming cycle is shown with a ratio of approximately 1.5:1.

A.2.1 Body components

Two rigid shells define the outer body shape of the robot, and provide structure for mounting the mechanical components used to generate cyclic opening and closing, or ‘flapping’ motion used in swimming. The shell components and integrated interior mounting structures were manufactured by fused-filament 3D printing of ABS plastic. A shell thickness of 2 mm was utilized to ensure sufficient rigidity under loading from the interior crank mechanism without causing visible deformation of the shell, while also maintaining low mass to achieve greater swimming performance. This dimension was chosen experimentally through various prototype iterations however, and was not formally optimized to maximize strength or minimize weight.

The overall contour and size of the body was modeled after the shape of scallop shells to reduce drag in water and achieve hydrodynamic efficiency at least similar to that of biological counterparts. A flow simulation using a 3D model of the shell and Solidworks Flow Simulation software was conducted to assess the drag coefficient of the designed body shape at different opening positions in constant fluid flow. The results of the simulation analysis are shown in Fig. A.3 (a) and indicate roughly linearly increasing drag for increasing shell opening angles. While the forward motion of scallops can be directly attributed to the thrust produced by water jets for propulsion, the difference in drag at different opening angles in relation to varying points of the swim cycle also indirectly contributes to enhance this net forward progress. When the robot shells are open, drag is at a maximum and forward thrust is at its minimum. When the shells are closed following a power stroke, forward thrust is approximately at its maximum. In this way, with complementary, inverted cycles of drag and thrust, resistance to forward motion is minimized. At the same time, the increased drag at different shell angles is expected to oppose motion in the reverse direction with the opposite trend. During the shell opening phase of the swimming cycle, the reverse thrust is at maximum when the drag is also maximum, and similarly minimal when the drag is also minimal. These phases are illustrated in Fig. A.3 (b). This convenient characteristic of drag beneficially coupled to thrust cycles plays a unique role in facilitating unidirectional forward swimming in scallop inspired locomotion.

A continuous, elastic membrane made from 0.1 mm thick synthetic soft nitrile polymer spans the opening of the articulated shells to seal the inner volume of the robot along the front edge where it is affixed in place with cyanoacrylate glue. The function of the membrane is similar to that of the velar lobes of biological scallops, with the exception that it is always intact and covering the front opening of the robot. With the membrane affixed in this way in contrast to the natural configuration of scallops, water enters the shells from the the rear of the robot rather than the front. When the shells start to close, all of the internal water is pressurized against the shell sides of the robot as well as the membrane. The membrane limits water from escaping through the front and forces it back inside the robot and out through rear aperture holes 4 mm in height and 10 mm in width to the sides of the hinge connecting both shells.

In addition to directing the flow of water used for thrust, the membrane helps to also balance moments produced by external hydrodynamic forces which develop over the shells during swimming. These forces have been studied and modeled in previous work for biological scallops with comparable morphology to the robot prototype [348]. As described for scallops, a velocity dependent effect termed pseudo-viscosity acts to continually open the shells of the robot when moving forward. The force of the membrane as it stretches during opening resists this moment, reducing the shell opening speed and torque load on the motor during closing. Additionally, external hydrodynamics produce an asymmetric pseudo-elasticity torque effect proportional to shell angle, which assists in opening but resists shell closing. Again, the membrane acts to balance the moment from these external forces, resisting the opening force and assisting in closing to increase the closing speed and reduce the speed of opening.

For the RoboScallop prototype robot, the difference in the duration of these events, with slower shell opening times and faster closing, helps produce greater thrust from water expulsion on the closing stroke than that from low pressure at the rear shell apertures generated on opening. Although this difference is not the main mechanism attributed to biological scallop swimming, it becomes a dominant factor for the robot which cannot intake water from the front.

A.2.2 Reciprocating Mechanism

The opening and closing of the robot is enabled by a 3D printed crank mechanism which is powered by a 12 V DC motor. The motor was chosen primarily because of its weight (9.5 g), size (10 × 12 × 26 mm), and speed (330 rpm, free) which roughly corresponds at 5.5 Hz to the frequency of biological scallop swimming of 3-5 Hz [21]. No effort was made to isolate or seal the motor and its internal components from water penetration, which allowed only short term use of the gearmotor before replacement was necessary. The mechanical structure of the prototype including the crank mechanism and body shells are shown in Fig. A.2.

A.3 Principles of RoboScallop Locomotion

The equation for thrust, T, can be borrowed from previous literature on squid locomotion to describe the mechanism of swimming for the RoboScallop [349], as shown in Eq. A.1. Both species produce thrust from momentum exchange with water ejected at their rear through small openings, derived from a single pressurized cavity contained within the animal body which is filled and expelled cyclically.

$$T = \rho Q u = \frac{\rho Q^2}{A} = \frac{\rho}{A}\left(\frac{\Delta V}{\Delta t}\right)^2 \tag{A.1}$$

In this equation, Q and u are the flow rate and velocity of the water through the jet orifice, respectively, and ρ is the water density. The volumetric flow rate can be represented by $Q = \Delta V / \Delta t$ as the change in cavity volume, V, over a corresponding change in time t, and the velocity can be written as $u = Q/A$. The variable A represents the cross sectional area of the jet orifice.

Like squid, since a single orifice at the rear of the RoboScallop is used for both water intake and jet propulsion, thrust is produced in both strokes of a swimming cycle but in opposite directions. The main condition for achieving net forward motion is that the forward thrust from jet propulsion during shell closing is greater than that from intake during shell opening, or $T_{closing} > T_{opening}$. Due to the cyclic swimming motion, $\Delta V_{closing} = \Delta V_{opening}$ and Eq. 1 simplifies to

$$\Delta t^2_{opening} A_{opening} > \Delta t^2_{closing} A_{closing} \tag{A.2}$$

which indicates that the magnitude of thrust produced is primarily a function of the time duration of the water jet, and the area of the orifice through which the jet is formed. If the area of the orifice is equal or nearly similar for both the opening and closing stroke, the net thrust is dictated by the difference in time spent during each phase, where faster relative closing time results in forward jet propulsion. Alternatively, equal phase timing can still produce net forward thrust over a swimming cycle by modulating the size of the orifice, reducing the cross sectional area during the closing stroke and increasing it during the opening, refill stroke.

Due to the fixed size of the shell orifice and the symmetry imposed by the cyclic mechanism for driving the shells, the RoboScallop employs only the first of these strategies to generate forward thrust. A difference in timing is, however, observed between opening and closing, and is indeed designed into the device through two main features: the orientation of the inner crank mechanism which produces asymmetric, non-harmonic oscillation as well as the presence of the elastic membrane across the shells which acts to resist motion in opening and assist in closing. From video tracking analysis, the ratio of opening times to closing times was found to be approximately 1.5:1, where the time interval of each phase was averaged from multiple successive video frames.

Scallops, in comparison, generate most of their thrust only in the forward direction by expelling water through rear jets, and by taking water in from the sides and front. We define the scallop swimming cycle as having only these two distinct phases, distinguished by the relative direction of shell motion either toward (closing) or away (opening) from each other. The effect of timing in the opening and closing phases of scallop swimming is not regarded as the dominant contribution to forward thrust, although it has been attributed to some portion of it. A difference in timing is observed in natural scallop swimming when these two phases are defined strictly by shell angular velocity [345]. Further evidence of this differential phase timing effect also exists in [346], where increases in whole-body performance metrics were measured (faster swimming speeds and higher acceleration) in association with decreased closing (adduction) times relative to opening (abduction) at higher environmental temperatures. Even for non-jetting species such as jellyfish, differential timing in cyclic swimming is

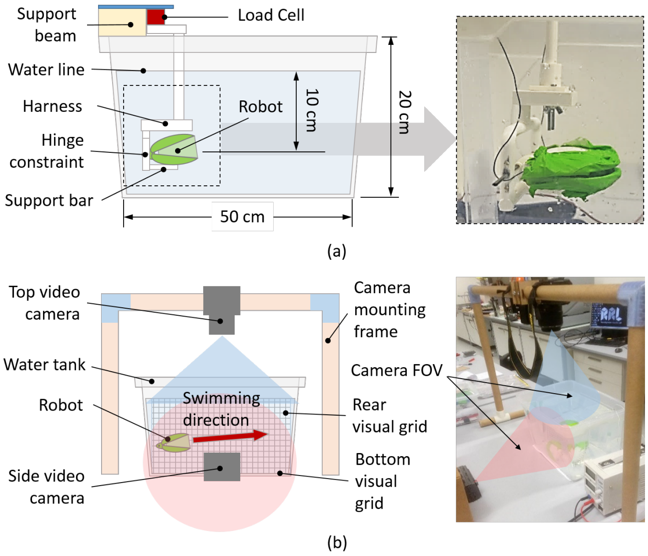

Figure A.4 – Experimental setups. The jet thrust blocked force test setup is depicted in (a). The test was conducted in a benchtop water tank using a rigid 3D printed harness to connect the robot held under water to a load cell mounted outside of the water. The free swimming speed test setup is shown in (b). Video cameras positioned above and in front of the translucent water tank captured the swimming trajectory of the robot for a series of swimming trials. The speed of the robot was estimated using video time data and a background grid pattern behind and below the tank, visible within each camera's field of view (FOV) for distance calibration.

also leveraged for locomotion, and has been demonstrated through prototypes in prior work [350, 351].

A.4 Experiments

A.4.1 General testing procedure

For all tests, electrical power was provided through a two-wire tether (1 m) from a power supply, routed symmetrically through the back side of the robot with one wire on each side of the hinge. To avoid physical interference with the robot during testing, the main power switch of the power supply was used for control, to activate and deactivate the drive motor. For the long distance free swimming test, an extra long tether (3 m) of flexible wire was utilized for extended range of motion.

For each of the three main tests conducted at different times and described in following sections, a new DC gearmotor was used to reduce the effect of component degredation on robot performance. While this may have introduced other effects from variability in the specific motor components and general robot assembly affecting any differences between tests, this is expected to be less than the effect from motor corrosion, which led to observable loss of speed and power between consecutive days of use.

A.4.2 Blocked force jet characterization

The force created by the propulsive jets was measured by placing the robot in a rigid harness suspended from above into a benchtop water tank to simulate a blocked force swimming condition. The top of the harness was attached to a Nano17, 6-axis load cell mounted above and outside of the water, which measured the force output of the robot produced by cyclic shell flapping. The harness and the robot were connected underwater through the shell hinge joint to prevent rotation of the robot along its horizontal and vertical axis. Rotation of the robot body about the axis of the hinge joint was limited by a bar supporting it in a horizontal resting position. The shells of the robot were still free to open and close as in normal swimming conditions since the motion of the upper shell was not impinged. The experimental setup can be seen in Fig. A.4a.

Measurements of the propulsive force were taken at different flapping frequencies, which were set by supplying a range of DC voltages to the mechanism drive motor. Within the operating range of the motor from 6 V to 12 V, measurements were taken at 2 V increments for a total of four trials. This voltage range corresponded to flapping frequencies ranging from 1.4 to 2.6 Hz. For each trial, the robot was run in the test setup described above for at least 10 cycles of flapping while the force on the load cell was logged continuously at a rate of 100 Hz, more than an order of magnitude above the expected flapping frequency.

The blocked force load cell measurements for each different flapping frequency trial were first segmented into single strokes identified by peaks in the qualitatively sinusoidal data. The ten individual strokes per trial were then interpolated and averaged to obtain a representative force profile over time for every condition. This profile was then analyzed by taking its time integral to calculate the impulse per stroke (one period), and by measuring the time T of the average profile to calculate the measured flapping frequency f as $1/T$. A separate integral was taken over the positive and negative force regions of each profile to yield positive, J_{pos}, and negative, J_{neg}, impulse produced, respectively. These values were summed to also obtain a net impulse, J_{net}, which determines the ultimate trajectory of the robot, with positive net impulse values corresponding to forward motion.

A.4.3 Swimming speed characterization

The speed of RoboScallop in free swimming was measured at different operating voltages, corresponding to different clapping frequencies, as described in the jet force characterization section. The benchtop water tank was again used but the robot was not constrained by a harness. The experimental setup is shown in Fig. A.4b. For the highest clapping frequency and resulting jet force, at least 10 swimming cycles were possible across the length of the tank. Measurements of the robot position were taken using video cameras and a visible background grid pattern comprised of one centimeter spaced lines for scaling reference. The grid was used to measure the distance traveled by the robot, marked by the joint center of the shell hinge, over a duration of elapsed time obtained from the difference between frame timestamps of the recorded video. The straight line distance between initial and final positions from the side view was used to calculate the speed over the measured timeframe, and accounted for motion in the horizontal and vertical plane. Lateral position deviations were neglected in this measurement of speed as the majority of motion produced by the jet propulsion was observed to be in the forward and upward directions. This test was repeated at least 5 times for each voltage input and from these quantities an average speed measurement was determined.

A second, simplified robot prototype was also tested to demonstrate to an extent the effect of outer shell shape on swimming speed. While all other aspects of its mechanical design remained equivalent to the biologically inspired design, this prototype featured square edged shells and a box-like shape. Three swimming trials were conducted in the benchtop water tank, and visually recorded with a camera in the same setup used in prior experiments.

A.4.4 Free swimming

A large (2 m x 6 m), shallow (30 cm depth) indoor pool was used to allow the robot to swim greater distances than possible in the benchtop water tank. This test was performed to visualize and study the performance of the robot in a more realistic setting of a large body of water, to minimize possible effects from water jet and flow interference with the tank walls. A waterproof GoPro Hero3 camera with a wide angle lens was used to capture the swimming behavior of the robot from underwater, set back the full width of the pool away to obtain the longest possible continuous recording as the robot swam across the camera in the direction of the pool length. No grid pattern or calibration features were used in this test to calculate speed, but overall distance traveled and average speed was estimated using the body length as a scale. The accuracy of this method was limited however, since the robot was observed to turn as it swam and the motion was not captured by the underwater camera which was alongside the robot, in the plane of the lateral deviation.

A.5 Results

A.5.1 Jet force

Our robot was shown to generate asymmetric thrust, with greater forward impulse than in the reverse direction, to achieve net forward motion. The quantified results of the jet force characterization test are shown in Fig. A.5. The robot produced a maximum peak thrust of 1.00 N, measured above 10 V, where the net impulse magnitude appears to saturate. In Fig. A.5b it is evident that above this control voltage corresponding to a swimming frequency of 1.4 Hz, the value of net impulse remains generally constant. The thrust measured closely matches results from similar experiments with biological scallops which generated 1.15 N of thrust impulse [346].

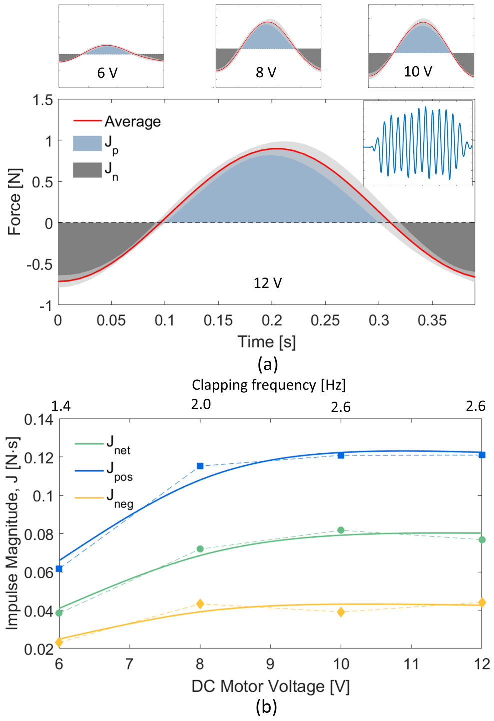

(a)

(b)

Figure A.5 – Jet force profile and thrust impulse in blocked force test. The average force output of the RoboScallop prototype over a 10 cycle blocked force test is shown in (a) with shaded regions representing the impulse produced. The test was repeated for several operating voltages between 6 and 12V, yielding different flapping frequencies between 1.4 and 2.6 Hz. For each test, the positive and negative regions of impulse are summed to calculate a net impulse which quantifies the effectiveness of the robot's locomotion. The relationship of impulse to driving frequency or DC motor voltage input is represented in (b), which indicates a limit to the thrust force produced by the robot. Square points represent the calculated impulse totals for different inputs, while the solid curve shows a spline fit.

Table A.1 – RoboScallop prototype parameters.

PROPERTY	SPECIFICATION
Dimensions	80 x 100 x 30 mm
Mass	65 g
Speed	16 cm/s or 2 BL/s (max)
Clapping frequency	2.6 Hz (max)
Actuators	Pololu HPCB Micro Metal Gearmotor, 100:1
Power	12V, 380 mA (typical), 560 mA (peak)

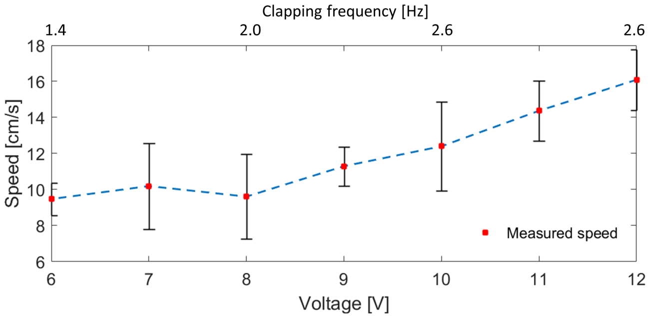

Figure A.6 – Swimming speeds measured in benchtop test. The swimming speed of the biologically inspired robot prototype is shown for varying input voltages. Red points represent the average measurement while error bars depict a single standard deviation for five trials.

A.5.2 Swimming speed

The fastest swimming speed we recorded for our robot with the benchtop water tank setup was 16 cm/s, or 2.0 Body Lengths/s (BL/s), obtained using a 12 V motor input to produce a 2.56 Hz flapping frequency. These free swimming speeds were also validated in tests conducted in a large open pool, which eliminated any effects that could have been caused by waterjet reaction force against the wall of the relatively small benchtop water tank. Fig. A.6 shows the measured speeds for varying input voltages.

The simplified shell prototype also tested in the benchtop setup can be seen in Fig.A.7. A linear fit was calculated for each of three swimming trials conducted, and the fits were then averaged to obtain an overall average swimming trajectory over time. The slope of this trajectory represented the average swimming speed over the three trials, and was found to be 10 cm/s or 1.3 BL/s. The results indicate a slower swimming speed with this design as expected. Notably however, vertical displacement coupled to the forward movement of the robot was also captured by the tracked marker position. While this was observed in both prototypes, the effect was most prevalent in the simplified, boxy version. In living scallops, this effect is widely known already, and used to achieve liftoff into open water from the seabed where they generally rest. Certain studies have in part attributed this directly to swimming velocity and body size [352], the former of which can be actively controlled to a degree by changing the waterjet opening at the rear of the animal, or regulated by varying the burst time of activation much like pulse width modulation. Although the exact mechanism which affects this forward and upward thrust coupling are beyond the scope of this study, it is worth future investigation as a method for underactuated control of movement in both dimensions for scallop inspired of other types of robots.

A.6 Discussion

The maximum speed measured for both the biologically inspired and simplified shell design is faster than the biological *Limaria Fragilis* scallop (3.64 cm/s), and slower than *Aequipecten opercularis* (37 cm/s) [344, 346]. In part these comparisons to biological scallops do not fully represent the performance capabilities of the robot however, as the swimming function in

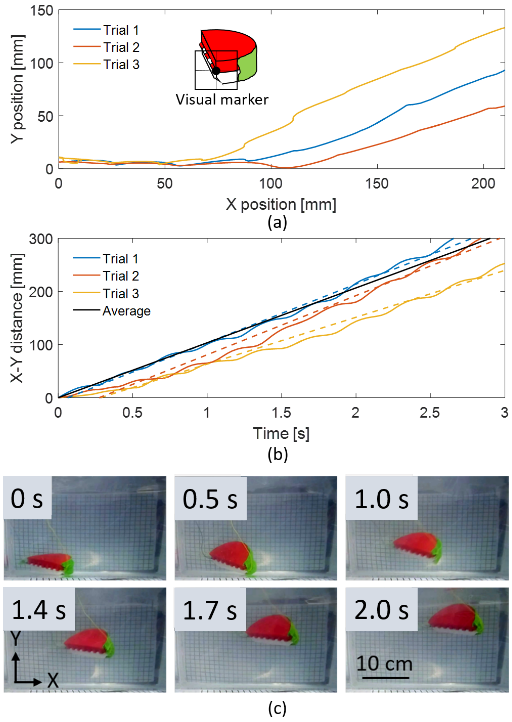

(a)

(b)

(c)

Figure A.7 – Trajectory and time series of RoboScallop prototype. The displacement of a visual marker located on the robot was tracked using a video camera for three swimming trials, and is shown in (a), while this trajectory over time can be seen in (b), where the average speed was found to be 10 cm/s for the depicted trials. A time series of video frames from one trial conducted in a benchtop water tank is shown in (c) using the simplified shell shape prototype.

the animals is primarily used for short distance escape maneuvers[343, 346], and does not allow sustained swimming for long periods of time due to adductor muscle fatigue [353] combined with the relatively poor efficiency of aquatic jet-propulsion itself, cited in prior work to be a factor of roughly three times lower for squid compared to fish of similar size [345]. Although the inefficiency of locomotion is fundamental to this style of swimming and thereby an inherent limitation of this robot design, the physical limitation of muscle (or motor) saturation is not present in the robot prototype, which can operate continuously to the limit of available electrical power. The current version of the robot receives power from an off-board supply which allows indefinite use, however, it is not without the limitations of a tether. The effects of tether drag or entanglement (through water and against test barriers) were assumed negligible for characterization of swimming performance because they were performed with thin, lightweight wires in wide, smooth, and uncluttered spaces, however this feature would hinder the effectiveness of such a system in more complex environmental conditions.

Future versions for use in the real world without a tether would incorporate on-board battery power and any control electronics. While the space and power available would vary with the size of an onboard battery, the design is fundamentally adaptable to different scales. Due to the generally self-contained design without exposed moving parts, such as fins, rudders, or spinning propellers, a design which includes onboard power would also be inherently robust in cluttered environments. Scallop inspired locomotion could be beneficial where entanglement presents a risk to the robot, or in other applications where the robot might pose a risk to the environment, such as operating near and around delicate ecosystems like a coral reef. Although some simple solutions exist to improve the robustness of more conventional underwater vehicles, including the use of ducts or hubless propellers to decrease entanglement risks [354], the bioinspired RoboScallop design does not utilize high velocity spinning components and is thus less susceptible to impact from small particle debris including sand, rocks, or shells, as well as relatively more safe to any small organisms which might other be harmed by fast spinning blades.

In order to improve the practical utility of the robot prototype, future versions would also incorporate a mechanism to allow directional steering, although some applications may not require this. Biological scallops are known to exhibit directional changes during swimming that follow an alternating pattern which results in a “zig-zag” trajectory, thought to be useful in evading predators. This strategy was found to be voluntary and independent of clapping motion used to produce thrust [355], and thought to be the result of a mechanism in place for regulating the flow at either of the two rear hinge openings where propulsive water jets are formed, although scallops are still generally regarded as having only one primary muscle used for locomotion. In a similar way, a future robot prototype could be developed using small scale actuators (joule heated shape memory alloys) for the sole purpose of changing the area of the jet orifice to reduce or increase the exit water velocity and jet thrust produced. By changing thrust produced at each orifice independently, a mechanism for steering could be implemented without the addition of additional drive mechanisms or rudders.

A.6.1 Design scalability and immediate applications

Utilizing only a reciprocating crank mechanism and a single drive motor, the simple design of the robot presented here is generally scalable to other dimensions, through various other materials, manufacturing methods, and alternative drive sources (Shape Memory Alloy actuators, voice coils, for example), although only one example robot prototype design was tested at a relatively high Reynolds number (Re). Similar to biological scallops, this prototype is relevant for swimming in fluids with Re on the order of 10^4. At very small scales, where Re is very low, the mechanism shown here may cease to function as a consequence of the Scallop Theorem that requires nonreciprocal motion as a condition for swimming in this regime. Furthermore, the efficiency of larger scallop locomotion in nature has been found to be lower than smaller ones [352]. Nevertheless, this may only be due to disproportionate scaling of mass and non-optimized hydrodynamic characteristics in animals which could be improved in engineered robots. Even without significant additions or improvements however, such robots as developed here could be used already for simple applications such as self-distributing sensor networks for communication or exploration, or water treatment operations. As the principle of operation for scallop inspired swimming is effectively that of a water pump, the integration of a filter or sensor in addition to the benefit of intrinsic mobility could offer a significant advantage in environmental cleaning or monitoring over large, remote areas utilizing a two-in-one solution. Moreover, the simplicity of the design is amenable to mass production of robot swarms to accomplish such tasks even more efficiently.

A.7 Conclusion

In this work, we studied the performance of a novel underwater locomotion method inspired by various bivalve species, including scallops, for use in expanding the accessibility and capability of operations in underwater environments. A prototype swimming robot was designed, fabricated, and tested in laboratory environments to measure the thrust generated and resulting swimming speed for different operating inputs. The experimental testing of the robot revealed the useful potential in achieving mobility with few and simple parts, suitable for developing future underwater swimming robots at various scales of size and number. These features which favor low fabrication and development costs allow such underwater robots to be employed in more locations and applications than previously feasible, leveraging the robust, bioinspired design and function adapted from bivalve swimming, compatible with a range of underwater environments.

B Rando: Passive dynamic walking robot for under $50

A low-cost bi-pedal walking robot kit with limited actuation and sensing capabilities was designed and built to achieve actively powered, passive dynamic walking locomotion over level ground. The walking system is composed of readily available parts and materials totaling less than $50 and can be assembled either from plans or pre-fabricated parts in less than a day. Indeed, the very first (and only) prototype was conceived and built in one day, and capable of walking within two more. In place of components utilized for the prototype shown and demonstrated, alternative parts and materials can be substituted and accommodated by relatively simple design changes, allowing this robot construction to be adapted to different resource availability, in some cases key to the success of research or education.

B.1 Introduction

Walking robots are fast becoming a new fixture of reality and not just a futuristic or academic curiosity. The main case in point of this is the current dominance of non-academic organizations leading the way in the development and implementation of sophisticated hardware and software for a variety of arguably very successful mobile walking platforms [357, 358]. While the most state-of-the-art robots have demonstrated advanced capabilities pushing the borders of research into daily application, their recent showcase at the DARPA Robotics Challenge has emphasized opposing and equally valid conclusions about the current state of the field: (1) walking robots are close to becoming useful in a practical sense, however, (2) there is plenty of work still left to be done to improve even the most advanced systems.

The material presented in this chapter is adopted from the following self-authored publications:

[356] **M. A. Robertson**, J. Paik, A. Ijspeert and A. Wu. "A low-cost, actuated passive dynamic walker kit for accessible research and education," *Talk at Dynamic Walking Conference*, Mariehamn, Finland, 2017.
The first author designed and fabricated the robot. The fourth author helped initiate the project, designed and programmed a working controller, and was consulted on robot design. The first and fourth author both contributed to the manuscript, and the second and third authors provided the resources necessary for completion of this project.

Among the many foreseeable improvements, first most including robustness, agility, and efficiency, the latter has been a favored topic among researchers in the community aiming to leverage the passive behavior of robotic systems to reduce the amount of energy required for over-ground walking. Many walking systems have been developed over the last few decades which take advantage of passive dynamics in this way to accomplish under-actuated walking [359, 360, 361, 362].

Furthermore, this effort has drawn interest and inspiration from work beyond the field of robotics, in biology [363, 364], biomechanics [365], biomedical engineering [366], neural systems and rehabilitation [367, 368], and mathematics [369]. In these applications, using robotic prototypes as test platforms to evaluate biological and scientific principles has proven to be a useful strategy.

Nevertheless, this approach is limited if only at the very least by the practical problem of accessibility. Nearly every study of passive dynamic walking for any purpose has been conducted using unique, and custom built platforms, although the precise functionality of those systems only varies slightly. This produces redundancy in design effort, and inherently restricts the undertaking to institutions, laboratories, or research groups with both the material and personnel resources to initiate and execute the development of a walking robot from scratch – which may be out of reach even for minimalist designs, and especially to non-engineering related fields.

For the benefit of such underequipped groups with practical interest in relevant research, we present a highly cost-effective robotic kit capable of passive dynamic locomotion to extend the availability of technology and methods conventionally reserved for only a narrow field. Current walking robot platforms vary from very expensive, highly capable machines to more specific prototypes with limited functionality built to study or demonstrate only certain concepts. Even the more simple devices, however, are built more or less at the human scale, requiring powerful motors, and high strength materials. This presents inhibitive monetary and safety costs, which in turn prevents their widespread adoption as viable tools for any variety of scientific or educational purposes.

B.2 Methods

Our servo-actuated passive walker, dubbed *Rando*, is built from simple, affordable components to accommodate a small scale yet conceptually functional device that can be easily built or assembled by non-technical researchers or educators (see Figure B.1). This provides the opportunity for more people to become involved in the exploration of advanced concepts involved in dynamic walking.

The primary objective in the design of an affordable passive walker was to enable generally non-technical users to fabricate or assemble a working walking device. For this reason, we followed a first principles approach in the selection of parts and materials, neglecting the

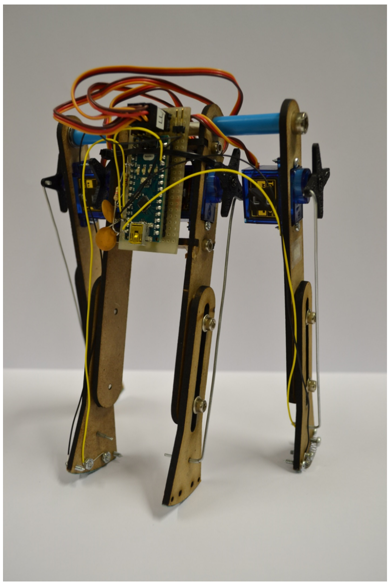

Figure B.1 – Rando: a low-cost, open-source walking robot.

paradigms established by many existing robotic prototypes in the world of research, and focusing more on parts and fabrication methods found in the hobby community. As one example, the use of aluminum and other metals was avoided for the requirement that the kit materials be easy to custom fabricate or modify, while still being robust. Instead, lightweight yet strong 3mm MDF board was chosen for the main structural components of the walker. This material is common to the hobby world as it facilitates easy cutting with a CNC laser, requiring only a 2D part file generated from any vector graphic software.

Functionally, Rando embodies a 4-legged bipedal passive walker with one primary difference: the ability to retract and extend its legs linearly for ground clearance and push-off, respectively. This motion is enabled by 9-gram onboard servos typically employed in hobby aircraft, connected by a stiff wire push-rod to the movable lower leg (the "foot"). Two sets of legs, an outer and inner pair, are constrained to rotate freely at the top through a common axis. The final critical mechanical element of the Rando is a pair of foot switches, one for each independent leg, each custom fabricated from compression springs. These sensors act as the only feedback to the system by activating reflexes for push-off, ground clearance, and extension without any prescribed gait pattern. Finally, the active response of the legs is delegated by an on-board Arduino Nano microcontroller.

B.3 Results and Discussion

A complete Rando prototype was built, tested and successfully achieved stable passive dynamic walking. The prototype, like many unpowered passive dynamic walkers exhibits sensitivity to initial conditions which make it difficult at times to initiate gait, but the simple reflex-based control scheme allows recovery and convergence on a stable gait for a small range of initial conditions around a presumed optimal.

While for the present version of Rando power is supplied through a tether from a supply unit, a future design incorporates a 9-volt battery onboard to also serve as a mass balance in place of passive hardware (washers) currently employed, which will allow for fully autonomous function.

Bibliography

[1] J. L. Pons, *Wearable Robots: Biomechatronic Exoskeletons.* John Wiley & Sons, Apr. 2008, google-Books-ID: ovCkTEKEmkkC.

[2] E. Guizzo and H. Goldstein, "The rise of the body bots [robotic exoskeletons]," *IEEE Spectrum*, vol. 42, no. 10, pp. 50–56, Oct. 2005.

[3] K. Kiguchi and Y. Hayashi, "An EMG-Based Control for an Upper-Limb Power-Assist Exoskeleton Robot," *IEEE Transactions on Systems, Man, and Cybernetics, Part B (Cybernetics)*, vol. 42, no. 4, pp. 1064–1071, Aug. 2012.

[4] S. Balasubramanian, a. M. Perez, B. Shepard, E. Koeneman, and J. K. and, "RUPERT: An exoskeleton robot for assisting rehabilitation of arm functions," in *2008 Virtual Rehabilitation*, Aug. 2008, pp. 163–167.

[5] J. Iqbal, N. G. Tsagarakis, and D. G. Caldwell, "Four-fingered lightweight exoskeleton robotic device accommodating different hand sizes," *Electronics Letters*, vol. 51, no. 12, pp. 888–890, May 2015. [Online]. Available: https://digital-library.theiet.org/content/journals/10.1049/el.2015.0850

[6] L.-F. Yeung, C. Ockenfeld, M.-K. Pang, H.-W. Wai, O.-Y. Soo, S.-W. Li, and K.-Y. Tong, "Design of an exoskeleton ankle robot for robot-assisted gait training of stroke patients," *IEEE ... International Conference on Rehabilitation Robotics: [proceedings]*, vol. 2017, pp. 211–215, 2017.

[7] A. R. Wu, F. Dzeladini, T. J. H. Brug, F. Tamburella, N. L. Tagliamonte, E. van Asseldonk, H. van der Kooij, and A. J. Ijspeert, "A Versatile Neuromuscular Exoskeleton Controller for Gait Assistance: A Preliminary Study on Spinal Cord Injury Patients," in *Wearable Robotics: Challenges and Trends*, ser. Biosystems & Biorobotics, J. González-Vargas, J. Ibáñez, J. L. Contreras-Vidal, H. van der Kooij, and J. L. Pons, Eds. Springer International Publishing, 2017, pp. 163–167.

[8] A. Chu, H. Kazerooni, and A. Zoss, "On the Biomimetic Design of the Berkeley Lower Extremity Exoskeleton (BLEEX)," in *Proceedings of the 2005 IEEE International Conference on Robotics and Automation*, Apr. 2005, pp. 4345–4352.

[9] P. H. Nguyen, C. Sparks, S. G. Nuthi, N. M. Vale, and P. Polygerinos, “Soft poly-limbs: Toward a new paradigm of mobile manipulation for daily living tasks,” *Soft robotics*, 2018.

[10] V. Vatsal and G. Hoffman, “Wearing your arm on your sleeve: Studying usage contexts for a wearable robotic forearm,” in *Robot and Human Interactive Communication (RO-MAN), 2017 26th IEEE International Symposium on.* IEEE, 2017, pp. 974–980.

[11] C. Davenport, F. Parietti, and H. H. Asada, “Design and biomechanical analysis of supernumerary robotic limbs,” in *ASME 2012 5th annual dynamic systems and control conference joint with the JSME 2012 11th motion and vibration conference.* American Society of Mechanical Engineers, 2012, pp. 787–793.

[12] I. Hussain, G. Salvietti, G. Spagnoletti, D. Cioncoloni, S. Rossi, and D. Prattichizzo, “A Soft Robotic Extra-Finger and Arm Support to Recover Grasp Capabilities in Chronic Stroke Patients,” in *Wearable Robotics: Challenges and Trends*, ser. Biosystems & Biorobotics, J. González-Vargas, J. Ibáñez, J. L. Contreras-Vidal, H. van der Kooij, and J. L. Pons, Eds. Springer International Publishing, 2017, pp. 57–61.

[13] Milia, “Neurorehabilitation in paraplegic patients with an active powered exoskeleton (Ekso).” [Online]. Available: http://www.digitmedicine.com/article.asp?issn=2226-8561;year=2016;volume=2;issue=4;spage=163;epage=168;aulast=Milia

[14] V. Lajeunesse, C. Vincent, F. Routhier, E. Careau, and F. Michaud, “Exoskeletons’ design and usefulness evidence according to a systematic review of lower limb exoskeletons used for functional mobility by people with spinal cord injury,” *Disability and Rehabilitation: Assistive Technology*, vol. 11, no. 7, pp. 535–547, Oct. 2016. [Online]. Available: https://doi.org/10.3109/17483107.2015.1080766

[15] R. Riener, “The Cybathlon promotes the development of assistive technology for people with physical disabilities,” *Journal of NeuroEngineering and Rehabilitation*, vol. 13, no. 1, p. 49, May 2016. [Online]. Available: https://doi.org/10.1186/s12984-016-0157-2

[16] S. Haddadin and E. Croft, “Physical Human–Robot Interaction,” in *Springer Handbook of Robotics*, ser. Springer Handbooks, B. Siciliano and O. Khatib, Eds. Cham: Springer International Publishing, 2016, pp. 1835–1874. [Online]. Available: https://doi.org/10.1007/978-3-319-32552-1_69

[17] P. A. Lasota, T. Fong, and J. A. Shah, “A Survey of Methods for Safe Human-Robot Interaction,” *Foundations and Trends® in Robotics*, vol. 5, no. 4, pp. 261–349, May 2017. [Online]. Available: https://www.nowpublishers.com/article/Details/ROB-052

[18] R. Du, S. Feng, P. Franklin, M. Gennert, J. P. Graff, P. He, A. Jaeger, J. Kim, K. Knoedler, L. Li, C. Y. Liu, X. Long, T. Padir, F. Polido, G. G. Tighe, and X. Xinjilefu, “What Happened at the DARPA Robotics Challenge , and Why ?” 2015.

[19] H. Rodrigue, W. Wang, M.-W. Han, T. J. Kim, and S.-H. Ahn, “An Overview of Shape Memory Alloy-Coupled Actuators and Robots,” *Soft Robotics*, vol. 4, no. 1, pp. 3–15, Feb. 2017. [Online]. Available: https://www.liebertpub.com/doi/full/10.1089/soro.2016.0008

[20] H. Jin, E. Dong, M. Xu, C. Liu, G. Alici, and Y. Jie, “Soft and smart modular structures actuated by shape memory alloy (SMA) wires as tentacles of soft robots,” *Smart Materials and Structures*, vol. 25, no. 8, p. 085026, Jul. 2016. [Online]. Available: https://doi.org/10.1088%2F0964-1726%2F25%2F8%2F085026

[21] T. Chen, O. R. Bilal, K. Shea, and C. Daraio, “Harnessing bistability for directional propulsion of soft, untethered robots,” *Proceedings of the National Academy of Sciences*, vol. 115, no. 22, pp. 5698–5702, May 2018. [Online]. Available: https://www.pnas.org/content/115/22/5698

[22] Y. Yang, Y. Chen, Y. Li, M. Z. Chen, and Y. Wei, “Bioinspired Robotic Fingers Based on Pneumatic Actuator and 3d Printing of Smart Material,” *Soft Robotics*, vol. 4, no. 2, pp. 147–162, Feb. 2017. [Online]. Available: https://www.liebertpub.com/doi/full/10.1089/soro.2016.0034

[23] M. Duduta, D. R. Clarke, and R. J. Wood, “A high speed soft robot based on dielectric elastomer actuators,” in *2017 IEEE International Conference on Robotics and Automation (ICRA)*, May 2017, pp. 4346–4351.

[24] C. T. Nguyen, H. Phung, T. D. Nguyen, H. Jung, and H. R. Choi, “Multiple-degrees-of-freedom dielectric elastomer actuators for soft printable hexapod robot,” *Sensors and Actuators A: Physical*, vol. 267, pp. 505–516, Nov. 2017. [Online]. Available: http://www.sciencedirect.com/science/article/pii/S0924424717309354

[25] N. Kellaris, V. G. Venkata, G. M. Smith, S. K. Mitchell, and C. Keplinger, “Peano-HASEL actuators: Muscle-mimetic, electrohydraulic transducers that linearly contract on activation,” *Science Robotics*, vol. 3, no. 14, p. eaar3276, Jan. 2018. [Online]. Available: http://robotics.sciencemag.org/content/3/14/eaar3276

[26] L. Hines, K. Petersen, G. Z. Lum, and M. Sitti, “Soft Actuators for Small-Scale Robotics,” *Advanced Materials*, vol. 29, no. 13, p. 1603483, Apr. 2017. [Online]. Available: https://onlinelibrary.wiley.com/doi/full/10.1002/adma.201603483

[27] K. C. Galloway, P. Polygerinos, C. J. Walsh, and R. J. Wood, “Mechanically programmable bend radius for fiber-reinforced soft actuators,” in *2013 16th International Conference on Advanced Robotics (ICAR)*, Nov. 2013, pp. 1–6.

[28] M. A. Robertson, H. Sadeghi, J. M. Florez, and J. Paik, “Soft pneumatic actuator fascicles for high force and reliability,” *Soft Robotics*, 10 2016, [Online; accessed 2016-11-04]. [Online]. Available: http://online.liebertpub.com/doi/abs/10.1089/soro.2016.0029

[29] P. Moseley, J. M. Florez, H. A. Sonar, G. Agarwal, W. Curtin, and J. Paik, “Modeling, Design, and Development of Soft Pneumatic Actuators with Finite Element Method,”

Advanced Engineering Materials, vol. 18, no. 6, pp. 978–988, 2016. [Online]. Available: https://onlinelibrary.wiley.com/doi/abs/10.1002/adem.201500503

[30] G. Agarwal, N. Besuchet, B. Audergon, and J. Paik, "Stretchable materials for robust soft actuators towards assistive wearable devices," *Scientific Reports*, vol. 6, p. 34224, 9 2016.

[31] D. Rus and M. T. Tolley, "Design, fabrication and control of soft robots," *Nature*, vol. 521, no. 7553, pp. 467–475, May 2015.

[32] A. D. Marchese, R. K. Katzschmann, and D. Rus, "A recipe for soft fluidic elastomer robots," *Soft Robotics*, vol. 2, no. 1, pp. 7–25, 3 2015.

[33] B. Tondu, "Modelling of the mckibben artificial muscle: A review," *Journal of Intelligent Material Systems and Structures*, vol. 23, no. 3, pp. 225–253, 2 2012.

[34] B. Mosadegh, P. Polygerinos, C. Keplinger, S. Wennstedt, R. F. Shepherd, U. Gupta, J. Shim, K. Bertoldi, C. J. Walsh, and G. M. Whitesides, "Pneumatic Networks for Soft Robotics that Actuate Rapidly," *Advanced Functional Materials*, vol. 24, no. 15, pp. 2163–2170, 2014. [Online]. Available: https://onlinelibrary.wiley.com/doi/abs/10.1002/adfm.201303288

[35] H. A. Sonar and J. Paik, "Soft Pneumatic Actuator Skin with Piezoelectric Sensors for Vibrotactile Feedback," *Frontiers in Robotics and AI*, vol. 2, 2016. [Online]. Available: https://www.frontiersin.org/articles/10.3389/frobt.2015.00038/full

[36] A. Firouzeh, M. Salerno, and J. Paik, "Soft pneumatic actuator with adjustable stiffness layers for multi-dof actuation." 2015 IEEE/RSJ International Conference on Intelligent Robots and Systems (IROS), 9 2015, pp. 1117–1124.

[37] J. M. Mckibben, "Artificial Muscle," Mar. 1960.

[38] J. Bishop-Moser and S. Kota, "Design and Modeling of Generalized Fiber-Reinforced Pneumatic Soft Actuators," *IEEE Transactions on Robotics*, vol. 31, no. 3, pp. 536–545, Jun. 2015.

[39] G. Krishnan, J. Bishop-Moser, C. Kim, and S. Kota, "Kinematics of a generalized class of pneumatic artificial muscles," *Journal of Mechanisms and Robotics*, vol. 7, no. 4, p. 041014, 11 2015.

[40] M. T. Tolley, R. F. Shepherd, B. Mosadegh, K. C. Galloway, M. Wehner, M. Karpelson, R. J. Wood, and G. M. Whitesides, "A Resilient, Untethered Soft Robot," *Soft Robotics*, vol. 1, no. 3, pp. 213–223, Aug. 2014.

[41] R. F. Shepherd, F. Ilievski, W. Choi, S. A. Morin, A. A. Stokes, A. D. Mazzeo, X. Chen, M. Wang, and G. M. Whitesides, "Multigait soft robot," *Proceedings of the National Academy of Sciences of the United States of America*, vol. 108, no. 51, pp. 20 400–20 403, Dec. 2011.

[42] J. M. Florez, B. Shih, Y. Bai, and J. K. Paik, "Soft pneumatic actuators for legged locomotion," in *2014 IEEE International Conference on Robotics and Biomimetics (ROBIO 2014)*, Dec. 2014, pp. 27–34.

[43] Calisti M., Picardi G., and Laschi C., "Fundamentals of soft robot locomotion," *Journal of The Royal Society Interface*, vol. 14, no. 130, p. 20170101, May 2017. [Online]. Available: https://royalsocietypublishing.org/doi/full/10.1098/rsif.2017.0101

[44] C. D. Onal and D. Rus, "A modular approach to soft robots," in *2012 4th IEEE RAS EMBS International Conference on Biomedical Robotics and Biomechatronics (BioRob)*, Jun. 2012, pp. 1038–1045.

[45] R. K. Katzschmann, A. D. Marchese, and D. Rus, "Autonomous Object Manipulation Using a Soft Planar Grasping Manipulator," *Soft Robotics*, vol. 2, no. 4, pp. 155–164, Dec. 2015. [Online]. Available: https://www.liebertpub.com/doi/full/10.1089/soro.2015.0013

[46] J. Paek, I. Cho, and J. Kim, "Microrobotic tentacles with spiral bending capability based on shape-engineered elastomeric microtubes," *Scientific Reports*, vol. 5, p. 10768, Jun. 2015. [Online]. Available: https://www.nature.com/articles/srep10768

[47] M. Cianchetti, T. Ranzani, G. Gerboni, T. Nanayakkara, K. Althoefer, P. Dasgupta, and A. Menciassi, "Soft Robotics Technologies to Address Shortcomings in Today's Minimally Invasive Surgery: The STIFF-FLOP Approach," *Soft Robotics*, vol. 1, no. 2, pp. 122–131, Jun. 2014.

[48] C. Escande, P. M. Pathak, R. Merzouki, and V. Coelen, "Modelling of multisection bionic manipulator: Application to RobotinoXT," in *2011 IEEE International Conference on Robotics and Biomimetics*, Dec. 2011, pp. 92–97.

[49] A. Al-Ibadi, S. Nefti-Meziani, and S. Davis, "Active Soft End Effectors for Efficient Grasping and Safe Handling," *IEEE Access*, vol. 6, pp. 23 591–23 601, 2018.

[50] J. H. Low, N. Cheng, P. M. Khin, N. V. Thakor, S. L. Kukreja, H. L. Ren, and C. H. Yeow, "A bidirectional soft pneumatic fabric-based actuator for grasping applications," in *2017 IEEE/RSJ International Conference on Intelligent Robots and Systems (IROS)*, Sep. 2017, pp. 1180–1186.

[51] R. Bogue, "Flexible and soft robotic grippers: the key to new markets?" *Industrial Robot: the international journal of robotics research and application*, vol. 43, no. 3, pp. 258–263, May 2016. [Online]. Available: https://www.emeraldinsight.com/doi/full/10.1108/IR-01-2016-0027

[52] M. G. Antonelli, W. D'Ambrogio, and F. Durante, "Development of a Pneumatic Soft Actuator As a Hand Finger for a Collaborative Robot," in *Proceedings of the 2018 2Nd International Conference on Mechatronics Systems and Control Engineering*, ser. ICMSCE 2018. New York, NY, USA: ACM, 2018, pp. 67–71, event-place: Amsterdam, Netherlands. [Online]. Available: http://doi.acm.org/10.1145/3185066.3185079

[53] E. C. Townsend, E. A. Mielke, D. Wingate, and M. D. Killpack, “Estimating Human Intent for Physical Human-Robot Co-Manipulation,” *arXiv:1705.10851 [cs]*, May 2017, arXiv: 1705.10851. [Online]. Available: http://arxiv.org/abs/1705.10851

[54] J. Amend, N. Cheng, S. Fakhouri, and B. Culley, “Soft Robotics Commercialization: Jamming Grippers from Research to Product,” *Soft Robotics*, vol. 3, no. 4, pp. 213–222, Oct. 2016. [Online]. Available: https://www.liebertpub.com/doi/full/10.1089/soro.2016.0021

[55] P. Polygerinos, Z. Wang, K. C. Galloway, R. J. Wood, and C. J. Walsh, “Soft robotic glove for combined assistance and at-home rehabilitation,” *Robotics and Autonomous Systems*, vol. 73, pp. 135–143, Nov. 2015. [Online]. Available: http://www.sciencedirect.com/science/article/pii/S0921889014001729

[56] C.-Y. Chu and R. M. Patterson, “Soft robotic devices for hand rehabilitation and assistance: a narrative review,” *Journal of NeuroEngineering and Rehabilitation*, vol. 15, no. 1, p. 9, Feb. 2018. [Online]. Available: https://doi.org/10.1186/s12984-018-0350-6

[57] C. T. O’Neill, N. S. Phipps, L. Cappello, S. Paganoni, and C. J. Walsh, “A soft wearable robot for the shoulder: Design, characterization, and preliminary testing,” in *2017 International Conference on Rehabilitation Robotics (ICORR)*, Jul. 2017, pp. 1672–1678.

[58] T. Jiralerspong, K. H. L. Heung, R. K. Y. Tong, and Z. Li, “A Novel Soft Robotic Glove for Daily Life Assistance,” in *2018 7th IEEE International Conference on Biomedical Robotics and Biomechatronics (Biorob)*, Aug. 2018, pp. 671–676.

[59] S. Jin, S. Guo, K. Hashimoto, X. Xiong, and M. Yamamoto, “A Soft Wearable Robotic Suit for Ankle and Hip Assistance: a Preliminary Study,” in *2018 40th Annual International Conference of the IEEE Engineering in Medicine and Biology Society (EMBC)*, Jul. 2018, pp. 1867–1870.

[60] B. Mosadegh, B. G. GERBERICH, and G. M. Whitesides, “Portable prosthetic hand with soft pneumatic fingers,” US Patent US9 687 362B2, Jun., 2017. [Online]. Available: https://patents.google.com/patent/US9687362B2/en

[61] T. J. Engen, “A Plastic Hand Orthosis,” *Orthopedic and Prosthetic Appliance Journal*, pp. 38–43, Sep. 1959.

[62] T. J. Engen and L. F. Ottnat, “Upper Extremity Orthotics: A Project Report,” *Orthopedic and Prosthetic Appliance Journal*, Jun. 1967.

[63] S. Lessard, P. Pansodtee, A. Robbins, L. B. Baltaxe-Admony, J. M. Trombadore, M. Teodorescu, A. Agogino, and S. Kurniawan, “CRUX: A compliant robotic upper-extremity exosuit for lightweight, portable, multi-joint muscular augmentation,” in *2017 International Conference on Rehabilitation Robotics (ICORR)*, Jul. 2017, pp. 1633–1638.

[64] J. Pocock, “The Softer Side of Robotics,” *ASEE Prism; Washington*, vol. 25, no. 2, p. 22, Oct. 2015. [Online]. Available: https://search.proquest.com/docview/1732956298/abstract/AD10890B4D524822PQ/1

[65] C. Paul, “Morphological computation: A basis for the analysis of morphology and control requirements,” *Robotics and Autonomous Systems*, vol. 54, no. 8, pp. 619–630, Aug. 2006. [Online]. Available: http://www.sciencedirect.com/science/article/pii/S0921889006000613

[66] K. Ghazi-Zahedi, R. Deimel, G. Montúfar, V. Wall, and O. Brock, “Morphological computation: The good, the bad, and the ugly,” in *2017 IEEE/RSJ International Conference on Intelligent Robots and Systems (IROS)*, Sep. 2017, pp. 464–469.

[67] M. A. Robertson and J. Paik, “New soft robots really suck: Vacuum-powered systems empower diverse capabilities,” *Science Robotics*, vol. 2, no. 9, 2017. [Online]. Available: http://robotics.sciencemag.org/content/2/9/eaan6357

[68] R. Ikeura and H. Inooka, “Variable impedance control of a robot for cooperation with a human,” vol. 3. Proceedings of 1995 IEEE International Conference on Robotics and Automation, 5 1995, pp. 3097–3102 vol.3.

[69] A. Calanca, R. Muradore, and P. Fiorini, “Impedance control of series elastic actuators using acceleration feedback,” in *Wearable Robotics: Challenges and Trends*. Springer, Cham, 2017, pp. 33–37.

[70] R. Pfeifer, M. Lungarella, and F. Iida, “Self-organization, embodiment, and biologically inspired robotics,” *Science*, vol. 318, no. 5853, pp. 1088–1093, 11 2007, pMID: 18006736.

[71] ——, “The challenges ahead for bio-inspired ’soft’ robotics,” *Communications of the ACM*, vol. 55, no. 11, p. 76, 11 2012.

[72] C. Laschi, B. Mazzolai, and M. Cianchetti, “Soft robotics: Technologies and systems pushing the boundaries of robot abilities,” *Science Robotics*, vol. 1, no. 1, p. eaah3690, 12 2016.

[73] C. Eppner, R. Deimel, J. Álvarez Ruiz, M. Maertens, and O. Brock, “Exploitation of environmental constraints in human and robotic grasping,” *The International Journal of Robotics Research*, vol. 34, no. 7, pp. 1021–1038, 6 2015.

[74] M. T. Tolley, R. F. Shepherd, B. Mosadegh, K. C. Galloway, M. Wehner, M. Karpelson, R. J. Wood, and G. M. Whitesides, “A resilient, untethered soft robot,” *Soft Robotics*, vol. 1, no. 3, pp. 213–223, 9 2014.

[75] F. Ilievski, A. D. Mazzeo, R. F. Shepherd, X. Chen, and G. M. Whitesides, “Soft robotics for chemists,” *Angewandte Chemie International Edition*, vol. 50, no. 8, pp. 1890–1895, 2 2011.

[76] D. Yang, M. S. Verma, J.-H. So, B. Mosadegh, C. Keplinger, B. Lee, F. Khashai, E. Lossner, Z. Suo, and G. M. Whitesides, "Buckling Pneumatic Linear Actuators Inspired by Muscle," *Advanced Materials Technologies*, vol. 1, no. 3, p. 1600055, Jun. 2016. [Online]. Available: https://onlinelibrary.wiley.com/doi/abs/10.1002/admt.201600055

[77] D. Yang, M. S. Verma, E. Lossner, D. Stothers, and G. M. Whitesides, "Negative-pressure soft linear actuator with a mechanical advantage," *Advanced Materials Technologies*, vol. 2, no. 1, p. 1600164, 1 2017.

[78] B. C. Mac Murray, X. An, S. S. Robinson, I. M. van Meerbeek, K. W. O'Brien, H. Zhao, and R. F. Shepherd, "Poroelastic foams for simple fabrication of complex soft robots," *Advanced Materials*, vol. 27, no. 41, pp. 6334–6340, 11 2015.

[79] A. Argiolas, B. C. Mac Murray, I. Van Meerbeek, J. Whitehead, E. Sinibaldi, B. Mazzolai, and R. F. Shepherd, "Sculpting soft machines," *Soft Robotics*, vol. 3, no. 3, pp. 101–108, 7 2016.

[80] I. M. Van Meerbeek, B. C. Mac Murray, J. W. Kim, S. S. Robinson, P. X. Zou, M. N. Silberstein, and R. F. Shepherd, "Morphing metal and elastomer bicontinuous foams for reversible stiffness, shape memory, and self-healing soft machines," *Advanced Materials*, vol. 28, no. 14, pp. 2801–2806, 4 2016.

[81] B. Trimmer, "Soft robots and size," *Soft Robotics*, vol. 2, no. 2, pp. 49–50, 6 2015.

[82] E. Brown, N. Rodenberg, J. Amend, A. Mozeika, E. Steltz, M. R. Zakin, H. Lipson, and H. M. Jaeger, "Universal robotic gripper based on the jamming of granular material," *Proceedings of the National Academy of Sciences*, vol. 107, no. 44, pp. 18 809–18 814, 11 2010.

[83] F. Tramacere, M. Follador, N. M. Pugno, and B. Mazzolai, "Octopus-like suction cups: from natural to artificial solutions," *Bioinspiration & Biomimetics*, vol. 10, no. 3, p. 035004, 2015.

[84] Y. J. Kim, S. Cheng, S. Kim, and K. Iagnemma, "A novel layer jamming mechanism with tunable stiffness capability for minimally invasive surgery," *IEEE Transactions on Robotics*, vol. 29, no. 4, pp. 1031–1042, 8 2013.

[85] N. G. Cheng, M. B. Lobovsky, S. J. Keating, A. M. Setapen, K. I. Gero, A. E. Hosoi, and K. D. Iagnemma, "Design and analysis of a robust, low-cost, highly articulated manipulator enabled by jamming of granular media." IEEE, 5 2012, pp. 4328–4333, [Online; accessed 2016-11-04]. [Online]. Available: http://ieeexplore.ieee.org/document/6225373/

[86] J. L. C. Santiago, I. D. Walker, and I. S. Godage, "Continuum robots for space applications based on layer-jamming scales with stiffening capability." 2015 IEEE Aerospace Conference, 3 2015, pp. 1–13.

[87] M. Cianchetti, T. Ranzani, G. Gerboni, T. Nanayakkara, K. Althoefer, P. Dasgupta, and A. Menciassi, “Soft robotics technologies to address shortcomings in today’s minimally invasive surgery: The stiff-flop approach,” *Soft Robotics*, vol. 1, no. 2, pp. 122–131, 6 2014.

[88] W. McMahan, V. Chitrakaran, M. Csencsits, D. Dawson, I. D. Walker, B. A. Jones, M. Pritts, D. Dienno, M. Grissom, and C. D. Rahn, “Field trials and testing of the octarm continuum manipulator.” Proceedings 2006 IEEE International Conference on Robotics and Automation, 2006. ICRA 2006., 5 2006, pp. 2336–2341.

[89] P. Qi, C. Qiu, H. Liu, J. S. Dai, L. D. Seneviratne, and K. Althoefer, “A novel continuum manipulator design using serially connected double-layer planar springs,” *IEEE/ASME Transactions on Mechatronics*, vol. 21, no. 3, pp. 1281–1292, 6 2016.

[90] M. W. Hannan and I. D. Walker, “The ‘elephant trunk’ manipulator, design and implementation,” vol. 1. 2001 IEEE/ASME International Conference on Advanced Intelligent Mechatronics, 2001. Proceedings, 2001, pp. 14–19 vol.1.

[91] K. Suzumori, S. Iikura, and H. Tanaka, “Development of flexible microactuator and its applications to robotic mechanisms.” 1991 IEEE International Conference on Robotics and Automation Proceedings, 4 1991, pp. 1622–1627 vol.2.

[92] G. S. Chirikjian, “Theory and applications of hyper-redundant robotic manipulators,” Ph.D. dissertation, 1992, [Online; accessed 2017-04-21]. [Online]. Available: http://resolver.caltech.edu/CaltechETD:etd-11082006-132210

[93] H. Marvi, C. Gong, N. Gravish, H. Astley, M. Travers, R. L. Hatton, J. R. Mendelson, H. Choset, D. L. Hu, and D. I. Goldman, “Sidewinding with minimal slip: snake and robot ascent of sandy slopes,” *Science (New York, N.Y.)*, vol. 346, no. 6206, pp. 224–229, 10 2014, pMID: 25301625.

[94] B. Bayat, A. Crespi, and A. Ijspeert, “Envirobot: A bio-inspired environmental monitoring platform.” Tokyo, Japan: IEEE/OES Conference on Autonomous Underwater Vehicles (AUV), 11 2016, [Online; accessed 2016-11-04].

[95] S. Hirose, *Biologically Inspired Robots: Serpentile Locomotors and Manipulators.* Oxford University Press, 1993.

[96] C. Wright, A. Buchan, B. Brown, J. Geist, M. Schwerin, D. Rollinson, M. Tesch, and H. Choset, “Design and architecture of the unified modular snake robot.” 2012 IEEE International Conference on Robotics and Automation, 5 2012, pp. 4347–4354.

[97] A. A. Stokes, R. F. Shepherd, S. A. Morin, F. Ilievski, and G. M. Whitesides, “A hybrid combining hard and soft robots,” *Soft Robotics*, vol. 1, no. 1, pp. 70–74, 7 2013.

[98] P. Liljeback, O. Stavdahl, and K. Y. Pettersen, “Modular pneumatic snake robot: 3d modelling, implementation and control,” *Modeling, Identification and Control: A Norwegian Research Bulletin*, vol. 29, no. 1, pp. 21–28, 2008.

[99] C. D. Onal and D. Rus, "Autonomous undulatory serpentine locomotion utilizing body dynamics of a fluidic soft robot," *Bioinspiration & Biomimetics*, vol. 8, no. 2, p. 026003, 6 2013.

[100] G. Gerboni, T. Ranzani, A. Diodato, G. Ciuti, M. Cianchetti, and A. Menciassi, "Modular soft mechatronic manipulator for minimally invasive surgery (mis): overall architecture and development of a fully integrated soft module," *Meccanica*, vol. 50, no. 11, pp. 2865–2878, 9 2015.

[101] J. Dai, M. Travers, T. Dear, C. Gong, H. C. Astley, D. I. Goldman, and H. Choset, "Robot-inspired biology: The compound-wave control template." 2015 IEEE International Conference on Robotics and Automation (ICRA), 5 2015, pp. 5879–5884.

[102] K. Melo and L. Paez, "Experimental determination of control parameter intervals for repeatable gaits in modular snake robots." 2014 IEEE International Symposium on Safety, Security, and Rescue Robotics (2014), 10 2014, pp. 1–7.

[103] M. Mori and S. Hirose, "Three-dimensional serpentine motion and lateral rolling by active cord mechanism acm-r3," vol. 1. IEEE/RSJ International Conference on Intelligent Robots and Systems, 2002, 2002, pp. 829–834 vol.1.

[104] M. Manti, V. Cacucciolo, and M. Cianchetti, "Stiffening in soft robotics: A review of the state of the art," *IEEE Robotics Automation Magazine*, vol. 23, no. 3, pp. 93–106, 9 2016.

[105] J. Ou, L. Yao, D. Tauber, J. Steimle, R. Niiyama, and H. Ishii, "jamsheets: Thin interfaces with tunable stiffness enabled by layer jamming," ser. TEI '14. New York, NY, USA: ACM, 2013, p. 65–72, [Online; accessed 2017-04-20].

[106] M. A. Robertson and J. Paik, "Practical control methods for vacuum driven soft actuator modules," in *2017 IEEE/RSJ International Conference on Intelligent Robots and Systems (IROS)*, Sep. 2017, pp. 1224–1229.

[107] M. A. Robertson, M. Murakami, W. Felt, and J. Paik, "A Compact Modular Soft Surface With Reconfigurable Shape and Stiffness," *IEEE/ASME Transactions on Mechatronics*, vol. 24, no. 1, pp. 16–24, Feb. 2019.

[108] M. A. Robertson and J. Paik, "Low-inertia vacuum-powered soft pneumatic actuator coil characterization and design methodology," in *2018 IEEE International Conference on Soft Robotics (RoboSoft)*, Apr. 2018, pp. 431–436.

[109] P. Polygerinos, S. Lyne, Z. Wang, L. F. Nicolini, B. Mosadegh, G. M. Whitesides, and C. J. Walsh, "Towards a soft pneumatic glove for hand rehabilitation," in *2013 IEEE/RSJ International Conference on Intelligent Robots and Systems*, Nov. 2013, pp. 1512–1517.

[110] D. Rus and M. T. Tolley, "Design, fabrication and control of soft robots," *Nature*, vol. 521, no. 7553, pp. 467–475, 5 2015.

[111] P. Maeder-York, T. Clites, E. Boggs, R. Neff, P. Polygerinos, D. Holland, L. Stirling, K. Galloway, C. Wee, and C. Walsh, “Biologically Inspired Soft Robot for Thumb Rehabilitation1,” *Journal of Medical Devices*, vol. 8, no. 2, pp. 020 933–020 933–3, Apr. 2014. [Online]. Available: http://dx.doi.org/10.1115/1.4027031

[112] F. A. Panizzolo, I. Galiana, A. T. Asbeck, C. Siviy, K. Schmidt, K. G. Holt, and C. J. Walsh, “A biologically-inspired multi-joint soft exosuit that can reduce the energy cost of loaded walking,” *Journal of NeuroEngineering and Rehabilitation*, vol. 13, p. 43, 2016.

[113] Y.-L. Park, B.-r. Chen, N. O. Pérez-Arancibia, D. Young, L. Stirling, R. J. Wood, E. C. Goldfield, and R. Nagpal, “Design and control of a bio-inspired soft wearable robotic device for ankle–foot rehabilitation,” *Bioinspiration & Biomimetics*, vol. 9, no. 1, p. 016007, 3 2014.

[114] A. D. Marchese, K. Komorowski, C. D. Onal, and D. Rus, “Design and control of a soft and continuously deformable 2d robotic manipulation system.” 2014 IEEE International Conference on Robotics and Automation (ICRA), 5 2014, pp. 2189–2196.

[115] S. Neppalli, B. Jones, W. McMahan, V. Chitrakaran, I. Walker, M. Pritts, M. Csencsits, C. Rahn, and M. Grissom, “Octarm - a soft robotic manipulator.” 2007 IEEE/RSJ International Conference on Intelligent Robots and Systems, 10 2007, pp. 2569–2569.

[116] R. F. Shepherd, F. Ilievski, W. Choi, S. A. Morin, A. A. Stokes, A. D. Mazzeo, X. Chen, M. Wang, and G. M. Whitesides, “Multigait soft robot,” *Proceedings of the National Academy of Sciences of the United States of America*, vol. 108, no. 51, pp. 20 400–20 403, 12 2011, pMID: 22123978 PMCID: PMC3251082.

[117] C. D. Onal, X. Chen, G. M. Whitesides, and D. Rus, “Soft mobile robots with on-board chemical pressure generation,” in *Robotics Research*, H. I. Christensen and O. Khatib, Eds. Cham: Springer International Publishing, 2017, vol. 100, pp. 525–540, [Online; accessed 2016-11-04]. [Online]. Available: http://link.springer.com/10.1007/978-3-319-29363-9_30

[118] J. Y. Lee, W. B. Kim, W. Y. Choi, and K. J. Cho, “Soft robotic blocks: Introducing sobl, a fast-build modularized design block,” *IEEE Robotics Automation Magazine*, vol. 23, no. 3, pp. 30–41, 9 2016.

[119] N. Napp, B. Araki, M. T. Tolley, R. Nagpal, and R. J. Wood, “Simple passive valves for addressable pneumatic actuation.” 2014 IEEE International Conference on Robotics and Automation (ICRA), 5 2014, pp. 1440–1445.

[120] A. Girard and J. S. Plante, “Influence vectors control for robots using cellular-like binary actuators,” *IEEE Transactions on Robotics*, vol. 30, no. 3, pp. 642–651, 6 2014.

[121] E. Tzorakoleftherakis, A. Mavrommati, and A. Tzes, “Design and implementation of a binary redundant manipulator with cascaded modules1,” *Journal of Mechanisms and Robotics*, vol. 8, no. 1, pp. 011 002–011 002–10, 8 2015.

[122] G. S. Chirikjian, “Inverse kinematics of binary manipulators using a continuum model,” *Journal of Intelligent and Robotic Systems*, vol. 19, no. 1, pp. 5–22, 5 1997.

[123] K. Maeda and E. Konaka, “Ellipsoidal outer-approximation of workspace of binary manipulator for inverse kinematics solution.” 2014 IEEE/ASME International Conference on Advanced Intelligent Mechatronics, 7 2014, pp. 1331–1336.

[124] *Fluidic Control Board.* The Soft Robotics Toolkit: http://softroboticstoolkit.com/book/control-board, [Online; accessed 2017-02-15]. [Online]. Available: http://softroboticstoolkit.com/book/control-board

[125] D. J. Page, “Reconfigurable surface,” U.S. Patent US6 903 871 B2, Jun., 2005, u.S. Classification 359/443, 359/446, 359/451, 359/277, 359/893; International Classification B29C45/00, B29C33/30; Cooperative Classification B29C45/00, G03B21/56, B29C33/308, B29C33/307; European Classification B29C33/30F. [Online]. Available: http://www.google.com/patents/US6903871

[126] B. Peters and E. Marion, “Methods and apparatus for a reconfigurable surface,” U.S. Patent US20 120 279 812 A1, Nov., 2012, u.S. Classification 188/67, 700/275; International Classification F16D63/00, F16D59/00, G05B15/02; Cooperative Classification G05B19/4099, G05B2219/49025, B21D37/02, F16D63/008. [Online]. Available: http://www.google.com/patents/US20120279812

[127] M. K. Rasmussen, E. W. Pedersen, M. G. Petersen, and K. Hornb\a ek, “Shape-changing Interfaces: A Review of the Design Space and Open Research Questions,” in *Proceedings of the SIGCHI Conference on Human Factors in Computing Systems,* ser. CHI ’12. New York, NY, USA: ACM, 2012, pp. 735–744. [Online]. Available: http://doi.acm.org/10.1145/2207676.2207781

[128] S. Follmer, D. Leithinger, A. Olwal, A. Hogge, and H. Ishii, “inFORM: dynamic physical affordances and constraints through shape and object actuation.” in *Uist*, vol. 13, 2013, pp. 417–426.

[129] I. Poupyrev, T. Nashida, S. Maruyama, J. Rekimoto, and Y. Yamaji, “Lumen: Interactive Visual and Shape Display for Calm Computing,” in *ACM SIGGRAPH 2004 Emerging Technologies*, ser. SIGGRAPH ’04. New York, NY, USA: ACM, 2004, pp. 17–. [Online]. Available: http://doi.acm.org/10.1145/1186155.1186173

[130] D. Leithinger and H. Ishii, “Relief: A Scalable Actuated Shape Display,” in *Proceedings of the Fourth International Conference on Tangible, Embedded, and Embodied Interaction*, ser. TEI ’10. New York, NY, USA: ACM, 2010, pp. 221–222. [Online]. Available: http://doi.acm.org/10.1145/1709886.1709928

[131] H. Iwata, H. Yano, F. Nakaizumi, and R. Kawamura, “Project FEELEX: Adding Haptic Surface to Graphics,” in *Proceedings of the 28th Annual Conference on Computer Graphics and Interactive Techniques*, ser. SIGGRAPH ’01. New York, NY, USA: ACM, 2001, pp. 469–476. [Online]. Available: http://doi.acm.org/10.1145/383259.383314

[132] G. M. Troiano, J. Tiab, and Y.-K. Lim, “SCI-FI: Shape-Changing Interfaces, Future Interactions,” in *Proceedings of the 9th Nordic Conference on Human-Computer Interaction*, ser. NordiCHI ’16. New York, NY, USA: ACM, 2016, pp. 45:1–45:10. [Online]. Available: http://doi.acm.org/10.1145/2971485.2971489

[133] D. Leonardis, L. Claudio, and A. Frisoli, “A survey on innovative refreshable braille display technologies,” in *AHFE International Conference on Applied Human Factors and Ergonomics, Advances in Design for Inclusion*, 2017.

[134] L. Yobas, D. M. Durand, G. G. Skebe, F. J. Lisy, and M. A. Huff, “A novel integrable microvalve for refreshable Braille display system,” *Journal of Microelectromechanical Systems*, vol. 12, no. 3, pp. 252–263, Jun. 2003.

[135] T. S. Prince, G. G. Skebe, F. J. Lisy, and R. N. Schmidt, “Refreshable braille display system with a flexible surface,” U.S. Patent US6 743 021 B2, Jun., 2004, u.S. Classification 434/113, 434/112; International Classification G09B21/00; Cooperative Classification G09B21/003; European Classification G09B21/00B3. [Online]. Available: http://www.google.com/patents/US6743021

[136] A. Russomanno, R. B. Gillespie, S. O’Modhrain, and M. Burns, “The design of pressure-controlled valves for a refreshable tactile display,” in *World Haptics Conference (WHC), 2015 IEEE*. IEEE, 2015, pp. 177–182.

[137] S. Lee, K. Jung, J. Koo, S. Lee, H. Choi, J. Jeon, J. Nam, and H. Choi, “Braille display device using soft actuator,” in *Smart Structures and Materials 2004: Electroactive Polymer Actuators and Devices (EAPAD)*, vol. 5385. International Society for Optics and Photonics, 2004, pp. 368–380.

[138] P. Yang, “Electroactive polymer actuator braille cell and braille display,” Apr. 19 2005, uS Patent 6,881,063.

[139] K. Ren, S. Liu, M. Lin, Y. Wang, and Q. M. Zhang, “A compact electroactive polymer actuator suitable for refreshable Braille display,” *Sensors and Actuators A: Physical*, vol. 143, no. 2, pp. 335–342, May 2008. [Online]. Available: http://www.sciencedirect.com/science/article/pii/S0924424707008114

[140] Y. Haga, W. Makishi, K. Iwami, K. Totsu, K. Nakamura, and M. Esashi, “Dynamic braille display using sma coil actuator and magnetic latch,” *Sensors and Actuators A: Physical*, vol. 119, no. 2, pp. 316–322, 2005.

[141] D. Chaves, I. Peixoto, A. Lima, M. Vieira, and C. De Araujo, “Microtuators of sma for braille display system,” in *Medical Measurements and Applications, 2009. MeMeA 2009. IEEE International Workshop on.* IEEE, 2009, pp. 64–68.

[142] P. Sapra, A. K. Parsurampuria, D. Gupta, S. Muralikrishnan, M. Raj, A. Anand, V. Darda, R. Paul, M. Balakrishnan, and P. Rao, “A compliant mechanism design for refreshable

braille display using shape memory alloy," in *ASME 2015 International Design Engineering Technical Conferences and Computers and Information in Engineering Conference.* American Society of Mechanical Engineers, 2015, pp. V009T07A054–V009T07A054.

[143] A. A. Stanley and A. M. Okamura, "Controllable surface haptics via particle jamming and pneumatics," *IEEE Transactions on Haptics*, vol. 8, no. 1, pp. 20–30, 2015.

[144] A. A. Stanley, J. C. Gwilliam, and A. M. Okamura, "Haptic jamming: A deformable geometry, variable stiffness tactile display using pneumatics and particle jamming," in *2013 World Haptics Conference (WHC)*, Apr. 2013, pp. 25–30.

[145] W. Nutzel, "Display surface for tactile information," U.S. Patent US5 086 287 A, Feb., 1992, u.S. Classification 340/407.1, 434/112, 434/115, 434/113; International Classification G09B21/00; Cooperative Classification G09B21/003; European Classification G09B21/00B3. [Online]. Available: http://www.google.com/patents/US5086287

[146] I. M. Koo, K. Jung, J. C. Koo, J.-D. Nam, Y. K. Lee, and H. R. Choi, "Development of soft-actuator-based wearable tactile display," *IEEE Transactions on Robotics*, vol. 24, no. 3, pp. 549–558, 2008.

[147] H. A. Sonar and J. Paik, "Soft pneumatic actuator skin with piezoelectric sensors for vibrotactile feedback," *Frontiers in Robotics and AI*, vol. 2, p. 38, 2016.

[148] M. Raitor, J. M. Walker, A. M. Okamura, and H. Culbertson, "Wrap: Wearable, restricted-aperture pneumatics for haptic guidance," in *Robotics and Automation (ICRA), 2017 IEEE International Conference on.* IEEE, 2017, pp. 427–432.

[149] R. M, G. SS, and R. PA, "Preventing pressure ulcers: A systematic review," *JAMA*, vol. 296, no. 8, pp. 974–984, 2006. [Online]. Available: +http://dx.doi.org/10.1001/jama.296.8.974

[150] G. Votolato, *Transport design: a travel history.* Reaktion Books, 2007.

[151] "WaveHandling | Festo Corporate," 2014. [Online]. Available: https://www.festo.com/group/en/cms/10225.htm

[152] B. Mosadegh, A. D. Mazzeo, R. F. Shepherd, S. A. Morin, U. Gupta, I. Zhalehdoust Sani, D. Lai, S. Takayama, and G. M. Whitesides, "Control of soft machines using actuators operated by a Braille display," *Lab on a Chip*, vol. 14, no. 1, pp. 189–199, 2014. [Online]. Available: http://pubs.rsc.org/en/Content/ArticleLanding/2014/LC/C3LC51083B

[153] Z. Deng, M. Stommel, and W. Xu, "A Novel Soft Machine Table for Manipulation of Delicate Objects Inspired by Caterpillar Locomotion," *IEEE/ASME Transactions on Mechatronics*, vol. 21, no. 3, pp. 1702–1710, Jun. 2016.

[154] D. F. Walczyk and D. E. Hardt, "Design and analysis of reconfigurable discrete dies for sheet metal forming," *Journal of Manufacturing Systems*, vol. 17, no. 6, pp. 436–454, Jan. 1998. [Online]. Available: http://www.sciencedirect.com/science/article/pii/S027861259980003X

[155] B. J. Peters, “Design and fabrication of a digitally reconfigurable surface,” Thesis, Massachusetts Institute of Technology, 2011. [Online]. Available: http://dspace.mit.edu/handle/1721.1/68541

[156] P. L. Hoffman, “Method for forming composite parts using reconfigurable modular tooling,” Dec. 8 1998, uS Patent 5,846,464.

[157] “Applications of the reconfigurable mould, the adaptive mould.” [Online]. Available: http://adapa.dk/applications/

[158] Z. Szabo and E. T. Enikov, “Development of Wearable Micro-actuator Array for 3-D Virtual Tactile Displays,” *Journal of Electromagnetic Analysis and Applications*, vol. 04, p. 219, Jun. 2012.

[159] S. Kim, C. Laschi, and B. Trimmer, “Soft robotics: a bioinspired evolution in robotics,” *Trends in Biotechnology*, vol. 31, no. 5, pp. 287–294, May 2013.

[160] R. Pfeifer and J. C. Bongard, *How the Body Shapes the Way We Think: A New View of Intelligence (Bradford Books)*. The MIT Press, 2006.

[161] R. Deimel and O. Brock, “A novel type of compliant and underactuated robotic hand for dexterous grasping,” *The International Journal of Robotics Research*, vol. 35, no. 1-3, pp. 161–185, Jan. 2016. [Online]. Available: https://doi.org/10.1177/0278364915592961

[162] N. Farrow, Y. Li, and N. Correll, “Morphological and Embedded Computation in a Self-contained Soft Robotic Hand,” *arXiv:1605.00354 [cs]*, May 2016, arXiv: 1605.00354. [Online]. Available: http://arxiv.org/abs/1605.00354

[163] V. Vikas, P. Grover, and B. Trimmer, “Model-free control framework for multi-limb soft robots,” in *2015 IEEE/RSJ International Conference on Intelligent Robots and Systems (IROS)*, Sep. 2015, pp. 1111–1116.

[164] C. Duriez, “Control of elastic soft robots based on real-time finite element method,” in *2013 IEEE International Conference on Robotics and Automation*, May 2013, pp. 3982–3987.

[165] H. Zhao, K. O’Brien, S. Li, and R. F. Shepherd, “Optoelectronically innervated soft prosthetic hand via stretchable optical waveguides,” *Science Robotics*, vol. 1, no. 1, p. eaai7529, Dec. 2016. [Online]. Available: http://robotics.sciencemag.org/content/1/1/eaai7529

[166] J. C. Yeo, H. K. Yap, W. Xi, Z. Wang, C.-H. Yeow, and C. T. Lim, “Flexible and Stretchable Strain Sensing Actuator for Wearable Soft Robotic Applications,” *Advanced Materials Technologies*, vol. 1, no. 3, p. 1600018, Jun. 2016. [Online]. Available: https://onlinelibrary.wiley.com/doi/abs/10.1002/admt.201600018

[167] M. Amjadi, K.-U. Kyung, I. Park, and M. Sitti, "Stretchable, Skin-Mountable, and Wearable Strain Sensors and Their Potential Applications: A Review," *Advanced Functional Materials*, vol. 26, no. 11, pp. 1678–1698, Mar. 2016. [Online]. Available: https://onlinelibrary.wiley.com/doi/abs/10.1002/adfm.201504755

[168] E. L. White, M. C. Yuen, J. C. Case, and R. K. Kramer, "Low-Cost, Facile, and Scalable Manufacturing of Capacitive Sensors for Soft Systems," *Advanced Materials Technologies*, vol. 2, no. 9, p. 1700072, Sep. 2017. [Online]. Available: https://onlinelibrary.wiley.com/doi/abs/10.1002/admt.201700072

[169] R. K. Kramer, C. Majidi, R. Sahai, and R. J. Wood, "Soft curvature sensors for joint angle proprioception," in *2011 IEEE/RSJ International Conference on Intelligent Robots and Systems*, Sep. 2011, pp. 1919–1926.

[170] H. O. Michaud, L. Dejace, S. d. Mulatier, and S. P. Lacour, "Design and functional evaluation of an epidermal strain sensing system for hand tracking," in *2016 IEEE/RSJ International Conference on Intelligent Robots and Systems (IROS)*, Oct. 2016, pp. 3186–3191.

[171] J. W. Boley, E. L. White, G. T.-C. Chiu, and R. K. Kramer, "Direct Writing of Gallium-Indium Alloy for Stretchable Electronics," *Advanced Functional Materials*, vol. 24, no. 23, pp. 3501–3507, Jun. 2014. [Online]. Available: https://onlinelibrary.wiley.com/doi/abs/10.1002/adfm.201303220

[172] M. G. Mohammed and R. Kramer, "All-Printed Flexible and Stretchable Electronics," *Advanced Materials*, vol. 29, no. 19, p. 1604965, May 2017. [Online]. Available: https://onlinelibrary.wiley.com/doi/abs/10.1002/adma.201604965

[173] R. L. Truby, M. Wehner, A. K. Grosskopf, D. M. Vogt, S. G. M. Uzel, R. J. Wood, and J. A. Lewis, "Soft Somatosensitive Actuators via Embedded 3d Printing," *Advanced Materials*, vol. 30, no. 15, p. 1706383, Apr. 2018. [Online]. Available: https://onlinelibrary.wiley.com/doi/abs/10.1002/adma.201706383

[174] A. Hirsch, L. Dejace, H. O. Michaud, and S. P. Lacour, "Harnessing the Rheological Properties of Liquid Metals To Shape Soft Electronic Conductors for Wearable Applications," *Accounts of Chemical Research*, Feb. 2019. [Online]. Available: https://doi.org/10.1021/acs.accounts.8b00489

[175] X. Wang, R. Guo, and J. Liu, "Liquid Metal Based Soft Robotics: Materials, Designs, and Applications," *Advanced Materials Technologies*, vol. 4, no. 2, Feb. 2019. [Online]. Available: https://onlinelibrary.wiley.com/doi/abs/10.1002/admt.201800549

[176] R. Herbert, J.-H. Kim, Y. Kim, H. Lee, W.-H. Yeo, R. Herbert, J.-H. Kim, Y. S. Kim, H. M. Lee, and W.-H. Yeo, "Soft Material-Enabled, Flexible Hybrid Electronics for Medicine, Healthcare, and Human-Machine Interfaces," *Materials*, vol. 11, no. 2, p. 187, Jan. 2018. [Online]. Available: https://www.mdpi.com/1996-1944/11/2/187

[177] S. P. Lacour, G. Courtine, and J. Guck, "Materials and technologies for soft implantable neuroprostheses," *Nature Reviews Materials*, vol. 1, no. 10, p. 16063, Oct. 2016. [Online]. Available: https://www.nature.com/articles/natrevmats201663

[178] N. Lu and D.-H. Kim, "Flexible and Stretchable Electronics Paving the Way for Soft Robotics," *Soft Robotics*, vol. 1, no. 1, pp. 53–62, Jul. 2013. [Online]. Available: https://www.liebertpub.com/doi/abs/10.1089/soro.2013.0005

[179] R. A. Bilodeau, E. L. White, and R. K. Kramer, "Monolithic fabrication of sensors and actuators in a soft robotic gripper," in *2015 IEEE/RSJ International Conference on Intelligent Robots and Systems (IROS)*, Sep. 2015, pp. 2324–2329.

[180] M. A. Robertson and J. Paik, "New soft robots really suck: Vacuum-powered systems empower diverse capabilities," *Science Robotics*, vol. 2, no. 9, 2017. [Online]. Available: http://robotics.sciencemag.org/content/2/9/eaan6357

[181] D. Yang, M. S. Verma, E. Lossner, D. Stothers, and G. M. Whitesides, "Negative-Pressure Soft Linear Actuator with a Mechanical Advantage," *Advanced Materials Technologies*, vol. 2, no. 1, p. 1600164, Oct. 2016. [Online]. Available: https://onlinelibrary.wiley.com/doi/abs/10.1002/admt.201600164

[182] A. Hirsch and S. P. Lacour, "A Method to Form Smooth Films of Liquid Metal Supported by Elastomeric Substrate," *Advanced Science*, vol. 5, no. 10, p. 1800256, 2018. [Online]. Available: https://onlinelibrary.wiley.com/doi/abs/10.1002/advs.201800256

[183] S. G. Nurzaman, F. Iida, L. Margheri, and C. Laschi, "Soft Robotics on the Move: Scientific Networks, Activities, and Future Challenges," *Soft Robotics*, vol. 1, no. 2, pp. 154–158, Jun. 2014. [Online]. Available: https://www.liebertpub.com/doi/10.1089/soro.2014.0012

[184] C. Majidi, "Soft Robotics: A Perspective—Current Trends and Prospects for the Future," *Soft Robotics*, vol. 1, no. 1, pp. 5–11, Jul. 2013. [Online]. Available: https://www.liebertpub.com/doi/10.1089/soro.2013.0001

[185] D. Trivedi, C. D. Rahn, W. M. Kier, and I. D. Walker, "Soft Robotics: Biological Inspiration, State of the Art, and Future Research," 2008. [Online]. Available: https://www.hindawi.com/journals/abb/2008/520417/abs/

[186] N. Tejima and D. Stefanov, "Fail-safe components for rehabilitation robots - a reflex mechanism and fail-safe force sensor," in *9th International Conference on Rehabilitation Robotics, 2005. ICORR 2005.*, Jun. 2005, pp. 456–460.

[187] F. Delcomyn, "The Effect of Limb Amputation on Locomotion in the Cockroach Periplaneta Americana," *Journal of Experimental Biology*, vol. 54, no. 2, pp. 453–469, Apr. 1971. [Online]. Available: http://jeb.biologists.org/content/54/2/453

[188] Y. Bar-Cohen, "Engineered muscle actuators: cells and tissues." in *Biomimetics: Biologically Inspired Technologies.* New York, NY, USA: Dennis R G, Herr H. CRC

Press, 2005, vol. Ch. 9, p. 234. [Online]. Available: https://www.crcpress.com/Biomimetics-Biologically-Inspired-Technologies/Bar-Cohen/p/book/9780849331633

[189] S. Wakimoto, K. Suzumori, and J. Takeda, "Flexible artificial muscle by bundle of McKibben fiber actuators," in *2011 IEEE/ASME International Conference on Advanced Intelligent Mechatronics (AIM)*, Jul. 2011, pp. 457–462.

[190] a. B. Hannaford, "Measurement and modeling of McKibben pneumatic artificial muscles," *IEEE Transactions on Robotics and Automation*, vol. 12, no. 1, pp. 90–102, Feb. 1996.

[191] M. B. Pritts and C. D. Rahn, "Design of an artificial muscle continuum robot," in *IEEE International Conference on Robotics and Automation, 2004. Proceedings. ICRA '04. 2004*, vol. 5, Apr. 2004, pp. 4742–4746 Vol.5.

[192] E. T. Roche, R. Wohlfarth, J. T. B. Overvelde, N. V. Vasilyev, F. A. Pigula, D. J. Mooney, K. Bertoldi, and C. J. Walsh, "A Bioinspired Soft Actuated Material," *Advanced Materials*, vol. 26, no. 8, pp. 1200–1206, 2014. [Online]. Available: https://www.onlinelibrary.wiley.com/doi/abs/10.1002/adma.201304018

[193] C. Laschi and M. Cianchetti, "Soft Robotics: New Perspectives for Robot Bodyware and Control," *Frontiers in Bioengineering and Biotechnology*, vol. 2, 2014. [Online]. Available: https://www.frontiersin.org/articles/10.3389/fbioe.2014.00003/full

[194] S. Kim, E. Hawkes, K. Choy, M. Joldaz, J. Foleyz, and R. Wood, "Micro artificial muscle fiber using NiTi spring for soft robotics," in *2009 IEEE/RSJ International Conference on Intelligent Robots and Systems*, Oct. 2009, pp. 2228–2234.

[195] K.-J. Cho, J.-S. Koh, S. Kim, W.-S. Chu, Y. Hong, and S.-H. Ahn, "Review of manufacturing processes for soft biomimetic robots," *International Journal of Precision Engineering and Manufacturing*, vol. 10, no. 3, pp. 171–181, Jul. 2009. [Online]. Available: https://doi.org/10.1007/s12541-009-0064-6

[196] K. Takashima, J. Rossiter, and T. Mukai, "McKibben artificial muscle using shape-memory polymer," *Sensors and Actuators A: Physical*, vol. 164, no. 1, pp. 116–124, Nov. 2010. [Online]. Available: http://www.sciencedirect.com/science/article/pii/S0924424710004012

[197] T. Noritsugu, "Pneumatic Soft Actuator for Human Assist Technology," in *Symposium on Fluid Power*, Nov. 2005, pp. 11–20.

[198] H. K. Yap, J. C. H. Goh, and R. C. H. Yeow, "Design and Characterization of Soft Actuator for Hand Rehabilitation Application," in *6th European Conference of the International Federation for Medical and Biological Engineering*, ser. IFMBE Proceedings, I. Lacković and D. Vasic, Eds. Springer International Publishing, 2015, pp. 367–370.

[199] D. Sasaki, T. Noritsugu, and M. Takaiwa, “Development of Active Support Splint driven by Pneumatic Soft Actuator (ASSIST),” in *Proceedings of the 2005 IEEE International Conference on Robotics and Automation*, Apr. 2005, pp. 520–525.

[200] H. Kobayashi, Y. Ishida, and H. Suzuki, “Realization of all motion for the upper limb by a muscle suit,” in *RO-MAN 2004. 13th IEEE International Workshop on Robot and Human Interactive Communication (IEEE Catalog No.04TH8759)*, Sep. 2004, pp. 631–636.

[201] M. Wehner, B. Quinlivan, P. M. Aubin, E. Martinez-Villalpando, M. Baumann, L. Stirling, K. Holt, R. Wood, and C. Walsh, “A lightweight soft exosuit for gait assistance,” in *2013 IEEE International Conference on Robotics and Automation*, May 2013, pp. 3362–3369.

[202] Y. Park, B. Chen, D. Young, L. Stirling, R. J. Wood, E. Goldfield, and R. Nagpal, “Bio-inspired active soft orthotic device for ankle foot pathologies,” in *2011 IEEE/RSJ International Conference on Intelligent Robots and Systems*, Sep. 2011, pp. 4488–4495.

[203] A. T. Asbeck, K. Schmidt, and C. J. Walsh, “Soft exosuit for hip assistance,” *Robotics and Autonomous Systems*, vol. 73, pp. 102–110, Nov. 2015. [Online]. Available: http://www.sciencedirect.com/science/article/pii/S0921889014002103

[204] D. P. Ferris, J. M. Czerniecki, and B. Hannaford, “An Ankle-Foot Orthosis Powered by Artificial Pneumatic Muscles,” *Journal of applied biomechanics*, vol. 21, no. 2, pp. 189–197, May 2005. [Online]. Available: https://www.ncbi.nlm.nih.gov/pmc/articles/PMC1351122/

[205] Y. Sun, Y. S. Song, and J. Paik, “Characterization of silicone rubber based soft pneumatic actuators,” in *2013 IEEE/RSJ International Conference on Intelligent Robots and Systems*, Nov. 2013, pp. 4446–4453.

[206] M. Calisti, M. Giorelli, G. Levy, B. Mazzolai, B. Hochner, C. Laschi, and P. Dario, “An octopus-bioinspired solution to movement and manipulation for soft robots,” *Bioinspiration & Biomimetics*, vol. 6, no. 3, p. 036002, Sep. 2011.

[207] A. T. Asbeck, S. M. De Rossi, K. G. Holt, and C. J. Walsh, “A biologically inspired soft exosuit for walking assistance,” *The International Journal of Robotics Research*, vol. 34, no. 6, pp. 744–762, May 2015. [Online]. Available: https://doi.org/10.1177/0278364914562476

[208] C. Suh, J. C. Margarit, Y. S. Song, and J. K. Paik, “Soft Pneumatic Actuator skin with embedded sensors,” *2014 IEEE/RSJ International Conference on Intelligent Robots and Systems*, pp. 2783–2788, 2014.

[209] Y. S. Song, Y. Sun, R. v. d. Brand, J. v. Zitzewitz, S. Micera, G. Courtine, and J. Paik, “Soft robot for gait rehabilitation of spinalized rodents,” in *2013 IEEE/RSJ International Conference on Intelligent Robots and Systems*, Nov. 2013, pp. 971–976.

[210] “Wacker Chemical Corporation, Elastosil® M4601.”

[211] B. Tondu and P. Lopez, “Modeling and control of McKibben artificial muscle robot actuators,” *IEEE Control Systems Magazine*, vol. 20, no. 2, pp. 15–38, Apr. 2000.

[212] F. Connolly, P. Polygerinos, C. J. Walsh, and K. Bertoldi, “Mechanical Programming of Soft Actuators by Varying Fiber Angle,” *Soft Robotics*, vol. 2, no. 1, pp. 26–32, Mar. 2015. [Online]. Available: https://www.liebertpub.com/doi/10.1089/soro.2015.0001

[213] P. Polygerinos, Z. Wang, J. T. B. Overvelde, K. C. Galloway, R. J. Wood, K. Bertoldi, and C. J. Walsh, “Modeling of soft fiber-reinforced bending actuators,” *IEEE Transactions on Robotics*, vol. 31, no. 3, pp. 778–789, 6 2015.

[214] L. Paez, G. Agarwal, and J. Paik, “Design and analysis of a soft pneumatic actuator with origami shell reinforcement,” *Soft Robotics*, vol. 3, no. 3, pp. 109–119, 9 2016.

[215] J. M. Florez, M. Shah, E. M. Moraud, S. Wurth, L. Baud, J. V. Zitzewitz, v. d. R. Brand, S. Micera, G. Courtine, and J. Paik, “Rehabilitative soft exoskeleton for rodents,” *IEEE Transactions on Neural Systems and Rehabilitation Engineering*, vol. 25, no. 2, pp. 107–118, 2 2017.

[216] I. Cho, J. Kim, and J. Paek, “Microrobotic tentacles with spiral bending capability based on shape-engineered elastomeric microtubes,” *Scientific Reports*, vol. 5, p. 10768, 6 2015.

[217] A. D. Marchese, C. D. Onal, and D. Rus, “Autonomous soft robotic fish capable of escape maneuvers using fluidic elastomer actuators,” *Soft Robotics*, vol. 1, no. 1, pp. 75–87, 3 2014, pMID: 27625912 PMCID: PMC4997624.

[218] D. Yang, M. S. Verma, J.-H. So, B. Mosadegh, C. Keplinger, B. Lee, F. Khashai, E. Lossner, Z. Suo, and G. M. Whitesides, “Buckling pneumatic linear actuators inspired by muscle,” *Advanced Materials Technologies*, vol. 1, no. 3, p. 1600055, 6 2016.

[219] A. Ainla, M. S. Verma, D. Yang, and G. M. Whitesides, “Soft, rotating pneumatic actuator,” *Soft Robotics*, vol. 4, no. 3, pp. 297–304, 5 2017.

[220] S. Li, D. M. Vogt, D. Rus, and R. J. Wood, “Fluid-driven origami-inspired artificial muscles,” *Proceedings of the National Academy of Sciences*, p. 201713450, 11 2017, pMID: 29180416.

[221] M. A. Robertson and J. Paik, “Trunk postural tracking of assistive soft pneumatic actuator belt,” Tech. Rep., 2016.

[222] G. Agarwal, M. A. Robertson, H. Sonar, and J. Paik, “Design and Computational Modeling of a Modular, Compliant Robotic Assembly for Human Lumbar Unit and Spinal Cord Assistance,” *Scientific Reports*, vol. 7, no. 1, p. 14391, Oct. 2017. [Online]. Available: https://www.nature.com/articles/s41598-017-14220-3

[223] S. Hauser, M. Robertson, A. Ijspeert, and J. Paik, “JammJoint: A Variable Stiffness Device Based on Granular Jamming for Wearable Joint Support,” *IEEE Robotics and Automation Letters*, vol. 2, no. 2, pp. 849–855, Apr. 2017.

[224] M. A. Robertson, O. Kara, and J. Paik, “Soft pneumatic actuator driven origami inspired modular robotic ”pneumagami”,” *International Journal of Robotics Research*, 2019, in review.

[225] R. P. Bunge, W. R. Puckett, J. L. Becerra, A. Marcillo, and R. M. Quencer, “Observations on the pathology of human spinal cord injury. A review and classification of 22 new cases with details from a case of chronic cord compression with extensive focal demyelination,” *Advances in Neurology*, vol. 59, pp. 75–89, 1993.

[226] F. Ben-Hatira, K. Saidane, and A. Mrabet, “A finite element modeling of the human lumbar unit including the spinal cord,” *Journal of Biomedical Science and Engineering*, vol. 05, p. 146, Mar. 2012.

[227] N. Yoganandan, S. Kumaresan, L. Voo, and F. A. Pintar, “Finite element applications in human cervical spine modeling,” *Spine*, vol. 21, no. 15, pp. 1824–1834, Aug. 1996.

[228] A. L. Behrman and S. J. Harkema, “Locomotor training after human spinal cord injury: a series of case studies,” *Physical Therapy*, vol. 80, no. 7, pp. 688–700, Jul. 2000.

[229] F. Ilievski, A. D. Mazzeo, R. F. Shepherd, X. Chen, and G. M. Whitesides, “Soft robotics for chemists,” *Angewandte Chemie (International Ed. in English)*, vol. 50, no. 8, pp. 1890–1895, Feb. 2011.

[230] H.-T. Lin, G. G. Leisk, and B. Trimmer, “GoQBot: a caterpillar-inspired soft-bodied rolling robot,” *Bioinspiration & Biomimetics*, vol. 6, no. 2, p. 026007, Jun. 2011.

[231] A. D. Marchese, R. K. Katzschmann, and D. Rus, “A Recipe for Soft Fluidic Elastomer Robots,” *Soft Robotics*, vol. 2, no. 1, pp. 7–25, Mar. 2015.

[232] G. Agarwal, N. Besuchet, B. Audergon, and J. Paik, “Stretchable Materials for Robust Soft Actuators towards Assistive Wearable Devices,” *Scientific Reports*, vol. 6, p. 34224, Sep. 2016.

[233] B. C. Mac Murray, X. An, S. S. Robinson, I. M. van Meerbeek, K. W. O’Brien, H. Zhao, and R. F. Shepherd, “Poroelastic Foams for Simple Fabrication of Complex Soft Robots,” *Advanced Materials*, vol. 27, no. 41, pp. 6334–6340, Nov. 2015.

[234] M. A. Robertson, H. Sadeghi, J. M. Florez, and J. Paik, “Soft Pneumatic Actuator Fascicles for High Force and Reliability,” *Soft Robotics*, vol. 4, no. 1, pp. 23–32, Oct. 2016.

[235] C. Laschi, M. Cianchetti, B. Mazzolai, L. Margheri, M. Follador, and P. Dario, “Soft Robot Arm Inspired by the Octopus,” *Advanced Robotics*, vol. 26, no. 7, pp. 709–727, Jan. 2012.

[236] P. Polygerinos, Z. Wang, J. T. B. Overvelde, K. C. Galloway, R. J. Wood, K. Bertoldi, and C. J. Walsh, “Modeling of Soft Fiber-Reinforced Bending Actuators,” *IEEE Transactions on Robotics*, vol. 31, no. 3, pp. 778–789, Jun. 2015.

[237] B. Tondu, “Modelling of the McKibben artificial muscle: A review,” *Journal of Intelligent Material Systems and Structures*, vol. 23, no. 3, pp. 225–253, Feb. 2012.

[238] C.-P. Chou and B. Hannaford, “Measurement and modeling of McKibben pneumatic artificial muscles,” *IEEE Transactions on Robotics and Automation*, vol. 12, no. 1, pp. 90–102, Feb. 1996.

[239] D. Yang, M. S. Verma, E. Lossner, D. Stothers, and G. M. Whitesides, “Negative-Pressure Soft Linear Actuator with a Mechanical Advantage,” *Advanced Materials Technologies*, vol. 2, no. 1, p. 1600164, 2017.

[240] D. Yang, B. Mosadegh, A. Ainla, B. Lee, F. Khashai, Z. Suo, K. Bertoldi, and G. M. Whitesides, “Buckling of Elastomeric Beams Enables Actuation of Soft Machines,” *Advanced Materials*, vol. 27, no. 41, pp. 6323–6327, 2015.

[241] A. Argiolas, B. C. Mac Murray, I. Van Meerbeek, J. Whitehead, E. Sinibaldi, B. Mazzolai, and R. F. Shepherd, “Sculpting Soft Machines,” *Soft Robotics*, vol. 3, no. 3, pp. 101–108, Jul. 2016.

[242] O. H. Yeoh, “Some Forms of the Strain Energy Function for Rubber,” *Rubber Chemistry and Technology*, vol. 66, no. 5, pp. 754–771, Nov. 1993.

[243] R. Ham, T. Sugar, B. Vanderborght, K. Hollander, and D. Lefeber, “Compliant actuator designs,” *IEEE Robotics & Automation Magazine*, vol. 16, no. 3, pp. 81–94, Sep. 2009.

[244] K. Melo, M. Garabini, G. Grioli, M. Catalano, L. Malagia, and A. Bicchi, “Open Source VSA-CubeBots for Rapid Soft Robot Prototyping,” in *RoMa, Robot Makers Workshop in RSS2014, Robotics Science and Systems*, 2014, pp. 1–5.

[245] J. Shang, D. P. Noonan, C. Payne, J. Clark, M. H. Sodergren, A. Darzi, and G.-Z. Yang, “An articulated universal joint based flexible access robot for minimally invasive surgery,” in *Robotics and Automation (ICRA), 2011 IEEE International Conference on.* IEEE, 2011, pp. 1147–1152.

[246] M. Vespignani, K. Melo, S. Bonardi, and A. J. Ijspeert, “Role of compliance on the locomotion of a reconfigurable modular snake robot,” in *Intelligent Robots and Systems (IROS), 2015 IEEE/RSJ International Conference on.* IEEE, 2015, pp. 2238–2245.

[247] D. Rollinson, Y. Bilgen, B. Brown, F. Enner, S. Ford, C. Layton, J. Rembisz, M. Schwerin, A. Willig, P. Velagapudi, and others, “Design and architecture of a series elastic snake robot.” in *IROS*, 2014, pp. 4630–4636.

[248] G. Robinson and J. B. C. Davies, “Continuum robots-a state of the art,” in *Robotics and Automation, 1999. Proceedings. 1999 IEEE International Conference on*, vol. 4. IEEE, 1999, pp. 2849–2854.

[249] U. Çulha and F. Iida, “Enhancement of finger motion range with compliant anthropomorphic joint design,” *Bioinspiration & Biomimetics*, vol. 11, no. 2, p. 026001, Feb. 2016.

[250] D. Guo and H. Hu, “Nonlinear stiffness of a magneto-rheological damper,” *Nonlinear Dynamics*, vol. 40, pp. 241–249, 2005.

[251] A. J. Liu and S. R. Nagel, “Nonlinear dynamics: Jamming is not just cool any more,” *Nature*, vol. 396, no. 6706, pp. 21–22, 1998.

[252] A. Jiang, G. Xynogalas, P. Dasgupta, K. Althoefer, and T. Nanayakkara, “Design of a variable stiffness flexible manipulator with composite granular jamming and membrane coupling,” in *2012 IEEE/RSJ International Conference on Intelligent Robots and Systems (IROS)*, Oct. 2012, pp. 2922–2927.

[253] E. Brown, N. Rodenberg, J. Amend, A. Mozeika, E. Steltz, M. R. Zakin, H. Lipson, and H. M. Jaeger, “Universal robotic gripper based on the jamming of granular material,” *Proceedings of the National Academy of Sciences*, vol. 107, no. 44, pp. 18 809–18 814, 2010.

[254] J. Amend, E. Brown, N. Rodenberg, H. Jaeger, and H. Lipson, “A positive pressure universal gripper based on the jamming of granular material,” *IEEE Transactions on Robotics*, vol. 28, no. 2, pp. 341–350, Apr. 2012.

[255] S. Hauser, P. Eckert, A. Tuleu, and A. Ijspeert, “Friction and damping of a compliant foot based on granular jamming for legged robots,” in *2016 6th IEEE International Conference on Biomedical Robotics and Biomechatronics (BioRob)*. IEEE, 2016, pp. 1160–1165.

[256] J. M. Bajkowski, B. Dyniewicz, and C. I. Bajer, “Damping properties of a beam with vacuum-packed granular damper,” *Journal of Sound and Vibration*, vol. 341, pp. 74–85, Apr. 2015.

[257] E. Steltz, A. Mozeika, N. Rodenberg, E. Brown, and H. Jaeger, “JSEL: Jamming Skin Enabled Locomotion,” in *2009 IEEE/RSJ International Conference on Intelligent Robots and Systems*. IEEE, Oct. 2009, pp. 5672–5677.

[258] A. J. Loeve, O. S. van de Ven, J. G. Vogel, P. Breedveld, and J. Dankelman, “Vacuum packed particles as flexible endoscope guides with controllable rigidity,” *Granular Matter*, vol. 12, no. 6, pp. 543–554, Dec. 2010.

[259] A. Jiang, A. Ataollahi, K. Althoefer, P. Dasgupta, and T. Nanayakkara, “A variable stiffness joint by granular jamming,” in *ASME 2012 International Design Engineering Technical Conferences and Computers and Information in Engineering Conference*. American Society of Mechanical Engineers, 2012, pp. 267–275.

[260] M. Hu, Q.-s. Mu, N. Luo, G. Li, and N.-b. Peng, “Behavior of hollow balls containing granules bouncing repeatedly off the ground,” *EPL (Europhysics Letters)*, vol. 103, no. 1, p. 14003, Jul. 2013. [Online]. Available: http://stacks.iop.org/0295-5075/103/i=1/a=14003?key=crossref.37082b1f5e0722e992e635de2b62ec14

[261] M. Sánchez, G. Rosenthal, and L. A. Pugnaloni, “Universal response of optimal granular damping devices,” *Journal of Sound and Vibration*, vol. 331, no. 20, pp. 4389–4394, 2012. [Online]. Available: http://www.sciencedirect.com/science/article/pii/S0022460X12003513

[262] F. Pacheco-Vázquez and S. Dorbolo, “Rebound of a confined granular material: combination of a bouncing ball and a granular damper,” *Scientific Reports*, vol. 3, Jul. 2013.

[263] S. Rosset, P. Gebbers, B. M. O’Brien, and H. R. Shea, “The need for speed,” in *SPIE Smart Structures and Materials+ Nondestructive Evaluation and Health Monitoring*. International Society for Optics and Photonics, Apr. 2012, pp. 834 004–834 004.

[264] W. Huo, S. Mohammed, J. C. Moreno, and Y. Amirat, “Lower Limb Wearable Robots for Assistance and Rehabilitation: A State of the Art,” *IEEE Systems Journal*, vol. 10, no. 3, pp. 1068–1081, Sep. 2016.

[265] H. Al-Fahaam, S. Davis, and S. Nefti-Meziani, “Power assistive and rehabilitation wearable robot based on pneumatic soft actuators,” in *2016 21st International Conference on Methods and Models in Automation and Robotics (MMAR)*, Aug. 2016, pp. 472–477.

[266] H. In, B. B. Kang, M. Sin, and K. Cho, “Exo-Glove: A Wearable Robot for the Hand with a Soft Tendon Routing System,” *IEEE Robotics Automation Magazine*, vol. 22, no. 1, pp. 97–105, Mar. 2015.

[267] W. McMahan, B. A. Jones, I. D. Walker *et al.*, “Design and implementation of a multisection continuum robot: Air-octor.” in *IROS*, 2005, pp. 2578–2585.

[268] M. Cianchetti, M. Follador, B. Mazzolai, P. Dario, and C. Laschi, “Design and development of a soft robotic octopus arm exploiting embodied intelligence,” in *Robotics and Automation (ICRA), 2012 IEEE International Conference on*. IEEE, 2012, pp. 5271–5276.

[269] F. Renda, M. Giorelli, M. Calisti, M. Cianchetti, and C. Laschi, “Dynamic model of a multibending soft robot arm driven by cables,” *IEEE Transactions on Robotics*, vol. 30, no. 5, pp. 1109–1122, 2014.

[270] R. Qi, A. Khajepour, W. W. Melek, T. L. Lam, and Y. Xu, “Design, kinematics, and control of a multijoint soft inflatable arm for human-safe interaction,” *IEEE Transactions on Robotics*, vol. 33, no. 3, pp. 594–609, 2017.

[271] S. Kurumaya, H. Nabae, G. Endo, and K. Suzumori, “Exoskeleton inflatable robotic arm with thin mckibben muscle,” in *2018 IEEE International Conference on Soft Robotics (RoboSoft)*. IEEE, 2018, pp. 120–125.

[272] H. Yang, M. Xu, W. Li, and S. Zhang, “Design and implementation of a soft robotic arm driven by sma coils,” *IEEE Transactions on Industrial Electronics*, 2018.

[273] X. Liang, H. Cheong, Y. Sun, J. Guo, C. K. Chui, and C.-H. Yeow, “Design, characterization, and implementation of a two-dof fabric-based soft robotic arm,” *IEEE Robotics and Automation Letters*, vol. 3, no. 3, pp. 2702–2709, 2018.

[274] C. D. Onal, R. J. Wood, and D. Rus, “Towards printable robotics: Origami-inspired planar fabrication of three-dimensional mechanisms,” in *Robotics and Automation (ICRA), 2011 IEEE International Conference on.* IEEE, 2011, pp. 4608–4613.

[275] J. K. Paik, A. Byoungkwon, D. Rus, and R. J. Wood, “Robotic origamis: Self-morphing modular robot,” Tech. Rep., 2012.

[276] S. Felton, M. Tolley, E. Demaine, D. Rus, and R. Wood, “A method for building self-folding machines,” *Science*, vol. 345, no. 6197, pp. 644–646, Aug. 2014. [Online]. Available: http://science.sciencemag.org/content/345/6197/644

[277] M. T. Tolley, S. M. Felton, S. Miyashita, L. Xu, B. Shin, M. Zhou, D. Rus, and R. J. Wood, “Self-folding shape memory laminates for automated fabrication,” in *Intelligent Robots and Systems (IROS), 2013 IEEE/RSJ International Conference on.* IEEE, 2013, pp. 4931–4936.

[278] S. Felton, K. Becker, D. Aukes, and R. Wood, “Self-folding with shape memory composites at the millimeter scale,” *Journal of Micromechanics and Microengineering*, vol. 25, no. 8, p. 085004, 2015.

[279] M. T. Tolley, S. M. Felton, S. Miyashita, D. Aukes, D. Rus, and R. J. Wood, “Self-folding origami: shape memory composites activated by uniform heating,” *Smart Materials and Structures*, vol. 23, no. 9, p. 094006, 2014.

[280] S. Miyashita, S. Guitron, M. Ludersdorfer, C. R. Sung, and D. Rus, “An untethered miniature origami robot that self-folds, walks, swims, and degrades,” in *Robotics and Automation (ICRA), 2015 IEEE International Conference on.* IEEE, 2015, pp. 1490–1496.

[281] Z. Zhakypov, M. Falahi, M. Shah, and J. Paik, “The design and control of the multi-modal locomotion origami robot, Tribot,” in *2015 IEEE/RSJ International Conference on Intelligent Robots and Systems (IROS)*, Sep. 2015, pp. 4349–4355.

[282] D.-Y. Lee, G.-P. Jung, M.-K. Sin, S.-H. Ahn, and K.-J. Cho, “Deformable wheel robot based on origami structure,” in *Robotics and Automation (ICRA), 2013 IEEE International Conference on.* IEEE, 2013, pp. 5612–5617.

[283] E. Vander Hoff, D. Jeong, and K. Lee, “Origamibot-i: A thread-actuated origami robot for manipulation and locomotion,” in *Intelligent Robots and Systems (IROS 2014), 2014 IEEE/RSJ International Conference on.* IEEE, 2014, pp. 1421–1426.

[284] C. D. Onal, R. J. Wood, and D. Rus, “An origami-inspired approach to worm robots,” *IEEE/ASME Transactions on Mechatronics*, vol. 18, no. 2, pp. 430–438, 2013.

[285] S.-J. Kim, D.-Y. Lee, G.-P. Jung, and K.-J. Cho, “An origami-inspired, self-locking robotic arm that can be folded flat,” *Science Robotics*, vol. 3, no. 16, p. eaar2915, 2018.

[286] M. Salerno, K. Zhang, A. Menciassi, and J. S. Dai, “A Novel 4-DOF Origami Grasper With an SMA-Actuation System for Minimally Invasive Surgery,” *IEEE Transactions on Robotics*, vol. 32, no. 3, pp. 484–498, Jun. 2016.

[287] K. Zhang, C. Qiu, and J. S. Dai, “An extensible continuum robot with integrated origami parallel modules,” *Journal of Mechanisms and Robotics*, vol. 8, no. 3, p. 031010, 2016.

[288] S. Mintchev, J. Shintake, and D. Floreano, “Bioinspired dual-stiffness origami,” *Science Robotics*, vol. 3, no. 20, p. eaau0275, Jul. 2018. [Online]. Available: http://robotics.sciencemag.org/content/3/20/eaau0275

[289] Z. Zhakypov, F. Heremans, A. Billard, and J. Paik, “An Origami-Inspired Reconfigurable Suction Gripper for Picking Objects With Variable Shape and Size,” *IEEE Robotics and Automation Letters*, vol. 3, no. 4, pp. 2894–2901, Oct. 2018.

[290] E. Rodriguez Leal and J. S. Dai, “From Origami to a New Class of Centralized 3-DOF Parallel Mechanisms,” pp. 1183–1193, Jan. 2007. [Online]. Available: http://dx.doi.org/10.1115/DETC2007-35516

[291] D. Rus and M. T. Tolley, “Design, fabrication and control of origami robots,” *Nature Reviews Materials*, vol. 3, no. 6, p. 101, Jun. 2018. [Online]. Available: https://www.nature.com/articles/s41578-018-0009-8

[292] T. Liu, Y. Wang, and K. Lee, “Three-Dimensional Printable Origami Twisted Tower: Design, Fabrication, and Robot Embodiment,” *IEEE Robotics and Automation Letters*, vol. 3, no. 1, pp. 116–123, Jan. 2018.

[293] Q. Ge, C. K. Dunn, H. J. Qi, and M. L. Dunn, “Active origami by 4d printing,” *Smart Materials and Structures*, vol. 23, no. 9, p. 094007, Aug. 2014. [Online]. Available: http://iopscience.iop.org/article/10.1088/0964-1726/23/9/094007/meta

[294] A. Firouzeh and J. Paik, “An under-actuated origami gripper with adjustable stiffness joints for multiple grasp modes,” *Smart Materials and Structures*, vol. 26, no. 5, p. 055035, 2017. [Online]. Available: http://stacks.iop.org/0964-1726/26/i=5/a=055035

[295] ——, “Robogami: A Fully Integrated Low-Profile Robotic Origami,” *Journal of Mechanisms and Robotics*, vol. 7, no. 2, pp. 021 009–021 009–8, May 2015. [Online]. Available: http://dx.doi.org/10.1115/1.4029491

[296] J.-H. Na, A. A. Evans, J. Bae, M. C. Chiappelli, C. D. Santangelo, R. J. Lang, T. C. Hull, and R. C. Hayward, “Programming Reversibly Self-Folding Origami with Micropatterned Photo-Crosslinkable Polymer Trilayers,” *Advanced Materials*, vol. 27, no. 1, pp. 79–85, Jan. 2015. [Online]. Available: https://onlinelibrary.wiley.com/doi/full/10.1002/adma.201403510

[297] J. Mu, C. Hou, H. Wang, Y. Li, Q. Zhang, and M. Zhu, "Origami-inspired active graphene-based paper for programmable instant self-folding walking devices," *Science Advances*, vol. 1, no. 10, p. e1500533, Nov. 2015. [Online]. Available: http://advances.sciencemag.org/content/1/10/e1500533

[298] S. Ahmed, Z. Ounaies, and M. Frecker, "Investigating the performance and properties of dielectric elastomer actuators as a potential means to actuate origami structures," *Smart Materials and Structures*, vol. 23, no. 9, p. 094003, 2014. [Online]. Available: http://stacks.iop.org/0964-1726/23/i=9/a=094003

[299] H. McClintock, F. Z. Temel, N. Doshi, J.-s. Koh, and R. J. Wood, "The milliDelta: A high-bandwidth, high-precision, millimeter-scale Delta robot," *Science Robotics*, vol. 3, no. 14, p. eaar3018, Jan. 2018. [Online]. Available: http://robotics.sciencemag.org/content/3/14/eaar3018

[300] M. Salerno, A. Firouzeh, and J. Paik, "A Low Profile Electromagnetic Actuator Design and Model for an Origami Parallel Platform," *Journal of Mechanisms and Robotics*, vol. 9, no. 4, pp. 041 005–041 005–11, May 2017. [Online]. Available: http://dx.doi.org/10.1115/1.4036425

[301] P. Polygerinos, N. Correll, S. A. Morin, B. Mosadegh, C. D. Onal, K. Petersen, M. Cianchetti, M. T. Tolley, and R. F. Shepherd, "Soft Robotics: Review of Fluid-Driven Intrinsically Soft Devices; Manufacturing, Sensing, Control, and Applications in Human-Robot Interaction," *Advanced Engineering Materials*, vol. 19, no. 12, p. 1700016, Dec. 2017. [Online]. Available: https://onlinelibrary.wiley.com/doi/full/10.1002/adem.201700016

[302] M. A. Robertson, H. Sadeghi, J. M. Florez, and J. Paik, "Soft pneumatic actuator fascicles for high force and reliability," *Soft robotics*, vol. 4, no. 1, pp. 23–32, 2017.

[303] R. Niiyama, D. Rus, and S. Kim, "Pouch motors: Printable/inflatable soft actuators for robotics," in *Robotics and Automation (ICRA), 2014 IEEE International Conference on*. IEEE, 2014, pp. 6332–6337.

[304] J. Santoso, E. H. Skorina, M. Luo, R. Yan, and C. D. Onal, "Design and analysis of an origami continuum manipulation module with torsional strength," in *2017 IEEE/RSJ International Conference on Intelligent Robots and Systems (IROS)*, Sep. 2017, pp. 2098–2104.

[305] C. H. Belke and J. Paik, "Mori: A modular origami robot," *IEEE/ASME Transactions on Mechatronics*, vol. 22, no. 5, pp. 2153–2164, 2017.

[306] H. Fang, Y. Fang, and K. Zhang, "Kinematics and workspace analysis of a novel 3-DOF parallel manipulator with virtual symmetric plane," *Proceedings of the Institution of Mechanical Engineers, Part C: Journal of Mechanical Engineering Science*, vol. 227, no. 3, pp. 620–629, Mar. 2013.

[307] M. Robertson, F. Efremov, and J. Paik, “RoboScallop: A Bivalve inspired swimming robot,” *IEEE Robotics and Automation Letters*, pp. 1–1, 2019.

[308] L. Whitcomb *et al.*, “Advances in Underwater Robot Vehicles for Deep Ocean Exploration: Navigation, Control, and Survey Operations,” in *Robotics Research.* Springer, London, 2000, pp. 439–448.

[309] R. Sparrow and G. Lucas, “When Robots rule the waves?” *Naval War College Review*, vol. 69, no. 4, pp. 49–78, 2016.

[310] A. Crespi and A. Ijspeert, “AmphiBot II: An Amphibious Snake Robot that Crawls and Swims using a Central Pattern Generator,” *Proceedings of the 9th International Conference on Climbing and Walking Robots (CLAWAR 2006)*, Jan. 2006.

[311] B. Bayat *et al.*, “Environmental monitoring using autonomous vehicles: a survey of recent searching techniques,” *Current Opinion in Biotechnology*, vol. 45, pp. 76–84, Jun. 2017.

[312] S. Ohata *et al.*, “Development of an autonomous underwater vehicle for observation of underwater structures,” in *Proceedings of OCEANS 2005 MTS/IEEE*, Sep. 2005, pp. 1928–1933 Vol. 3.

[313] M. K. Habib and Y. Baudoin, “Robot-Assisted Risky Intervention, Search, Rescue and Environmental Surveillance,” *International Journal of Advanced Robotic Systems*, vol. 7, no. 1, p. 10, Mar. 2010.

[314] A. Mazumdar *et al.*, “A compact, maneuverable, underwater robot for direct inspection of nuclear power piping systems,” in *2012 IEEE International Conference on Robotics and Automation*, May 2012, pp. 2818–2823.

[315] E. M. H. Zahugi, M. M. Shanta, and T. V. Prasad, “Oil Spill Cleaning Up Using Swarm of Robots,” in *Advances in Computing and Information Technology*, ser. Advances in Intelligent Systems and Computing. Springer, Berlin, Heidelberg, 2013, pp. 215–224.

[316] C. v. Alt *et al.*, “Hunting for mines with REMUS: a high performance, affordable, free swimming underwater robot,” in *MTS/IEEE Oceans 2001. An Ocean Odyssey. Conference Proceedings (IEEE Cat. No.01CH37295)*, vol. 1, 2001, pp. 117–122 vol.1.

[317] B. Allotta *et al.*, “The ARROWS project: adapting and developing robotics technologies for underwater archaeology,” *IFAC-PapersOnLine*, vol. 48, no. 2, pp. 194–199, Jan. 2015.

[318] N. E. Hussey *et al.*, “Aquatic animal telemetry: A panoramic window into the underwater world,” *Science*, vol. 348, no. 6240, p. 1255642, Jun. 2015.

[319] Office for Coastal Management. National Oceanic and Atmospheric Administration (NOAA), “NOAA Report on the Ocean and Great Lakes Economy,” Charleston, SC: NOAA Office for Coastal Management, Tech. Rep., 2017. [Online]. Available: https://coast.noaa.gov/digitalcoast/training/econreport.html

[320] J. Yuh, "Design and Control of Autonomous Underwater Robots: A Survey," *Autonomous Robots*, vol. 8, no. 1, pp. 7–24, Jan. 2000.

[321] A. Raj and A. Thakur, "Fish-inspired robots: design, sensing, actuation, and autonomy—a review of research," *Bioinspiration & Biomimetics*, vol. 11, no. 3, p. 031001, 2016.

[322] C. Stefanini *et al.*, "A novel autonomous, bioinspired swimming robot developed by neuroscientists and bioengineers," *Bioinspiration & Biomimetics*, vol. 7, no. 2, p. 025001, 2012.

[323] E. Kelasidi *et al.*, "Experimental investigation of efficient locomotion of underwater snake robots for lateral undulation and eel-like motion patterns," *Robotics and Biomimetics*, vol. 2, no. 1, p. 8, Dec. 2015.

[324] B. Bayat, A. Crespi, and A. Ijspeert, "Envirobot: A bio-inspired environmental monitoring platform," in *2016 IEEE/OES Autonomous Underwater Vehicles (AUV)*, Nov. 2016, pp. 381–386.

[325] A. D. Marchese, C. D. Onal, and D. Rus, "Towards a Self-contained Soft Robotic Fish: On-Board Pressure Generation and Embedded Electro-permanent Magnet Valves," in *Experimental Robotics*, ser. Springer Tracts in Advanced Robotics. Springer, Heidelberg, 2013, pp. 41–54, dOI: 10.1007/978-3-319-00065-7_4.

[326] S. F. Masoomi *et al.*, "The Kinematics and Dynamics of Undulatory Motion of a Tuna-Mimetic Robot," *International Journal of Advanced Robotic Systems*, vol. 12, no. 7, p. 83, Jul. 2015.

[327] P. Kodati *et al.*, "Microautonomous Robotic Ostraciiform (MARCO): Hydrodynamics, Design, and Fabrication," *IEEE Transactions on Robotics*, vol. 24, no. 1, pp. 105–117, Feb. 2008.

[328] D. Lachat, A. Crespi, and A. J. Ijspeert, "BoxyBot: a swimming and crawling fish robot controlled by a central pattern generator," in *The First IEEE/RAS-EMBS International Conference on Biomedical Robotics and Biomechatronics, 2006. BioRob 2006.*, Feb. 2006, pp. 643–648.

[329] K. Mohseni and R. Mittal, *Synthetic Jets: Fundamentals and Applications.* CRC Press, Sep. 2014, google-Books-ID: I_jRBQAAQBAJ.

[330] A. P. Thomas *et al.*, "Synthetic Jet Propulsion for Small Underwater Vehicles," in *Proceedings of the 2005 IEEE International Conference on Robotics and Automation*, Apr. 2005, pp. 181–187.

[331] A. A. Moslemi and P. S. Krueger, "Propulsive efficiency of a biomorphic pulsed-jet underwater vehicle," *Bioinspiration & Biomimetics*, vol. 5, no. 3, p. 036003, 2010.

[332] A. Polsenberg Thomas, “Exploration into the feasibility of underwater synthetic jet propulsion,” phd, California Institute of Technology, 2007.

[333] X. Lin and S. Guo, “Development of a Spherical Underwater Robot Equipped with Multiple Vectored Water-Jet-Based Thrusters,” *Journal of Intelligent & Robotic Systems*, vol. 67, no. 3-4, pp. 307–321, Sep. 2012.

[334] D. S. Barrett, “Propulsive efficiency of a flexible hull underwater vehicle,” Thesis, Massachusetts Institute of Technology, 1996.

[335] G. D. Weymouth, V. Subramaniam, and M. S. Triantafyllou, “Ultra-fast escape maneuver of an octopus-inspired robot,” *Bioinspiration & Biomimetics*, vol. 10, no. 1, 2015.

[336] F. Renda *et al.*, “Modelling cephalopod-inspired pulsed-jet locomotion for underwater soft robots,” *Bioinspiration & Biomimetics*, vol. 10, no. 5, p. 055005, 2015.

[337] F. Giorgio-Serchi, A. Arienti, and C. Laschi, “Underwater soft-bodied pulsed-jet thrusters: Actuator modeling and performance profiling,” *The International Journal of Robotics Research*, vol. 35, no. 11, pp. 1308–1329, Sep. 2016.

[338] K. Mohseni, “Pulsatile vortex generators for low-speed maneuvering of small underwater vehicles,” *Ocean Engineering*, vol. 33, no. 16, pp. 2209–2223, Nov. 2006.

[339] I. Vasilescu *et al.*, “Data Collection, Storage, and Retrieval with an Underwater Sensor Network,” in *Proceedings of the 3rd International Conference on Embedded Networked Sensor Systems*, ser. SenSys ’05. New York, NY, USA: ACM, 2005, pp. 154–165.

[340] A. Boch *et al.*, “A swarm of autonomous miniature underwater robot drifters for exploring submesoscale ocean dynamics,” *Nature Communications*, vol. 8, p. ncomms14189, Jan. 2017.

[341] T. Schmickl *et al.*, “CoCoRo – The Self-Aware Underwater Swarm,” in *2011 Fifth IEEE Conference on Self-Adaptive and Self-Organizing Systems Workshops*, Oct. 2011, pp. 120–126.

[342] T. Qiu *et al.*, “Swimming by reciprocal motion at low Reynolds number,” *Nature Communications*, vol. 5, p. 5119, Nov. 2014.

[343] J. D. Moore and E. R. Trueman, “Swimming of the scallop, Chlamys opercularis (L.),” *Journal of Experimental Marine Biology and Ecology*, vol. 6, no. 3, pp. 179–185, Apr. 1971.

[344] D. Donovan, J. P. Elias, and J. Baldwin, “Swimming behavior and morphometry of the file shell Limaria fragilis,” *Marine and Freshwater Behaviour and Physiology*, vol. 37, pp. 7–16, Mar. 2004.

[345] J.-Y. Cheng, I. G. Davison, and M. E. Demont, “Dynamics and energetics of scallop locomotion,” *Journal of Experimental Biology*, vol. 199, no. 9, pp. 1931–1946, Sep. 1996.

[346] D. M. Bailey and I. A. Johnston, "Scallop swimming kinematics and muscle performance: Modelling the effects of "within-animal" variation in temperature sensitivity," *Marine and Freshwater Behaviour and Physiology*, vol. 38, no. 1, pp. 1–19, Mar. 2005.

[347] I. Tremblay, M. Samson-Dô, and H. E. Guderley, "When Behavior and Mechanics Meet: Scallop Swimming Capacities and Their Hinge Ligament," *Journal of Shellfish Research*, vol. 34, no. 2, pp. 203–212, Aug. 2015.

[348] J.-Y. Cheng and M. E. DeMont, "Hydrodynamics of scallop locomotion: unsteady fluid forces on clapping shells," *Journal of Fluid Mechanics*, vol. 317, pp. 73–90, Jun. 1996.

[349] R. K. O'dor, "The Forces Acting on Swimming Squid," *Journal of Experimental Biology*, vol. 137, no. 1, pp. 421–442, Jul. 1988.

[350] M. Sfakiotakis, A. Kazakidi, and D. P. Tsakiris, "Octopus-inspired multi-arm robotic swimming," *Bioinspiration & Biomimetics*, vol. 10, no. 3, p. 035005, 2015.

[351] A. A. Villanueva, K. J. Marut, T. Michael, and S. Priya, "Biomimetic autonomous robot inspired by the Cyanea capillata (Cyro)," *Bioinspiration & Biomimetics*, vol. 8, no. 4, p. 046005, 2013.

[352] A. E. Carsen, B. G. Hatcher, and R. E. Scheibling, "Effect of flow velocity and body size on swimming trajectories of sea scallops, Placopecten magellanicus (Gmelin): a comparison of laboratory and field measurements," *Journal of Experimental Marine Biology and Ecology*, vol. 203, no. 2, pp. 223–243, Oct. 1996.

[353] I. Tremblay and H. Guderley, "Scallops Show That Muscle Metabolic Capacities Reflect Locomotor Style and Morphology," *Physiological and biochemical zoology : PBZ*, vol. 87, pp. 231–244, Mar. 2014.

[354] "Hydromea auv technology." [Online]. Available: http://www.hydromea.com/technology.html

[355] C. W. Fay, R. J. Neves, and G. B. Pardue, "Species profiles: life histories and environmental requirements of coastal fishes and invertebrates (mid-Atlantic): bay scallop," U.S. Fish and Wildlife Service, Federal Government Series 82/11.12, 1983.

[356] M. A. Robertson, J. Paik, A. Ijspeert, and A. R. Wu, "A low-cost, actuated passive dynamic walker kit for accessible research and education," Mariehamn, Finland, 2017.

[357] E. Ackerman, "IHMC's ATLAS Robot Learning to Do Some Chores," Jan. 2016. [Online]. Available: https://spectrum.ieee.org/automaton/robotics/humanoids/atlas-does-some-chores

[358] "Boston Dynamics: Dedicated to the Science and Art of How Things Move." [Online]. Available: https://www.bostondynamics.com/

[359] T. McGeer, "Passive Dynamic Walking," *The International Journal of Robotics Research*, vol. 9, no. 2, pp. 62–82, Apr. 1990. [Online]. Available: http://ijr.sagepub.com/content/9/2/62

[360] S. H. Collins and A. Ruina, "A Bipedal Walking Robot with Efficient and Human-Like Gait," in *Proceedings of the 2005 IEEE International Conference on Robotics and Automation*, Apr. 2005, pp. 1983–1988.

[361] P. A. Bhounsule, J. Cortell, A. Grewal, B. Hendriksen, J. G. D. Karssen, C. Paul, and A. Ruina, "Low-bandwidth reflex-based control for lower power walking: 65 km on a single battery charge," *The International Journal of Robotics Research*, vol. 33, no. 10, pp. 1305–1321, Sep. 2014. [Online]. Available: https://doi.org/10.1177/0278364914527485

[362] M. Wisse, D. G. E. Hobbelen, and A. L. Schwab, "Adding an Upper Body to Passive Dynamic Walking Robots by Means of a Bisecting Hip Mechanism," *IEEE Transactions on Robotics*, vol. 23, pp. 112–123, 2007.

[363] A. Seyfarth, H. Geyer, and H. Herr, "Swing-leg retraction: a simple control model for stable running," *The Journal of Experimental Biology*, vol. 206, no. Pt 15, pp. 2547–2555, Aug. 2003.

[364] M. Srinivasan and A. Ruina, "Computer optimization of a minimal biped model discovers walking and running," *Nature*, vol. 439, no. 7072, pp. 72–75, Jan. 2006. [Online]. Available: http://www.nature.com/nature/journal/v439/n7072/full/nature04113.html

[365] A. D. Kuo, "Energetics of actively powered locomotion using the simplest walking model," *Journal of Biomechanical Engineering*, vol. 124, no. 1, pp. 113–120, Feb. 2002.

[366] M. Vukobratovic and D. Juricic, "Contribution to the Synthesis of Biped Gait," *IEEE Transactions on Biomedical Engineering*, vol. BME-16, no. 1, pp. 1–6, Jan. 1969.

[367] H. Geyer and H. Herr, "A muscle-reflex model that encodes principles of legged mechanics produces human walking dynamics and muscle activities," *IEEE transactions on neural systems and rehabilitation engineering: a publication of the IEEE Engineering in Medicine and Biology Society*, vol. 18, no. 3, pp. 263–273, Jun. 2010.

[368] E. Todorov and M. I. Jordan, "Optimal feedback control as a theory of motor coordination," *Nature Neuroscience*, vol. 5, no. 11, pp. 1226–1235, Nov. 2002.

[369] A. Ruina, "Nonholonomic stability aspects of piecewise holonomic systems," *Reports on Mathematical Physics*, vol. 42, no. 1, pp. 91–100, Aug. 1998. [Online]. Available: http://www.sciencedirect.com/science/article/pii/S0034487798800062

Address
EPFL STI IGM RRL
1015 Lausanne
Switzerland

Matthew A. Robertson

Robotics & Mechanical Design Engineer
thethoughtfulroboticist.com
Curriculum Vitae

Contact
matthew.robertson@epfl.ch
mattarobertson@gmail.com
(857) 243-1055

EDUCATION

2016-Present **Ph.D. Candidate** in Robotics, École Polytechnique Fédérale de Lausanne (EPFL), Lausanne Switzerland

2011 **M.S.E.** Mechanical Engineering: Control Theory, University of Michigan, Ann Arbor, MI, USA

2009 **S.B.** Mechanical Engineering: Robotics, Massachusetts Institute of Technology (MIT), Cambridge, MA, USA

EXPERIENCE

2016-Present **Graduate Student** — Reconfigurable Robotics Laboratory

Proposed thesis investigates soft robotic technologies and systems for wearable or assistive devices. Conceived, implemented and tested new fabrication, control, and system integration concepts with complex, multi-DoF soft actuation-based mechanical prototypes.

2015 **Robotics Mechanical Engineer** — HStar Technologies

Conceptual and detailed design and development of personal robotic systems for home and healthcare industries. Includes telepresence robots and assistive technologies for nursing.

2011-2015 **Research Engineer** — Intelligent Prosthetic Systems

Project Lead handling scientifically motivated design, fabrication, assembly and testing of advanced prosthetic devices under research. Includes novel mechanisms, low-power actuation, microcontroller and sensor integration (Inertial Measurement Units), and management of human-subject testing protocols and analysis.

2011-2015 **Research Engineering Assistant** — University of Michigan HBCL

Providing laboratory management, engineering support for graduate students in university Human Biomechanics and Control Laboratory.

2009-2012 **Contract Consulting** — MA, MI

Design and fabrication services for mechanical/electrical hardware prototypes. Completed projects include: windmill, tattoo machine, robotic positioning systems, marine mammal research testing apparatus, mechatronic children’s museum exhibit

2011 **Robotics Engineer** — Vishwa Robotics

Project Lead and design engineer for various DOD SBIR contract engineering projects.

2010-2011 **Graduate Research** — University of Michigan GRRC

Investigation and design of a pneumatic binary-actuation hyper-redundant robotic manipulator-arm.

2010 **Air Force Research Lab Internship** — Kirtland Air Force Base

Studied, designed, and modeled deployable systems for CubeSat standard micro satellites.

2009 **Research & Development Internship** — Aurora Flight Sciences

Designed, modeled, fabricated, and tested hardware, software, and electronics for prototype Micro Air Vehicles (MAV) and autonomous multi-vehicle coordination testing and demonstration.

2008 **Undergraduate Research** MIT D'Arbeloff Laboratory

Designed and built a heavy-duty, 2-axis, dual gantry system to position 60 lb payloads throughout a large workspace with 0.01 inch accuracy. Independent management of design, project planning, requisition, fabrication, and assembly.

2008 **Undergraduate Research** MIT D'Arbeloff Laboratory

Designed, built, and tested alpha-prototype robotic platform to investigate the feasibility of active pneumatic suction cup adhesion to aluminum aircraft "skin" for robotic assembly research.

TEACHING

2016-2018 **Graduate Teaching Assistant** EPFL / RRL Mechanical Engineering

Assisted Master's-level graduate course "ME-410: Mechanical product design and development", with focus on wearable and assistive technology. Specific topics include soft robotics and smart materials. Helped plan curriculum, taught lectures, designed and ran practical sessions, weekly update meetings, and semester-long project development.

2016 **Graduate Teaching Assistant** EPFL / RRL Mechanical Engineering

Assisted undergraduate course "ME-302: Mechanical Design Principles". Staffed weekly homework assistance, taught exam review session, and graded assignments and exams.

2007-2008 **Engineering Design Teacher** MIT Edgerton Center / TEC

Taught at MIT and instructed on subjects of design, computer modeling, physics, motor dynamics, and machine tool use. Students designed and fabricated remote controlled robots for competitions, and ridable machines (go-kart, DIY-Segway). Saturday program during multiple semesters, and month long summer / winter sessions.

SKILLS

- **Mechanical Design**
- **Soft Materials Robot Fabrication**
- **Modeling -** Solidworks, Alibre
- **Manufacturing -** Bridgeport, Smithy, Hardinge, Colchester, Makerbot, Epilog
- **Materials Testing -** Instron
- **Programming -** C/C++, Matlab, Java, VBA, Scheme, Processing
- **CNC Programming -** MasterCAM, OMAX, AlibreCAM
- **PCB, Circuit Fabrication**
- **Concept Sketch Drawing**

ACTIVITIES

- **FIRST Robotics** Team mentor, former student participant, 7 years
- **Singing** Men's college a cappella group, soloist, MITLogs.com
- **Art** Wood Carving, Painting, Drawing (various media)
- **Rock Climbing/Bouldering, Running, Hiking, Tough Mudder…ing?** Any excuse to be outside
- **Home Renovation** Demolition and Reconstruction of first owned house (3 years)
- Dreaming and Doing at **Hacker/Maker-spaces**
- **Hobby Engineering** Designing and building things for fun

GENERAL INTEREST KEYWORDS

Novel actuators
Soft robotic systems
Heuristic design
Dynamic walking robots
Decentralized control
Modular robotics
Smart materials
Bioinspired machines

PUBLICATIONS

M. A. Robertson, O. Kara, J. Paik, Soft pneumatic actuator driven origami inspired modular robotic ”pneumagami”, in **International Journal of Robotics Research,** In review, Submitted Jan. 2019.

M. A. Robertson, M. Murakami, W. Felt, J. Paik, A Compact Modular Soft Surface with Reconfigurable Shape and Stiffness, in **IEEE Transactions on Mechatronics.** vol. 24, no. 1, pp. 16-24, Feb. 2019.

M. A. Robertson, F. Efremov, J. Paik. RoboScallop: Bivalve inspired swimming robot. **IEEE Robotics and Automation Letters,** doi: 10.1109/LRA.2019.2897144, Feb. 2019

M. A. Robertson and J. Paik. New soft robots really suck: Vacuum-powered systems empower diverse capabilities, in **Science Robotics**, vol. 2, num. 9, p. eaan6357, 2017.

M. A. Robertson, H. Sadeghi, J. M. Florez and J. Paik. Soft Pneumatic Actuator Fascicles for High Force and Reliability, in **Soft Robotics**, vol. 4, num. 1, p. 23-32, 2017.5

G. Agarwal, M. A. Robertson, H. A. Sonar and J. Paik. Design and Computational Modeling of a Modular, Compliant Robotic Assembly for Human Lumbar Unit and Spinal Cord Assistance, in **Scientific Reports**, vol. 7, p. 14391, 2017.

S. Hauser, M. A. Robertson, A. J. Ijspeert,J. Paik. JammJoint: A Variable Stiffness Device Based on Granular Jamming for Wearable Joint Support. **IEEE Robotics and Automation Letters**. PP. 1-1. 10.1109/LRA.2017.2655109. 2017.

CONFERENCES

M. A. Robertson, F. Efremov, J. Paik. RoboScallop: A bivalve inspired swimming robot. *2019 IEEE International Conference on Robotics and Automation (ICRA).* Montreal, Canada, May 20-24, 2019.

M. A. Robertson, L. Dejace, S. Lacour, J. Paik. Bi-modal control of vacuum-powered soft pneumatic actuators with embedded liquid metal-based strain sensitive. *2019 IEEE International Conference on Soft Robotics (RoboSoft)*, Seoul, Korea, April 14-18, 2019.

M. A. Robertson, J. Paik. Low-inertia vacuum-powered soft pneumatic actuator coil characterization and design methodology. *2018 IEEE International Conference on Soft Robotics (RoboSoft)*, Livorno, Italy, April 24-28, 2018.

W. Felt, M. A. Robertson, J. Paik. Modeling Vacuum Bellows Soft Pneumatic Actuators with Optimal Mechanical Performance. *2018 IEEE International Conference on Soft Robotics (RoboSoft),* Livorno, Italy, April 24-28, 2018.

S. Walker, A. Firouzeh, M. Robertson, Y. Menguc, J. Paik. 3D Printed Soft Sensor-Actuator Wearable for Facial Rehabilitation, Initial Work. *2018 IEEE International Conference on Soft Robotics (RoboSoft),* Livorno, Italy, April 24-28, 2018.

M. A. Robertson and J. Paik. Foam-based Vacuum-powered Soft Pneumatic Actuators (V-SPAs) for safe robots. *Talk at Humanoids Conference Workshop: Can We Build Baymax? Part III*, November 15, 2017.

H. A. Sonar, S. D. Joshi, M. A. Robertson and J. Paik. Interactive soft pneumatic actuator skin. *Presented at IEEE/RSJ International Conference on Intelligent Robots and Systems*, Vancouver, BC, Canada, 2017.

M. A. Robertson and J. Paik. Practical control methods for vacuum driven soft actuator modules. *Talk at IEEE Intl. Conf. on Intelligent Robots and Systems (IROS) 2017,* September 24-28, 2017.

M. A. Robertson, J. Paik, A. Ijspeert and A. Wu. A low-cost, actuated passive dynamic walker kit for accessible research and education. *Talk at Dynamic Walking Conference*, Mariehamn, Finland, 2017.

M. A. Robertson and J. Paik. Trunk postural tracking of assistive soft pneumatic actuator belt. *Presented at Dynamic Walking Conference*, Holly, MI, 2016.

P. G. Adamczyk, M. A. Robertson, and A. D. Kuo. RoboFrog? Explosive Power from Elastic Tendons Without Escapements. *Presented at Dynamic Walking Conference,* Pensacola, FL, 2012.

4 of 3

Ce document a été imprimé au Centre d’impression EPFL,
imprimerie climatiquement neutre, certifiée myClimate.